

Chemical Evolution of Galactic Systems

by

Yeshe Fenner, BSc (Hons)

A dissertation presented in fulfillment
of the requirements for the degree of
Doctor of Philosophy
at Swinburne University Of Technology

March, 2005



Abstract

This thesis explores the chemical signatures of galaxy formation and evolution using a software package designed specifically for this investigation. We describe the development of this multi-zone chemical evolution code, which simulates the space-time evolution of stars, gas and a vast array of chemical elements within galactic systems. We use this tool to analyse observations of a wide range of astrophysical systems.

The chemical evolution code is first calibrated using empirical constraints from the Milky Way. These simulations help shed light on the nature of the gas accretion processes that fueled the formation of our Galaxy. We demonstrate the importance of low- and intermediate-mass stars in explaining the elemental and isotopic abundance patterns measured in Galactic stars. An intriguing question in astrophysics is whether pollution from intermediate-mass stellar winds is responsible for anomalous abundances in globular cluster stars. We test this scenario by modelling the formation and chemical evolution of a globular cluster.

Recently, the most detailed abundance pattern ever measured beyond the local universe was obtained for a high-redshift quasar absorption cloud, providing an exciting opportunity to explore early conditions of galaxy formation. We compare the chemical abundances in this distant object with predictions from a series of models, in order to gain insight into the protogalaxy's age and star formation history. We continue investigating the high-redshift universe, turning our attention to the issue of space-time variations in the fine-structure constant, as suggested by quasar absorption-line constraints. An excess abundance of heavy Mg isotopes in the absorbing clouds could partly account for the data, without needing to invoke variations in fundamental constants of nature. An enhanced early population of intermediate-mass stars could lead to such extreme Mg isotopic ratios, but we show that additional chemical consequences of this scenario conflict with observations.

In the beginning the Universe was created. This has made a lot of people very angry and been widely regarded as a bad move

– *Douglas Adams*

Everything is vague to a degree you do not realize till you have tried to make it precise

– *Bertrand Russell*

It is nice to know that the computer understands the problem. But I would like to understand it too

– *Eugene Wigner*

Acknowledgements

It is an enormous pleasure to thank my supervisor, Brad Gibson, for his unceasing support, generosity and good advice. It was through Brad's initiative and encouragement that I was lucky enough to become involved in many rewarding intercollegiate, interstate and international collaborations during my PhD. His appreciation of the importance of communication and collaboration is a valuable lesson that I hope will stay with me. I am especially indebted to Brad for showing so much faith in me and looking out for my interests. On a personal level, it has been a joy to work with someone so fun, friendly and enthusiastic.

A special thanks must go to the Monash gang - John Lattanzio, Amanda Karakas, Simon Campbell - for running innumerable nucleosynthesis models and providing calculations prior to publication. Their results influenced the direction of much of my thesis and I'm grateful to them for granting me early access.

I wish to thank: Marco Limongi, Alessandro Chieffi, Maria Lugaro and Roberto Gallino, for sharing their model predictions prior to publication; Jason Prochaska, for hosting me at UC Santa Cruz and introducing me to the fascinating DLAs; Chris Flynn; Charley Lineweaver; Michael Murphy; Lisa Kewley; David Yong and so many others.

Thanks to all the students, staff and astronomers at Swinburne. Special thanks to Paul Bourke, for working his magic with format conversions *every* time the poster competition rolled around.

I'm grateful to Swinburne University for a Chancellor's Research Scholarship that kept me off the streets for the last few years, to the AFUW for a Daphne Elliot bursary, and to the ASA for a travel grant.

Thanks to all my family: Mum - for telling me that I was capable of doing anything (except paint!) - and Dad; Tahli - I'm chuffed that we got to share the experience of doing our PhDs in the same city at the same time. The same *can't* be said for you, Nic! But you nevertheless warrant a huge thank-you for coercing me into going on holiday precisely when I was supposed to be submitting this thesis!

Contents

Declaration	vii
Publications	viii
1 Introduction	1
2 Galactic Chemical Evolution	6
2.1 Introduction	6
2.2 Structure and Formation of the Galaxy	7
2.3 Homogeneous Models	9
2.3.1 Basic Ingredients	9
2.3.2 Observational Constraints	14
2.3.3 Uncertainties and Weaknesses	18
3 The Metallicity Distribution Function	22
3.1 Introduction	22
3.2 The Model	24
3.2.1 Infall scheme	24
3.2.2 Star formation formalism	25
3.2.3 Initial mass function	25
3.2.4 Properties of the halo, thick disk, and thin disk components	25
3.3 Yields	26
3.3.1 Massive stars	26
3.3.2 Low- and intermediate-mass stars	27
3.3.3 Type Ia supernovae	27
3.4 Results	27
3.4.1 The solar neighbourhood	27
3.4.2 Lifetime effects and MDFs in external galaxies: A note of caution	32
3.5 Conclusions	34
4 Chemical Evolution of Magnesium Isotopes	37
4.1 Introduction	37
4.2 The Chemical Evolution Model	38

4.3	Results & Discussion	39
4.4	Conclusions	46
5	The Galactic Habitable Zone	48
5.1	Introduction	48
5.2	Method	48
5.3	Results	51
6	Globular cluster self-pollution	55
6.1	Introduction	55
6.2	The chemical evolution model	57
6.2.1	First stage: Initial enrichment	57
6.2.2	Second stage: Globular cluster formation and evolution	58
6.2.3	Chemical yields from AGB stars	58
6.3	Results	60
6.4	Conclusions	68
7	Stellar abundance gradients	70
7.1	Introduction	70
7.2	Absorption Line Imaging	72
7.2.1	The Taurus Tunable Filter (TTF) Instrument	72
7.2.2	Choice of Lick indices and blocking filters	72
7.2.3	Wavelength calibration	74
7.3	Stellar observations and calibration	74
7.4	Galaxy Observations	79
7.5	Galaxy data reduction and analysis	79
7.5.1	Data Reduction	80
7.5.2	Data Analysis	81
7.5.3	Errors	83
7.6	Results	84
7.7	Individual Galaxies	86
7.7.1	NGC 5968 - SBab	86
7.7.2	NGC 6221 - SBc	87
7.7.3	NGC 6753 - Sb	87
7.7.4	NGC 6814 - SBbc	88
7.7.5	NGC 6935 - SBa	88
7.7.6	NGC 7213 - Sa	88
7.7.7	NGC 7412 - SBb	89
7.7.8	NGC 7637 - Sc	89
7.8	Summary	89

8	Chemical Evolution of DLAs	99
8.1	Introduction	99
8.2	Observations	100
8.3	The Model	102
8.3.1	Analytical Prescriptions	103
8.3.2	Stellar Yields and Lifetimes	103
8.4	Results	106
8.4.1	Model versus Data	106
8.4.2	Model Sensitivity	107
8.4.3	Discussion of Individual Elements	116
8.5	Summary and Future Directions	122
9	Varying α and AGB pollution	124
9.1	Introduction	124
9.1.1	Evidence for varying α from QSO absorption systems?	125
9.1.2	Isotopic abundance evolution?	127
9.2	Nucleosynthesis of magnesium isotopes	130
9.3	Chemical evolution models	130
9.3.1	Infall scheme	131
9.3.2	Initial mass function (IMF)	132
9.3.3	Stellar Yields and Lifetimes	133
9.3.4	Comparison with Ashenfelter et al. (2004)	134
9.4	Results	136
9.4.1	Type Ia supernova rate and the age-metallicity relationship	136
9.4.2	Magnesium isotopic ratio	139
9.4.3	Nitrogen	140
9.4.4	$^{13}\text{C}/^{12}\text{C}$ abundance ratio	143
9.4.5	Silicon, aluminium and phosphorus	144
9.4.6	Uncertainties	147
9.5	Discussion	150
9.5.1	Summary of Results	150
9.5.2	Other arguments for and against an early, IM-enhanced IMF	151
9.6	Conclusions	153
10	Conclusions	155
10.1	Summary	155
10.2	Future directions	157
	References	160
A	Nomenclature	177

List of Figures

2.1	Nucleosynthesis production factors for massive stars	11
2.2	Radial variation of the Milky Way MDF	18
2.3	Mg isotopic evolution at the solar radius	19
2.4	Evolution of Type II SN rate and metallicity	20
3.1	SFR and MDF at the solar radius	29
3.2	Solar radius age-metallicity-relation	30
3.3	SFR for a halo model	33
3.4	Predicted halo MDFs	34
3.5	Cumulative MDF for model halo	35
4.1	Mg isotopic evolution at the solar radius as a function of AGB con- tribution	40
4.2	Mg isotopic evolution as a function of radius with AGBs	41
4.3	Mg isotopic evolution as a function of radius without AGBs	42
4.4	Mg isotopic evolution as a function of yields	44
4.5	$^{26}\text{Mg}/^{24}\text{Mg}$ yield vs initial stellar mass	45
4.6	Mg isotopic evolution for different IMF	47
5.1	Age-metallicity relation	50
5.2	Evolution of the supernova danger factor	51
5.3	Space-time distribution of the Galactic habitable zone for complex life	52
5.4	Space-time distribution of the Galactic habitable zone for any life . .	53
6.1	Na-O and Al-Mg anti-correlations in globular cluster NGC 6752	61
6.2	Mg isotopic ratios versus O, Na, Mg and Al for NGC 6752	64
6.3	[N/Fe] versus [C/Fe] for NGC 6752	66
6.4	Predicted evolution of C, N, O in NGC 6752	68
7.1	Stellar spectral scan with the TTF	75
7.2	Relationship between measured TTF and Lick indices for Mg ₂ and Fe5270	78
7.3	TTF results for NGC 5968	90
7.4	TTF results for NGC 6221	91

7.5	TTF results for NGC 6753	92
7.6	TTF results for NGC 6814	93
7.7	TTF results for NGC 6935	94
7.8	TTF results for NGC 7213	95
7.9	TTF results for NGC 7412	96
7.10	TTF results for NGC 7637	97
8.1	Logarithmic difference between the observed and predicted DLA abundance pattern	107
8.2	Predicted abundance pattern as a function of age	108
8.3	Predicted abundance pattern as a function of metallicity	112
8.4	Massive star elemental production factors	113
8.5	Sensitivity of DLA abundance pattern to IMF upper mass limit	115
8.6	Predicted DLA abundance pattern with different massive star yields	116
8.7	Evolution of [S/Fe] and [S/Zn] versus time and metallicity	119
9.1	Isotopic structures for Mg and Si transitions and sensitivity of $\Delta\alpha/\alpha$ to Mg and Si variations	128
9.2	Evolution of isotopic ratios with metallicity for C, Mg, Si, Ti, Cr, Fe, Ni and Zn	129
9.3	Shape of the IM-enhanced IMF	133
9.4	Evolution of Type Ia supernovae rate and metallicity as a function of IMF	138
9.5	Mg isotopic ratio as a function of [Fe/H] with and without IM-enhanced IMF	141
9.6	Evolution of [N/ α] as a function of [α /H]	142
9.7	Sensitivity of [N/ α] vs [α /H] to the star formation efficiency	143
9.8	Present-day gas surface density profile	144
9.9	Evolution of $^{13}\text{C}/^{12}\text{C}$ as a function of [Fe/H]	145
9.10	Evolution of $(^{29}\text{Si}+^{30}\text{Si})/^{28}\text{Si}$ as a function of [Fe/H]	146
9.11	Variation of [Al/Fe] as a function of [Fe/H]	147
9.12	Variation of [P/Fe] as a function of [Fe/H]	148

List of Tables

2.1	Milky Way Properties	8
6.1	Intermediate Mass Stellar Yields	60
7.1	Stellar Lick index fit parameters	77
7.2	Galaxy Properties	79
7.3	Galaxy observation log	80
7.4	Central indices and disk gradients	86
8.1	Elemental Abundances in DLA-B/FJ0812+32	101

Declaration

This thesis contains no material that has been accepted for the award of any other degree or diploma. To the best of my knowledge, this thesis contains no material previously published or written by another author, except where due reference is made in the text of the thesis. All work presented is primarily that of the candidate. Brad Gibson was involved in the planning and direction of much of this thesis. The co-authors on the following list of publications contributed ideas for the content and/or editing of the papers. For papers on which I am not the first author, further details of the relative contributions of the respective authors are given below.

Portions of Chapter 2 have been published as Gibson, B. K., Fenner, Y., Renda, A., Kawata, D. & Lee, H. C. “Galactic Chemical Evolution”, *PASA*, 20, 401, 2004.

Chapter 3 has been published as Fenner, Y. & Gibson, B. K., “Deriving the Metallicity Distribution Function of Galactic Systems”, *PASA*, 20, 189, 2003.

Chapter 4 has been published as Fenner, Y., Gibson, B.K., Lee, H., Karakas, A., Lattanzio, J., Chieffi, A., Limongi, M. & Yong, D., “The Chemical Evolution of Magnesium Isotopic Abundances in the Solar Neighbourhood”, *PASA*, 20, 340, 2003.

Lineweaver, C. H., Fenner, Y. & Gibson, B. K., “The Galactic Habitable Zone and the Age Distribution of Complex Life in the Milky Way”, *Science*, 303, 2004, forms the basis of Chapter 5. Charley Lineweaver initiated this investigation and contributed to the text of the manuscript, while I performed the modelling and analysis and prepared the text of the paper.

Chapter 6 has been published as Fenner, Y., Campbell, S., Karakas, A. I., Lattanzio, J. C. & Gibson, B. K., “Modelling self-pollution of globular clusters from AGB stars”, *MNRAS*, 353, 789, 2004.

Ryder, S. D., Fenner, Y. & Gibson, B. K., “Stellar abundance gradients in galactic disks. I. Method and spectral line gradients”, *MNRAS*, 358, 1337, 2005, forms the basis of Chapter 7. Stuart Ryder initiated this study and was chiefly responsible for obtaining the observations, choosing the telescope setup and preparing sections 7.1 & 7.2. I was involved in the data collection and was responsible for data reduction, analysis, and writing sections 7.3-7.8.

Chapter 8 has been published as Fenner, Y., Prochaska, J. X. & Gibson, B. K., “Constraints on Early Nucleosynthesis from the Abundance Pattern of a Damped Ly-alpha System at $z = 2.626$ ”, *ApJ*, 606, 116, 2004.

Chapter 9 has been published as Fenner, Y., Murphy, M. T. & Gibson, B. K., “On variations in the fine-structure constant and limits on AGB pollution of quasar absorption systems”, *MNRAS*, 358, 468, 2005.

Minor alterations have been made to these works in order to maintain consistency of style.

Yeshe Fenner

March, 2005

Publications

The following publications have arisen from the work presented in this thesis:

1. *On variations in the fine-structure constant and limits on AGB pollution of quasar absorption systems*
Fenner, Y., Murphy, M. T. & Gibson, B. K.
Monthly Notices of the Royal Astronomical Society, 2005, accepted
2. *Stellar abundance gradients in galactic disks. I. Method and spectral line gradients*
Ryder, S. D., Fenner, Y. & Gibson, B. K.
Monthly Notices of the Royal Astronomical Society, 2005, accepted
3. *Modelling self-pollution of globular clusters from AGB stars*
Fenner, Y., Campbell, S., Karakas, A. I., Lattanzio, J. C. & Gibson, B. K.
Monthly Notices of the Royal Astronomical Society, 2004, 353, 789
4. *Contrasting the chemical evolution of the Milky Way and Andromeda galaxies*
Renda, A., Kawata, D. K., Fenner, Y & Gibson, B. K.
Monthly Notices of the Royal Astronomical Society, in press
5. *On the origin of fluorine in the Milky Way*
Renda, A., Fenner, Y, Gibson, B. K., Karakas, A. I., Lattanzio, J. C., Campbell, S., Chieffi, A., Cunha, K. & Smith, V. V.
Monthly Notices of the Royal Astronomical Society, 2004, 361
6. *Constraints on Early Nucleosynthesis from the Abundance Pattern of a Damped Ly-alpha System at $z = 2.626$*
Fenner, Y., Prochaska, J. X. & Gibson, B. K.
The Astrophysical Journal, 606, 116, 2004
7. *The Galactic Habitable Zone and the Age Distribution of Complex Life in the Milky Way*
Lineweaver, C. H., Fenner, Y. & Gibson, B. K.
Science, 303, 2004
8. *Photometric Properties of White Dwarf Dominated Halos*
Lee, H.-c., Gibson, B., Fenner, Y., Brook, C., Kawata, D., Renda A., Holopainen, J., Flynn, C.
Publications of the Astronomical Society of Australia, 2004, 21, 153
9. *Galactic Chemical Evolution*
Gibson, B. K., Fenner, Y., Renda, A., Kawata, D. & Lee, H. C.
Publications of the Astronomical Society of Australia, 20, 401, 2004

10. *The Chemical Evolution of Magnesium Isotopic Abundances in the Solar Neighbourhood*
Fenner, Y., Gibson, B. K., Lee, H.-c., Karakas, A. I., Lattanzio, J. C., Chieffi, A., Limongi, M. & Yong, D.
Publications of the Astronomical Society of Australia, 20, 340, 2003
11. *Deriving the Metallicity Distribution Function of Galactic Systems*
Fenner, Y. & Gibson, B.K.
Publications of the Astronomical Society of Australia, 20, 189, 2003
12. *A Limit on the Metallicity of Compact High-Velocity Clouds*
Sembach, K. R., Gibson, B. K., Fenner, Y. & Putman, M. E.
The Astrophysical Journal, 572, 178, 2002
13. *Galaxy Evolution tool: Construction and Applications*
Fenner, Y., Gibson, B. K. & Limongi, M.
Astrophysics and Space Science, 281, 537, 2002

Chapter 1

Introduction

The Big Bang created hydrogen, helium and trace amounts of lithium, but what produced the heavier elements that pervade the universe and from which planets and we ourselves are composed? Fred Hoyle (1946) provided the answer to this most fundamental of questions when he surmised that the hot dense environments of stars were ideal kitchens for manufacturing metals¹ using the basic ingredients of H and He. Thus, generations of stars coalescing, synthesising new elements, and releasing their nuclear debris when they evolve and die, are largely responsible for the abundance of the elements throughout the cosmos. By investigating Galactic Chemical Evolution (GCE), one hopes to trace the distribution of the elements from the present-day back to the early universe and in doing so, gain insight into the lives of galaxies.

The study of galaxy formation and evolution is one of the most active fields in cosmology and extragalactic astronomy. From a theoretical perspective, models which detail the evolution and distribution of chemical elements within stars and the interstellar medium provide great insight into the behaviour of galaxies and their interaction with the environment. Chemical abundance patterns reflect the cumulative history of star formation and gas exchange and GCE models are powerful tools for interpreting these chemical signatures. They take advantage of the fact that chemical species have different characteristic production sites. Thus the *relative* abundance of the elements reveals the role played by different types of chemical factories, which helps us decipher the history of galactic systems.

Knowledge of the distribution of the elements began to blossom in the 1920s when Cecilia Payne-Gaposhkin (1925) lay the groundwork for interpreting stellar

¹The terms *metals* and *heavy elements* are used by astronomers to denote all elements heavier than helium.

spectra, followed shortly thereafter with Henry Norris Russell’s (1929) analysis of the solar abundance pattern. Observers have since measured abundances in an extraordinary number of local and extragalactic stars, planetary nebulae, as well as in the intervening gas *between* stars and galaxies. Indeed, the observational progress has been so rapid that theoretical models have struggled to keep pace. While the models have certainly had reasonable success in reproducing the mean behaviour of many chemical elements in nearby stars, wide variations and intriguing trends in elemental abundances in a vast range of objects tell of details and complexities that we are only beginning to understand.

This thesis describes the development and application of a multi-zone chemical evolution code that simulates the space-time evolution of chemical elements, stars, and gas within galactic systems. This galaxy evolution tool (`GEtool`) has the power to interpret observed chemical properties of a range of astrophysical systems in terms of distinctive formation and evolutionary scenarios, thus shedding light on conditions in the early universe and the path leading to the cosmos as we see it today. The flexibility of `GEtool` has allowed its application to the study of not only galaxies, but also some of the earliest tracers of galaxy formation; from ancient globular clusters to massive gas clouds in the distant universe. Specific applications are discussed in Chapters 3 – 9: progressing from the local galactic neighbourhood in earlier chapters to the high-redshift universe in later chapters. A broad range of systems will be investigated that, at first glance, may not seem closely connected. However, objects like globular clusters and high-redshift absorption systems are likely building blocks of present-day galaxies, including our own Milky Way. This thesis is itself a building block in the ambitious quest to reveal the universal principles governing the formation and evolution of galaxies and their environments.

Firstly, we present the framework of the code in Chapter 2. Chemical evolution models of galaxies need to account for the collapse of gas and metals into stars, the synthesis of new elements within these stars, and the subsequent release of metal-enriched gas as the stars lose mass and die. `GEtool` numerically solves the equations governing the rate of change of gas mass and elemental abundances due to star formation, supernovae feedback, and gas flows in and out of a galactic system, as a function of location and time. The attraction of this type of model is its detailed treatment of the production of chemical species from different types of stars². Chapter 2 summarises the details of `GEtool`, emphasising the key inputs,

²An alternative method of studying galaxy evolution using chemo-dynamical simulations yields

outputs and observational constraints.

Having built the computational framework, the code is then calibrated against the wealth of observations of our own Galaxy, since they provide the most stringent set of empirical constraints. In Chapter 3, we subject `GEtool` to one of the strongest constraints - the metallicity distribution function (MDF) of long-lived stars in the solar neighbourhood. A reliable MDF of local stars yields important information about the age and formation history of our pocket of Milky Way, and we demonstrate that the exceptionally accurate recent K-dwarf survey from Kotoneva et al. (2002) gives a better distribution of metallicities than previous surveys based on the slightly more massive G-dwarf stars. In particular, we caution that G-dwarf MDFs can be biased toward *higher* metallicities as finite stellar lifetimes preferentially remove older metal-poorer stars from the sample. We show that the K-dwarf MDF is well matched by allowing moderate metal-enrichment of the accreting disk-gas, as motivated by recent detections of metals in high-velocity clouds (Sembach, Gibson, Fenner & Putman 2002).

In recent years, higher precision instruments have enabled the abundance of individual isotopes of Mg to be measured in nearby stars. Magnesium is one of the few elements whose isotopic composition can be determined in stars and this information provides a useful probe into the nucleosynthesis history of the Milky Way because each isotope is produced preferentially in different classes of star. The evolution of Mg isotopes in the local Galaxy is simulated in Chapter 4, incorporating detailed calculations of intermediate-mass stellar yields of ^{25}Mg and ^{26}Mg . The abundance of the neutron-rich magnesium isotopes observed in metal-poor stars is explained as a consequence of the metallicity-dependent contribution from intermediate-mass stars (IMS).

Having successfully applied `GEtool` to explain stellar abundances in the solar neighbourhood, we turn our attention to the Milky Way as a whole. The search for terrestrial planets around other stars is one of the highest profile areas of astronomy and is the driving force behind upcoming large NASA and ESA satellite missions, including Kepler, Darwin, and the Terrestrial Planet Finder. Terrestrial planets capable of harbouring complex life are more likely to reside where there is favourable metallicity for planet-formation, sufficient time for evolution, and freedom from frequent nearby supernova explosions. These minimum requirements define the so-

important kinematic and structural information but tends to come at the expense of precise chemical information.

called Galactic Habitable Zone (GHZ). In Chapter 5, we identify the position, size, and time evolution of the GHZ using simulations of Galactic chemical evolution. Irrespective of the *absolute* probability of the existence of extraterrestrial life, we predict an age distribution for complex life that *might* inhabit our Galaxy – with most of the stars in the GHZ being older than the Sun.

The important chemical contribution from IMS, which was highlighted in Chapter 4, is further explored in Chapter 6 in an effort to explain anomalous abundances in globular clusters (GCs). Occupying the Galactic halo, GCs were historically considered to be the simplest stellar populations, being both coeval and monometallic. But these very old, gravitationally-bound clusters of stars are much more complex than first thought – many exhibit huge star-to-star variations in certain elements, which is not seen in field stars at the same metallicity. The peculiar abundances are evident in GC stars at very different stages of evolution, implying that the abundance anomalies were already present in the gas from which the stars formed. A popular theory in the literature has involved “self-pollution” of the GC from the weak stellar winds of IMS. To test this scenario, Chapter 6 presents the first-ever quantitative model of the formation and chemical evolution of a globular cluster. We find that current theories of IMS nucleosynthesis are unable to account for the observations.

While many aspects of our own Galaxy’s history are well understood, it is essential to compare against external galaxies if we are to uncover general properties of galaxy evolution. Chapter 7 describes an observational initiative to measure the radial variation of Fe and Mg in disk galaxies spanning a wide morphological range. Relative abundances of elements like Mg and Fe, whose release into the interstellar medium occur on different characteristic timescales, provide clues to a galaxy’s star formation history and is a vital constraint on theories of galaxy evolution. While O, N, and S have long been observed in emission from H II regions in external galaxies, this study is one of the first to measure Mg and Fe across the face of spiral disks from stellar absorption features. We present radial profiles of the Lick/IDS spectral indices Mg_2 and Fe5270 in eight spiral galaxies and discuss signatures of phenomena including merger-induced star formation, H II rings, and galactic bars in individual galaxies.

Having been well calibrated against the Milky Way, the chemical evolution code is extended for application to high-redshift galaxies and protogalaxies. A cosmologically important group of high-redshift objects are Damped Lyman- α Absorbers

(DLAs). These high column density neutral gas clouds pervade the universe and are detected from their absorption of light from a background quasar. Despite accounting for most of the neutral hydrogen at all redshifts their nature remains a mystery – are they outer regions of protospirals, are they dwarf galaxies, do they probe different galactic populations and evolutionary stages at different redshifts? Analysis of their chemical properties will help answer these questions. Recently, the most detailed abundance pattern ever measured beyond the local universe was obtained for a high- z DLA (Prochaska, Howk & Wolfe 2003), providing a new avenue for exploring early conditions of galaxy formation. We study the chemical evolution of this DLA in Chapter 8, finding its abundance pattern consistent with the predictions of a model in which the interstellar enrichment is dominated by massive stars with a moderate contribution from Type Ia supernovae. We also suggest that this unique high- z testbed of nucleosynthesis points to a possible need for supplemental sources of Mg and Zn.

In the past few years, evidence has emerged that the fine-structure constant, $\alpha \equiv e^2/\hbar c$, may have been smaller in high-redshift quasar absorption systems than the value measured today on Earth (e.g. Murphy, Webb & Flambaum 2003). This result relies on comparing relative wavelength separations between spectral lines in absorption systems with those in the laboratory. This technique is sensitive to the isotopic composition of a crucial “anchor” element like Mg, as it shifts the line centroid. If absorbers used in these studies contained enhanced populations of intermediate-mass stars – the dominant factories for the heavy Mg isotopes at low metallicities – spurious wavelength shifts will be introduced that mimic a variation in α . In Chapter 9, lower-redshift quasar absorption-line data are combined with DLA data at higher redshift, to limit the level of pollution of these systems from IMS. We show that a significantly enhanced population of IMS at early times would produce vastly more nitrogen than is observed in DLAs, and we make the testable prediction that these absorbers would exhibit a detectable excess of ^{13}C relative to ^{12}C .

Understanding how individual galactic systems form is itself an enormous challenge, yet one ultimately wishes to go even further, and reveal how these separate objects relate to each other. In Chapter 10, we summarise the results presented in this thesis and outline future research plans aimed at uncovering connections between galaxies and the intergalactic medium at low- and high-redshift.

Chapter 2

Galactic Chemical Evolution

This chapter is based upon Sections 1-3, written by Y. Fenner, contained in Gibson et al. 2004, PASA, 20, 401

2.1 Introduction

Stars and interstellar gas in galaxies exhibit diverse chemical element abundance patterns that are shaped by their environment and formation histories. The aim of Galactic Chemical Evolution (GCE) is to use the observed abundances to unlock earlier epochs in the Universe, probe the mechanisms of galaxy formation, and gain insight into the evolution of stellar systems.

Models for the chemical evolution of galaxies need to account for the collapse of gas and metals into stars, the synthesis of new elements within these stars, and the subsequent release of metal-enriched gas as stars lose mass and die. An additional feature of most models is the ongoing accretion of gas from outside the system. The most sophisticated models also incorporate a self-consistent treatment of the system's dynamics - both collisionless and dissipative components - either under idealised (semi-cosmological) conditions or within a full cosmological framework. Coupling GCE codes to a spectrophotometric evolution package further ensures that the models are constantly tested against the observational constraints.

Semi-analytic homogeneous models make simplifying assumptions that enable the *mean* trends of galactic systems to be calculated by numerically solving a set of equations governing the formation, destruction, and distribution of the elements as they cycle through gas and stars. One strength of these models is that they typically have the fewest number of free-parameters, making convergence to a *unique* solution more likely. A weakness of homogeneous models is the inherent assumption that stellar ejecta from dying stars is instantly mixed back into the ambient

interstellar medium (ISM). Inhomogeneous GCE models relax this so-called “instantaneous mixing approximation” in a semi-analytical manner, allowing consideration of observed trends in *dispersion* in various galactic observables. The self-consistent treatment of not only GCE, but the dynamics of a galaxy’s gas, stars, and dark matter, remains the purview of chemodynamical codes. Each of the above are complementary tools for deconstructing the formation and evolution of systems such as our Milky Way: semi-analytical models can cover a range of parameter space that a chemodynamical code cannot, due to the many orders of magnitude difference in the respective computational demands, while the latter afford a coupling of the dynamics of the system to that of the GCE, in a manner not otherwise available.

This chapter presents an overview of contemporary research in the field of Galactic chemical evolution. We describe the most popular formation and evolutionary scenarios, the relationships between different components of the Galaxy, and the principles of homogeneous semi-analytical models. For seminal reviews tracing the development and principles of this topic, the reader is referred to Tinsley (1980), Matteucci (2001), and references therein.

2.2 Structure and Formation of the Galaxy

The thin disk and bright inner bulge are the brightest components of the Milky Way. They are housed within a much more extended and diffuse spheroidal stellar halo – as distinct from the dark matter halo. In addition, a fourth main component – the thick disk – was identified by Gilmore & Reid (1983). They found that star counts obtained by an extensive UK Schmidt photometric survey were well fitted by a multi-component model of stellar distribution consisting of: 1) a thin disk, 2) thick disk and 3) halo. This three-component model breaks down within the central kpc of the Galaxy where a dense metal-rich bulge begins to dominate (Gilmore, Wyse & Kuijken 1989). The thick disk component has an exponential scale height of 1350 pc – about four times greater than the scale height of the thin disk – and comprises $\sim 2\%$ of the nearby stars. Photometric studies of external galaxies had already established that thick disks are common to spirals (van der Kruit & Searle 1982). A popular explanation for the presence of thick disks is that mergers with smaller satellites during early times heated the thin disk (Wyse & Gilmore 1993).

In order to distinguish individual populations of stars, one wishes to know not

Table 2.1: Milky Way Properties

	mean	mean	Scaleheight	Scalelength
	Age (Gyr) ^a	[Fe/H] ^a	(kpc)	(kpc)
Halo	14	-1.78	Effective Radius	$\sim 2.7^b$
Thick disk	11	-0.78	$\sim 0.75^c$	3.5^c
Thin disk	5-7	-0.14	$\sim 0.33^c$	2.25^c
Bulge	10	0	Effective Radius	$\sim 1.2^d$

^aRobin et al. 2003^bde Vaucouleurs profile - Buser et al. 1998^cChen et al. 2001^dde Vaucouleurs profile - Yoshii & Rodgers 1989

just the spatial distribution of stars, but also their kinematics, chemical abundances, and ages. A complete dataset of this information should enable one to reconstruct the formation and evolution of the Milky Way. Through a number of surveys, including the Basel Halo Program and the Hipparcos mission, we are in a position to piece together the history of our Galaxy and answer questions relating to the order in which the Galactic components formed, whether they evolved independently of one another, and how important merging has been in assembling the Milky Way. The mean age and metallicity of the halo, thick disk, thin disk, and bulge are presented in Table 2.1.

Traditionally two scenarios have competed to explain the formation of the Milky Way:

- 1) The first scenario, proposed by Eggen, Lynden-Bell & Sandage (1962), describes the rapid monolithic collapse of a protogalactic gas cloud to form the halo. The Galactic disk would have subsequently formed as the residual gas dissipationally collapsed. This would naturally give rise to two populations of stars: an older, more metal-poor group found in the halo; and a younger, metal-rich group orbiting closer to the Galactic midplane.
- 2) Searle & Zinn (1978) offered an alternative to the monolithic collapse picture, proposing that the Galaxy was constructed from smaller cloud fragments, in which stars may have already started forming.

The Galaxy's true formation history is likely to lie somewhere between the two extremes of primordial collapse and hierarchical formation. Chemical properties of stars provide important clues into puzzle of the Galaxy's formation. The relative abundances of certain elemental species act as "cosmic clocks", by which the forma-

tion timescales of various stellar populations can be determined. A popular cosmic clock is the ratio of an element like oxygen, that is born mostly in massive very short-lived stars, and an element like iron, whose creation is linked to lower mass longer-lived progenitors (Gilmore, Wyse, & Kuijken 1989).

2.3 Homogeneous Models

Homogeneous GCE models have traditionally formed the cornerstone of this field and consequently have a rich literature to draw upon. The basic ingredients, observational constraints, and several weaknesses are highlighted below.

2.3.1 Basic Ingredients

The main ingredients of homogeneous GCE models are outlined below and we discuss their relationship to one another through the basic set of chemical evolution equations.

- **Stellar Yields and Lifetimes:** Almost all elements heavier than helium originate from stars. Stars enrich the ISM with their own unique pattern of elements depending on their mass and initial metallicity. The predicted stellar yields consequently form the backbone of the study of GCE. The grids of yields utilised in the models are the outcome of computations of stellar evolution and vast networks of nuclear reactions. For the purposes of chemical evolution, stars are often divided into three categories:

Massive stars ($m \gtrsim 10 M_{\odot}$) evolve more quickly than lower mass stars, despite having a greater supply of fuel to exhaust. This is because larger gravitational potential energy leads to higher core temperatures and densities, which hastens the rate of nuclear reactions and fuel consumption. The death of massive stars is marked by a violent supernova (SN), leaving behind a neutron star or black hole. Although massive stars are much rarer than their lower mass counterparts, they are the main source of most of the heavy elements (i.e. metals) in the Galaxy. Figure 2.1 shows the production factors from massive stars predicted by the detailed nucleosynthesis calculations of Woosley & Weaver (1995, *left panel*) and the FRANEC code (kindly provided by A. Chieffi, private communication;

FRANEC is described in Chieffi & Limongi 2002, *right panel*).¹ The dotted line at $[X/O] = 0$ indicates the solar elemental abundance pattern relative to O. The solar abundance pattern of most metals is adequately reproduced by massive stars but C, N and the iron-peak elements require additional production sites.

Low- and intermediate-mass stars (LIMS) live longer than their massive star counterparts, because their lower densities imply decreased nuclear fuel consumption rates. LIMS greatly outnumber the heavier stars but do not produce significant quantities of many elements besides helium, carbon, nitrogen, and certain isotopes, which are created through hydrostatic burning and expelled in stellar winds and planetary nebulae (e.g. van den Hoek & Groenewegen 1997). Very low mass stars ($m \lesssim 1 M_{\odot}$) have lifetimes comparable to the age of the Galaxy and therefore serve to lock up the gas supply.

LIMS in binary systems may culminate in powerful supernovae explosions classed as Type Ia. The exact physical mechanisms behind Type Ia supernovae (SNe Ia) are still an open question but one popular theory holds that the mass lost by a binary star as it evolves is accreted by its smaller white dwarf (WD) companion until the WD can no longer be sustained by electron degenerate pressure. Then the entire mass of the WD is ejected in a violent explosion that converts much of the stellar material into iron (e.g. Iwamoto et al. 1999).

- **Initial Mass Function (IMF):** The precise form of the IMF dictates the number of stars born in a given mass interval in each generation of stars. This in turn sets the rate at which different elements are released into the ISM, thus influencing both the *relative* and *absolute* elemental abundances. Most IMFs in the literature consist of simple single- or multi-component power law specified over a mass range from $m \sim 0.1 M_{\odot}$ to an upper mass limit typically between 40–100 M_{\odot} (e.g. Salpeter 1955; Scalo 1986; Kroupa, Tout & Gilmore 1993).
- **Star Formation Rate (SFR):** While laws of star formation can be calculated from first principles, chemical evolution models invariably use a functional

¹Another comparison of massive star yields can be found in Gibson, Loewenstein & Mushotzky (1997).

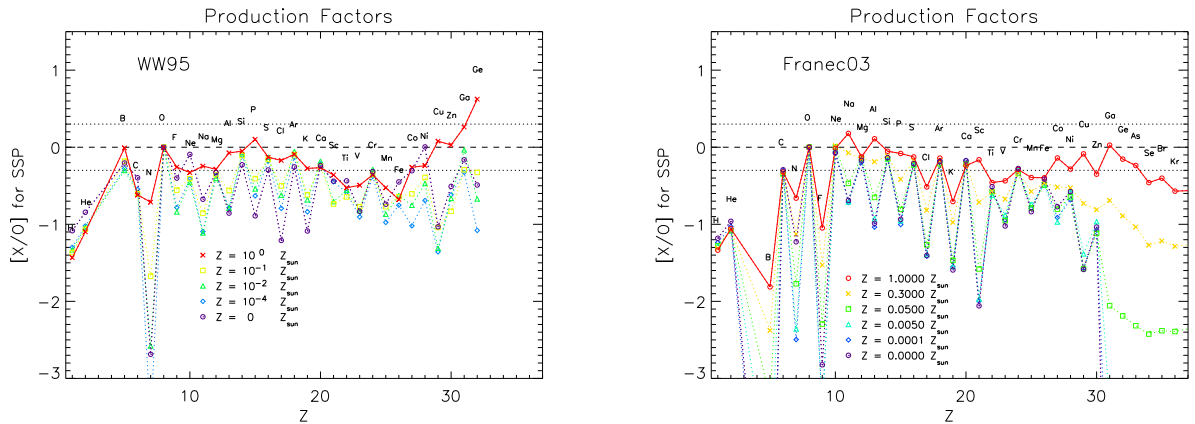


Figure 2.1: Production factors relative to O on a solar logarithmic scale from a single generation of massive stars using the metallicity-dependent yields of Woosley & Weaver 1995 (left panel) and those of FRANEC 2003 (right panel). The latter were kindly provided by A. Chieffi (2003, private communication). Yields were integrated over a Salpeter (1955) IMF from 12-40 M_{\odot} . The dashed line indicates the solar values (where $\log(N_{\text{O}}/N_{\text{H}})_{\odot} + 12 = 8.73$ (Holweger 2001)) and dotted lines indicate deviations from scaled solar by a factor of two. For both sets of yields C, N, and some of the iron-peak elements are subsolar because they require additional sources such as lower mass stars and Type Ia SNe. The strength of the “odd-even” effect increases with decreasing metallicity in both cases, however the effect is more pronounced for FRANEC 2003.

form that has been derived empirically. An ample supply of gas is the first condition needed for star formation, so it is not surprising that one of the simplest laws has $\text{SFR} \propto \sigma_{\text{gas}}^k$, where σ_{gas} is the surface density of gas and the exponent k may range from 1–2 (Schmidt 1959). Other star formation laws presume that factors such as total mass density and/or Galactocentric radius play a role. Dopita & Ryder (1994) found that a law given by $\text{SFR} \propto \sigma_{\text{gas}}^{5/3} \sigma_{\text{total}}^{1/3}$ satisfactorily describes the correlation between H_{α} emission and I-band surface brightness in spiral galaxies.

- **Gas Flows:** In the simplest scenario, our model Galaxy in each radial bin can be considered a closed-box consisting of primordial gas from which stars are born according to the chosen SF and IMF prescriptions. In the classic closed-box model (e.g. Pagel & Patchett 1975) there is no gas loss or gain; at time = 0 all Galactic matter is present as primordial gas from which stars immediately form. This type of model, characterised by an intense period of early star formation, provides a reasonable account of the formation of the halo and bulge of the Milky Way. When applied to the Galactic disk, however, the

basic closed-box model leads to an excess of metal-poor stars with respect to the observed metallicity distribution of nearby long-lived stars: the so-called “G-dwarf problem” (Pagel & Patchett 1975). More realistic models overcome this problem by allowing the Galactic disk to form via continual accretion of gas. The infall rate as a function of radius r and time t often takes the form:

$$\frac{d}{dt}\sigma_{gas}(r, t) = A(r)e^{-t/\tau(r)}, \quad (2.1)$$

where $\tau(r)$ is the exponential infall timescale and the coefficient $A(r)$ must satisfy the constraint that $\int_0^{t_{now}} A(r)e^{-t/\tau(r)} dt = \sigma_{gas}(r)$, where $\sigma_{gas}(r)$ is the present-day surface density profile. Infall models often adopt exponentially-decaying infall rates, with timescales 5–9 Gyr for the solar neighbourhood, in order to match the observed stellar metallicity distribution (e.g. Lacey & Fall 1983; Chiappini, Matteucci & Gratton 1997). The radial dependence of the infall coefficient is weakly constrained by the observed chemical abundance gradients (Romano et al. 2000). Recent hydrodynamical simulations of galaxy formation support these simple infall prescriptions (Sommer-Larsen, Götz & Portinari 2003). Many elliptical and dwarf galaxies are expected to have undergone periods in which the energy from supernova explosions exceeds the gravitational energy of the system, causing the interstellar gas to be expelled in a galactic wind (Larson 1974; Dekel & Silk 1986; Matteucci & Tornambe 1987; Gibson 1997; Recchi, Matteucci, & D’Ercole 2001). However, the outflow of gas is not expected to feature in the history of most spiral galaxies and is usually neglected in the models. Radial flows of gas have also been investigated within the homogeneous GCE paradigm (e.g. Portinari & Chiosi 2000).

- **Galactic Components:** The infall of gas described above might occur in multiple episodes that correspond to the formation of the individual halo, bulge, thick disk and thin disk components. Recent works have adopted different premises regarding the extent to which these components interact with each other through gas exchange. For instance, enriched halo gas might be funnelled into the bulge or else might collapse further to form the disk. Alternatively, the halo and thin disk might evolve coevally yet independently. The answer to these questions is partly clouded by challenges in distinguishing the

various stellar populations. The properties that we wish to measure in each population, such as metallicity and kinematics, are also the properties used to define the populations.

The Equations

The chemical composition of the interstellar medium as a function of time and Galactocentric radius is described by equations that balance: 1) processes that *deplete* chemical elements from the interstellar medium - namely star formation and perhaps Galactic winds; and 2) processes that *replenish* the ISM - such as stellar winds, SNe, and infalling gas. The GCE equations can be solved analytically if one assumes that stars release their ejecta instantaneously at the time of their birth. This approximation is reasonable only for very massive and short-lived stars and it precludes one from reproducing the relative trends of elements that are restored to the ISM by different mass stars on different characteristic timescales. For GCE models to have the power to interpret the variation of diagnostic abundance ratios, the “instantaneous recycling approximation” must be relaxed. There is another assumption, however, that few GCE models relax: namely, that the stellar yields are instantaneously mixed into the ISM. For this reason, homogeneous GCE models are not the ideal tools for studying the Galaxy in its infancy, when chemical abundances in the ISM could be traced to individual supernovae (Ryan 2000) (or for present-day observables that originate from that era - e.g. the Galactic halo).

Standard models of spiral galaxy chemical evolution assume azimuthal symmetry and collapse the object into a flat disk such that radius is the only spatial variable. Defining $\sigma_i(r, t)$ as the mass surface density of species i at radius r and time t , then the rate of change of $\sigma_i(r, t)$ is given by:

$$\begin{aligned} \frac{d}{dt}\sigma_i(r, t) = & \int_{m_{low}}^{m_{up}} \psi(r, t - \tau_m) Y_i(m, Z_{t-\tau_m}) \frac{\phi(m)}{m} dm \\ & + \frac{d}{dt}\sigma_i(r, t)_{infall} \\ & - X_i(r, t) \psi(r, t) \\ & - \frac{d}{dt}\sigma_i(r, t)_{outflow} \end{aligned} \quad (2.2)$$

where the four terms on the right-hand side of equation (2.2) correspond to the

stellar ejecta, gas infall, star formation, and gas outflow rates, respectively. ψ is the SFR, $Y_i(m, Z_{t-\tau_m})$ is the stellar yield of i (in mass units) from a star of mass m and metallicity $Z_{t-\tau_m}$, $\phi(m)$ is the IMF by mass, and X_i is the mass fraction of element i . By definition, the sum of X_i over all i is unity, and the total surface mass density is identical to the integral over the infall and outflow rates. m_{low} and m_{up} are the lower and upper stellar mass limits, respectively, and τ_m is the lifetime of a star of mass m . In practice, the first term is split into three equations that deal separately with LIMS, Type Ia SNe progenitors, and massive stars (see Greggio & Renzini 1983 and Matteucci & Greggio 1986 for details).

2.3.2 Observational Constraints

The most thoroughly observed and best understood galaxy is the Milky Way, and in particular, the “local” solar neighbourhood. So extensive is the Milky Way dataset that many model ingredients can be well-constrained empirically. Thus our own Galaxy is often the gauge by which chemical evolution models are calibrated. Indeed, studies of the cosmic evolution of disk galaxies often adopt scaling laws based on the Milky Way (e.g. Boissier & Prantzos 2000). The extent to which the Milky Way’s IMF, star formation law, and nucleosynthetic behaviour can be applied to other types of objects at earlier epochs depends on how universal these prescriptions are and on whether we live in a prototypical galaxy. A minimal set of observational constraints for GCE models is described below.

- **Solar abundance pattern:** Galactic chemical evolution models must be able to reproduce the solar abundance pattern, i.e. the pattern in the ISM 4.5 Gyr ago at the radius where the Sun was born. The Sun is the single star with the most complete set of abundance measurements. For consistency, one can also compare the chemical composition of solar system meteorites with estimates based on stellar spectral lines. As discussed above, the predicted solar enrichment pattern is chiefly controlled by the yields released in 1) Type II supernova (SN II) explosions of massive stars, 2) planetary nebulae and stellar winds of LIMS, and 3) Type Ia SN explosions of binary systems of LIMS. In addition, the predictions are sensitive to the stellar mass distribution (i.e. the IMF) and the SFR, since these set the relative contribution and enrichment timescale from different types of stars. A seminal attempt to simulate the evolution of all elements up to and including zinc was made by Timmes, Woosley

& Weaver (1995, hereafter TWW95) using the comprehensive grid of mass- and metallicity-dependent yields calculated by Woosley & Weaver (1995). Impressively, TWW95 reproduced the abundances of most elements in the Sun to within a factor of two.

It is worth noting that even our understanding of the solar abundance pattern still has the power to surprise us. As recently as a decade ago, the solar oxygen abundance was assumed to be $\log(N_{\text{O}}/N_{\text{H}})_{\odot} + 12 = 8.93$ (Anders & Grevesse 1989); it has become clear recently though that accounting for solar granulation, non-LTE effects, and Ni I line-blending leads to a *significant* downward revision in the Sun's oxygen abundance by almost a factor of two (to $\log(N_{\text{O}}/N_{\text{H}})_{\odot} + 12 = 8.69$ - Allende Prieto, Lambert & Asplund 2001). Such a shift partially resolves the long-standing dichotomy between the Sun's oxygen abundance and that of the local ISM.

- **G-dwarf distribution:** A much stronger constraint on GCE models is the distribution of stars as a function of metallicity, since this represents the convolution of the age-metallicity relationship and the star formation history. In order to probe the early Galaxy, one needs a sample of low mass stars such as G- or K-dwarfs whose main-sequence lifetimes are comparable to, or older than, the age of the Universe. GCE models have demonstrated that the paucity of low-metallicity dwarf stars can be explained if the Galactic halo formed first on a rapid timescale, followed by a slow build-up of the thin disk (e.g. Chiappini, Matteucci & Gratton 1997; Alibés, Labay & Canal 2001; Fenner & Gibson 2003). The excess of metal-poor stars predicted by simple closed-box models can also be avoided by assuming prompt initial enrichment, perhaps by a first generation of extremely massive Population III stars. If this were the case, then the abundance pattern of Pop III ejecta should be evident in the lowest metallicity stars. It has also been suggested that there are no very metal-poor stars left because they all had relatively short lifetimes due to low metallicity environments favouring the formation of higher mass stars (e.g. Nakamura & Umemura 2001). A further consideration is that an initially pristine zero-metallicity star might have had its surface layers polluted by the accretion of metals from the ISM over the past ~ 12 Gyr (e.g. Shigeyama, Tsujimoto & Yoshii 2003).
- **Evolution of abundance ratios:** If elements X_1 and X_2 have different origins

and different characteristic timescales for release into the ISM, then $[X_1/X_2]$ vs $[X_2/H]$ acts as a clock by which chemical evolution can be measured (e.g. Wyse & Gilmore 1988). For example, readily observable features of oxygen and iron in stellar spectra has encouraged the wide use of $[O/Fe]$ vs $[Fe/H]$ to diagnose the overall star formation history of galactic systems. As with most elements heavier than C and N, oxygen is produced chiefly in massive and short-lived stars. Thus, oxygen enrichment immediately follows the onset of star formation. In contrast, at least half of the iron in the Galaxy probably originated from Type Ia SNe (e.g. Alibés, Labay, & Canal 2001), whose lower-mass and longer-lived progenitors introduce a time delay for iron enrichment. The remaining iron comes largely from Type II SNe. The combination of high $[Fe/H]$ and high $[O/Fe]$ is understood to arise in systems that formed stars so rapidly that high metallicities were reached before SNe Ia had a chance to lower the $[O/Fe]$ value (Smecker-Hane & Wyse 1992). Similarly, one might interpret low $[Fe/H]$ and low $[O/Fe]$ as a sign of a slowly evolving system.

- **SFR and SN rates:** The present-day star formation and Type II and Type Ia SNe rates must be matched by a successful chemical evolution model. However these are fairly weak constraints given that we can only be reasonably certain about the current SFR and mean past rate. Finer details of the Galactic star formation history are difficult to recover and are quite uncertain. The most direct way to infer the SFH is by determining the age distribution of stars; a method that relies upon unreliable stellar ages and assumptions about the IMF, stellar evolution, scale height corrections, and stellar kinematics (Rocha-Pinto et al. 2000). This technique is also somewhat circular, in that a SFH must have been assumed in order to derive the IMF.
- **Age-metallicity relationship:** This is an important constraint, but again, a weak one given that the scatter in the observations (e.g. Ibukiyama & Arimoto 2002) can accommodate most model predictions. Moreover, the very existence of an AMR, which had been well established by earlier studies (e.g. Twarog 1980; Edvardsson et al. 1993; Rocha-Pinto et al. 2000), has recently been challenged by investigations demonstrating large intrinsic scatter and no significant trend of metallicity with age (e.g. Feltzing, Holmberg, & Hurley 2001).

- **Gas and Abundance gradients:** It has long been known that the Milky Way is more metal-rich toward its centre and more metal-poor at large Galactocentric distance (Tinsley 1980, and references therein). Using the oxygen abundance observed in HII regions and OB stars to trace metallicity, a metallicity gradient of $-0.07 \text{ dex kpc}^{-1}$ has been established (e.g. Smartt & Rolleston 1997). The abundance of metals in a region of gas is particularly sensitive to the balance between the star formation and gas accretion rates. Therefore the predicted metallicity gradient of the Galactic disk depends strongly on how the star formation prescription and gas infall rate are assumed to vary with radius. Good fits to the data are obtained by “inside-out” formation scenarios, whereby the innermost disk is built-up on the shortest timescale (e.g. Larson 1976; Chiappini, Matteucci & Gratton 1997). Portinari & Chiosi (1999) showed that a SFR such as the Schmidt (1959) law, which varies only with the gas surface density, produces a radial abundance profile that is too flat unless one assumes an unreasonably large variation in formation timescale from the inner to outer disk such that the far disk would currently be accreting at much higher rates than observed. The Dopita & Ryder (1994) law, with a mild dependence on *total* mass surface density, yields a better fit to the metallicity gradient (Portinari & Chiosi 1999). The theoretical metallicity distribution of long-lived stars as a function of Galactocentric radius is shown in Figure 2.2, assuming a Dopita & Ryder (1994) star formation law.
- **Isotopic abundances:** Traditionally, chemical evolution studies have been concerned with monitoring the *total* abundance (or dominant isotope) of specific elements in order to unravel the Galaxy’s history. Recent advances in instrumentation have paved the way for research into individual isotopes that provides new challenges for nucleosynthesis theory. For instance, Type II SNe models appeared capable of explaining the magnesium isotopic ratios in intermediate to solar metallicity stars, but the results from the solar neighbourhood model shown in Figure 2.3 reveal an underproduction of $^{26}\text{Mg}/^{24}\text{Mg}$ at low metallicities (*dotted line*) with respect to the latest data. The missing piece of the puzzle may be low metallicity intermediate mass stars on the asymptotic giant branch (AGB), whose helium-shells may be hot enough to generate ^{25}Mg and ^{26}Mg by triggering α -capture onto ^{22}Ne (Karakas & Lattanzio 2003). As we will show in Chapter 4, the data at $[\text{Fe}/\text{H}] \lesssim -1$ is much better matched

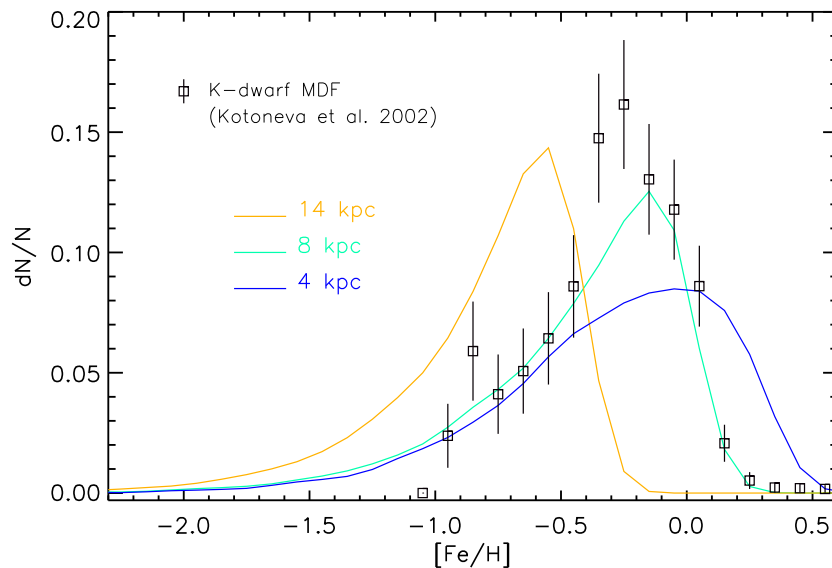


Figure 2.2: The metallicity distribution function (MDF) of long-lived stars predicted by a single infall model at three different Galactocentric radii; 4, 8, and 14 kpc. Open squares with error bars correspond to the MDF of nearby K-dwarfs (i.e. at a radius ~ 8 -8.5 kpc) observed by Kotoneva et al. (2002). The theoretical MDF has been convolved with a Gaussian of dispersion $\sigma = 0.1$ dex in $[\text{Fe}/\text{H}]$ to simulate the empirical uncertainties.

after incorporating the Karakas & Lattanzio AGB nucleosynthesis calculations in a chemical evolution model (*solid line*). Such detections of isotopic ratios in field stars and globular clusters may reveal a great deal about the relative role of different types of stars in various environments.

2.3.3 Uncertainties and Weaknesses

- **Iron-peak Yields:** Iron-peak elements are buried deep within the cores of massive stars near the radius that separates the ejected material from the remnant. The location of this so-called “mass cut” is a free-parameter in stellar models, one which controls the relative abundances of the iron-peak elements as well as the X_i/Fe ratio in the ejecta. Abundances in very metal-poor stars can help constrain the choice of mass cut, however in order to simultaneously eject iron-peak elements in the correct proportions *and* recover the high observed $[\alpha/\text{Fe}]$ ratios, models need to incorporate mixing and fallback (Umeda & Nomoto 2002) or asymmetrical explosions. Multi-dimensional simulations

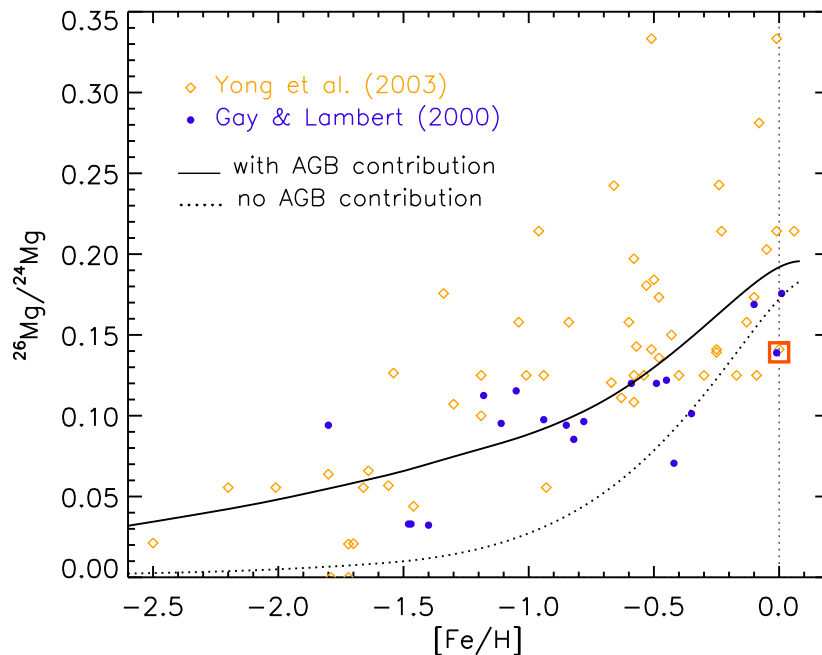


Figure 2.3: The predicted metallicity evolution of magnesium isotopic ratio $^{26}\text{Mg}/^{24}\text{Mg}$ for the solar neighbourhood both with (solid curve) and without (dotted curve) a contribution from intermediate-mass AGB stars (from Fenner et al. 2003). Stellar data are from Gay & Lambert (2000, blue circles) and from halo and thick disk stars from Yong et al. (2003, orange diamonds). The red square denotes the solar ratio.

of explosive nucleosynthesis may reveal more about these processes (Travaglio, Kifonidis & Müller 2003).

- **Shape and evolution of the IMF:** A time-invariant IMF remains the best choice for modelling the general evolution of our own Galaxy (Chiappini, Matteucci & Padoan 2000), but peculiar abundance patterns in extremely metal-poor stars support the notion that the first generation of stars was biased towards higher masses (Chieffi & Limongi 2002). The upper limit of the stellar IMF, m_{up} , is also uncertain and impacts upon the total amount of metals produced by each stellar generation. Figure 2.4 illustrates the sensitivity of metal-growth in the solar neighbourhood to the upper IMF mass. Increasing m_{up} from $40 M_{\odot}$ to $100 M_{\odot}$ is expected to raise the metallicity by as much as 30%. This is due to the steeply increasing yield of O (which is the most abundant metal in the interstellar gas) as a function of stellar mass.

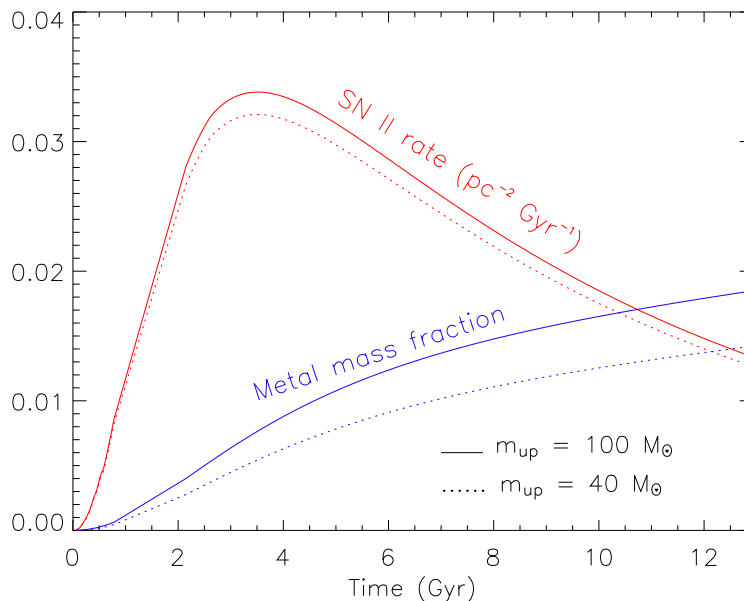


Figure 2.4: Evolution of Type II SN rate (red lines) and metallicity (blue lines) predicted by a single infall phase model of the solar neighbourhood for an IMF upper mass limit of $40 M_{\odot}$ (dotted lines) and $100 M_{\odot}$ (solid lines). Metallicity is defined as the mass fraction of elements heavier than He in the interstellar medium (ISM). The SN II rate is barely affected by changes in the upper limit to the (Kroupa et al. 1993) IMF, however metallicity is about 30% higher for the $m_{\text{up}}=100 M_{\odot}$ case. This reflects the steep increase in the yield of O (which is the dominant element contributing to metallicity) as a function of initial stellar mass.

- **Black hole mass limit:** Essentially a free parameter in Type II SNe models, the mass above which most of the stellar material collapses to form a black hole must be addressed *a posteriori*, in an empirical manner (to recover the observable constraints alluded to earlier). Black hole progenitors are expected to release most of their oxygen, carbon, etc., via pre-SN stellar winds, but heavier elements such as iron are expected to fall back onto the remnant. One may expect the mass range corresponding to black hole collapse is sensitive to metallicity (e.g. Maeder 1992).
- **Limited dataset:** Many conclusions about cosmic chemical evolution have been drawn in part from studies of the Milky Way, but the Milky Way is only one object. How unique or typical the Milky Way is amongst other galaxies is unknown and it can be dangerous to take the Milky Way's evolutionary path as representative of most spirals. For instance, a system such as M31, that

resembles the Milky Way in terms of size and morphology, shows evidence for dramatically different metallicity distributions of its stellar populations (Worthey & Espana 2003). As an example of the perils of drawing conclusions based on the solar neighbourhood, the almost constant ratio of Zn/Fe versus metallicity might be taken as a sign that zinc, like iron, owes much of its production to Type Ia SNe (Matteucci et al. 1993; Mishenina et al. 2002). It is possible, however, that zinc comes primarily from Type II SNe, with a strongly metallicity-dependent yield that mimics the time-delay associated with a SN Ia source (e.g. Timmes et al. 1995). As a consequence, zinc would not always vary in lockstep with iron but would depend on specific formation histories. It is worthwhile to bear this in mind, as zinc is often used as a proxy for iron in the high-redshift universe.

Chapter 3

Deriving the Metallicity Distribution Function of Galactic Systems

This chapter is based upon Fenner & Gibson, 2003, PASA, 20, 189

3.1 Introduction

The metallicity distributions of stars in different environments yield important information about the age and formation history of stellar systems. Particular attention has been paid to the Metallicity Distribution Function (MDF) of G-dwarfs in the solar neighbourhood, as this provides one of the strongest constraints on Galactic Chemical Evolution models, as discussed in the previous chapter. The over-prediction of low-metallicity stars, the so-called “G-dwarf problem”, is typically resolved by allowing the disk of the Milky Way to form gradually from accreting gas on a timescale of about 7 Gyr. Recent models (e.g. Chiappini, Matteucci & Gratton 1997; Goswami & Prantzos 2000) have successfully reproduced the observed G-dwarf MDF using dual-phase accretion models in which the halo/thick disk component evolves independently of the thin disk and on a rapid timescale.

An implicit assumption of most theoretically predicted G-dwarf metallicity distributions is that all G-dwarfs have lifetimes older than the age of the Milky Way. In fact, the stars in the Rocha-Pinto & Maciel (1996) sample have masses ranging from $0.7 M_{\odot}$ to $1.1 M_{\odot}$, while Wyse & Gilmore’s (1995) dataset spans $0.8 M_{\odot}$ to $1.2 M_{\odot}$. Some of these stars have lifetimes shorter than the age of the disk. Furthermore, the earliest formed G-dwarfs will have even shorter lifetimes owing to their low metallicity, which reduces their opacity and raises their luminosity. For instance, a $1.3 M_{\odot}$ star leaves the main-sequence after about 4 Gyr at solar metallicity, or after less than 3 Gyr for $Z = 0.05 Z_{\odot}$ (Schaller et al. 1992). In the low-metallicity environment of

the early Milky Way, a $1 M_{\odot}$ star is expected to leave the main-sequence after about 6 Gyr. The preferential loss of the oldest G-dwarfs from empirical datasets tends to bias the MDF towards higher metallicity and suppresses the low-metallicity tail. However, the protracted formation history of the Galactic disk means that stellar lifetime effects alone cannot account for the paucity of metal-poor G-dwarfs with respect to “closed box” models of chemical evolution. We have investigated the impact of these effects on the shape and peak of measured MDFs in different stellar environments, the results of which are presented in Section 3.4.2. Rocha-Pinto & Maciel (1997) and Bazan & Mathews (1990) should be referred to for additional commentary in this regard.

Since K-dwarfs are less massive than G-dwarfs, their lifetimes are longer than the age of the Galaxy. The K-dwarf metallicity distribution should therefore trace the “true” MDF because surveys of this stellar population should not suffer from incompleteness due to stars evolving off the main-sequence. Because of their faintness, however, accurate metallicities of large numbers of K-dwarfs have only recently been obtained. Kotoneva et al. (2002) constructed a K-dwarf distribution using a sample of 220 nearby K-dwarfs drawn from the Hipparcos catalogue (ESA 1997). They were able to select K-dwarfs by absolute magnitude and restrict the mass range to $0.7 - 0.9 M_{\odot}$, for which evolutionary effects are unimportant.

GEtool was used to numerically solve the equations governing the rate of change of gas mass and elemental abundances due to star formation, supernovae feedback, and the continual accretion of gas onto the disk. The model presented here is capable of reproducing the main observed properties of the Milky Way, including the present day radial gas distribution, radial abundance gradients, age-metallicity relation, stellar metallicity distribution and elemental abundance ratios. Section 3.2 outlines the features of the model, while Section 3.3 describes the adopted stellar nucleosynthetic prescriptions. The predicted K-dwarf metallicity distribution is presented in Section 3.4.1, where it is compared against the measured K-dwarf MDF in order to infer the possible formation history of the Galaxy. In Section 3.4.2 are shown results from a study into the effect of finite stellar lifetimes on the measured MDFs of populations in different star forming environments.

3.2 The Model

3.2.1 Infall scheme

Our Galactic evolution model assumes two main formation phases. The formation of halo stars is associated with the first episode of infalling material, while the second phase leads to disk formation. To aid the comparison with other dual-phase Galactic chemical evolution studies the model is restricted to simulate *two* rather than *three* infall phases. The thick disk is assumed to correspond to a merger heated thin disk and is therefore chiefly associated with the early stages of the second formation epoch. The difficulty inherent in using this kind of dual-phase model to describe a three component system is further discussed in Section 3.4.1. Simulating the evolution of a separate thick disk component will be explored in forthcoming work.

The initial phase of star formation occurs on a timescale of ~ 0.5 Gyr and enriches the initially primordial gas to a metallicity of $[\text{Fe}/\text{H}] \approx -1.2$. The second formation phase is delayed by 1 Gyr with respect to the first phase and has a more protracted star formation history; High-Velocity Clouds (HVCs) may represent the present-day source of this Galactic star formation fuel. Drawing on observations of the chemical composition of these clouds (Wakker et al. 1999; Gibson et al. 2001; Sembach et al. 2002), the second accretion phase assumes the gas is slightly metal-enriched ($Z = 0.1 Z_\odot$) with an enhancement of α -elements relative to iron. The adopted value of $[\alpha/\text{Fe}] = +0.4$ is consistent with α/Fe ratios found in metal-poor stars (e.g. Ryan, Norris & Beers, 1996).

After Chiappini et al. (1997), we assume that the rate at which material is accreted during these phases declines exponentially. The evolution of total surface mass density $\sigma_{tot}(r, t)$ is given by

$$\frac{d\sigma_{tot}(r, t)}{dt} = A(r)e^{-t/\tau_H(r)} + B(r)e^{-(t-t_{delay})/\tau_D(r)} \quad (3.1)$$

where the infall rate coefficients $A(r)$ and $B(r)$ are chosen in order to reproduce the present-day surface mass density of the halo and disk components, which we take to be 10 and $45 M_\odot \text{pc}^{-2}$, respectively. These values are comparable with 17 and $54 M_\odot \text{pc}^{-2}$ used by Chiappini et al. (2001). The adopted timescales for the infall phases are $\tau_H = 0.5$ Gyr and $\tau_D = 7.0$ Gyr at the solar radius $r_\odot = 8$ kpc. The “inside-out” functional form for $\tau_D(r)$ (Romano et al. 2000) is adopted, with the

Milky Way age taken to be 13 Gyr.

3.2.2 Star formation formalism

We adopt a star formation prescription which is based upon the hypothesis that star formation is triggered by the compression of interstellar material from spiral arm motion (e.g. Prantzos & Silk 1998). This implies that the star formation rate (SFR) is proportional to the angular frequency of the spiral pattern and therefore inversely proportional to radius. The star formation law incorporated in this model is given by

$$\psi(r, t) = \nu \sigma_{gas}^2(r, t) \left(\frac{r_{\odot}}{r} \right) \quad (3.2)$$

where the value of the efficiency factor ν is constrained by the present day gas fraction.

3.2.3 Initial mass function

The shape of the stellar initial mass function (IMF) influences the quantity of Galactic material locked up in stars of different masses, which in turn determines the rate at which different elements are released into the interstellar medium. The models presented in Section 3.4.1 use the Kroupa, Tout & Gilmore (1993) three-component IMF. With respect to the Salpeter (1955) and Scalo (1986) IMFs, this function has a steeper slope for high masses, resulting in less material being processed by massive stars. We impose an upper mass limit of $60 M_{\odot}$ on stellar formation in order to recover the observed trend of [O/Fe] at low metallicity (e.g. Carretta, Gratton & Sneden 2000, Melendez, Barbuy & Spite 2001) while avoiding the overproduction of oxygen.

3.2.4 Properties of the halo, thick disk, and thin disk components

The ratio of the local number density of thick disk to thin disk stars lies between 1% and 6% (Gilmore, Wyse & Jones 1995). Both disk components are well-fitted in vertical height, z , with exponential functions. Taking the thick and thin disk scale heights to be 1 kpc and 330 pc, respectively (Gilmore et al. 1995), the ratio of the thick to thin disk surface densities lies between 2% and 20%. The local stellar density

of halo stars relative to thin disk stars is only $\sim 0.1\%$ with a mean metallicity of $[\text{Fe}/\text{H}] = -1.7$ (Norris & Ryan 1991), while thick disk stars have typical metallicities in the interval $-0.4 < [\text{Fe}/\text{H}] < -1.2$ with a mean of -0.7 (Gilmore et al. 1995). In comparison, the MDF of thin disk stars peaks near $[\text{Fe}/\text{H}] = -0.2$ (McWilliam 1997). In addition to metallicity, kinematic behaviour is used to distinguish between these three components. Thick disk kinematics lie somewhere between those of the halo and the thin disk, and describe a distinct population.

3.3 Yields

The observed behaviour of elemental ratios such as $[\text{O}/\text{Fe}]$ with $[\text{Fe}/\text{H}]$ are important observational constraints on chemical evolution models. Oxygen is chiefly produced in massive stars, whereas a significant fraction of iron is supplied by Type Ia supernovae involving binary systems of lower mass stars. The characteristic timescale on which oxygen is ejected into the ISM is therefore much shorter than that of iron, owing to the mass dependence of main-sequence lifetimes.

In order to recover the observed behaviour of elemental abundance ratios, the instantaneous recycling approximation has been relaxed. Mass and metallicity-dependent lifetimes were taken from Schaller et al. (1992).

3.3.1 Massive stars

The present work incorporates an updated set of stellar yields from Limongi et al. (2000; 2002), supplemented with a finer mass coverage grid (kindly provided by Marco Limongi), covering a range of stellar initial masses and metallicities ($13 < m/M_{\odot} < 80$ and $Z/Z_{\odot} = 0, 10^{-3}, 1$). Stellar yields are one of the most important ingredients in Galactic chemical evolution models, yet questions remain concerning the composition of ejected material, owing to the uncertain role played by processes such as mass loss, rotation, fall-back, and the location of the mass cut in supernovae, which separates the remnant from the ejected material.

The amount of iron released in supernova explosions of massive stars is particularly sensitive to fall-back and the location of the mass cut. There are few supernova observations with which to directly infer the amount of iron ejected. We have therefore taken the opposite approach of using the observed trend of abundance ratios to indirectly constrain iron yields. The Limongi et al. (2000; 2002) yields are pre-

sented for a range of mass cuts, allowing a self-consistent treatment of all yields (c.f. Goswami & Prantzos 2000; Argast et al. 2002). We have found that the trend of [O/Fe] with [Fe/H] is best recovered by suppressing the ejection of iron in stars more massive than about $30 M_{\odot}$. This leads to a smaller contribution to the interstellar iron abundance from Type II supernovae than is obtained from the canonical Woosley & Weaver (1995) model. A preliminary relationship between the mass cut and iron yield was presented in Fenner, Gibson & Limongi (2002).

3.3.2 Low- and intermediate-mass stars

The metallicity-dependent yields of Renzini & Voli (1981) were used for stars in the $1 \leq m/M_{\odot} \leq 8$ range. Yields for stars with masses between $8 M_{\odot}$ and $13 M_{\odot}$ were estimated by interpolating between the highest mass in Renzini & Voli and the lowest mass in Limongi et al (2000; 2002). It should be noted, however, that it is not yet clear whether stars in the range $8 < m/M_{\odot} < 13$ contribute to interstellar enrichment, or whether the processed material becomes trapped in the remnant following core-collapse.

3.3.3 Type Ia supernovae

The yields for Type Ia SNe were taken from the W7 model of Thielemann, Nomoto & Hashimoto (1993). The fraction of binaries resulting in Type Ia supernovae was fixed by requiring that the model reproduce the local age-metallicity relation; a fraction of 3% was adopted, leading to model predictions consistent with observation. Type Ia supernovae supply about one half of the interstellar iron abundance in this model.

3.4 Results

3.4.1 The solar neighbourhood

The predicted star formation rate in the solar vicinity (*solid line*) is shown as a function of time in the upper panel of Figure 3.1 along with the range of measured values (*vertical bar*). The star formation rate in the halo peaks at almost $3 M_{\odot} \text{ pc}^{-2} \text{ Gyr}^{-1}$ after 500 Myr. The predicted present day rate of star formation in the thin disk of $2.7 M_{\odot} \text{ pc}^{-2} \text{ Gyr}^{-1}$ agrees with observations (Chiappini et al. 2001) and is about

2.5 times lower than the maximum rate of star formation which occurred ~ 10 Gyr ago, 2-3 Gyr after the onset of the second infall phase.

The dotted line in the upper panel of Figure 3.1 depicts the star formation rate given by the Chiappini et al. (2001) dual-phase Galactic chemical evolution model. Like the Milky Way model presented in this chapter, the Chiappini et al. model is consistent with many observational constraints, including the Kotoneva et al. (2002) empirical MDF. Despite both models satisfying key empirical constraints such as the K-dwarf metallicity distribution, they do predict very different properties for the halo, thick disk, and thin disk components of the Milky Way. This is largely a consequence of different star formation rates in the earliest epoch of Galactic evolution. The predicted number of stars born during the first billion years differs by a factor of 2.5 between the two models, whereas the *total* number of stars formed differs by less than 20%. The higher initial rate of star formation in Chiappini et al. leads to a more rapid enrichment of the interstellar medium, when compared against the model presented here. The implications of these differences in terms of the Milky Way's stellar components are quantified further below.

First, the model we have employed here is successful in reproducing the new Kotoneva et al. (2002) K-dwarf MDF, as shown in the lower panel of Figure 3.1. The predicted MDF has been convolved with a $\sigma = 0.1$ dex Gaussian in $[\text{Fe}/\text{H}]$, consistent with the observational uncertainties in the data. Plotted against the model results (*solid curve*) is the K-dwarf MDF from Kotoneva et al. (*squares with error bars*) and the G-dwarf MDF from Hou et al. (1998) (*dotted line histogram*). The model MDF provides a satisfactory agreement with the Kotoneva et al. dataset, although the model peaks ~ 0.2 dex higher in $[\text{Fe}/\text{H}]$. The model also follows closely the Hou et al. G-dwarf MDF, which exhibits a longer metal-poor tail than the K-dwarf distribution. While most authors measure the peak of the local G-dwarf metallicity distribution to lie between -0.2 and -0.3 dex (e.g. Wyse & Gilmore 1995; Rocha-Pinto & Maciel 1996), there is still not complete agreement. Haywood (2001) found that the MDF of a colour-selected sample was centered on solar metallicity, however Kotoneva et al. showed that a bias toward metal-rich stars might arise due to a systematic trend between metallicity distribution and stellar colour.

The complete absence of stars with $[\text{Fe}/\text{H}] < -1$ in the Kotoneva et al. (2002) sample is not reproduced by our model (*solid curve*). In Chiappini et al. (1997; 2001) and Kotoneva et al. (2002), any low-metallicity tail in the theoretical MDF is suppressed by neglecting either: 1) stars with $[\text{Fe}/\text{H}] < -1.2$ (e.g. Chiappini et al.

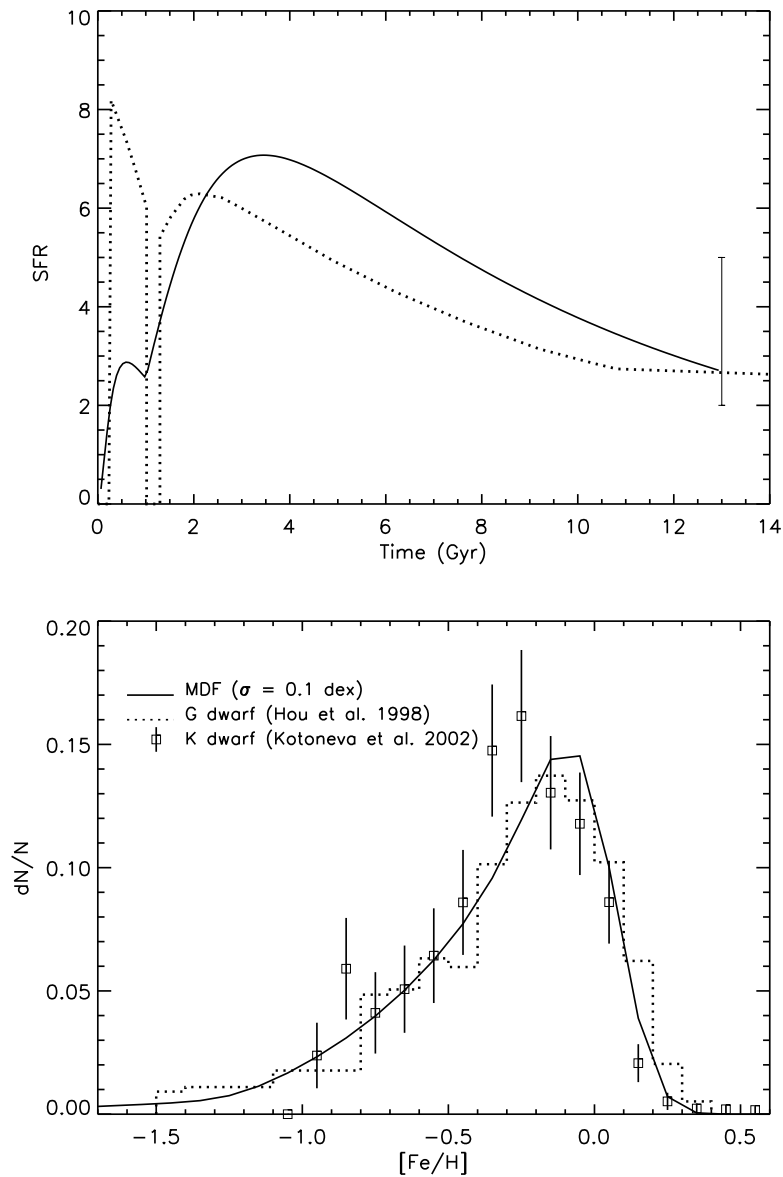


Figure 3.1: **Upper panel:** Evolution of the star formation rate (SFR) predicted by the dual-phase infall model described here (solid line). The dotted line illustrates the stronger initial burst of star formation in the Chiappini et al. (2001) dual-infall model. While the total integrated star formation differs between the two models by less than 20%, during the first 1 Gyr the Chiappini et al. model supplies ~ 2.5 times more stars than in our model. The SFR in the Chiappini et al. disk phase also peaks 1.5 Gyr earlier than in our model. The vertical bar denotes the observed limit on the present-day value. **Lower panel:** The calculated K-dwarf distribution (solid curve) is plotted against the datasets of Hou, Chang & Fu (1998 - dotted histogram), and Kotoneva et al. (2002 - open squares). The theoretical MDF has been convolved with a Gaussian of dispersion $\sigma = 0.1$ dex in $[Fe/H]$, consistent with the known empirical uncertainties.

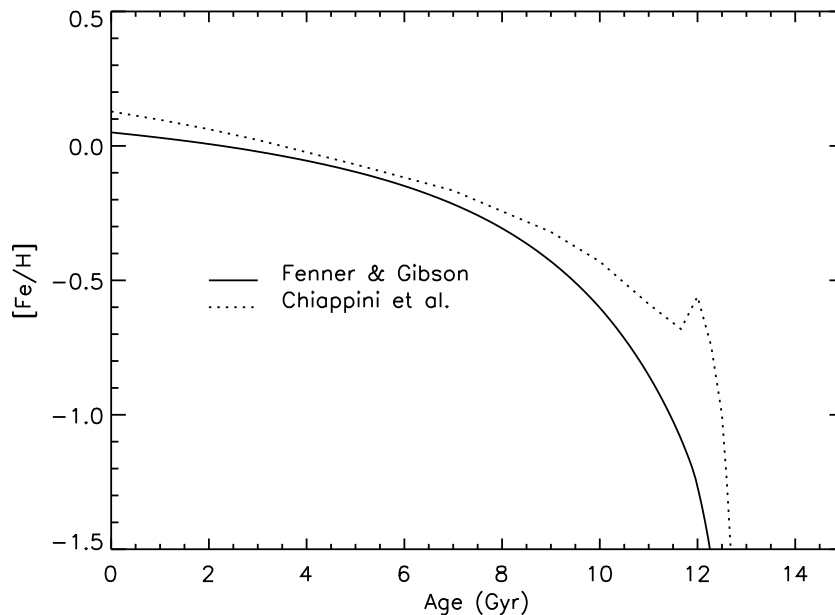


Figure 3.2: The age-metallicity relation (AMR) in the solar neighbourhood predicted by our model (solid curve) and by Chiappini et al. (2001 - dotted line). While similar present-day iron abundances are predicted by both models, in Chiappini et al. the ISM is polluted on a much shorter timescale. Our model assumes a Galactic age of 13 Gyr, whereas Chiappini et al. (2001) take a value of 14 Gyr. In comparing the two AMRs, we have shifted the Chiappini et al. curve by 1 Gyr such that both models span 13 Gyr.

1997; Kotoneva et al. 2002); or 2) stars born before $t = 1$ Gyr (which effectively ignores stars with $[\text{Fe}/\text{H}] < -0.6$) (e.g. Chiappini et al. 2001). In comparison, we have included *all* long-lived stars in the metallicity distribution function. Stars with $[\text{Fe}/\text{H}] < -1.2$ represent a very small fraction of present-day stars in the Chiappini et al. model due to their strong initial burst of star formation. Efficient, early, star formation leads to a metallicity $[\text{Fe}/\text{H}] = -1.2$ being reached on a very short timescale (< 0.1 Gyr). Such rapid initial enrichment is one of the main differences between the present model and that of Chiappini et al. We assume a more moderate initial phase of star formation, leading to a metal-poor tail (i.e. $[\text{Fe}/\text{H}] < -1.2$) in the MDF which contains $\sim 4\%$ of the stars. The age associated with this metal-poor tail is 12.5 Gyr, while the median age of our predicted thin disk dwarfs is 7.5 Gyr. This is in excellent agreement with Hansen et al. (2002) who derive ages of 7.3 ± 1.5 Gyr and 12.7 ± 0.7 Gyr for Galactic thin disk white dwarfs and for the halo globular cluster M4, respectively.

The age-metallicity relation (AMR) for our dual-infall model is shown in Figure 3.2 (*solid curve*). It takes ~ 1 Gyr to enrich the interstellar medium in the solar neighbourhood to a metallicity of $[\text{Fe}/\text{H}] = -1.25$. In contrast, the Chiappini et al. (2001) model (*dotted curve*) reaches the much greater metallicity of $[\text{Fe}/\text{H}] \approx -0.5$ over the same time interval. The AMR from Chiappini et al. (2001) differs from that in the 1997 version of their two-infall model, owing to different timescales for the first episode of infall. Their halo/thick disk accumulates on a timescale of 2 Gyr in the 1997 model, with a 2 Gyr delay before the thin disk starts to form. In the later model, these timescales are shortened to ~ 1 Gyr, giving rise to an even steeper AMR than in the 1997 paper. The kink seen in the Chiappini et al. AMR is due to the metallicity of the ISM becoming diluted when the second phase of infall commences at 1 Gyr. It is not until the thin disk gas surface density reaches a threshold of $7 M_{\odot} \text{ pc}^{-2}$ that Chiappini et al. allow thin disk stars to form. No such star formation threshold is incorporated in our model.

We wish to stress that caution must be employed when drawing conclusions regarding the nature of *three* stellar population components of the Milky Way (thin disk, thick disk, halo), when the models are inherently limited by their *dual*-infall nature. That said, *if* one adopts a chemical criterion of $-1.0 < [\text{Fe}/\text{H}] < -0.5$ for the definition of “thick disk”, then the age of the thick disk predicted under the Chiappini et al. formalism would be centered upon 12.5 Gyr, with a vanishingly small age-spread (< 0.2 Gyr), and possess kinematics closely aligned with the first of the infall phases (i.e. the halo). Conversely, the thick disk predicted under our formalism would be 2–3 Gyr younger, with an age-spread an order-of-magnitude larger (~ 2 Gyr), and possess kinematics more closely resembling those of the second infall phase (i.e. the disk). The Kotoneva et al. (2002) sample of solar neighbourhood K-dwarfs identified only 2 of 431 stars as having halo kinematics. Thus halo stars are rare, whereas the Chiappini model would associate a large fraction of stellar mass with the halo component.

In the Chiappini et al. model of Galaxy formation, the first infall phase is associated with the formation of the halo and thick disk. Thus these components are coeval and form prior to, and independently of the thin disk. In such a scenario, the thick disk would have little dispersion in age and the stars would exhibit primarily halo kinematics. The model presented here associates the first infall phase with the build up of the halo. In contrast with Chiappini et al., the formation of the thick disk overlaps with the early evolution of the thin disk (during the second

infall phase). Our thick disk, as defined by metallicity, would have predominantly disk-like kinematics and a broader range of ages.

While both formalisms clearly have problems in describing a three-component system, we favour the scenario presented in this chapter, in which the intermediate metallicity population (thick disk) has a typical age several Gyrs younger than the halo (as inferred by observation - e.g. Chayboyer, Sarajedini & Armandroff 2000; Ibukiyama & Arimoto 2002) and kinematics akin to that of disk-like population, and not a rapid-collapse halo population. In that sense, our model is more consistent with the favoured model of Galactic thick disk formation whereby an existing stellar thin disk “puffs up” during the process of a merger (e.g. Wyse 2001).

3.4.2 Lifetime effects and MDFs in external galaxies: A note of caution

Recent progress has been made in measuring the metallicity distribution in the stellar halos of external galaxies (e.g. Durrell, Harris & Pritchett 2001; Harris & Harris 2000, 2002). The observed metallicity distribution of these systems, which presumably formed early and on a short timescale, is likely to be biased by the effect of finite stellar lifetimes. In an attempt to quantify the discrepancy between the observed and “true” MDF due to lifetime effects, we constructed a “toy” model of the NGC 5128 halo using our chemical evolution code. This NGC 5128 halo model has some key differences with respect to the Milky Way model described in this chapter. The main differences are: a single phase of star formation; a shorter formation timescale (~ 1 Gyr); and initial composition of gas is primordial.

In stellar systems such as halos, a significant fraction of stars classified as G-dwarfs may have evolved off the main-sequence. This has the effect of preferentially removing older and therefore more metal-poor stars from the observed present-day G-dwarf population. In a similar way, the metal-poor tail in the measured G-dwarf MDF is further suppressed by the shorter lifetimes of low mass, metal-poor stars (e.g. Schaller et al 1992). On the other hand, the disk of our own Galaxy has a more extended star formation history, with the lengthier timescale and the higher proportion of young to old stars acting to mitigate the “loss” of G-dwarfs from the present-day MDF.

In Figure 3.3, the star formation history of the Milky Way disk is compared with a more burst-dominated star formation history, which we here assume to be

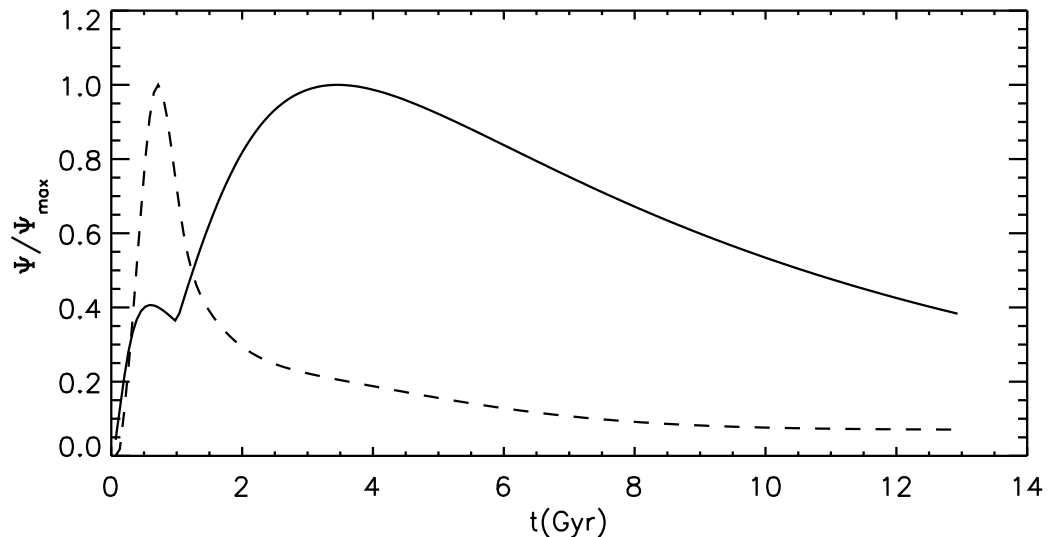


Figure 3.3: Evolution of the star formation rate in a typical halo chemical evolution model (dashed curve) and in the Milky Way model (solid curve).

representative of ellipticals (or pure halo systems). The bulk of the stars in this burst model are born during the first 1.5 Gyr, after which the gas supply is depleted and the star formation rate declines rapidly. Conversely, it takes > 5 Gyr for the majority of stars to form in the disk model.

Figure 3.4 shows the predicted MDF of truly long-lived stars (*black lines*) and G-dwarfs (defined as having masses in the range $0.8 < m/M_{\odot} < 1.4$) (*gray lines*) for the halo (*dashed lines*) and Milky Way (*solid lines*) models. The observed MDF of the NGC 5128 outer halo (Harris & Harris 2002) is plotted as a histogram, where we have used the relation $[\text{Fe}/\text{H}] = [\text{m}/\text{H}] - 0.25$ to transform the published values of $[\text{m}/\text{H}]$ into units of $[\text{Fe}/\text{H}]$. The black lines show the MDF that is expected if all G-dwarfs had lifetimes longer than the age of the galaxy (i.e. masses $m < 0.8 M_{\odot}$). These curves have been normalised to contain the same area as the histogram. The gray curves show the MDF that would be measured if the mass range of stars in the sample is $0.8 < m/M_{\odot} < 1.4$. These have been normalised to reflect the loss of stars in each metallicity bin owing to evolution off the main-sequence. The dotted line also shows the finite lifetime halo model MDF, scaled to illustrate the fit to the data. The loss of stars from a present-day sample of G-dwarfs can be seen to narrow the MDF and shift the distribution toward higher metallicities. While evident in both models, this behaviour is more pronounced in environments such as halos, where

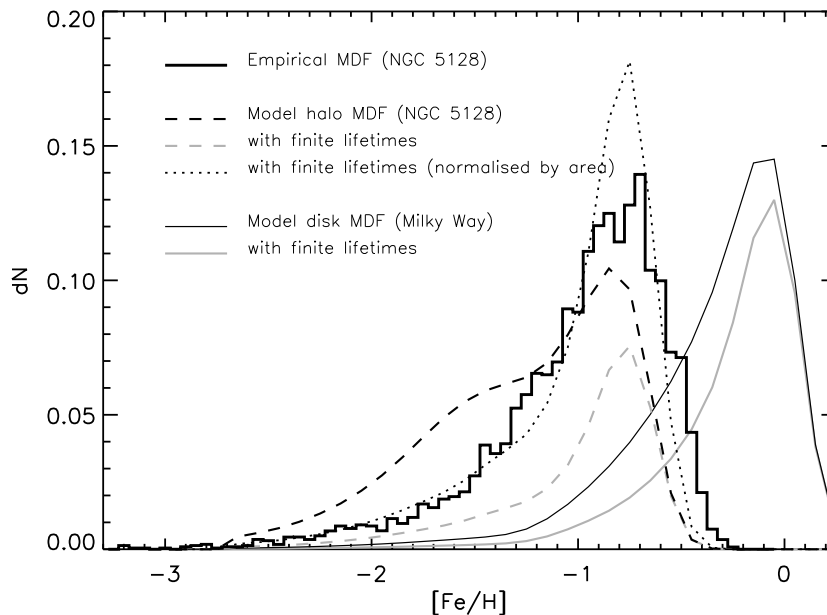


Figure 3.4: Predicted metallicity distributions compared with observations of the outer halo of NGC 5128 (Harris & Harris 2000 - histogram). We assumed the relation $[\text{Fe}/\text{H}] = [\text{m}/\text{H}] - 0.25$ when plotting the observed NGC 5128 MDF. Dashed curves correspond to a halo model, while solid curves represent the Milky Way model. The true MDF is indicated by black lines. Gray curves show the expected MDF of the G-dwarfs that remain in the sample at $t=15$ Gyr and thus demonstrate the loss of stars from the sample due to finite lifetimes. To illustrate the good fit, the dotted line presents the finite lifetime halo model results, normalized to the NGC 5128 MDF sample size. Model predictions have been convolved with a Gaussian of $\sigma = 0.1$ dex in metallicity.

the bulk of the stars presumably formed >10 Gyr ago.

By ignoring lifetime effects, one can overestimate the true mean metallicity of long-lived stars. To gauge the magnitude of this effect, we plot the cumulative metallicity distribution in Figure 3.5. For this particular halo model, mass-dependent stellar lifetimes serve to shift the median metallicity of the population by $\Delta[\text{Fe}/\text{H}] = +0.3$.

3.5 Conclusions

We have reproduced the metallicity distribution of nearby K-dwarfs using a model in which the Milky Way formed during two accretion episodes. Several key differences between this and other dual-phase infall models are (i) the assumption that the

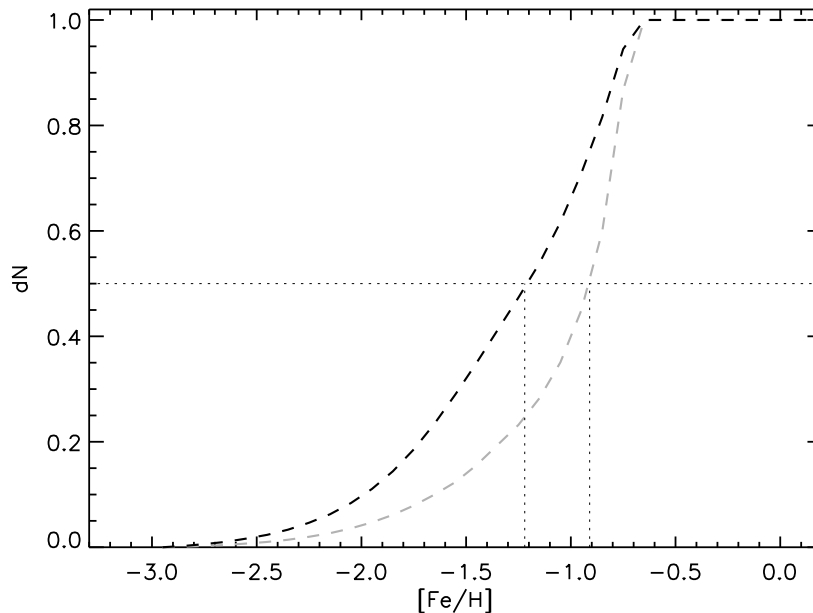


Figure 3.5: Cumulative metallicity distribution function for a model NGC 5128 halo. The black dashed line corresponds to the metallicity distribution of long-lived stars, while the gray dashed line shows the expected observed MDF for a sample of stars in the mass range $0.8 < m/M_{\odot} < 1.4$, taking into account finite lifetimes. The median metallicity of a population corresponds to 0.5 on the vertical axis, as indicated by the horizontal dotted line. The evolution off the main sequence of older metal-poor G-dwarfs increases the median metallicity of the sample by ~ 0.3 dex.

thin disk formed from metal-enriched α -enhanced extragalactic material, (ii) the adoption of a new comprehensive set of stellar yields from Limongi et al. (2000; 2002) for calculating the contribution to the enrichment of the ISM from massive stars, and (iii) a more gentle initial phase of (halo) star formation, resulting in a shallower (but still observationally consistent) age-metallicity relation.

Taking the stellar halo as having $[\text{Fe}/\text{H}] < -1.2$ we predict that this component has an age of 12–13 Gyr and formed on a timescale of ~ 1 Gyr. If stars with metallicity $-1.0 < [\text{Fe}/\text{H}] < -0.5$ are assigned to the thick disk, then the median age of this population is predicted to be ~ 10 Gyr with a greater scatter in ages ($\sim \pm 2$ Gyrs) than for the halo. The age difference of ~ 5 Gyr between the halo and thin disk in our model is consistent with empirical estimates based upon white dwarf luminosity functions (Hansen et al. 2002).

The model presented in this chapter was compared with a similar dual-phase infall model from Chiappini et al. (2001) that also reproduces the observed K-dwarf

metallicity distribution. We showed that even though differences in the rate of star formation in the early Galaxy might not be apparent in present-day observables such as the MDF, they do lead to different predictions for the ages and kinematics of the halo, thick, and thin disk components. This degeneracy is inherent in dual-infall models when applied to the modelling of three-component systems.

Chapter 4

Evolution of magnesium isotopes in the solar neighbourhood

This chapter is based upon Fenner et al., 2003, PASA, 20, 340

4.1 Introduction

Magnesium is one of the few elements for which the stellar abundance of individual isotopes can be reliably measured. The relative abundances of Mg isotopes provide a useful probe into the nucleosynthesis history of the Milky Way because they have their origin in different classes of stars. According to standard theories of stellar evolution, most of the Mg isotopes originate from massive stars. The heavy Mg isotopes behave as secondary elements inside massive stars and their production scales with the number of initial “seed” nuclei. Consequently, very little $^{25,26}\text{Mg}$ is synthesised by massive stars until an initial $[\text{Fe}/\text{H}]$ of ~ -1 is reached, whereas the generation of ^{24}Mg operates fairly independently of initial metallicity.

^{25}Mg and ^{26}Mg are detected in metal-poor stars in higher proportions than one would expect if these neutron-rich isotopes originated exclusively from massive stars (Gay & Lambert 2000). Detailed models of the evolution of Mg isotopic ratios find that massive stars alone are insufficient to account for the values of $^{25,26}\text{Mg}/^{24}\text{Mg}$ at low $[\text{Fe}/\text{H}]$, hinting at an additional production site (Timmer et al. 1995; Alibés et al. 2001; Goswami & Prantzos 2000).

Karakas & Lattanzio (2003a,b) have shown that ^{25}Mg and ^{26}Mg production is substantial in metal-poor intermediate-mass stars (IMS). In the low-metallicity regime, asymptotic giant branch (AGB) stars are believed to generate ^{25}Mg and ^{26}Mg from alpha capture onto ^{22}Ne triggered by He-shell thermal pulsing. More massive AGB stars ($4 < m/M_{\odot} < 6$) are less common than lower mass stars but

may be a significant production site for ^{25}Mg and ^{26}Mg . Temperatures at the base of the convective envelope in these stars can be high enough to burn ^{24}Mg via hot bottom burning (HBB) as well as synthesise large amounts of ^{25}Mg and ^{26}Mg . We explore the possibility that AGB stars produce sufficient quantities of ^{25}Mg and ^{26}Mg to resolve the discrepancy between observations and previous model predictions.

4.2 The Chemical Evolution Model

The temporal and radial evolution of the isotopic abundances in the Milky Way was calculated under the assumption that the Galaxy formed via the accretion of gas at a rate decreasing exponentially with time. For the sake of simplicity, we assumed only a single episode of primordial gas accretion, with a timescale of 7 Gyr at the solar radius. However the results were not significantly different for a two-phase accretion model. We traced the chemical elements through the ongoing cycles of star formation, nucleosynthesis, and ejection into the interstellar medium via supernovae explosions and stellar winds. In order to precisely monitor the abundances of isotopes with different production sites, mass- and metallicity-dependent stellar lifetimes and yields were employed.

The rate of star formation in this model varies with the square of the gas surface density and inversely with Galactocentric radius. This type of radially-dependent law is motivated by the idea that spiral arm patterns trigger star formation (e.g. Prantzos & Silk 1998). The mass distribution of each new generation of stars was governed by the Kroupa, Tout & Gilmore (1993) three-component initial mass function (IMF), with lower and upper mass limits of 0.8 and 100 M_{\odot} , respectively.

Three basic models were constructed, differing only in the adopted nucleosynthesis prescriptions. Firstly, *LSC + AGB* refers to a combination of low and intermediate-mass stellar yields from Karakas & Lattanzio (2003a,b) and a grid of mass and metallicity dependent ($Z = 0, 10^{-3}$ & 0.02) massive star yields provided by Limongi (2001), calculated using the FRANEC code described in Limongi, Straniero & Chieffi (2000) and Limongi & Chieffi (2002). The second model, *LSC no AGB*, is identical to the first model but ignores the AGB contribution to ^{25}Mg and ^{26}Mg production. Finally, the model *WW no AGB* replicates *LSC no AGB* but using metallicity-dependent Woosley & Weaver (1995) yields for massive stars. All models adopt yields for Type Ia SNe from the W7 model of Iwamoto et al. (1999).

The SNe Ia contribution to chemical evolution was calculated following the method from Matteucci & Greggio (1986). It was assumed that 3% of binaries culminate in SNe Ia, since this fraction provides a good fit to the present-day SNe Ia rate (e.g. Alibés et al. 2001). For stars whose metallicity lies below (above) the range covered by the nucleosynthesis models we estimate their yields by extrapolating from the two lowest (highest) metallicity grids.

The Karakas & Lattanzio (2003a,b) stellar models comprise a grid of Mg isotopic yields covering a range of low to intermediate stellar mass ($1 \leq m/M_{\odot} \leq 6$) and a variety of compositions ($Z = 0.004, 0.008$ & 0.02 , supplemented by an unpublished 0.0001 grid calculated with the same code) that is well-suited for chemical evolution models. These models have been evolved from the pre-main sequence to near the end of the thermal-pulsing AGB phase. The nucleosynthesis calculations are performed separately to determine the production of the isotopes.

4.3 Results & Discussion

Figure 4.1 shows the predicted evolution of magnesium isotopic ratios with $[\text{Fe}/\text{H}]$ from the models *LSC + AGB* (*solid line*) and *LSC no AGB* (*dotted line*) for the solar region. $^{25}\text{Mg}/^{24}\text{Mg}$ and $^{26}\text{Mg}/^{24}\text{Mg}$ are shown in the upper and lower panels, respectively, along with measured abundance ratios in local dwarfs from Gay & Lambert (2000) and cool subdwarfs from Yong, Lambert & Ivans (2003b). Representative observational errors are indicated by the large crosses. Although the quoted errors for ^{25}Mg and ^{26}Mg are identical in both studies, ^{26}Mg is expected to be more accurately determined than ^{25}Mg because the ^{26}MgH line is less blended with ^{24}MgH . Both models shown in Figure 4.1 predict ratios larger than solar (indicated by squares) but consistent with the data of Gay & Lambert. It is not surprising that the models reach similar present-day values irrespective of whether AGBs are included, because massive stars are responsible for most of the neutron-rich Mg isotopes in the present-day ISM. In this model 10% of ^{26}Mg present in the ISM at $[\text{Fe}/\text{H}] = 0$ comes from AGB stars compared with $\sim 70\%$ at $[\text{Fe}/\text{H}] = -1$ and nearly 90% at $[\text{Fe}/\text{H}] = -2$.

The dotted lines reveal that below $[\text{Fe}/\text{H}] \sim -1$, massive stars alone seriously under produce ^{25}Mg and ^{26}Mg with respect to ^{24}Mg . Much better agreement is obtained by including the contribution from AGB stars. In particular, most of the

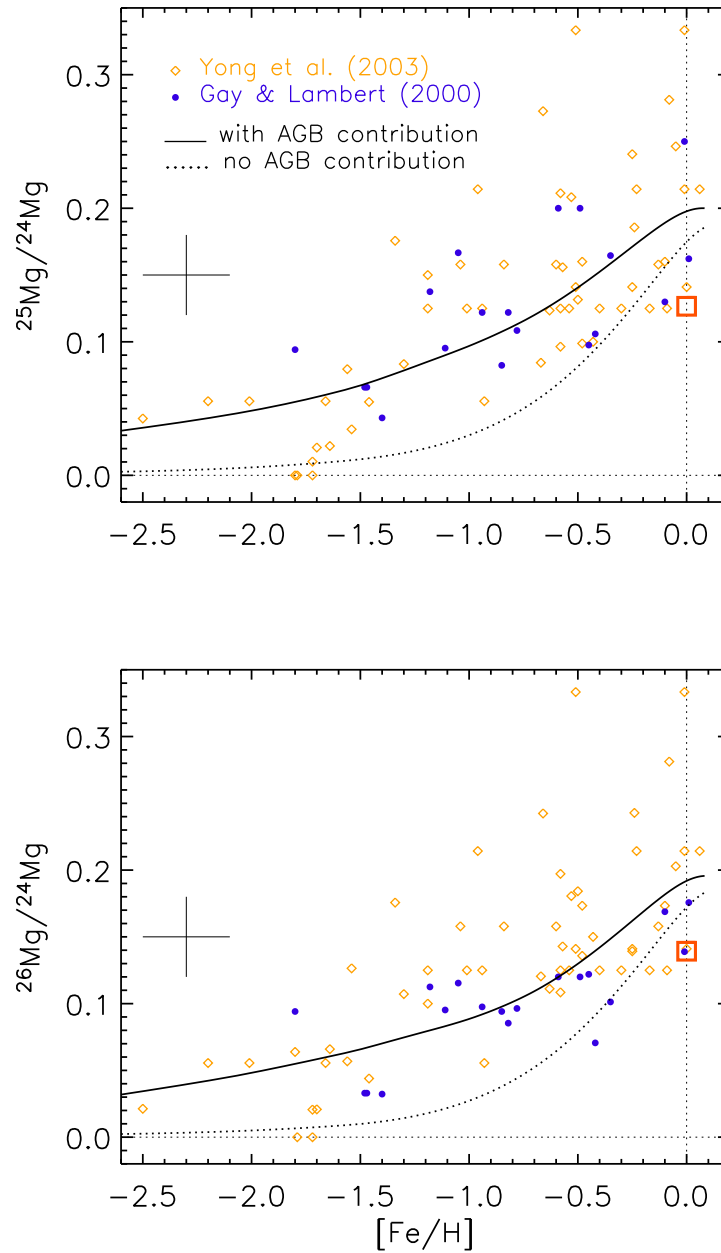


Figure 4.1: Variation of magnesium isotopic ratios with metallicity $[\text{Fe}/\text{H}]$. $^{25}\text{Mg}/^{24}\text{Mg}$ and $^{26}\text{Mg}/^{24}\text{Mg}$ are shown in the upper and lower panels, respectively. Circles correspond to stellar abundances observed by Gay & Lambert (2000), while diamonds represent a sample of halo and thick disk stars from Yong et al. (2003b). The large cross appearing in both panels indicates typical observational errors. Solar values appear as squares. The predicted trend of our solar neighbourhood model incorporating Mg isotopic yields from AGBs (solid line) is shown against a model without the AGB contribution (dotted line). Both models arrive at similar present-day values, however only the AGB model matches the empirical data at low metallicities.

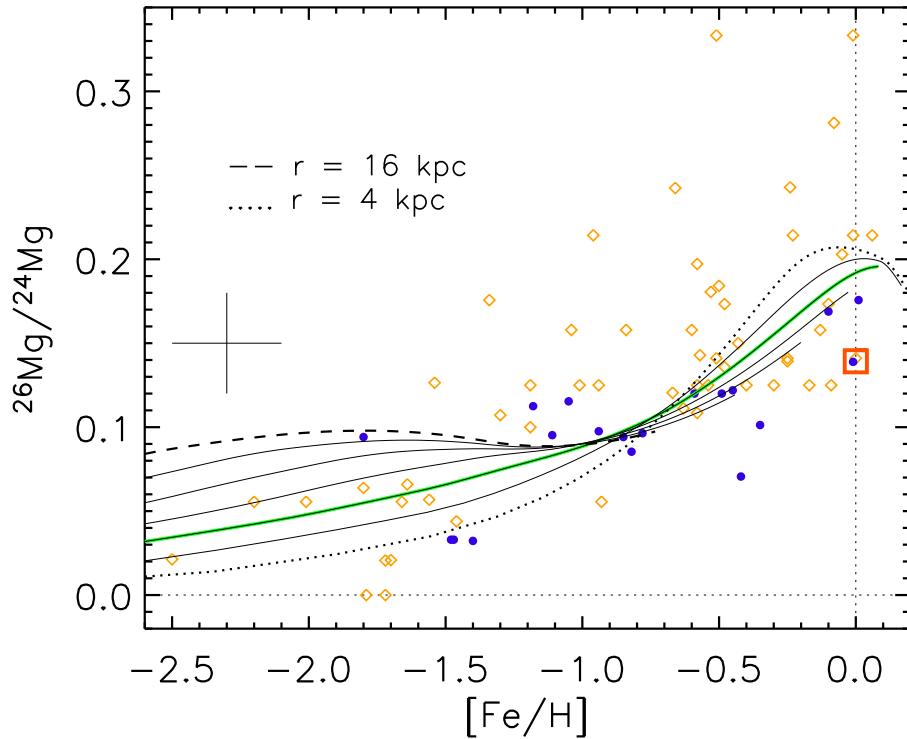


Figure 4.2: Evolution of $^{26}\text{Mg}/^{24}\text{Mg}$ as a function of $[\text{Fe}/\text{H}]$ at different Galactic radii. Symbols have the same meaning as in Fig 4.1. The curves correspond to predicted behaviour at seven evenly spaced radii, ranging from 4-16 kpc for the LSC + AGB model. The green line indicates the solar radius (8 kpc).

heavy Mg isotopic abundance at low metallicity is controlled by the 4–6 M_{\odot} stars that undergo hot bottom burning and whose He-shells are hot enough to trigger the $^{22}\text{Ne}(\alpha, n)^{25}\text{Mg}$ and $^{22}\text{Ne}(\alpha, \gamma)^{26}\text{Mg}$ reactions (Karakas & Lattanzio 2003a,b). These stars typically have lifetimes between 60 and 170 Myr.

The high abundances of ^{25}Mg and ^{26}Mg from the Yong et al. (2003b) data-set pose more of a challenge and are difficult to reconcile with our models, even with an AGB contribution. These stars were selected by their large transverse velocities as part of an effort to compile a sample of metal-poor unevolved subdwarfs (Yong & Lambert 2003). Based on their high reduced proper motion, it is likely that most of the sample is distinct from the thin disk, belonging instead to the halo at low metallicities or the thick disk at higher metallicities. One might expect that stars enhanced in ^{25}Mg and ^{26}Mg are also either 1) rich in *s*-process elements if they have

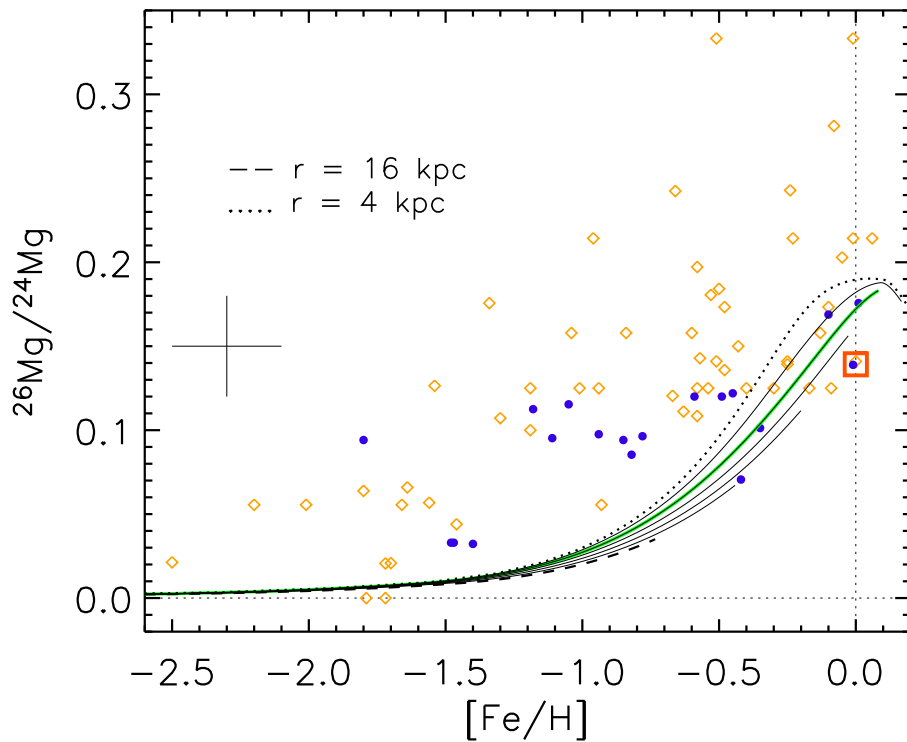


Figure 4.3: Same as Fig 4.2. but for model LSC no AGB (see text for details).

been heavily contaminated by AGB stars; or 2) α -enhanced if they belong to the halo/thick disk. Yong et al. (2003b) reports that there does not appear to be an obvious relationship between high values of $^{25,26}\text{Mg}$ and the abundance of s -process or α -elements.

The predicted trend of $^{26}\text{Mg}/^{24}\text{Mg}$ with $[\text{Fe}/\text{H}]$ is plotted in Figure 4.2 at different Galactic radii for the *LSC + AGB* model. The dotted curve corresponds to the innermost radius of the model (4 kpc) and the dashed curve to the outermost radius (16 kpc). The exponential timescale for infalling gas was assumed to increase linearly with radius, taking on a value of 7 Gyr at the solar radius. Due to this “inside-out” accretion scenario and the radially-dependent star formation law, the timescale of SF is much longer in the outer disk. Only $^{26}\text{Mg}/^{24}\text{Mg}$ is plotted because the ^{25}MgH line is less reliably determined than the ^{26}MgH line due to more severe blending with the ^{24}MgH feature (Gay & Lambert 2000). This model predicts a greater spread in $^{26}\text{Mg}/^{24}\text{Mg}$ in metal-poor stars versus metal-rich stars throughout the Galaxy.

The dispersion in the metal-poor regime reflects the dependence of ^{25}Mg and ^{26}Mg abundance on the timescale of star formation. Since the lowest metallicity AGB models predict the highest ^{25}Mg and ^{26}Mg yields, environments such as the outer disk, with protracted star formation and slowly increasing metallicity over time, encourage generations of IMS to elevate $^{25}\text{Mg}/^{24}\text{Mg}$ and $^{26}\text{Mg}/^{24}\text{Mg}$. The inner Galaxy by contrast, is believed to have experienced intense star formation very early in its history, rapidly enriching the ISM with metals. Once $[\text{Fe}/\text{H}]$ exceeds about -1 , massive stars begin to surpass IMS as the chief source of neutron-rich Mg isotopes. The spread becomes smaller for $[\text{Fe}/\text{H}] > -1$, at which point metallicity rather than star formation history drives $^{26}\text{Mg}/^{24}\text{Mg}$.

Figure 4.3 illustrates the lack of dispersion across different radii for the *LSC no AGB* model. There is some scatter in $^{26}\text{Mg}/^{24}\text{Mg}$ at high $[\text{Fe}/\text{H}]$ that stems from the delayed release of iron from Type Ia SNe. As most of the ejecta from SNe Ia is in the form of iron, these events increase $[\text{Fe}/\text{H}]$ to a greater extent than overall metallicity. A consequence of the characteristic SNe Ia time delay of about 1 Gyr is that *for the same abundance of iron*, the inner disk is expected to be α -enhanced and therefore have greater total abundance of nuclei than the outer disk. With more seed nuclei, the inner disk for a given value of $[\text{Fe}/\text{H}]$ should see higher values of $^{26}\text{Mg}/^{24}\text{Mg}$ than the outer disk. Precisely this effect is revealed in Figure 4.3.

For the sake of comparing how robust our results are to explosive SNe yields from different authors, we plot in Figure 4.4 the predicted evolution of $^{25}\text{Mg}/^{24}\text{Mg}$ and $^{26}\text{Mg}/^{24}\text{Mg}$ for the solar neighbourhood for the *LSC no AGB* and *WW no AGB* models. There is excellent agreement between the two models, although Woosley & Weaver's (1995) nucleosynthesis models predict about 20% less ^{25}Mg than ^{26}Mg , while Limongi et al. (2000; 2002) produce these isotopes in roughly equal numbers. The Mg isotopic yields depend on the adopted $^{12}\text{C}(\alpha,\gamma)^{16}\text{O}$ rate (Imbriani et al. 2001). Specifically, lowering the value of $^{12}\text{C}(\alpha,\gamma)^{16}\text{O}$ leads to higher final yields of ^{24}Mg but leaves the heavier Mg isotopes relatively unaffected. The Limongi et al. yields employed in this Milky Way model use a large $^{12}\text{C}(\alpha,\gamma)^{16}\text{O}$ rate, hence producing low ^{24}Mg yields. The $^{25}\text{Mg}/^{24}\text{Mg}$ and $^{26}\text{Mg}/^{24}\text{Mg}$ ratios could be decreased with a lower $^{12}\text{C}(\alpha,\gamma)^{16}\text{O}$ value such as that from Kunz et al. (2002) which is used in the latest version of the FRANEC code (Limongi & Chieffi 2003). In this case, the Mg isotopic ratios could be reconciled with solar values, but at the expense of obtaining a good fit to the Gay & Lambert (2000) data.

One of the greatest uncertainties in the model concerns the precise form of the

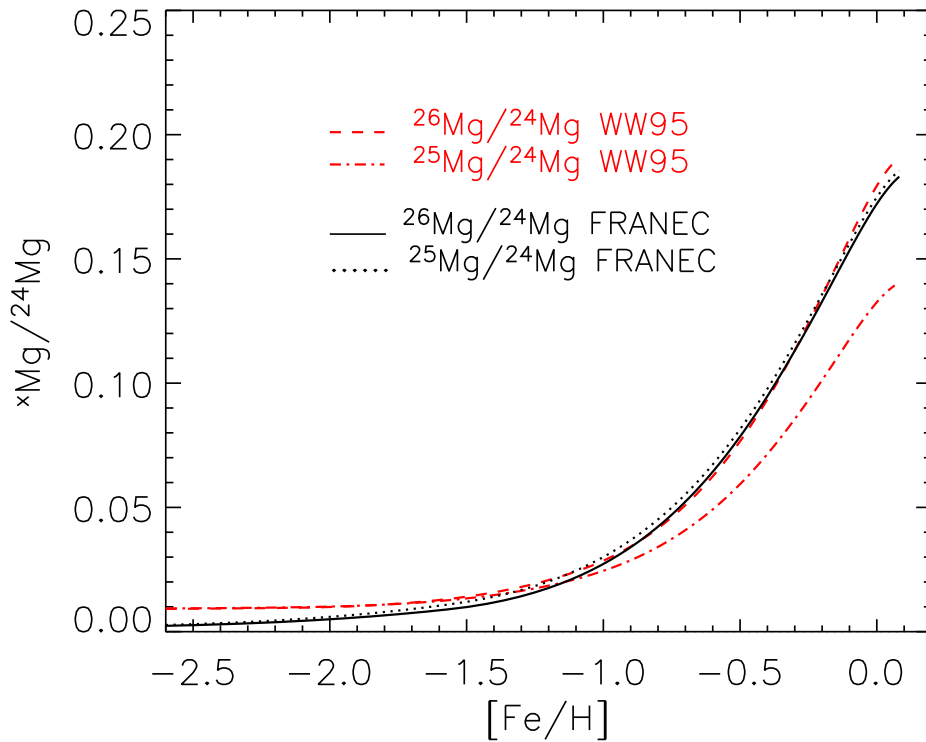


Figure 4.4: Evolution of magnesium isotopic ratios for models using different nucleosynthetic prescriptions for massive star yields. Red lines denote massive star yields from Woosley & Weaver (1995) and black lines denote yields from Limongi et al. (2000; 2002). The AGB contribution has been ignored for the sake of comparison. There is good agreement between the two sets of yields.

stellar IMF. While most elemental yields are fairly robust to changes in the slope and limits of the IMF, this is not the case for the heavy Mg isotopes, whose production in solar metallicity massive stars rises very sharply with stellar mass. Thus, the most massive stars play a crucial role in determining $^{25}\text{Mg}/^{24}\text{Mg}$ and $^{26}\text{Mg}/^{24}\text{Mg}$ despite being vastly outnumbered by lower mass stars. Figure 4.5 displays the yield of ^{26}Mg relative to ^{24}Mg as a function of initial mass for the solar metallicity models of Karakas & Lattanzio (2003a,b) and Limongi et al. (2000; 2002) (*solid line*). The solar metallicity massive star yields extend only as far as $35 M_{\odot}$ and were linearly extrapolated up to $100 M_{\odot}$. The largest mass in the AGB models is $6 M_{\odot}$. For most chemical species, including Fe and ^{24}Mg , the yields between $6\text{--}8 M_{\odot}$ were derived by extrapolating up from the AGB models. However we conservatively assumed that

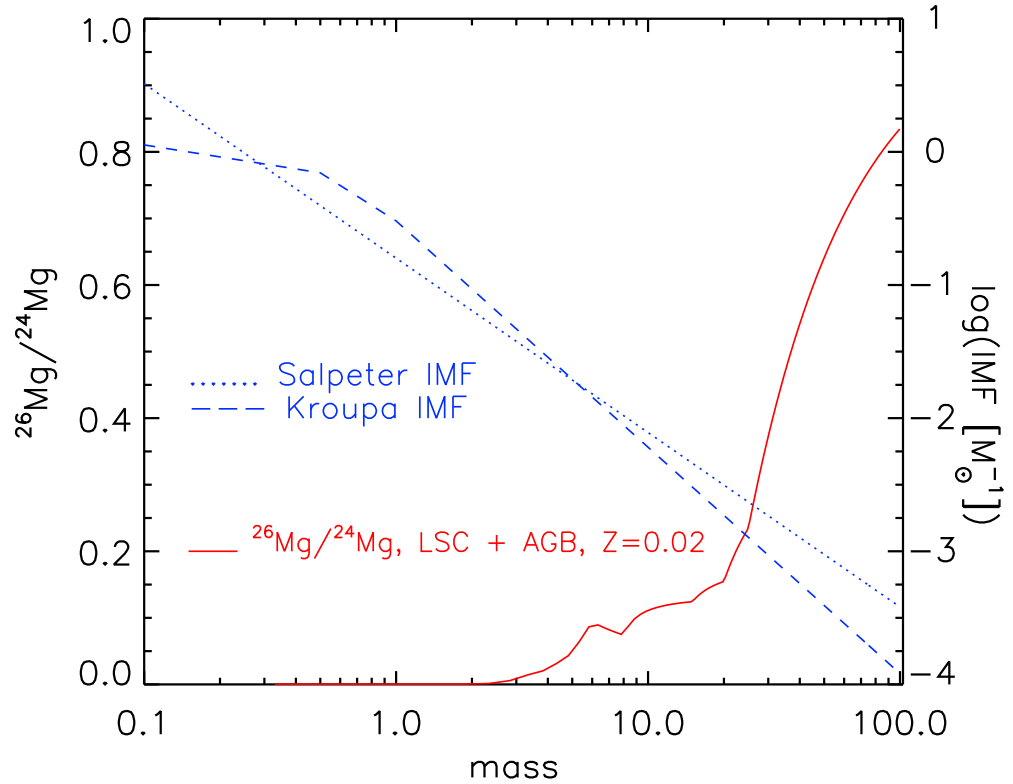


Figure 4.5: Yield of $^{26}\text{Mg}/^{24}\text{Mg}$ vs initial stellar mass for solar metallicity nucleosynthesis models (solid line). Yields for low and intermediate-mass stars are from Karakas & Lattanzio (2003a,b) and from Limongi et al. (2000; 2002) for massive stars. The dotted line corresponds to the Salpeter (1955) initial mass function (IMF) and the dashed line indicates the Kroupa, Tout & Gilmore (1993) IMF. Both functions are normalised to unity over the mass range $0.08\text{--}100 M_{\odot}$ (the scale appears on the right-hand vertical axis).

the $6\text{--}8 M_{\odot}$ stars eject the same quantity of ^{25}Mg and ^{26}Mg as the $6 M_{\odot}$ star. This causes a dip in $^{26}\text{Mg}/^{24}\text{Mg}$ at $8 M_{\odot}$. Superimposed on the same figure are IMFs from Salpeter (1955) (*dotted line*) and Kroupa, Tout & Gilmore (1993) (*dashed line*) normalized over the mass range $0.08\text{--}100 M_{\odot}$. The Salpeter IMF has the form of a single slope power-law (this model uses an index of 1.31) and places a higher proportion of the mass of a stellar generation into both the lower and upper extremes of the mass distribution when compared with the Kroupa et al. (1993) IMF. It is apparent that the role of stars between $0.3 \leq m/M_{\odot} \leq 6$ is emphasised by adopting a Kroupa et al. IMF, whereas the frequency of high mass stars is increased with the Salpeter IMF.

One can anticipate that a Kroupa et al. (1993) IMF would give rise to more AGB

stars than a Salpeter (1955) function, leading to higher values of $^{26}\text{Mg}/^{24}\text{Mg}$ at low metallicity. At metallicities approaching solar however, the Salpeter IMF should generate the highest $^{26}\text{Mg}/^{24}\text{Mg}$ ratios, since it favours the birth of massive stars when compared with the Kroupa et al. law. The influence of the IMF can be seen by comparing the results presented in Figure 4.6, which were derived using the Salpeter function, with those from Figure 4.2. A ratio of $^{26}\text{Mg}/^{24}\text{Mg} \sim 0.3$ at $[\text{Fe}/\text{H}] = 0$ is obtained with a Salpeter IMF. This is $\sim 50\%$ higher than in the Kroupa et al. case and over twice the solar value. Owing to the production of fewer AGB stars, $^{26}\text{Mg}/^{24}\text{Mg}$ at $[\text{Fe}/\text{H}] = -2$ in the Salpeter case is about half the value derived with the Kroupa IMF. The Kroupa et al. model is in better agreement with the Gay & Lambert (2000) data set. Although the large values of $^{26}\text{Mg}/^{24}\text{Mg}$ measured by Yong et al. (2003b) in higher metallicity stars could be attained by increasing the role of massive stars, this comes at the expense of satisfying observations at low $[\text{Fe}/\text{H}]$. Multi-component IMFs with steeper slopes at high mass are favoured over the Salpeter single power law on both observational and theoretical grounds (e.g. Kroupa et al. 1993; Scalo 1986).

It has been suggested that the mass distribution of a stellar generation is influenced by factors including the thermal energy and chemical composition of the star-forming gas (Larson 1998). Accordingly, the IMF might be expected to evolve over time. There are theoretical arguments that the IMF of primordial gas would be biased toward higher mass stars, while higher metallicity environments would form relatively more low-mass stars (Kroupa 2001). If the IMF followed this trend then the fit between our model predictions and empirical constraints would worsen. At present however, the observational evidence for a variable IMF is not overwhelming.

4.4 Conclusions

Thermally-pulsing AGB stars are shown to be excellent candidates for the additional production site of neutron-rich Mg isotopes needed to account for observations at low metallicities. The failure of previous chemical evolution models to match $^{25}\text{Mg}/^{24}\text{Mg}$ and $^{26}\text{Mg}/^{24}\text{Mg}$ observed in local metal-poor stars may be resolved if intermediate-mass stars produce ^{25}Mg and ^{26}Mg in quantities given by the calculations of Karakas & Lattanzio (2003a,b).

According to the chemical evolution model presented in this chapter, massive

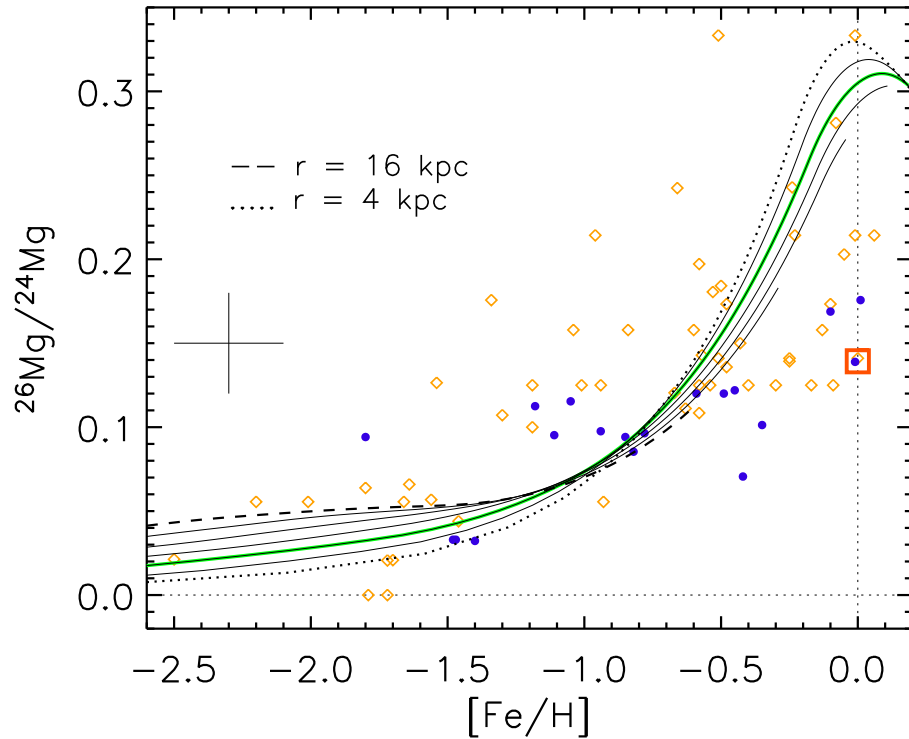


Figure 4.6: Same as Figure 4.2. but for the case of a single component Salpeter (1955) initial mass function in place of Kroupa, Tout & Gilmore (1993).

stars are responsible for most of the heavy Mg isotopes in the present-day ISM, but played a secondary role to 4–6 M_{\odot} AGB stars at earlier epochs. A consequence of this model is that the spread in $^{25}\text{Mg}/^{24}\text{Mg}$ and $^{26}\text{Mg}/^{24}\text{Mg}$ should be greater at low metallicities across the Milky Way, although this conclusion was shown to be sensitive to the adopted initial mass function. While the high ratios of $^{25}\text{Mg}/^{24}\text{Mg}$ and $^{26}\text{Mg}/^{24}\text{Mg}$ in the Yong et al. (2003b) halo and thick disk sample remain a mystery and warrant further investigation, our model provides an excellent match to the measurements of local stars from Gay & Lambert (2000).

Chapter 5

The Galactic Habitable Zone and the Age Distribution of Complex Life in the Milky Way

This chapter is based upon Lineweaver, Fenner & Gibson, 2004, Science, 303

5.1 Introduction

As we learn more about the Milky Way Galaxy, extrasolar planets and the evolution of life on Earth, qualitative discussions of the prerequisites for life in a Galactic context can become more quantitative (Tucker 1981; Trimble 1997; Gonzalez, Brownlee & Ward 2001a). The Galactic habitable zone (GHZ) (Gonzalez, Brownlee & Ward 2001b), analogous to the concept of the circumstellar habitable zone (Kasting, Whitmire & Reynolds 2001), is an annular region lying in the plane of the Galactic disk possessing the heavy elements necessary to form terrestrial planets and a sufficiently clement environment over several billion years to allow the biological evolution of complex multicellular life. In order to more quantitatively estimate the position, size and time evolution of the GHZ, we couple our calibrated model of the evolution of the Galaxy with metallicity constraints derived from extrasolar planet observations (Lineweaver 2001).

5.2 Method

Of the factors that determine the location of the GHZ, the abundance of elements heavier than hydrogen and helium is particularly crucial because these elements are what terrestrial planets are composed of. The current metallicity of the Galaxy can be directly measured, however, modelling is needed to identify the metallicity distribution throughout the history of the Milky Way.

We simulate the formation of the Galaxy using two overlapping episodes of accretion that correspond to the build-up of the halo and disk. The gas accretion rate falls off exponentially on a small (~ 1 Gyr) time scale for the first phase and a longer time scale (~ 7 Gyr) for the second phase. Although there is a 1 Gyr delay between the onset of halo formation and the onset of thin disk formation, the formation of these two components overlap in time. In our model we monitor the creation of heavy elements and the exchange of matter between stars and gas. Model parameters have been chosen to reproduce the key observational constraints – namely, the radial distribution of stars, gas and metals, the metallicity distribution of nearby stars, and the chemical composition of the Sun.

Statistical analyses of extrasolar planets show a correlation between the presence of large close-orbiting massive planets and high metallicity of the host star (Santos et al. 2003; Laws et al. 2003). Whether these planets slowly migrate in or are gravitationally perturbed into these close orbits, they may destroy Earth-mass planets as they pass through the circumstellar habitable zone. Thus, there is a Goldilocks zone of metallicity: with too little metallicity Earth-mass planets are unable to form; with too much metallicity, giant planets destroy Earth-mass planets. A metallicity-dependent probability, P_{metals} , of harbouring terrestrial planets (Lineweaver 2001) has been assigned to the space time distribution of metals (Figure 5.1).

Estimates of the GHZ need to include sufficient time to allow the biological evolution of complex life. This took ~ 4 Gyr on Earth. Various arguments have been presented as to why this duration should or should not be considered typical of the time scale for the evolution life in general (Carter 1983; McKay 1996; Livio 1999). Without making any assumption about how probable the evolution of complex life is, we assume that Earth’s time scale is typical and adopt 4 ± 1 Gyr as the characteristic time required for the evolution of complex life. We include this constraint as a probability $P_{evol}(t)$, defined as the cumulative integral of a normal distribution of mean 4 Gyr and dispersion 1 Gyr.

The deaths of massive stars (more than ~ 8 times the mass of the Sun) produce supernovae that trigger blast waves and release cosmic rays, γ -rays, and X-rays that can be fatal to life on nearby Earth-mass planets (Clark, McCrea, & Stephenson 1977). However, there are large uncertainties concerning how robust organisms are to high radiation doses and climatic disturbances (Scalo & Wheeler 2002). The effects of nearby explosions depend sensitively on the thickness and composition of an atmosphere, and on the density of intervening dust and gas. Massive but

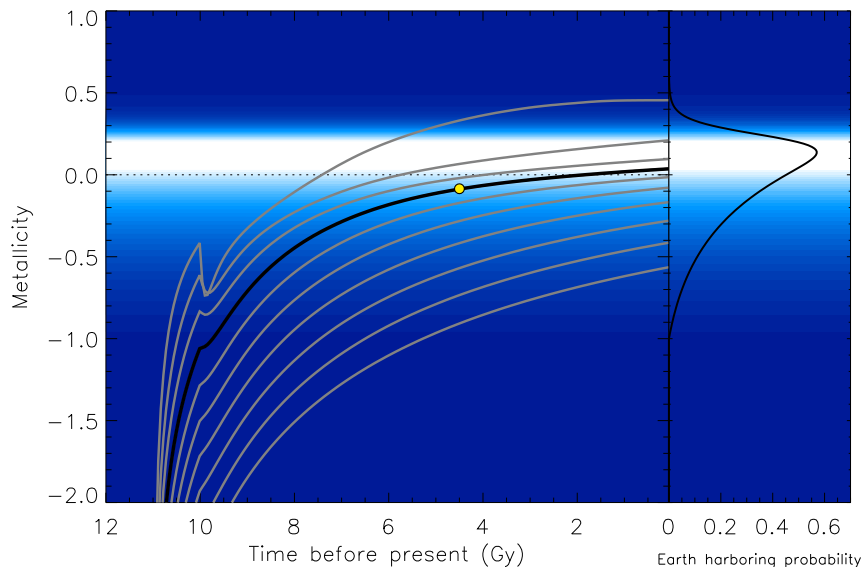


Figure 5.1: The build-up of metals in our Galaxy as a function of time predicted by our simulations. Metallicities at different Galactocentric distances can be compared with the probability of harbouring terrestrial planets as a function of the metallicity of the host star (right panel, see reference (Lineweaver 2001) for details). Galactocentric distances from 2.5 kpc (upper curve) to 20.5 kpc (lower curve) are shown in 2 kpc increments. The yellow dot indicates the Sun’s time of formation and Galactocentric distance of 8.5 kpc. The inner Galaxy accrues metals early and rapidly due to a high rate of star formation, while the most distant regions remain deficient in the metals needed to form terrestrial planets. The metallicity is the log of the ratio of the amount of iron to hydrogen in the stars relative to the Sun.

incomplete extinction of life may slow or speed up the evolution of complex life. In the face of these unknowns, we define the supernova danger factor $\xi(r,t)$ at Galactocentric distance r and the time of a star’s formation t , as the supernova rate integrated over the interval t to $t + 4$ billion years (Figure 5.2). We normalize relative to Earth. That is, we set the probability that complex life survives supernovae to be $P_{SN} = 0.5$ for ξ equal to twice that of Earth (at a Galactocentric distance of 8.5 kiloparsecs), $P_{SN} \sim 0$ for ξ equal to four times that of Earth and $P_{SN} \sim 1$ for ξ equal to half that of Earth (Figure 5.2). This Earth normalization is somewhat arbitrary since we have only imprecise notions of the vulnerability of terrestrial life to supernovae.

To describe the GHZ we define a probability $P_{GHZ}(r,t)$ as the product of four terms:

$$P_{GHZ} = \text{SFR} \times P_{metals} \times P_{evol} \times P_{SN}, \quad (5.1)$$

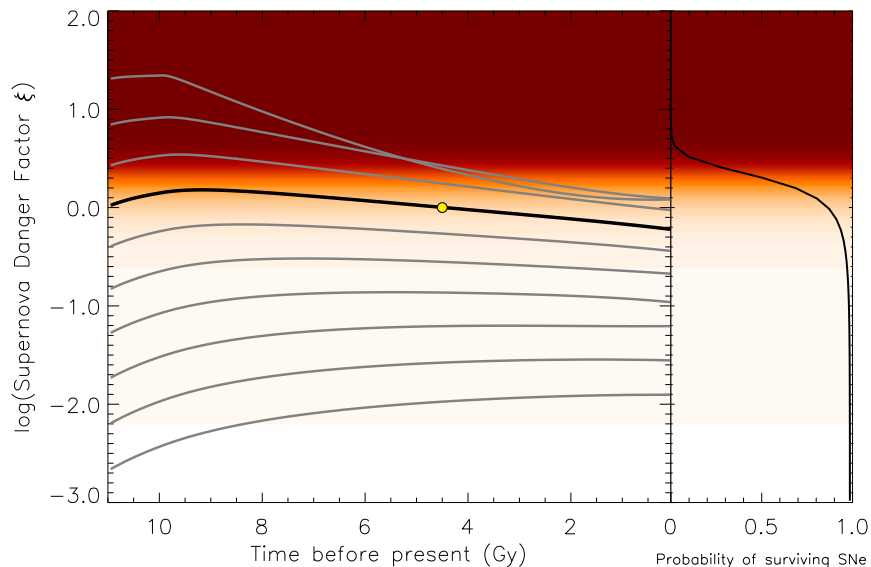


Figure 5.2: The supernova danger factor ξ , defined as the integral of the supernova rate from t to $t+4$ billion years, in units of the Earth's ξ and plotted as a function of time for the same set of Galactocentric distances shown in Figure 5.1. In the inner disk, the threat from supernovae was once 20 times greater than that faced by the Earth. The inner disk began to run out of fuel for making stars within several billion years, causing both the star formation and supernova rates to decline.

where P_{metals} , P_{evol} and P_{SN} are described above. Multiplication by the star formation rate SFR, expresses the fact that if there are more new stars in a given region, there are more potential homes for life. The stellar initial mass function used here is described in (Kroupa, Tout, & Gilmore 1993). Although P_{SN} is not independent of the SFR, the sign of the effect is opposite: with a higher SFR, the supernova danger increases and therefore P_{SN} decreases. With these inputs, $P_{GHZ}(r,t)$ is the relative number of potentially suitable planetary systems as a function of space and time. The regions encompassing 68% and 95% of these systems (Figure 5.3) identify the GHZ. The 68% contour contains less than $\sim 10\%$ of the stars ever formed in the Milky Way.

5.3 Results

Early intense star formation toward the inner Galaxy provided the heavy elements necessary for life, but the supernova frequency remained dangerously high there for several billion years. Poised between the crowded inner bulge and the barren outer

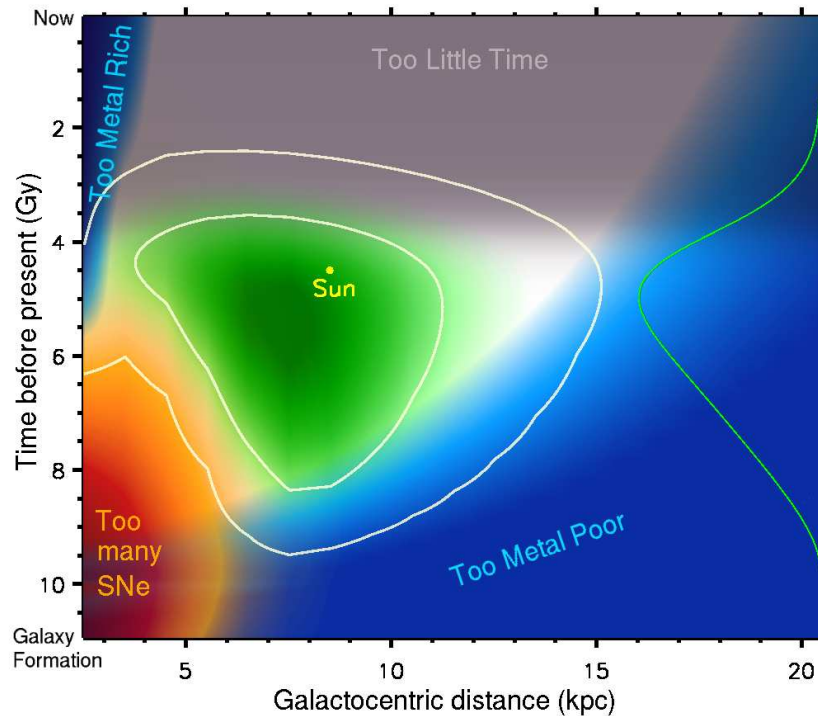


Figure 5.3: The Galactic habitable zone in the disk of the Milky Way based on the star formation rate, metallicity (blue), sufficient time for evolution (grey) and freedom from life-extinguishing supernova explosions (red). The white contours encompass 68% and 95% of the origins of stars with the highest potential to be harbouring complex life today. The green line on the right is the age distribution of complex life and is obtained by integrating $P_{GHZ}(r,t)$ over r .

Galaxy, a habitable zone emerged about 8 Gyr (68% contour) that expanded with time as metallicity spread outward in the Galaxy and the supernovae rate decreased. By comparing the age distribution on the right of Figure 5.3 to the origin of the Sun we find that $\sim 75\%$ of the stars that harbour complex life in the Galaxy are older than the Sun and that their average age is ~ 1 Gyr older than the Sun.

We do not assume that life or complex life is probable. The space-time distribution for the prerequisites of life determined here should be valid whether life is rare or common in the Galaxy. It is not surprising that the Sun lies within the GHZ because we have used our local conditions as a template for finding similar systems. The Sun's value of ξ , solar metallicity and Earth's biological time scale were used to help define the GHZ. However, independent information comes from extrasolar planet host metallicities, the supernova rate and the metallicity evolution of the

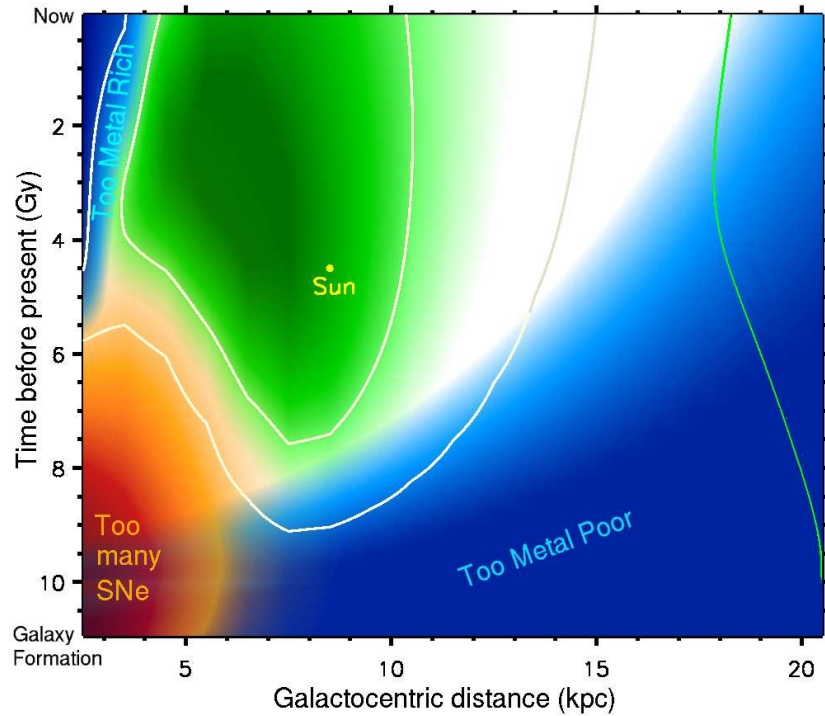


Figure 5.4: The Galactic habitable zone as in the previous figure but without requiring 4 ± 1 Gyr for the evolution of complex life. Thus, the white contours here circumscribe the origins of stars with the highest potential to be currently harbouring any life, not just complex life. The green line on the right is the resulting age distribution of life within the GHZ and is obtained by integrating $P_{GHZ}(r,t)$ over r .

Galaxy. Our procedure is solar-centric but not to the extent of putting the Sun in the center of the GHZ.

The probability P_{metals} will be improved when we learn more about extrasolar planets and the dependence of terrestrial planet formation on the metallicity of the pre-stellar nebula (Zinnecker 2003). The parameters used to set P_{SN} and P_{evol} have the virtue of being explicit and are easily modified to accommodate new information, however they are somewhat simplistic. Assuming a 4 Gyr typical time scale for life in the universe is highly speculative. However, if we are interested in all life (not just complex life) we can drop this assumption and exclude P_{evol} from Eq. 5.1. The resulting GHZ (Figure 5.4) resembles the GHZ of Figure 5.3, but extends all the way to today. Integrating this GHZ to obtain the age distribution of life yields the result that $\sim 30\%$ of stars harbouring life in the Galaxy are older than the Sun and their average age is ~ 1 Gyr younger than the Sun.

The Milky Way contains populations of stars belonging to an inner bulge component, a diffuse halo component, and a thick disk component; none of which appear as hospitable to life as the thin disk modelled here. Low metallicity makes it unlikely that the halo and thick disk are home to many terrestrial planets. Conversely, the bulge suffers from a high density of stars which result in a pervasive, intense radiation field (Scalo & Wheeler 2002), and more numerous close encounters between stars.

A previous analysis (Gonzalez, Brownlee & Ward 2001b) based on the outward spread of a narrow range of metallicity, found that the GHZ has been slowly creeping outward. We find that the GHZ remains centered at ~ 8 kpc but broadens with time (compare their Figure 2 with our Figure 5.3).

Using a chemical evolution model of the Galaxy to trace four plausible prerequisites of life, we have identified the space time regions most likely to harbour complex life. This result depends on the assumption that the terrestrial time scale for biological evolution is representative of life elsewhere. These results will be directly tested within a few decades when we are able to obtain a statistical distribution of terrestrial planets over a large range of Galactocentric distances.

These results can be improved by better modelling of the Galaxy and a better understanding of the effects of various elements on the origin and evolution of life. For example, the abundances of radioactive species such as ^{26}Al play an important role in planet heating. However, to first order the overall metallicity is a good gauge of the abundances of other elements; the abundance (relative to solar) of most elemental species usually falls within a factor of two of the iron abundance (relative to solar) in nearby stars with a wide range of metallicity. Other factors that may play an important role should be visited in future studies. These include the frequency of grazing impacts with molecular clouds, the circularity of stellar orbits and their proximity to the corotation circle, and the effect of starbursts and an active Galactic nucleus in the early history of the most central regions of the Milky Way (Clarke 1981). If these additional constraints are used to further constrain the GHZ, it will encompass fewer stars and the 10% quoted here will be recognized as an upper limit to the number of stars in the GHZ.

Chapter 6

Self-pollution of globular clusters from AGB stars

This chapter is based upon Fenner et al. 2004, MNRAS, 353, 789

6.1 Introduction

Most Galactic globular clusters (GCs) consist of stars that share the same characteristic Fe abundance and are consequently considered monometallic. However, recent studies have found broad variations in the abundance of some lighter metals. There is a growing list of globular clusters known to have CNO inhomogeneities and O-Na and Mg-Al anticorrelations in stars at different stages of evolution, from the red giant branch to the main-sequence. These abundance anomalies are not seen in field stars at the same metallicity – they are peculiar to the cluster environment. The two main competing hypotheses to explain the curious chemical properties of globular cluster stars are: 1) deep mixing, involving processes occurring within stellar interiors during the course of their evolution; and 2) chemical pollution from previous stellar generations.

The deep mixing mechanism, which brings freshly processed material to the surface, is expected to operate in evolved low and intermediate mass stars (IMS). Support for this hypothesis comes from the decreasing C abundance during the red giant branch (RGB) ascent (Grundahl et al. 2002). Temperatures in stars below the turnoff are not high enough to synthesise Na and Al, nor do they possess a deep convective layer. Thus the detection of O-Na and Mg-Al anticorrelations in less evolved stars (Gratton et al. 2001; Grundahl et al. 2002; Yong et al. 2003) suggests that these chemical patterns were already present in the gas from which these stars formed, or in gas that accreted onto the surface of cluster stars. The most popular candidates for introducing Na- and Al-rich, O- and Mg-poor gas into the cluster are 4–7 M_{\odot} intermediate mass stars (IMS) on the asymptotic giant branch (AGB).

Cottrell & Da Costa (1981) described one variety of AGB pollution whereby GC stars are born from gas contaminated by AGB ejecta. Another possibility involves the accretion of AGB matter into the atmospheres of existing stars (e.g. D’Antona et al. 1983, Jehin et al. 1998, Parmentier et al. 1999).

We have tested the AGB pollution scenario by calculating the chemical evolution of globular cluster NGC 6752 using a two stage formation scenario similar to the model developed by Parmentier et al. (1999). Parmentier et al. investigated primarily the *dynamical* evolution of globular clusters, finding that protoclusters can sustain a series of SNe II explosions without being disrupted. They assumed two distinct evolutionary episodes. Firstly, the birth of stars from a primordial gas cloud leads to a SNe II phase whose expanding shell sweeps up the ISM into a dense layer. This triggers the formation of a second generation of stars. In the second phase, intermediate mass stars from the second stellar generation lose their envelopes due to stellar winds. This nuclear-processed material can then be accreted onto the surfaces of lower mass stars.

Thoul et al. (2002) further explored this scenario by calculating the amount of AGB ejecta retained by globular clusters as well as the efficiency with which low mass stars can accrete the intracluster material. They estimate that as much as 95% of the gas in NGC 6752 has been accreted by cluster stars. They arrive at this value by assuming that stars have chaotic motions and spend 20% of their time in the central homogeneous reservoir of gas. It should be noted that their results are quite sensitive to the choice of core radius and stellar velocity, for which they adopted present-day values. Furthermore, they assume that the only method for gas-removal is via tidal sweeping as the cluster crosses the Galactic plane. On the other hand, Smith (1999) proposed that main-sequence stars may generate winds capable of sweeping all the ejecta from globular clusters, provided that the line-of-sight velocity dispersion is less than 22 km/s.

Denissenkov & Herwig (2003) have recently modelled the surface abundance of a single metal-poor $5 M_{\odot}$ star and found that it is very difficult to simultaneously deplete O and enhance Na. Furthermore, they found that excess Na is correlated with higher ^{26}Mg and ^{25}Mg abundances, whereas Yong et al. (2003) only observed a correlation between Na and ^{26}Mg in NGC 6752. Given the fine-tuning required to deplete O, and the conflict between the predicted surface composition of the heavy Mg isotopes and the data, Denissenkov & Herwig (2003) question the role of hot-bottom burning (HBB) during the thermally-pulsing AGB phase in imposing the

anticorrelations. In another recent study, Denissenkov & Weiss (2004) point out that the combination of subsolar $[\text{C}/\text{Fe}]$ and $[\text{O}/\text{Fe}]$ and very high $[\text{N}/\text{Fe}]$ observed in GC subgiants cannot be explained by the operation of HBB in AGB stars. We reach similar conclusions to these authors, but based on a fully self-consistent chemical evolution model of NGC 6752 using yields from 1.25–6.5 M_{\odot} stars with initial compositions determined by the products of population III stars.

We present a globular cluster chemical evolution (GCCE) model that examines in detail whether the impact of AGB stellar winds on the chemical composition of the intracluster medium is consistent with empirical constraints. This model doesn't discriminate between the case where clusters stars form from gas already contaminated by AGB ejecta or the case where existing stars accrete AGB material¹. The details of the model are described in Section 6.2. The theoretical predictions are shown in Section 6.3 and compared with observations. Finally, the relevance of this study to the understanding of globular cluster formation and evolution is discussed in Section 6.4.

6.2 The chemical evolution model

The chemical evolution of NGC 6752 was predicted using a two stage formation model. The first stage traced the chemical evolution of initially primordial gas following the formation of population III stars. This stage effectively acted as a prompt initial enrichment, bringing the gas up to a metallicity of $[\text{Fe}/\text{H}] = -1.4$ (Gratton et al. 2001 reported a cluster metallicity of $[\text{Fe}/\text{H}] = -1.42$, while Yong et al. 2003 found $[\text{Fe}/\text{H}] = -1.62$) and imprinting it with the signature of pop III ejecta. During the second stage, globular cluster stars formed from this low-metallicity, α -enhanced gas.

6.2.1 First stage: Initial enrichment

The conversion of primordial gas into stars was governed by a bimodal initial mass function (IMF) (Nakamura & Umemura 2001) favouring the formation of massive stars. Star formation occurred in a single burst, with newly synthesised elements

¹In the latter case, our model gives the composition of the accreted matter only. When the star ascends the giant branch, and experiences the first dredge-up, the (polluted) envelope is mixed with the (original) interior to produce a different surface composition. This is not likely to alter our conclusions, however.

being returned on timescales prescribed by mass dependent lifetimes (Gusten & Mezger 1982). The set of zero-metallicity yields from Chieffi & Limongi (2002) were used to calculate the enrichment from stars with mass $13 < m/M_{\odot} < 80$. For more massive stars, yields were given by Umeda & Nomoto (2002), which cover the mass range $150 < m/M_{\odot} < 270$. Yields for intermediate and low mass stars were from the code described in Karakas & Lattanzio (2003), supplemented with yields for additional isotopes as well as unpublished yields for metallicity $Z = 0.0001$. It should be emphasised that intermediate mass stars played a negligible role in shaping the abundance pattern imposed by the initial enrichment stage, due to the “top-heavy” IMF.

6.2.2 Second stage: Globular cluster formation and evolution

A second generation of stars was then formed from the $[\text{Fe}/\text{H}] = -1.4$ gas enriched by the Population III burst. It has been suggested that expanding shells from the first Type II SNe may trigger further star formation (e.g. Thoul et al. 2002). This model adopted a timescale of 10^7 yr for the second epoch of star formation. A standard Kroupa et al. (1993) IMF was adopted, however we assumed that the globular cluster retains the ejecta from stars with $m \leq 6.5 M_{\odot}$. Thus, only the yields from intermediate mass stars impact upon the chemical evolution of the intracluster medium during this second stage. No contribution from Type Ia SNe was included in this GCCE model. The observed uniform iron abundance implies that SNe Ia cannot have polluted the cluster during the second formation stage, while their relatively long characteristic timescales precludes them from participating during the first phase of enrichment. We imposed a high efficiency for converting gas into stars, such that at the end of our simulation the chemical composition is a blend of roughly 1 part Pop III enriched gas to 3 parts AGB ejecta. Different assumptions will give different mixtures, but will not alter our main conclusions.

6.2.3 Chemical yields from AGB stars

A grid of yields in the mass range $1.25\text{--}6.5 M_{\odot}$ was specifically calculated for this investigation by Campbell et al. (2005, in prep) using the Mount Stromlo Stellar Structure code (described in Frost & Lattanzio 1996; Karakas & Lattanzio 2003).

Table 6.1 presents the total mass (in solar mass units) of C, N, O, Na, Al and the Mg isotopes released from a star during its lifetime, as a function of initial stellar mass.

The initial elemental abundances of these detailed stellar models were imposed by the chemical composition of the gas enriched by the Pop III burst. In this way, the chemical evolution model is fully consistent with the adopted nucleosynthetic prescriptions.

In order to estimate the sensitivity of our results to the prescriptions used in the stellar evolution calculations, additional models were run using an alternative: 1) set of reaction rates and 2) AGB mass-loss prescription – two of the key factors influencing the final yields in stellar evolution models. The fiducial set of AGB yields was calculated using a Reimers (1975) mass-loss law on the RGB and the Vassiliadis & Wood (1993) mass-loss law during AGB evolution, while most of the reaction rates came from the Reaclib Data Tables (Thielemann, Arnould & Truran 1991). The reader is referred to Karakas & Lattanzio (2003) for greater details of the stellar models. For comparison with the fiducial set of yields, stellar models were run for two representative masses, 2.5 and 5 M_{\odot} , with the following modifications: 1) “standard” reaction rates² were replaced with NACRE (Angulo et al. 1999) values for the Ne-Na, Mg-Al and $^{22}\text{Ne}+\alpha$ -capture chains; and 2) the Vassiliadis & Wood (1993) AGB mass-loss law was replaced with the Reimers (1975) law ($\eta_{AGB} = 3.5$). For almost all species considered in this chapter, the final yields predicted using the two sets of reaction rates agree to within 0.1 dex. The yields are more sensitive to the change in mass-loss law, as is discussed in Section 6.3. The efficiency of dredge-up in AGB stars is another crucial factor influencing the chemical yields. While sensitivity to dredge-up was not explicitly investigated in the present study, Karakas & Lattanzio (2003) tested the effects of reducing the third-dredge-up parameter to about a third its standard value for the final thermal pulses in the most massive AGB stars. They found that the yields of ^{23}Na , C, N and O changed by only a few percent and ^{25}Mg , ^{26}Mg and ^{27}Al yields changed by less than 0.15 dex (see their Table 4). A more detailed analysis of the dependence on dredge-up will be published elsewhere.

²While most reaction rates in the fiducial AGB models come from the Reaclib library (Thielemann, Arnould & Truran 1991), many of the important rates for producing Mg and Al isotopes have been updated. These include: $^{24}\text{Mg}(p,\gamma)^{25}\text{Al}$ (Powell et al. 1999); $^{25}\text{Mg}(p,\gamma)^{26}\text{Al}$ (Iliadis et al. 1996); $^{26}\text{Mg}(p,\gamma)^{27}\text{Al}$ (Iliadis et al. 1990); $^{22}\text{Ne}(\alpha, n)^{25}\text{Mg}$ and $^{22}\text{Ne}(\alpha, \gamma)^{26}\text{Mg}$ (Kaeppeler et al. 1994).

Table 6.1: Intermediate Mass Stellar Yields (in solar masses)¹

	Initial stellar mass [M_{\odot}]				
	1.25	2.5	3.5	5.0	6.5
C	8.0×10^{-4}	1.9×10^{-2}	1.6×10^{-2}	9.1×10^{-3}	7.5×10^{-3}
N	4.7×10^{-5}	2.6×10^{-3}	3.6×10^{-4}	6.7×10^{-2}	4.0×10^{-2}
O	6.8×10^{-4}	2.1×10^{-3}	3.0×10^{-3}	2.1×10^{-3}	1.4×10^{-3}
²⁴ Mg	3.4×10^{-5}	1.0×10^{-4}	1.5×10^{-4}	8.6×10^{-5}	1.2×10^{-5}
²⁵ Mg	5.0×10^{-8}	1.6×10^{-5}	3.5×10^{-5}	5.5×10^{-4}	4.4×10^{-4}
²⁶ Mg	4.0×10^{-8}	1.2×10^{-5}	6.1×10^{-5}	1.4×10^{-3}	6.1×10^{-4}
Na	4.3×10^{-7}	2.0×10^{-5}	2.4×10^{-6}	8.7×10^{-4}	7.8×10^{-5}
Al	3.0×10^{-7}	1.1×10^{-6}	3.1×10^{-6}	6.3×10^{-5}	5.8×10^{-5}

¹ additional AGB models to appear in Campbell et al. 2005, in prep

6.3 Results

Figure 6.1 compares the observed Na-O (*upper panel*) and Al-Mg (*lower panel*) anticorrelations in NGC 6752 with model predictions. Data from Grundahl et al. (2002) and Yong et al. (2003) show Na-O and Al-Mg anticorrelations in stars that are both brighter and fainter than the RGB bump. We note that Gratton et al. (2001) observed similar general abundance trends, but owing to larger scatter we have omitted their data from this figure. Moreover, we caution that Yong et al. (2003) found systematic offsets of +0.2 dex and +0.4 dex for [Mg/Fe] and [Al/Fe], respectively, with respect to Gratton et al. (2001). Such discrepancies are indicative of uncertainties and difficulties yet to be overcome in the analysis of spectroscopic data. There are ~ 1 dex spreads measured in O, Na, and Al relative to Fe and a 0.3 dex spread in Mg. The observed anticorrelation between [Na/Fe] and [O/Fe] is poorly matched by the theoretically predicted chemical evolution of the NGC 6752 intracluster medium. The enrichment from Pop III stars brings the gas initially to the lower right-hand part of the curve (i.e. [Na/Fe] ~ -0.45 and [O/Fe] $\sim +0.45$). The composition of the intracluster gas then progresses along the curve toward increasing Na, as the material processed within IMS is released through stellar winds. The shape of the curve can be understood by examining the predicted yields from AGB stars, shown in both panels of Figure 6.1 by five diamonds whose size indicates the corresponding stellar mass (i.e. 1.25, 2.5, 3.5, 5, or 6.5 M_{\odot}). The 6.5 M_{\odot} model (*largest diamond*) is the first star to evolve off the main-sequence and release its processed material into the cluster environment. Consequently, the theoretical curve

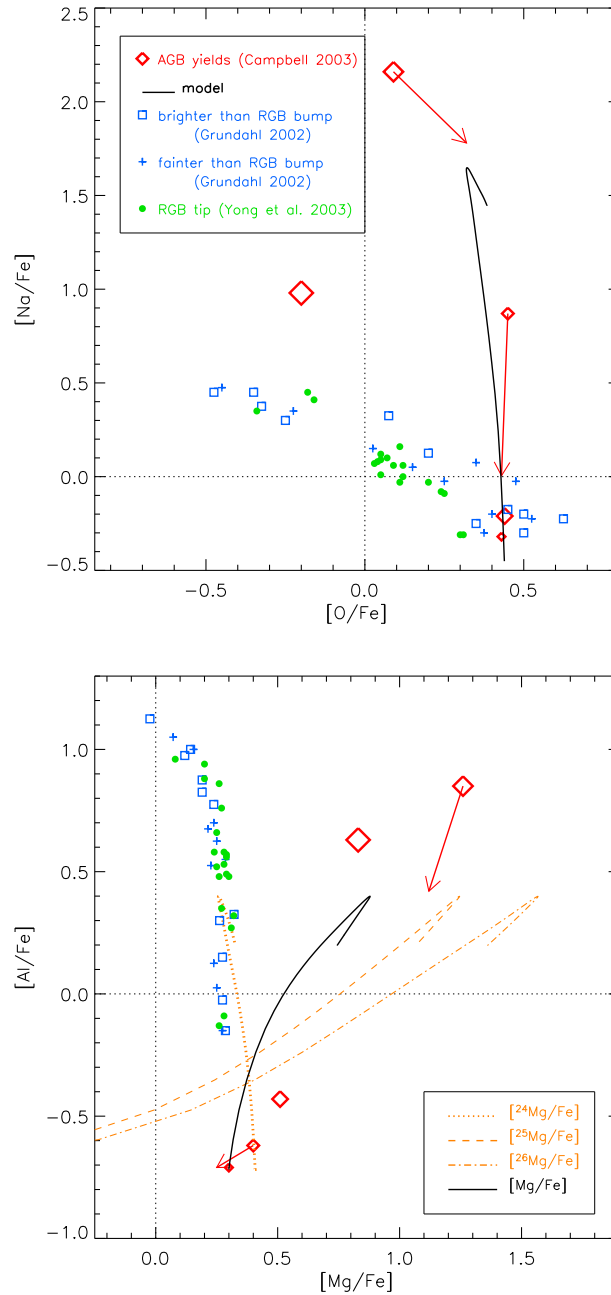


Figure 6.1: Predicted trend of $[\text{Na}/\text{Fe}]$ versus $[\text{O}/\text{Fe}]$ (a) and $[\text{Al}/\text{Fe}]$ versus $[\text{Mg}/\text{Fe}]$ (b) (thick curve) shown against observational data from Grundahl et al. 2002 (squares and pluses) and Yong et al. 2003 (circles). Data from Yong et al. were shifted onto the Grundahl et al. scale. Diamonds correspond to the 1.25, 2.5, 3.5, 5, and 6.5 M_{\odot} stellar models of Campbell et al. 2005, where the size of the symbol indicates the stellar mass. Arrows indicate the effects of changing the mass-loss law for 2.5 and 5 M_{\odot} stars (see text for details). In the lower panel, the evolution of $[\text{}^{24}\text{Mg}/\text{Fe}]$, $[\text{}^{25}\text{Mg}/\text{Fe}]$, and $[\text{}^{26}\text{Mg}/\text{Fe}]$ are shown by dotted, dashed, and dot-dashed lines, respectively.

(*solid line*) initially begins to move from the O-rich, Na-poor region of the diagram toward the $6.5 M_{\odot}$ diamond. Over time, the products of progressively lower mass stars influence the shape of the curve, bearing in mind that low mass stars greatly outnumber higher mass stars due to the power law IMF.

Only the most massive ($6.5 M_{\odot}$) AGB model is capable of significantly depleting O on a scale approaching the 1 dex spread in observations. However, given that the reduction in $[O/Fe]$ for the $6.5 M_{\odot}$ star is still only ~ -0.6 dex, even a contrived situation whereby only $6-7 M_{\odot}$ stars pollute the intracluster medium leaves the very subsolar $[O/Fe]$ stars unexplained. Moreover, not enough mass is ejected by $6-7 M_{\odot}$ stars to form the number of low-O stars observed.

The AGB models have no difficulty generating Na. Matter ejected by the $5 M_{\odot}$ star has $[Na/Fe] \sim 2.2$ – almost 500 times higher than the initial Na abundance – yet the corresponding O depletion is a mere ~ 0.3 dex. The operation of hot-bottom burning in more massive IMS is a major production site for Na (as well as Al and Mg isotopes), and Na is ultimately overproduced by this GCCE model. Since stars with $m > 4 M_{\odot}$ are the chief Na production site, the predicted Na/Fe could be reduced by imposing a more severe upper mass limit for retaining stellar ejecta. Our model took $6.5 M_{\odot}$ as the upper mass limit, however, this value depends on many uncertain properties such as the concentration of mass within the globular cluster and stellar wind strength and mass loss. The predicted Na/Fe could also be reduced if there were increased dilution of the Na-rich AGB ejecta by the Na-poor Pop III material.

The problem here is that the sodium produced is *primary*. Helium burning has produced C which has been dredged into the envelope. The H shell (and HBB) process this into primary N which then captures two alphas during the thermal pulse to produce ^{22}Ne . Some of this Ne is dredged to the surface where the H shell (and HBB) turn it into the excess Na seen in Figure 6.1. The observations demand some Na, but not the huge amounts seen in the models, and this is due to the origin of the Na being the C produced by helium burning.

Arrows in both panels of Figure 6.1 indicate the effects of changing the mass-loss formalism for the 2.5 and $5 M_{\odot}$ stellar models. Replacing the “standard” Vassiliadis & Wood (1993) mass-loss law with Reimers (1975) prescription, as described in Section 6.2.3, leads to decreases in $[Na/Fe]$ of roughly -0.9 and -0.4 dex for the 2.5 and $5 M_{\odot}$ models, respectively. Oxygen is almost unchanged for $2.5 M_{\odot}$ while at $5 M_{\odot}$, $[O/Fe]$ is about 0.2 dex higher in the Reimers mass-loss case. Only the shift

due to mass-loss is plotted because it dominates over the effect from changing the reaction rates. Sodium yields are significantly higher with the Vassiliadis & Wood (1993) mass-loss law, owing to the increased number of third dredge-up episodes that progressively increase the Na abundance at the surface, and to the fact that much of the convective envelope is lost during the final few thermal pulses, when the surface abundance of Na is at its highest. Because the rate of mass-loss proceeds more steadily under the Reimers (1975) law, more material is lost earlier on in the AGB phase, prior to the high envelope abundance of Na. While the adoption of Reimers (1975) mass-loss helps remedy the problem of Na overproduction, it only worsens the oxygen discrepancy. This is because depletion of ^{16}O in the stellar envelope is due to HBB, which operates for a shorter time in models with Reimers mass-loss (due to the faster initial mass-loss rate as compared to Vassiliadis & Wood (1993)). In addition, ^{16}O is only significantly depleted in models with $m \gtrsim 5 M_{\odot}$, since these models exhibit (high temperature) HBB.

We stress that a disagreement between the GCCE model and the data would exist regardless of the precise shape of the IMF. Indeed, inspection of the individual yields of AGB stars of various masses reveals that no choice of IMF would reproduce the observations.

The lower panel of Figure 6.1 shows that this GCCE model predicts about a 1 dex spread in $[\text{Al}/\text{Fe}]$. The predicted spread is consistent with the star-to-star variation, but the absolute values are ~ 0.6 dex lower than observed. In stark contrast to the measured Al-Mg anticorrelation, we predict that the total Mg abundance *increases* with increasing Al. This discrepancy would not be resolved by any choice of IMF, since none of the yields of individual stars are depleted in total Mg. Once again, the shape of the theoretical curve reflects the yields from different mass AGB stars (*diamonds*) with different lifetimes and the arrows reflect the effect of changing the mass-loss law. It is evident that both mass-loss cases lead to a discrepancy with the data. The Pop III burst leaves a high-Mg, low-Al chemical signature on the gas from which the intermediate and low mass stars begin to form. The intracluster gas is then enriched in both Mg and Al, which are produced by the AGB stars and expelled through stellar winds. The increase in $[\text{Mg}/\text{Fe}]$ is entirely due to the enhanced abundance of the heaviest magnesium isotopes, ^{25}Mg and ^{26}Mg , which are produced primarily in the He-burning shell of intermediate-mass AGB stars (Karakas & Lattanzio 2003). The dramatic increase in the heavier Mg isotopes is revealed by the dashed and dot-dashed lines showing the behaviour of $^{25}\text{Mg}/\text{Fe}$ and $^{26}\text{Mg}/\text{Fe}$,

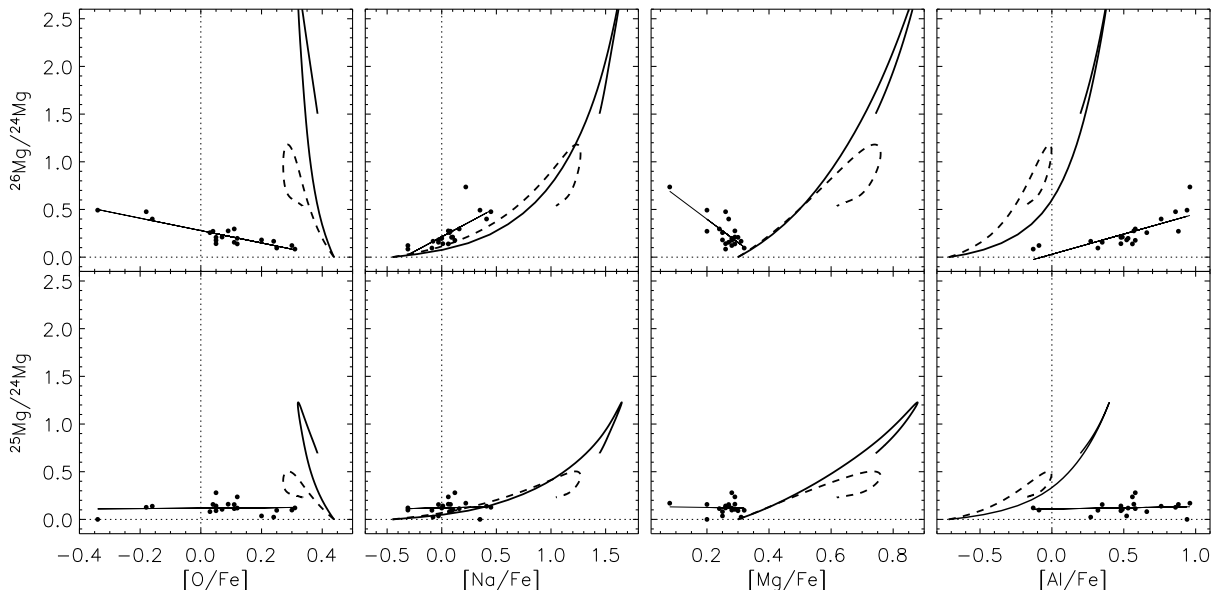


Figure 6.2: The trend of Mg isotopic ratios with O, Na, Mg, and Al abundance predicted by the NGC 6752 model presented in this chapter. The thick solid lines show predictions for $^{25}\text{Mg}/^{24}\text{Mg}$ (top panels) and $^{26}\text{Mg}/^{24}\text{Mg}$ (bottom panels). Dashed lines show predictions from the Reimers (1975) AGB mass-loss model, as described in the text. Circles correspond to data from Yong et al. 2003 showing positive correlations between $^{26}\text{Mg}/^{24}\text{Mg}$ and $[\text{Na}, \text{Al}/\text{Fe}]$; anticorrelations between $^{26}\text{Mg}/^{24}\text{Mg}$ and $[\text{O}, \text{Mg}/\text{Fe}]$; and no correlation for $^{25}\text{Mg}/^{24}\text{Mg}$. The lines of best fit to the data are represented by thin lines.

respectively. Isolating $^{24}\text{Mg}/\text{Fe}$ (*dotted line*), we recover an anticorrelation resembling the data, albeit offset to lower $[\text{Al}/\text{Fe}]$ values. Hot-bottom burning in the more massive AGB stars is responsible for this slight depletion of ^{24}Mg , which is converted into ^{25}Mg . However, this only occurs for $m \gtrsim 5 M_{\odot}$, where temperatures in the H-shell exceed 90 million K. It should be noted that the uncertainty in the $^{26}\text{Mg}(p, \gamma)^{27}\text{Al}$ reaction rate permits significantly more ^{27}Al being produced at the expense of ^{26}Mg (Arnould, Goriely, & Jorissen 1999) than in the present models.

Once again, the problem is the products of helium burning. The primary ^{22}Ne mentioned earlier also suffers alpha captures to produce the heavy Mg isotopes via $^{22}\text{Ne}(\alpha, n)^{25}\text{Mg}$ and $^{22}\text{Ne}(\alpha, \gamma)^{26}\text{Mg}$. Thus the Mg seen in these AGB stars is again primary, and due to Helium burning. The anti-correlation seen in many globular clusters between Mg and Al is totally swamped by the production of Mg in the helium burning region. Thus our models predict an *increase* in total Mg whereas the data show a *decrease*.

Isotopic ratios have the potential to offer more insight into the source of anoma-

lous chemical patterns than elemental abundances alone. Unfortunately, the important reaction rates for the production of Mg isotopes are beset by uncertainties. In particular, the yield of $^{26}\text{Mg}/^{25}\text{Mg}$ from AGB stars is sensitive to the $^{22}\text{Ne}(\alpha, n)^{25}\text{Mg}$ and $^{22}\text{Ne}(\alpha, \gamma)^{26}\text{Mg}$ rates, neither of which are tightly constrained (see Figure 12 from Arnould, Goriely, & Jorissen 1999). In Figure 6.2 we show the variation in Mg isotopic ratios as a function of O, Na, Mg, and Al abundance. The circles represent measurements of stars at the tip of the red giant branch in NGC 6752 by Yong et al. (2003). The thick solid lines are predictions from our standard model with Vassiliadis & Wood (1993) mass-loss. Predictions from the Reimers (1975) AGB mass-loss model are indicated by dashed lines (where we interpolated and extrapolated the uncertainty calculated for the 2.5 and 5 M_{\odot} stars to other masses). The behaviour of $^{26}\text{Mg}/^{24}\text{Mg}$ and $^{25}\text{Mg}/^{24}\text{Mg}$ is shown in the upper and lower series of panels, respectively. Yong et al. (2003) revealed clear anticorrelations between $^{26}\text{Mg}/^{24}\text{Mg}$ and $[\text{O}, \text{Mg}/\text{Fe}]$ and positive correlations between $^{26}\text{Mg}/^{24}\text{Mg}$ and $[\text{Na}, \text{Al}/\text{Fe}]$. Conversely, there is no evidence that $^{25}\text{Mg}/^{24}\text{Mg}$ varies with the abundance of these four elements. A similar, and possibly even more extreme, anticorrelation between O and $(^{25}\text{Mg} + ^{26}\text{Mg})/^{24}\text{Mg}$ has also been found in another globular cluster, M13 (Snedden et al. 2004). Stars in M13 span a factor of 25 in $[\text{O}/\text{Fe}]$, with some stars exhibiting very severe oxygen depletion ($[\text{O}/\text{Fe}] \lesssim -0.8$) along with strong enhancement in the heavy Mg isotopes ($(^{25}\text{Mg} + ^{26}\text{Mg})/^{24}\text{Mg} \gtrsim 0.8$). Thus, the processes responsible for the anomalous abundances in NGC 6752 are likely to be in operation to an even greater extent in the cluster M13.

Theoretical predictions based on current theories of AGB nucleosynthesis deviate markedly from the observations in a number of important ways: 1) Al-rich and O-poor stars are expected to have much higher $(^{25}\text{Mg} + ^{26}\text{Mg})/^{24}\text{Mg}$ ratios than is observed, 2) the ^{25}Mg abundance is tightly linked to ^{26}Mg abundance in the models, counter to observations, and 3) the predicted trend of $^{25,26}\text{Mg}/^{24}\text{Mg}$ with total Mg abundance (i.e. $[\text{Mg}/\text{Fe}]$) moves in the opposite direction to the data, due to the primary production of Mg in these AGB stars. Regarding the first point, we stress that the overproduction of $^{25,26}\text{Mg}$ by our GCCE model is not disastrous for the AGB self-pollution scenario. Lower values of $(^{25}\text{Mg} + ^{26}\text{Mg})/^{24}\text{Mg}$ could be obtained by diluting the AGB ejecta with more of the initial gas. Moreover, the dashed lines demonstrate that a factor of ~ 2 reduction in the AGB yield of $(^{25}\text{Mg} + ^{26}\text{Mg})/^{24}\text{Mg}$ can be attained by adopting a “steadier” rate of AGB mass-loss, such as the Reimers (1975) prescription described in Section 6.2.3. However, points 2 and 3, listed above,

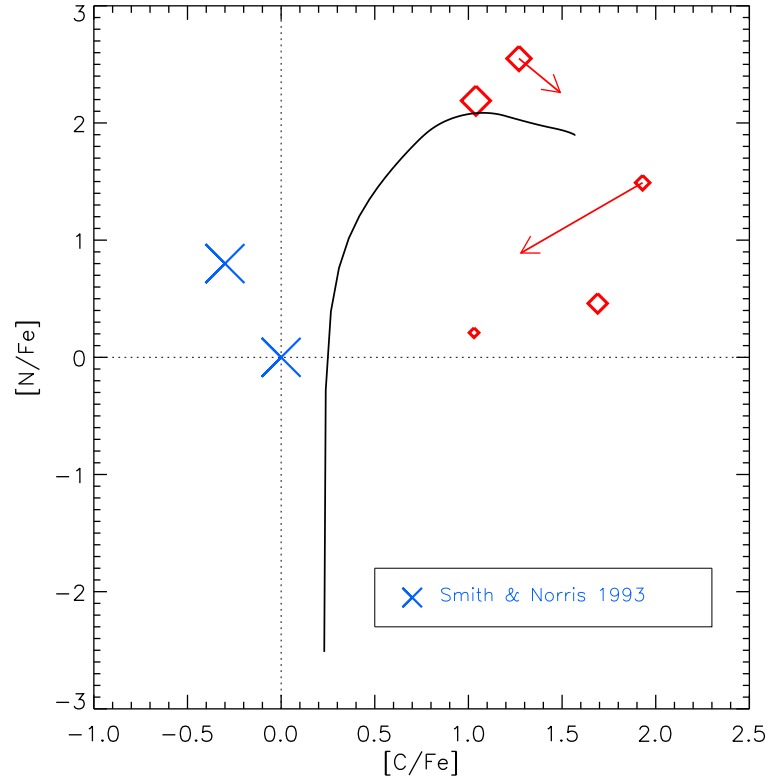


Figure 6.3: Predicted evolution of $[N/Fe]$ with $[C/Fe]$ (solid line). Symbols have the same meaning as in Figure 6.1 except that crosses denote data from Smith & Norris 1993.

represent more serious problems for the AGB self-pollution picture, and are robust to the variations in stellar inputs considered in this study.

Figure 6.3 compares the predicted trend of $[N/Fe]$ versus $[C/Fe]$ from the AGB pollution model (*solid line*) against observations of AGB stars in NGC 6752 from Smith & Norris (1993) (*crosses*). Diamonds correspond to yields from the AGB models for five initial masses from 1.25 to 6.5 M_{\odot} , and arrows reflect the effect of changing the mass-loss law. Red giants in NGC 6752 have been found to exhibit bimodal C and N abundances with one group having roughly solar $[C/Fe]$ and $[N/Fe]$, and the other group being N-rich and C-poor (e.g. da Costa & Cottrell 1980; Norris et al. 1981; Smith & Norris 1993). The empirical data points to an anticorrelation between C and N that has previously been explained in terms of the operation of a deep mixing mechanism in evolved stars. The dependence of the molecular CN-band strength on stellar luminosity (e.g. Suntzeff & Smith 1991) is readily understood as a

result of increased mixing of N-rich, C-poor material from within the stellar interior to the surface, as a function of evolutionary stage. More recently, however, Grundahl et al. (2002) found an anticorrelation between $[C/Fe]$ and $[N/Fe]$ in NGC 6752 stars that is independent of luminosity. Cannon et al. (1998) found a similar CN bimodality and anticorrelation in 47 Tuc from a sample of stars that included not just giants, but also unevolved main-sequence stars whose shallow convective layers preclude dredge-up of CNO-cycled material. The presence of the same CN trend in both dwarfs and giants led Cannon et al. (1998) to conclude that deep mixing was not singularly responsible for CN abundance anomalies in 47 Tuc. It seems likely that the CN patterns in NGC 6752 stars arise from a combination of deep mixing and some form of external pollution.

Figure 6.3 casts doubt on AGB stars being a major source of external pollution. All the AGB models from $1.25 - 6.5 M_{\odot}$ expel material that is enhanced in both N *and* C. From Figure 6.3 it is clear that main-sequence stars severely polluted by AGB material are expected to also exhibit heightened C and N abundances. The positive correlation between C and N in the intracluster gas predicted by our GCCE model fails to match the empirical trend, however, we note that our calculations only reflect the chemical evolution of the intracluster medium. The abundance pattern of the gas at a particular time corresponds to the initial composition of stars born at that time, whereas the observed abundance of elements like CNO in evolved red giants are likely to differ from their starting abundances due to internal synthesis and mixing.

Figure 6.4 reveals an almost order of magnitude rise in $[C+N+O/Fe]$ in the intracluster gas within 1 Gyr of formation. A slight drop in the O abundance is more than compensated for by a dramatic increase in C and N. This robust prediction is based on intermediate mass stellar nucleosynthesis and poses further difficulties for the AGB pollution scenario as an explanation for globular cluster abundance anomalies, since $C+N+O$ is found to be approximately constant in many GCs (Ivans et al. 1999). AGB stars have been proposed in the literature as promising candidates for producing the observed GC abundance anomalies because they exhibit the required hot H burning via hot-bottom burning. However, because these stars also dredge-up the products of He-burning, $C+N+O$ is not conserved in the models, in conflict with the data.

We note that in order to achieve an order of magnitude increase in the intracluster abundance of Al via the AGB pollution scenario, our models simultaneously predict

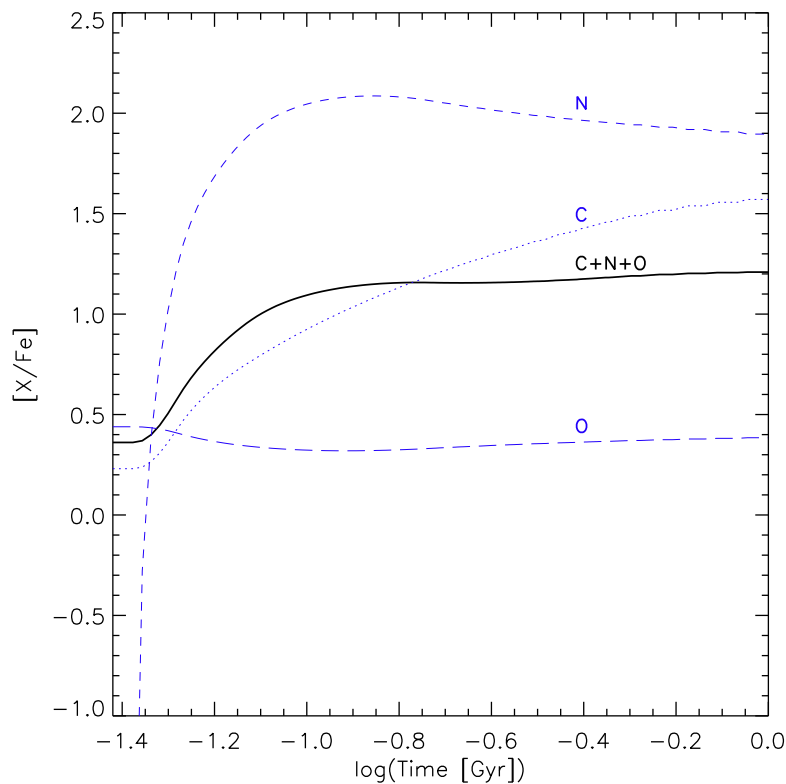


Figure 6.4: Temporal evolution of $[C/Fe]$ (dotted line), $[N/Fe]$ (short dashed line), $[O/Fe]$ (long dashed line), and $[C+N+O/Fe]$ (solid line). In contrast to observations in NGC 6752 and other globular clusters, $C+N+O$ abundance is predicted to vary by an order of magnitude if AGB stars are responsible for the Na and Al enhancement.

an intracluster medium helium mass fraction, Y , approaching 0.3. This represents a ~ 0.05 increase in Y over the primordial value. D’Antona et al. (2002) have found that the effects on stellar evolution due to this level of He enrichment would be difficult to measure observationally but could lead to extended blue tails in the horizontal branch morphology.

6.4 Conclusions

The presence of variations in C, N, O, Mg, Na, and Al in globular cluster stars yet to ascend the red giant branch provides compelling evidence for these chemical patterns already being in place in the gas from which cluster stars formed, or in gas that later polluted their atmospheres. Otherwise, one would expect to see

chemical homogeneity in stars below a certain luminosity, unless our understanding of deep mixing is seriously flawed. We have constructed a self-consistent model of the chemical evolution of the intracluster gas, that included custom-made detailed stellar models, to test whether the observed inhomogeneities may be caused by contamination from material processed by intermediate mass stars during their AGB phase. This model is compatible with either a scenario in which there is coeval and stochastic sweeping of the intermediate mass stellar ejecta by existing lower mass stars, or one in which new stars form from AGB polluted material. In the latter case, there would be a small age spread with Na-rich stars being a few hundred million years younger than Na-poor stars.

We find that, regardless of either the mechanism for polluting cluster stars with AGB material or the level of dilution of Pop III material by AGB ejecta, intermediate mass stars are unlikely to be responsible for most of the abundance anomalies. While metal-poor AGB models generate large quantities of Na and Al that may account for the observed spread in these elements in NGC 6752, the AGB pollution scenario encounters a number of serious problems: 1) O is not depleted within AGB stars to the extent required by observations, 2) Mg is *produced* when it should be *destroyed*, 3) C+N+O does not remain constant in AGB processed material, and 4) ^{25}Mg is correlated with ^{26}Mg in the modelled AGB ejecta, conflicting with the Yong et al. (2003) observations.

Note that all of these problems stem from the addition of helium burning products into the AGB star ejecta. Perhaps a generation of AGB stars which experience HBB but almost no dredge-up would fit the data better!

The model presented in this chapter could be generalised for application to other globular clusters by varying three main parameters: the initial metallicity; the upper mass limit beyond which stellar winds are too energetic for the cluster to retain the ejecta (this depends on the mass concentration and gravitational potential); and the efficiency and duration of star formation.

Chapter 7

Stellar abundance gradients in galactic disks

This chapter is based upon Ryder, Fenner & Gibson, 2005, MNRAS, 358, 1337.

7.1 Introduction

The preceding chapters have described chemical evolution in our own Galaxy and its components. It is natural for an investigation into galactic chemical evolution to focus firstly on the galaxy whose properties are best characterised – the Milky Way. In this way, one can use the largest possible set of empirical constraints to test the theoretical models. However, we should be careful not to assume that any individual galaxy necessarily follows a “typical” evolutionary path. It is therefore imperative to compare the Milky Way with other similar spiral galaxies and against different morphological classes of galaxies. With this aim in mind, we now describe the methodology of, and first results from, an observational program designed to measure radial gradients of Fe and Mg in disk galaxies with a range of morphologies. Ultimately, one hopes to account for similarities and differences in abundance gradients amongst galaxies using theoretical models such as `GEtool`.

Radial gradients in the abundances of elements such as oxygen, nitrogen, and sulphur have long been observed in the disk of the Milky Way (Shaver et al., 1983), as well as in the disks of many nearby spiral galaxies (Zaritsky et al., 1994; Ryder, 1995). The gas-phase abundances of these elements in H II regions are relatively straightforward to determine on the basis of their bright emission-line ratios (see the review by Henry & Worthey (1999)). Analyses by Vila-Costas & Edmunds (1992) and others have revealed interesting correlations between the slope of these abundance gradients, and global galaxy characteristics. A variety of mechanisms have been proposed to account for the fact that the inner regions of spiral galaxies are generally more metal-rich than the outer parts, including ongoing infall of metal-

poor gas, and radial inflow of enriched gas. The presence of a bar has been shown to homogenise the abundances somewhat, resulting in a flatter abundance profile than in an un-barred galaxy of similar Hubble type (Martin, 1998).

Since oxygen is a primary element produced in massive stars, its abundance is a useful measure of the *cumulative* massive star formation rate. In order to build up a proper star formation *history* however, it is necessary to be able to measure the relative abundances of other elements such as iron and magnesium, which are produced in different types of stars and released into the interstellar medium on different characteristic timescales. Abundance determinations from absorption line studies of these elements are commonplace for stars in our own Galaxy, (e.g. Friel & Janes 1993; Gilmore et al. 1995), in the integrated light of elliptical galaxies, bulges, and extragalactic globular clusters (e.g. Huchra et al. 1996; Trager et al. 1998; Cohen, Blakeslee, & Côté 2003), and as a function of radius for inner galactic regions (Raimann, Storchi-Bergmann, Bica, & Alloin 2001; Jablonka, Gorgas, & Goudfrooij 2002; Proctor & Sansom 2002; Worthey 2004). However, such measurements become much more difficult in galactic disks, due to the fact that the surface brightness of the unresolved stellar population (against which a weak absorption feature must be measured) is much lower. Fortunately, interference filter imaging offers almost an *order of magnitude* gain in effective signal-to-noise over a long-slit spectrograph of the same resolution, as demonstrated by Beauchamp & Hardy (1997) and Mollá, Hardy & Beauchamp (1999). Despite a modest telescope aperture, and the need for expensive, custom-made filters with broader bandpasses than one would like ($\sim 60 \text{ \AA}$, to be able to cover a useful range in galaxy redshift), these pioneering studies have revealed the existence of shallow radial gradients in the $\text{Mg}_2\lambda 5176$ and $\text{Fe}\lambda 5270$ features in the disks of NGC 4303, NGC 4321, and NGC 4535.

In this chapter, we describe the application of narrow-band absorption-line imaging techniques using the wavelength agility, wide field-of-view, and charge-shuffling ability of the Taurus Tunable Filter (TTF) at the Anglo-Australian Telescope (AAT) to almost triple the number of face-on spiral galaxies for which stellar radial abundance gradients have been measured. We begin by outlining the TTF's characteristics in Section 7.2, before demonstrating the sensitivity of our technique on stars with a range of known abundances in Section 7.3. Our galaxy imaging and surface photometry techniques are presented in Sections 7.4 and 7.5, and the radial gradients in "Lick/IDS" spectral line indices (Faber et al. 1985; Worthey et al. 1994) in Section 7.6. The Lick spectral indices do not measure abundances *per se*, but can be

transformed to quantities like $[\text{Fe}/\text{H}]$ via the method of spectral synthesis. In future work, we will present models and tools for converting between absolute elemental abundances and line indices in the observer’s plane, and thus place new constraints on the star formation histories of the galaxies presented here.

7.2 Absorption Line Imaging

7.2.1 The Taurus Tunable Filter (TTF) Instrument

The TTF is a tunable Fabry-Perot Interferometer consisting of two highly polished glass plates whose separation is controlled to high accuracy by piezoelectric stacks. Unlike most Fabry-Perot etalons which have resolving powers $R > 1000$, the TTF is designed to work at plate separations $\sim 10 \mu\text{m}$ or less, delivering $R = 100 - 1000$, comparable to conventional fixed narrow-band interference filters (see Bland-Hawthorn & Jones (1998) and Bland-Hawthorn & Kedziora-Chudczer (2003) for summaries of the optical design and practical applications of the TTF). The TTF is mounted in the collimated beam of the Taurus II focal reducer, and at the $f/8$ Cassegrain focus of the 3.9 m AAT delivers a field of view up to 10 arcmin in diameter (depending on the clear aperture of the blocking filter in use). The EEV 2048 \times 4096 CCD detector used for these observations has a scale of 0.33 arcsec pixel $^{-1}$, and a quantum efficiency near 90 percent in the 5000 – 6000 Å wavelength range.

By enabling an adjustable passband anywhere between 3700 and 10000 Å, the TTF obviates the need for an entire suite of narrow-band filters, and makes possible monochromatic imaging of almost any feature of interest over an expansive redshift range. Another important aspect of our observing method is the use of charge-shuffling synchronised with passband-switching, which overcomes many of the systematic errors which plague conventional narrow-band imaging, while allowing accurate differential measurements under less than ideal observing conditions.

7.2.2 Choice of Lick indices and blocking filters

In their work, Beauchamp & Hardy (1997) and Mollá, Hardy & Beauchamp (1999) concentrated on the Mg_2 and Fe5270 features, two of the most prominent “Lick/IDS” indices (Faber et al. 1985; Worthey, Faber, Gonzalez & Burstein 1994), in part to limit the number of expensive narrow-band filters that would be required. We chose

to image our sample galaxies in these same two lines in order to be consistent with their study and to facilitate comparison with the large body of observational and theoretical work performed with these two indices. Nevertheless, as Tripicco & Bell (1995) point out, these features are susceptible to some contamination by other elements, such as Ca and C.

To simplify the transformations from our observed measurements of the absorption line and continuum flux ratios to the Lick indices, we have endeavoured to match as closely as possible the original line and continuum bandpass definitions laid down by Faber et al. (1985). While selecting the narrowest possible bandpass for the TTF will ensure the maximum contrast between the absorption line core flux and continuum band, the overall signal-to-noise (S/N) of each measurement (and more significantly, of their ratio which defines the index) will suffer from the reduced throughput. On the other hand, the broadest bandpass will improve the throughput, but at the expense of diluting the absorption feature. Because narrowing the gap between the plates in order to broaden the passband risks irreparable damage to the plates should their coatings or dust come into contact with each other, we opted for a minimum plate spacing of 2.5 microns, which yields a Lorentzian passband with Full Width at Half-Maximum (FWHM) $\sim 15 \text{ \AA}$ at 5100 \AA . This is four times narrower than the fixed filters employed by Beauchamp & Hardy (1997), and being of the same order as the equivalent widths of the Mg_2 and Fe5270 features, is a good compromise between contrast and S/N.

Like all Fabry-Perot etalons, the TTF has a periodic transmission profile, with a finesse $N = 40$, i.e. an inter-order spacing of $40\times$ the instrumental FWHM. Thus, to ensure only a single order of the TTF reaches the detector, we require a blocking filter with $\text{FWHM} < 600 \text{ \AA}$, but broad enough to contain the full Mg_2 and Fe5270 passbands. Unfortunately, none of the existing TTF blocking filters meets both these requirements, and the f126 blocking filter we used, a 380 \AA FWHM interference filter centred on 5220 \AA , was not ideal. As Figure 7.1 shows, the blue continuum of the Mg_2 feature lies just outside the blue cutoff of the f126 filter, while the transmission peaks at barely 70 percent, and varies by up to 35 percent over just 100 \AA . In addition, the clear aperture of just 63 mm limits the usable field of view to about 6 arcmin in diameter. Nevertheless, as we show in the following sections, this blocking filter adequately met the goals of this project. To cover the blue continuum of the Mg_2 feature, we used the TTF's B4 blocking filter, with a $\text{FWHM} = 320 \text{ \AA}$ centred on 5000 \AA , a clear aperture of 122 mm, and a peak throughput of 76 percent.

7.2.3 Wavelength calibration

The plate separation and parallelism in the TTF is set by three piezoelectric stacks, and servo-stabilised against drifting by a capacitance bridge. Tuning to the desired wavelength is performed by fine adjustment of the plate separation through a Queensgate Instruments CS100 controller. In order to define the relationship between a given plate separation (Z , in analog-to-digital units) and central wavelength of the TTF passband (λ , in Å), we illuminate the TTF uniformly with an arc lamp, and record the lamp spectrum while scanning the TTF progressively in wavelength. For the region of interest (4800 – 6400 Å), a combination of deuterium, helium, and neon lamps yielded sufficient lines for this purpose.

As noted by Jones et al. (2002), at plate separations $\lesssim 3$ microns the multi-layer coating thickness becomes a significant fraction of the actual plate spacing. Since the depth within the coatings where reflection occurs is wavelength-dependent, the net effect is that the relation between Z and λ is no longer linear as it is for larger plate spacings (or equivalently, narrower bandpasses). Indeed, we found it necessary to apply a quadratic (second order) fit to the $Z(\lambda)$ relation. Incorrectly assuming a linear relation could result in the passband being off by the equivalent of the FWHM at the extreme wavelength settings.

7.3 Stellar observations and calibration onto the Lick system

In order to derive a function for converting absorption line-strengths measured with the TTF into the Lick/IDS system, we applied our technique to 31 Lick standard stars for which Mg₂ and Fe5270 indices are available in Worthey et al. (1994). These stars spanned a broad range in metallicity, and thus in their Lick indices. Stars were imaged at ~ 6 Å intervals in a wavelength range from a minimum of either 5100 Å or 4870 Å to a maximum 5400 Å, with the TTF set to a bandpass of FWHM ~ 17 Å. In this way, a low-resolution spectrum was built-up from the series of individual images for each star. Each stellar image was trimmed, bias corrected, and flux within a fixed aperture measured using tasks within the IRAF package.

Figure 7.1 compares a TTF spectral scan (*solid line*) for the star HD131977 against a Coudé Feed stellar spectrum of the same star (found at *The Indo-U.S. Library of Coudé Feed Stellar Spectra* home page at <http://www.noao.edu/cfib/>),

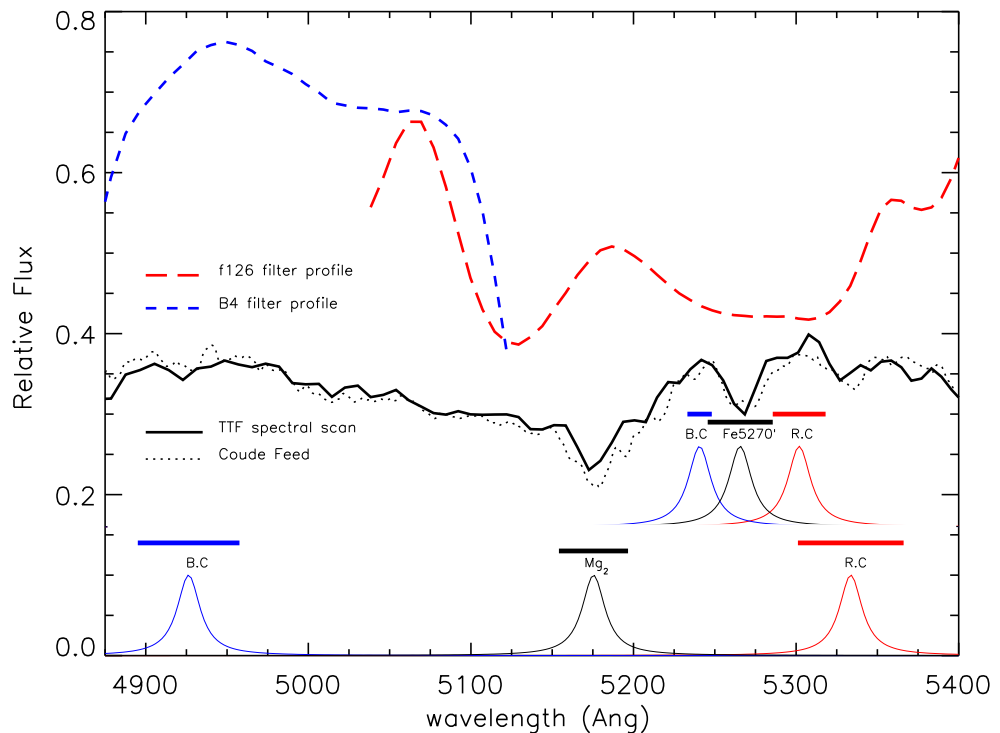


Figure 7.1: TTF spectral scan (solid curve) for the star HD131977 versus a Coudé Feed stellar spectrum, degraded to match the resolution of the TTF data (dotted curve). The TTF spectrum has been corrected for the transmission profiles of the f126 and B4 blocking filters (dashed lines). The Lorentzian profiles with FWHM of 17 Å illustrate the shape of the TTF bandpass. They are centred on the Mg_2 and Fe5270 absorption features and their corresponding red and blue continua, whose locations were defined by Faber et al. 1985. Thick horizontal lines indicate the Lick bandpasses.

degraded to match the resolution of the TTF data (*dotted line*). The TTF spectrum has been corrected for the transmission profiles of the f126 and B4 blocking filters (described in Section 7.2.2). The filter transmission profiles (*dashed lines*) were obtained by dividing our TTF spectral scans of the flux standards HR7596 and HR5501 by the flux calibrated spectra from Hamuy et al. (1992). The alignment between the spectral features seen in the TTF scan and those of the Coudé Feed spectrum confirms that the quadratic $Z(\lambda)$ relation described in Section 7.2.3 leads to good wavelength calibration. The location of the Lorentzian profiles shown in Figure 7.1 indicates the central wavelengths of the Mg_2 and Fe5270 absorption features and the corresponding red and blue continua, as defined by Faber et al. (1985). The shape of the Lorentzians illustrates that of the TTF bandpass used in this study, particularly the broad wings.

The full stellar spectral scans provide a means for checking not just the wavelength calibration, but just as importantly, in gauging the sensitivity of this imaging technique to picking out the spectral features. However, the Mg_2 and Fe5270 indices would have to be derived using only the images at the (velocity-corrected) line and continuum wavelengths. Instrumental indices were calculated from the following expressions:

The full stellar spectral scans provide a means for checking not just the wavelength calibration, but just as importantly, in gauging the sensitivity of this imaging technique to spectral features. However, the Mg_2 and Fe5270 indices were not calculated from the full spectral scans. Instead, they were derived using only the images at the (velocity-corrected) line and continuum wavelengths, since this is the technique to be applied to the galaxies. Instrumental indices were calculated from the following expressions:

$$\text{Mg}_{2\text{TTF}} = -2.5 \log_{10} \left(\frac{\mathcal{F}_{\text{Mg}_2}}{\mathcal{F}_c} \right) \text{ [mag]} \quad (7.1)$$

$$\text{Fe5270}_{\text{TTF}} = \Delta\lambda \left(1 - \frac{\mathcal{F}_{\text{Fe5270}}}{\mathcal{F}_c} \right) \text{ [\AA]} \quad (7.2)$$

where $\mathcal{F}_{\text{Mg}_2}$ and $\mathcal{F}_{\text{Fe5270}}$ denotes the sky-subtracted, filter profile-corrected flux at the Mg_2 and Fe5270 line wavelengths, respectively. The continuum flux, \mathcal{F}_c , is given by:

$$\mathcal{F}_c = a \mathcal{F}_{RC} + b \mathcal{F}_{BC}, \quad (7.3)$$

where $a + b = 1$, and \mathcal{F}_{RC} and \mathcal{F}_{BC} are the sky-subtracted, filter profile-corrected flux at the red and blue continua, respectively. We varied the weighting given to the red and blue continua and found that the strongest correlation between our TTF indices and the Lick values was obtained by using the red continuum only (i.e. $a = 1$ and $b = 0$). Table 7.1 presents the gradients, y-intercepts, associated errors and chi-squared values for the fit between TTF and Lick Fe5270 indices obtained using only the red continuum (column 3), only the blue continuum (column 4) and with equal weighting (column 5). Table 7.1 only shows the $a = 1$ case for Mg_2 (column 2) because our spectral scans only extended down to $\sim 4870 \text{ \AA}$ for about half of the stars, however, this case gave the best fit. Not only does the inclusion of the blue continuum worsen the fit to the Lick indices, but in the case of Mg_2 , observing the

Table 7.1: Stellar Lick index fit parameters ^a

$\mathcal{F}_c =$	Mg ₂	Fe5270		
	\mathcal{F}_{RC}	\mathcal{F}_{RC}	\mathcal{F}_{BC}	$(\mathcal{F}_{RC} + \mathcal{F}_{BC})/2$
gradient	1.00	1.22	1.16	1.44
Δ gradient	0.02	0.08	0.24	0.13
y-intercept	0.02	0.2	1.5	0.4
Δ y-intercept	0.01	0.2	0.4	0.3
chi-squared	0.02	5.4	26	9

^a for the equations $\text{Mg}_{2\text{Lick}} = \text{gradient} \times \text{Mg}_{2\text{TTF}} + \text{y-intercept}$ and $\text{Fe5270}_{\text{Lick}} = \text{gradient} \times \text{Fe5270}_{\text{TTF}} + \text{y-intercept}$.

blue continuum introduces further complications. Firstly, measuring $\text{Mg}_{2,BC} \lambda 4926$ involves changing from the f126 to the B4 blocking filter. Since filters could not be switched while in charge-shuffle mode, one would lose some of the advantage of this differential observing technique to average over temporal variations in air mass and photometric conditions during exposures. Secondly, the blue continuum range of $4895.125 - 4957.625 \text{ \AA}$, as defined by Worthey et al. (1994), is contaminated in many active galaxies by [O III] $\lambda 4959$ emission. Our sample of eight galaxies contains three Seyferts, for which this [O III] emission is likely to contribute to the flux in the $\text{Mg}_{2,BC}$ images. For these reasons, and considering the fit parameters shown in Table 7.1, the value \mathcal{F}_c in equations 7.1 and 7.2, was determined exclusively from red continuum images for both Mg₂ and Fe5270.

Figure 7.2 compares the Mg₂ and Fe5270 indices obtained for our sample of 31 stars using the absorption-line imaging technique described in this study against the published Lick values. The following equations allow the transformation of $\text{Mg}_{2\text{TTF}}$ and $\text{Fe5270}_{\text{TTF}}$ into the Lick system, and were used for subsequent galaxy data analysis:

$$\text{Mg}_{2\text{Lick}} = 1.00(\pm 0.02) \text{Mg}_{2\text{TTF}} + 0.02(\pm 0.01) \text{ [mag]} \quad (7.4)$$

$$\text{Fe5270}_{\text{Lick}} = 1.22(\pm 0.08) \text{Fe5270}_{\text{TTF}} + 0.2(\pm 0.2) \text{ [\AA]} \quad (7.5)$$

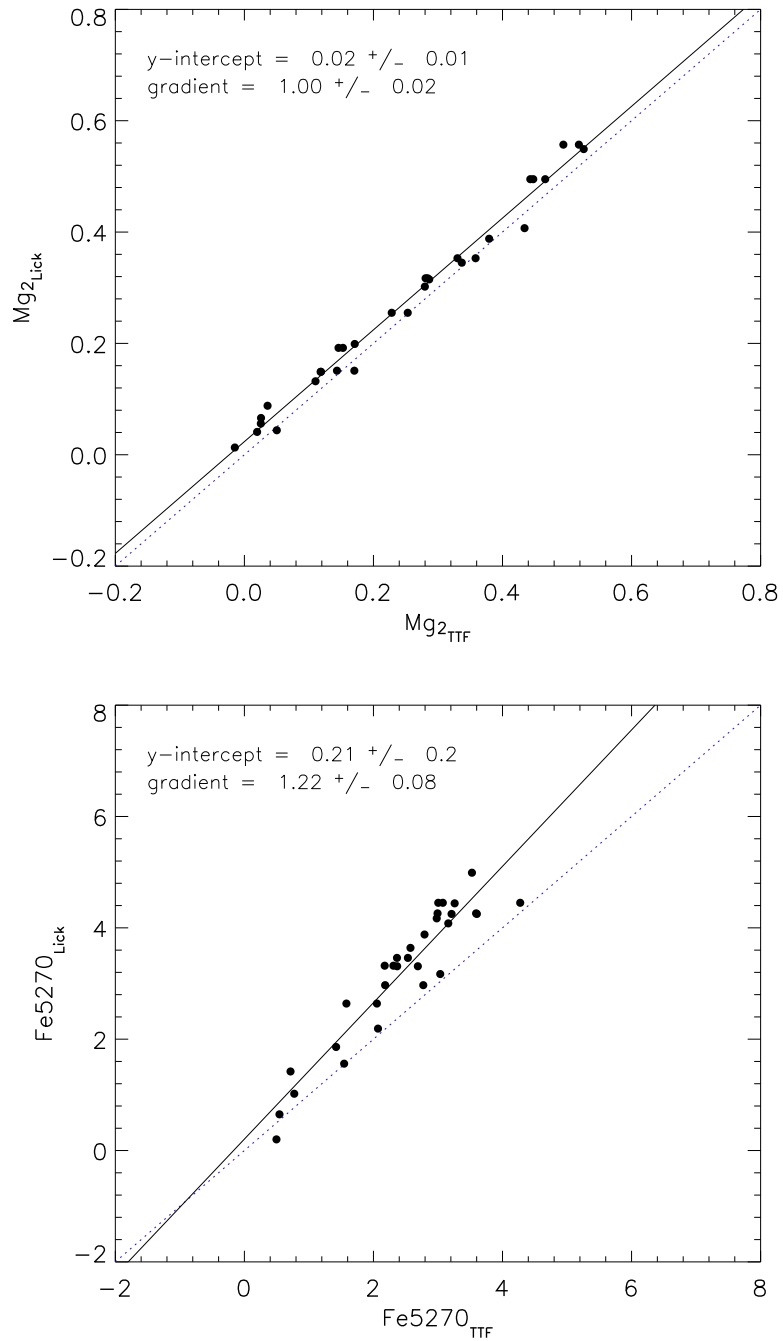


Figure 7.2: Top panel: Relationship between measured TTF Mg_2 index and the published Lick Mg_2 value, where our TTF index was derived using the line and red continuum measurements only, as described in the text. Dotted line shows the one-to-one relationship. Bottom panel: Same as top panel, but for the $Fe5270$ index.

7.4 Galaxy Observations

Having established the credentials of our technique using Lick standard stars, we observed a sample of eight spiral galaxies, selected in order to satisfy the following needs: 1) to span a range of morphologies, from early to late Hubble types; 2) to be roughly face-on; and 3) to fill enough of our CCD such that the galactic disk covers a large number of pixels but leaves sufficient area from which to estimate the background sky level. The last criterion meant that all our galaxies have diameters between about 2 and 4 arcmin. Choosing galaxies with low inclination angles ensures that the stellar rotational velocity dispersion “fits” within the bandpass used in this study. Some properties of the galaxies are summarised in Table 7.2.

Galaxy observations consisted of 10 minutes of integration at each wavelength, with the TTF passband being switched between the redshifted line core and red continuum wavelengths each minute, while synchronously shuffling the charge back and forth across the CCD between an “exposure” and a “storage” location. Thus, temporal variations in atmospheric and seeing conditions were smoothed out over both spectral passbands (see Maloney & Bland-Hawthorn (2001) for a detailed description of this charge-shuffle technique). Multiple charge-shuffled exposures were taken of each galaxy, with the total exposure times for Mg₂ and Fe5270 given in Table 7.3.

7.5 Galaxy data reduction and analysis

In this section, we describe each of the steps involved in reducing and analysing the galaxy data in order to evaluate the Mg₂ and Fe5270 radial profiles.

Table 7.2: Galaxy Properties

Galaxy	Hubble Type ^a	Recession Vel.(km s ⁻¹) ^a	Dist. (Mpc) ^b	Incl. (deg) ^c	m _B (mag) ^a	Scale (pc arcsec ⁻¹)	mean surf brightness ^c	D ₂₅ (arcmin) ^c
NGC 5968	SAB(r)bc	5448	77	22	13.1	352	22.7	2.2
NGC 6221	SB(s)bc pec	1482	20	62	10.7	96	21.5	4.5
NGC 6753	(R')SA(r)b	3124	42	31	12.0	202	20.8	2.6
NGC 6814	SAB(rs)bc	1563	21	65	12.1	101	22.0	3.3
NGC 6935	(R)SA(r)a	4587	61	31	12.8	296	21.7	2.2
NGC 7213	SA(s)0 LINER	1792	24	29	11.0	116	20.7	3.0
NGC 7412	SAB(s)c	1717	23	41	11.9	111	22.1	4.1
NGC 7637	SA(r)bc	3680	49	28	13.2	238	22.4	2.2

^a de Vaucouleurs et al. 1991

^b Based on recession velocity and assuming a Hubble constant of 75 km s⁻¹ Mpc⁻¹

^c LEDA

Table 7.3: Galaxy observation log

Galaxy	Lick Feature	Date	Total Exp [min]	Notes
NGC 5968	Mg ₂ line + R.C.	31 Jul 2003	120	poor seeing, some clouds
	Fe5270 line + R.C.	28 Jul 2003	60	
NGC 6221	Mg ₂ line + R.C.	7 Aug 2002	120	poor seeing
	Fe5270 line + R.C.	6 Aug 2002	60	
NGC 6753	Mg ₂ line + R.C.	29 Jul 2003	120	
	Fe5270 line + R.C.	28 Jul 2003	60	
NGC 6814	Mg ₂ line + R.C.	8 Aug 2002	40	
	Fe5270 line + R.C.	8 Aug 2002	60	
NGC 6935	Mg ₂ line + R.C.	31 Jul 2003	120	poor seeing
	Fe5270 line + R.C.	28 Jul 2003	60	
NGC 7213	Mg ₂ line + R.C.	7 Aug 2002	120	poor seeing, some clouds
	Fe5270 line + R.C.	6 Aug 2002	60	
NGC 7412	Mg ₂ line + R.C.	7 Aug 2002	80	some clouds
	Fe5270 line + R.C.	8 Aug 2002	60	
NGC 7637	Mg ₂ line + R.C.	31 Jul 2003	100	poor seeing
	Fe5270 line + R.C.	28 Jul 2003	60	

7.5.1 Data Reduction

Reduction of raw galaxy images

Due to the charge-shuffle technique, the line and continuum images are located in different regions on a single CCD image. After bias subtraction, each image was bisected into the line and continuum component. These images were trimmed for compatibility with the flat-field images, which were not charge-shuffled and occupied a slightly smaller area of the CCD. Galaxy images were then averaged to produce four images per galaxy, corresponding to the Mg₂ and the Fe5270 line and red continuum wavelengths.

Flat-field correction

Correctly flat-fielding the galaxy images is crucial for eliminating spatial variations in the pixel to pixel response due to filter transmission and with wavelength/etalon spacing. Any residual large-scale structure in the images will compromise subsequent surface photometry. After each night's observing, a series of dome flats was taken, with the etalon set to the same spacings/wavelengths at which the galaxies were observed. Typically, three 10 second exposures were taken per wavelength. Each set of three flat-fields was combined into a single image, that was then normalised

and divided into the appropriate 288 galaxy image, as part of the IRAF flat-fielding procedures.

Ellipse procedure

The ELLIPSE package within IRAF/STSDAS was used to analyse separately, but identically, the radial surface brightness profiles of the line and continuum images. There were four images per galaxy, taken at the Mg₂ line and continuum and Fe5270 line and continuum wavelengths. Position angle and ellipticity were fitted interactively to one of the images, with the same settings being applied to the remaining three images and fixed at all radii. Linear radial steps were used and the average flux within each ellipse was calculated with the ELLIPSE package using the median area integration mode. Discrepant data points were eliminated within ELLIPSE by imposing 2- and 3-sigma upper and lower clipping criteria, respectively, and by iterating the clipping algorithm four times. H II regions were not masked, but they are not expected to significantly affect the measured surface brightness profile because they generally occupy a small fraction of pixels per ellipse and therefore should have a negligible influence on the median flux. Moreover, the clipping algorithm removes many pixels associated with bright H II regions.

The ELLIPSE procedure yields radial surface brightness profiles for Mg₂ and Fe5270 in the line and continuum for each galaxy. Each line and continuum pair of surface brightness profiles then needed to be sky-subtracted, filter-profile corrected, converted to instrumental indices via equations 7.1 and 7.2, and finally transformed into the Lick system using equations 7.4 and 7.5. These steps are described in the following section.

7.5.2 Data Analysis

Sky subtraction

The sky level was estimated from the mean flux in an elliptical annulus whose inner radius and width was selected to ensure that the radial variation in surface brightness was less than the pixel-to-pixel dispersion in each ellipse. In this way, the sky was taken from a “flat” part of the radial surface brightness profile and, in most cases, the sky annulus lay well outside the isophotal radius. For each galaxy, the same sky annulus was used for all four Mg₂ and Fe5270 line and continuum

images. The average brightness in the sky annulus was then subtracted from the surface brightness profile.

Filter profile correction

Two methods of correcting for the wavelength-dependent filter transmission profile were tested. In the first instance, we divided each surface brightness profile by the value of the filter profile (shown in Figure 7.1) at the corresponding wavelength, i.e. the same technique as for the standard stars. However, better results were obtained by instead applying a scaling factor to the radial profiles such that the value of the line and continuum sky levels were equal. This forces the TTF instrumental Mg₂ and Fe5270 indices to have an average value of zero in the sky annuli.

There are several reasons why the second approach was more accurate than the first approach, despite its success when used on standard stars. Firstly, inspection of Figure 7.1 reveals that the Fe5270 line and red continuum fall on a fairly flat part of the f126 filter profile, such that filter transmission is not very sensitive to drifts in wavelength calibration (that can be as large as 4 Å, as will be discussed in Section 7.5.3 below). Although the Mg₂ line and red continuum fall on steeper parts of profile, small shifts in wavelength calibration would change the transmission of the line and continuum by similar amounts. Thus, the *relative* transmission of the line and continuum features for both Mg₂ and Fe5270 is fairly robust to wavelength calibration drifts for objects at or near rest-wavelength. The recessional velocities of our sample of galaxies (given in Table 7.2) shift the spectral features toward longer wavelengths by 30–100 Å. This tends to place the galaxy line and continua in regions of the spectrum where their *relative* transmission is far more sensitive to small wavelength drifts. Secondly, unlike the stellar observations, the galaxy exposures lasted at least an hour, during which time the TTF alternated between line and continuum wavelengths at one minute intervals. As a result, the amount of light reaching the CCD varied smoothly with changing airmass but also varied unpredictably with fluctuating photometric conditions. If one applies the filter profile correction factor to the surface brightness profiles, it is still necessary to scale the images to account for residual differences in atmospheric conditions. Conversely, by using the relative line and red continuum sky levels to correct for filter transmission, one naturally corrects for variable observing conditions during exposures. However, this approach assumes that the intensity of the background

sky is the same at both the line and red continuum wavelengths.

Conversion to Lick system

Finally, equations 7.1 and 7.2 were used to derive instrumental indices and equations 7.4 and 7.5 allowed the transformation into the Lick system.

7.5.3 Errors

Our results are subject to various sources of uncertainty, the most important of which are: 1) sky subtraction, 2) filter transmission profile correction, and 3) TTF to Lick conversion. Each of these sources of error act on the calculated radial line-strength profiles in different ways. The foremost factor influencing the line-strength *gradients* is the estimation and subtraction of the background sky level, which introduces very large errors toward the outer galactic disk, where the galaxy surface brightness is very low relative to the sky. The sky subtraction uncertainty, σ_{sky} , was evaluated from the flux dispersion in the annulus designated as the sky region. The position of this sky annulus was somewhat subjective and was chosen to minimise the rms dispersion.

The error, σ_{filter} , due to correcting for the wavelength-dependent filter transmission profile does not influence the shape or gradient of the radial line-strength profile, but instead can uniformly shift the radial profile vertically.

Converting the instrumental indices into the Lick system introduces the errors specified in equations 7.4 and 7.5. These errors affect both the profile shape and the absolute values of the line-strengths. It should be emphasised that the uncertainty in the profile shape due to sky subtraction overwhelms that associated with TTF-to-Lick conversion.

Although we frequently re-calibrated our $Z(\lambda)$ relation between galaxy exposures, the wavelength tuning was found to drift by up to 5\AA over the course of a night. Such a drift introduces errors into the measured indices in two ways: firstly, one loses sensitivity to the absorption-line as the bandpass shifts too far from the centroid of the absorption feature; and secondly, the blocking filter transmission profile is strongly wavelength-dependent – especially for $\lambda \gtrsim 5300\text{\AA}$ and $\lesssim 5230\text{\AA}$, as evident in Figure 7.1. The error introduced by this wavelength calibration drift is, however, already folded into the TTF-to-Lick conversion error. This is because the stellar observations used to transform TTF instrumental indices into the Lick sys-

tem were themselves subject to calibration drift, and this contributes to the scatter seen in Figure 7.2.

Seeing varied from less than 1 arcsec to about 4 arcsec in the worst conditions, but because the flux was azimuthally averaged in ~ 5 arcsec spaced radial bins, poor seeing is only likely to have affected the calculated line-strengths in the innermost radii. Moreover, since the radial gradients listed in Table 7.4 refer to the disk only, excluding the central bulge, our calculations are barely affected by changing seeing conditions.

7.6 Results

Figures 7.3–7.10 illustrate the main results of this study. Images of each galaxy are presented along with plots of the radial variation of surface brightness and the Mg_2 and Fe5270 indices. In each figure a 288×288 arcsec image of the galaxy in the Fe5270 line is presented in panel (a), overlaid with two ellipses indicating the inner and outer bounds of the region from which the background sky level was calculated. For each individual galaxy, the ellipse geometry was fitted using the technique described in Section 7.5.1 and fixed for all radii. Panel (b) in each figure shows the radial variation in surface brightness, with the thick solid line denoting the location of the background sky annulus. Panels (c) and (d) show the radial gradients of the Mg_2 and Fe5270 Lick indices, respectively, calculated using the method described in Section 7.5. Note that the surface brightness profile plots extend to greater radii than the line strength gradient plots. The total uncertainty due to sky subtraction, filter transmission correction and transformation into the Lick system is shown by thin error bars, while the thick bars display the error due to sky subtraction alone. The dashed line indicates the sky subtraction error-weighted line of best fit to the disk. Since the radial gradients are most sensitive to uncertainty in sky subtraction, they were calculated using only sky subtraction errors to weight the data points. As pointed out in Section 7.5.3, the errors from filter transmission correction and transformation into the Lick system act to uniformly shift the curves vertically, but do not change the gradient. The inner bulge, whose extent was determined from the surface brightness profiles, was excluded when calculating the disk gradient.

Table 7.4 summarises the Mg_2 and Fe5270 indices derived for the inner bulge

along with the gradient and vertical intercept of the linear fit to the radial line-strength profiles in the disk of the eight galaxies in our sample. The disk gradients exclude the galactic bulge and are expressed with respect to the apparent radius, $R_{25} = D_{25}/2$, where D_{25} is listed in Table 7.2.

One motivation for this kind of study is to test the dependence of abundance gradients in disk galaxies on Hubble type. In an investigation into line-strength gradients in SO galaxies, Fisher, Franx & Illingworth (1996) found evidence for a strong relationship, with the shallowest gradients being found in SO galaxies and the steepest in later-type spirals. We find no clear trend between Hubble type and gradient in our small sample, but we note that the only SO galaxy in our sample also has the only positive gradient. Unfortunately, our sample is too small to draw statistically significant conclusions.

As this study presents the first ever measurements of Lick indices across the disks of these eight galaxies, a direct comparison of our main results with the literature was not possible. Restrictions imposed by the availability of targets meeting the selection criteria outlined in Section 7.4 prevented any overlap between our sample and that of Beauchamp & Hardy (1997) and Mollá, Hardy & Beauchamp (1999). Idiart, de Freitas Pacheco & Costa (1996) measured Lick indices in the bulge of one of our galaxies, NGC 6935, finding $Mg_2 = 0.243 \pm 0.009$ mag and $Fe5270 = 2.3 \pm 0.23$ Å. Reassuringly, our value of $Fe5270 = 2.4 \pm 0.4$ Å in the central galaxy is in very good agreement with Idiart et al. (1996), although our value of $Mg_2 = 0.29 \pm 0.03$ mag is slightly higher. We note that, unlike Idiart et al. (1996), our values have not been corrected for velocity dispersion, nor reddening. However, Beauchamp & Hardy (1997) demonstrated that spectral broadening due to stellar velocity dispersion is small for face-on spirals like those in our sample. From the results of Beauchamp & Hardy (1997), we also expect that any reddening corrections are less than uncertainties in the data and would not significantly affect the index gradients. We emphasise that the chief sources of error affecting the *absolute* values of our derived Mg_2 and $Fe5270$ in the bulge come from correcting for the filter transmission profile and transforming into the Lick system. For each galaxy, these uncertainties translate into roughly the same offset in absolute value for all radii. The following discussions concentrate on the radial behaviour and *gradients* of the line-strengths: properties that are robust to most sources of uncertainty aside from sky subtraction.

Cid Fernandes, Storchi-Bergmann & Schmitt (1998) measured radial variations

Table 7.4: Central indices and disk gradients

Galaxy	Mg ₂ (r=0)	Fe5270(r=0)	$\Delta\text{Mg}_2 / R_{25}$ ^a	$\Delta\text{Fe5270} / R_{25}$ ^a	Mg ₂ intercept ^b	Fe5270 intercept ^b
NGC 5968	0.22 ± 0.03	3.2 ± 0.4	-0.15 ± 0.05	-0.8 ± 0.7	0.26 ± 0.02	3.0 ± 0.3
NGC 6221	0.17 ± 0.03	1.9 ± 0.3	0.0 ± 0.06	-1.5 ± 1	0.17 ± 0.02	1.6 ± 0.3
NGC 6753	0.40 ± 0.03	2.6 ± 0.4	-0.09 ± 0.02	-1 ± 0.5	0.268 ± 0.005	2.8 ± 0.1
NGC 6814	0.23 ± 0.03	1.0 ± 0.3	-0.1 ± 0.05	-2 ± 1	0.27 ± 0.01	2.3 ± 0.2
NGC 6935	0.29 ± 0.03	2.4 ± 0.4	-0.15 ± 0.03	-1.7 ± 0.4	0.32 ± 0.01	2.8 ± 0.1
NGC 7213	0.23 ± 0.03	1.7 ± 0.3	0.15 ± 0.04	2 ± 1	0.15 ± 0.01	1.1 ± 0.2
NGC 7412	0.16 ± 0.03	2.0 ± 0.4	-0.05 ± 0.1	-1 ± 1.5	0.15 ± 0.02	2.0 ± 0.2
NGC 7637	0.24 ± 0.03	2.2 ± 0.3	-0.15 ± 0.03	-1.5 ± 0.5	0.253 ± 0.005	2.9 ± 0.1

^a Disk gradient (excluding inner bulge), expressed with respect to the apparent radius, $R_{25}=D_{25}/2$, listed in Table 7.2.

^b Vertical intercept of the linear fit to the disk radial line-strength profiles – i.e. the extrapolation to zero radius of the dashed lines seen in the panels *b*) and *c*) of Figures 7.3–7.10.

in stellar absorption features in the inner regions of active galaxies, including the three Seyfert galaxies in our sample; NGC 6221, NGC 6814 and NGC 7213. They did not use the Lick system to measure spectral lines, however their radial profiles of the equivalent width (EW) of the Mg I + Mg H feature allow for a qualitative comparison with our Mg₂ measurements. Their wavelength window of 5156–5196 Å for Mg I + Mg H matches the Lick definition for Mg₂, but Cid Fernandes et al. (1998) use different pseudo-continua. As will be discussed in more detail below, the shape of their Mg I + Mg H profiles compare well with our Mg₂ profiles for all three galaxies, although their measurements only extend to radii less than a quarter those reached in this investigation.

7.7 Individual Galaxies

In this section, we comment on the radial line-strength profiles for each galaxy individually.

7.7.1 NGC 5968 - SBab

This galaxy has a small bright nucleus, a short bar, thin, knotty arms (RC3), and the lowest mean surface brightness of the galaxies in our sample (see Table 7.2). The same overall features are seen in both the Mg₂ and Fe5270 profiles (Figure 7.3), however the Mg₂ gradient is steeper than that of Fe5270, giving NGC 5968 the highest ratio of $\Delta\text{Mg}_2/\Delta\text{Fe5270}$ in our sample.

7.7.2 NGC 6221 - SBc

This galaxy exhibits peculiar morphology and asymmetric arms due to interaction with its neighbour NGC 6215 and several smaller dwarf galaxies (Koribalski & Dickey, 2004). A thick bar is evident and most of the current star formation is offset from the nucleus. Cid Fernandes et al. (1998) measured the MgI+MgH EW out to a radius of 12 arcsec in NGC 6221. Their EW peaked at about 5 arcsec before becoming diluted by about 50% toward the nucleus (see their figure 43). Our Mg₂ profile peaks at a similar radius, but shows only moderate diminishment towards the nucleus. This disagreement may be due to the different methods used for continuum determination. The cause of the dilution of this absorption feature is likely to be the presence of an AGN. NGC 6221, NGC 6814 and NGC 7213 are all classified as Seyfert galaxies and therefore produce non-thermal continuum radiation and broad emission lines in the nucleus. The superposition of an active galactic nucleus (AGN) continuum on top of the stellar spectrum can act to decrease the measured strength of the absorption features in the galaxy's core.

Curiously, the Fe5270 feature dips between about 5–10 arcsec and rises toward the centre. The Mg₂ line-strength shows no radial variation in the disk, while the Fe5270 feature decreases fairly steeply, such that NGC 6221 has the lowest ratio of $\Delta\text{Mg}_2/\Delta\text{Fe5270}$ of the galaxies in our sample.

7.7.3 NGC 6753 - Sb

NGC 6753 has a nuclear ring-lens surrounded by a pseudo-ring, an intermediate spiral region, and finally an outer pseudo-ring (Crocker, Baugus & Buta, 1996). The arms are thin and have only small to moderate current star formation rate (Sandage & Bedke, 1994). We find that Mg₂ increases steeply for this early-type galaxy in the inner 10 arcsec. Eskridge et al. (2003) found a similar rise in the (NUV – I₈₁₄) colour over this radial range. We find evidence for a bump in Mg₂ at about 45 arcsec that seems to correspond to an outer ring of ongoing star formation, which contains many H II regions. Neither the Mg₂ bump at 45 arcsec, nor the change in slope at 10 arcsec, is reflected in the Fe5270 profile.

7.7.4 NGC 6814 - SBbc

This galaxy has a thick bar and a grand design spiral structure (Márquez et al. 1999), whose spiral arms contain many H II regions (Gonzalez Delgado et al. 1997). NGC 6814 is another Seyfert galaxy observed by Cid Fernandes et al. (1998). They found that the Mg I + Mg H feature was diluted by 22% in the nuclei, in agreement with a $\sim 20\%$ decrease in the Mg₂ EW we observe between 5 and 0 arcsec. The Fe5270 line-strength also appears significantly diluted in the nuclear region. The line-strength gradients of both spectral features show moderate declines with radius.

7.7.5 NGC 6935 - SBa

This galaxy is highly circular with a boxy inner H α ring, tightly wound spiral arms, and a small bright nucleus (Crocker et al. 1996). It is separated from NGC 6937 by 246 arcsec (Sandage & Bedke 1994) but the pair do not appear to be interacting. As mentioned above, there is good agreement between our central Fe5270 value and that from Idiart et al. (1996), whereas we obtain a slightly higher value for Mg₂. The strength of both indices show clear radial declines in the galactic disk and maxima at around 10 arcsec. Both indices decrease in the inner 10 arcsec, while Fe5270 drops significantly at a radius of few arcsec.

7.7.6 NGC 7213 - Sa

This well-studied LINER/Seyfert galaxy has the highest surface brightness and earliest Hubble-type in our sample. NGC 7213 is also unique among our galaxies in having *positive* Mg₂ and Fe5270 gradients in the disk.

Interestingly, Cid Fernandes et al. (1998) found no dilution of the Mg I + Mg H EW in the heart of NGC 7213, but strong dilution of features at shorter wavelengths. The EW of their Mg feature increases by about 50% from 25 arcsec to the nucleus. We found that our Mg₂ ebbs at a radius of ~ 15 arcsec before increasing by $\sim 35\%$ (in EW) toward the core. Fe5270 shows much less pronounced enhancement toward the core but a comparable steep positive gradient in the outer disk. The positive gradients may be associated with a ring of H II regions located at 20–40 arcsec in radius (Evans et al. 1996).

Corsini et al. (2003) note that the gaseous and stellar disks of NGC 7213 are decoupled within 40 arcsec. They point out that the H II circumnuclear ring is not

coincident with the stellar disk identified by Mulchaey, Regan & Kundu (1997). H II and H α measurements reveal that NGC 7213 is a disturbed system undergoing a merger process that has warped its disk (Hameed et al. 2001) and may be responsible for the gaseous/stellar decoupling.

7.7.7 NGC 7412 - SBb

The radial line-strength gradients for NGC 7412 are fairly flat and featureless: possible evidence of smoothing due to the presence of the bar with length 30 arcsec (Saraiva Schroeder et al. 1994). Photometry results from these authors show that the $V - I$ and $V - R$ colours are almost constant along the bar. Unfortunately, our estimated gradients are particularly uncertain for this galaxy due to large uncertainties in the background sky level.

7.7.8 NGC 7637 - Sc

This late-type galaxy (Corwin, de Vaucouleurs & de Vaucouleurs 1985) shows considerable radial variation in Mg₂ and Fe5270. It is interacting with a companion at a distance of about 2.4 arcmin (evident in the corner of the image in Figure 7.10) that is likely responsible for asymmetrical spiral arms and tidal features. We observe dips in both spectral indices at the galaxy core as expected for an AGN host, despite NGC 7637 not having a Seyfert classification. We note that Pastoriza, Donzelli & Bonatto (1999) have also postulated that this galaxy has an active nucleus, based on their analysis of its emission spectrum. Our results support this proposition.

The Mg₂ and Fe5270 features do not trace each other perfectly. For instance, Mg₂ declines sharply from ~ 5 to 15 arcsec in radius followed by a bump at about 20 arcsec, whereas Fe5270 continues to fall from ~ 5 to 20 arcsec with a possible bump around 25–30 arcsec. Further investigation is required to interpret the apparent offsets in the Mg₂ and Fe5270 behaviour as a function of radius.

7.8 Summary

We have calibrated the technique of absorption line imaging with the Anglo-Australian Telescope's Taurus Tunable Filter using Lick standard stars and have demonstrated the sensitivity of this method to the detection of Mg₂ and Fe5270 absorption fea-

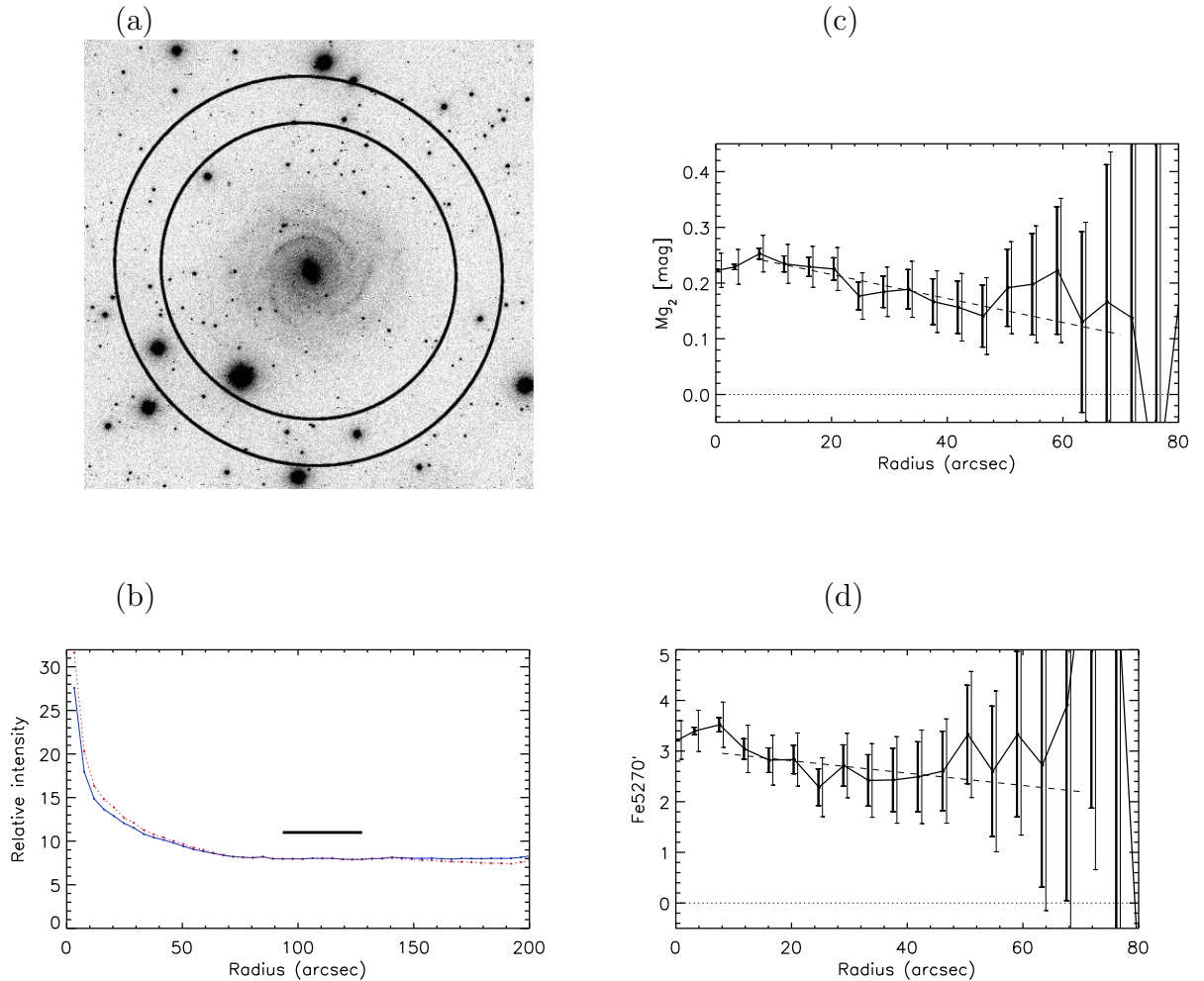


Figure 7.3: NGC 5968: a) 288×288 arcsec image of the galaxy in the Fe5270 line. The two overlaid ellipses indicate the inner and outer bounds of the area from which the background sky level was estimated (see text for details); b) Surface brightness profile in the Mg₂ line (solid curve) and continuum (dotted curve). The thick straight line indicates the annulus from where the background sky level was estimated and the dots show the location of each ellipse; c) Mg₂ index, transformed into the Lick system using equation 7.4. Two error bars are plotted for each data point. The thin bars show total error, including uncertainty associated with sky subtraction, filter transmission correction and transformation into the Lick system. The thick error bars show the contribution from sky subtraction only. The dashed line is the line of best fit to the data for the disk only (excluding the inner bulge). In deriving the line-strength gradient, only the error from sky subtraction was used to weight the data points, since this is the chief source of uncertainty affecting the measured gradient. Errors due to filter transmission correction and transformation into the Lick system act to uniformly shift the curve vertically, but do not change the gradient; d) Fe5270 index, transformed into the Lick system using equation 7.5. Error bars and dashed line have the same meaning as in panel c).

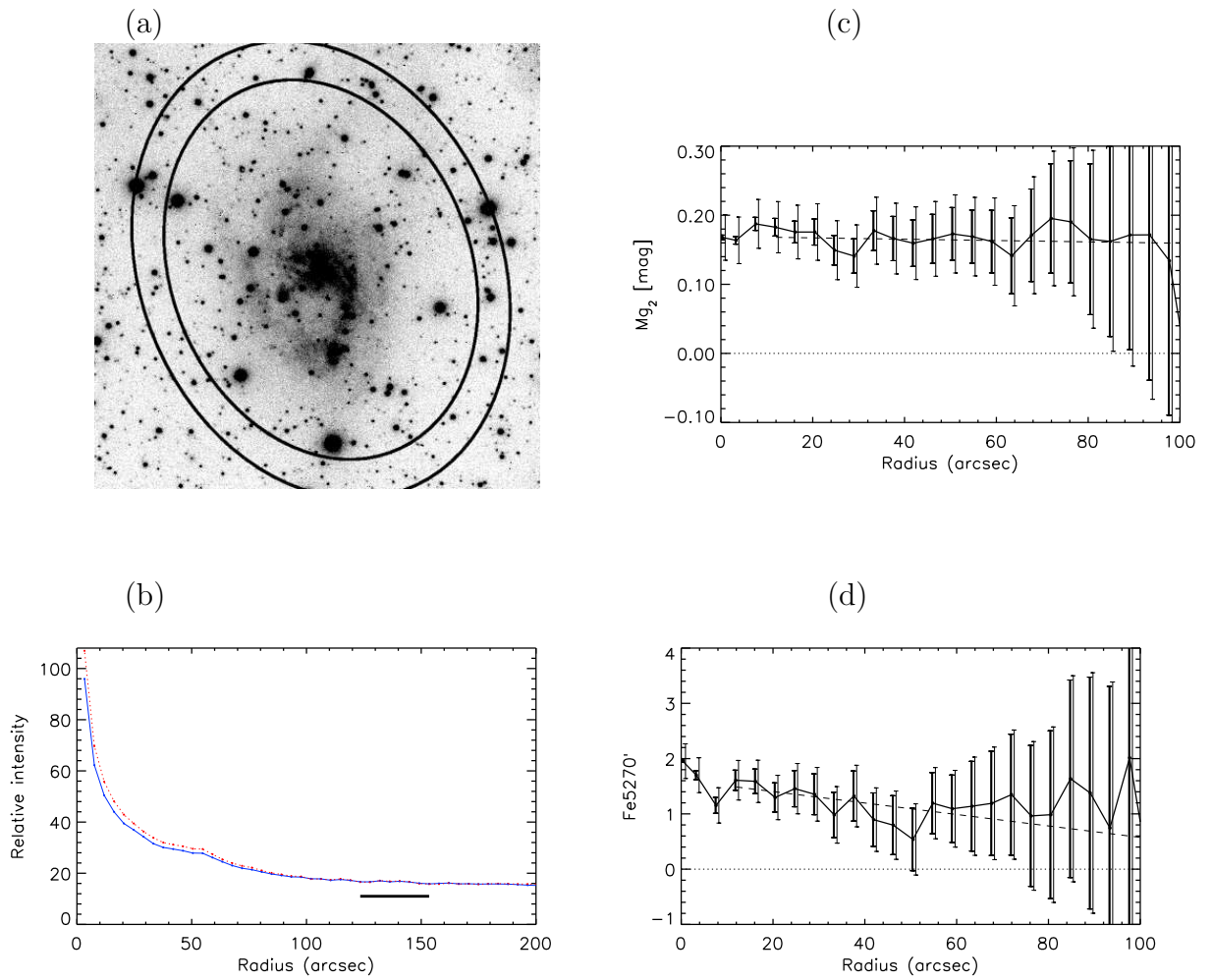


Figure 7.4: Same as Figure 7.3 but for NGC 6221

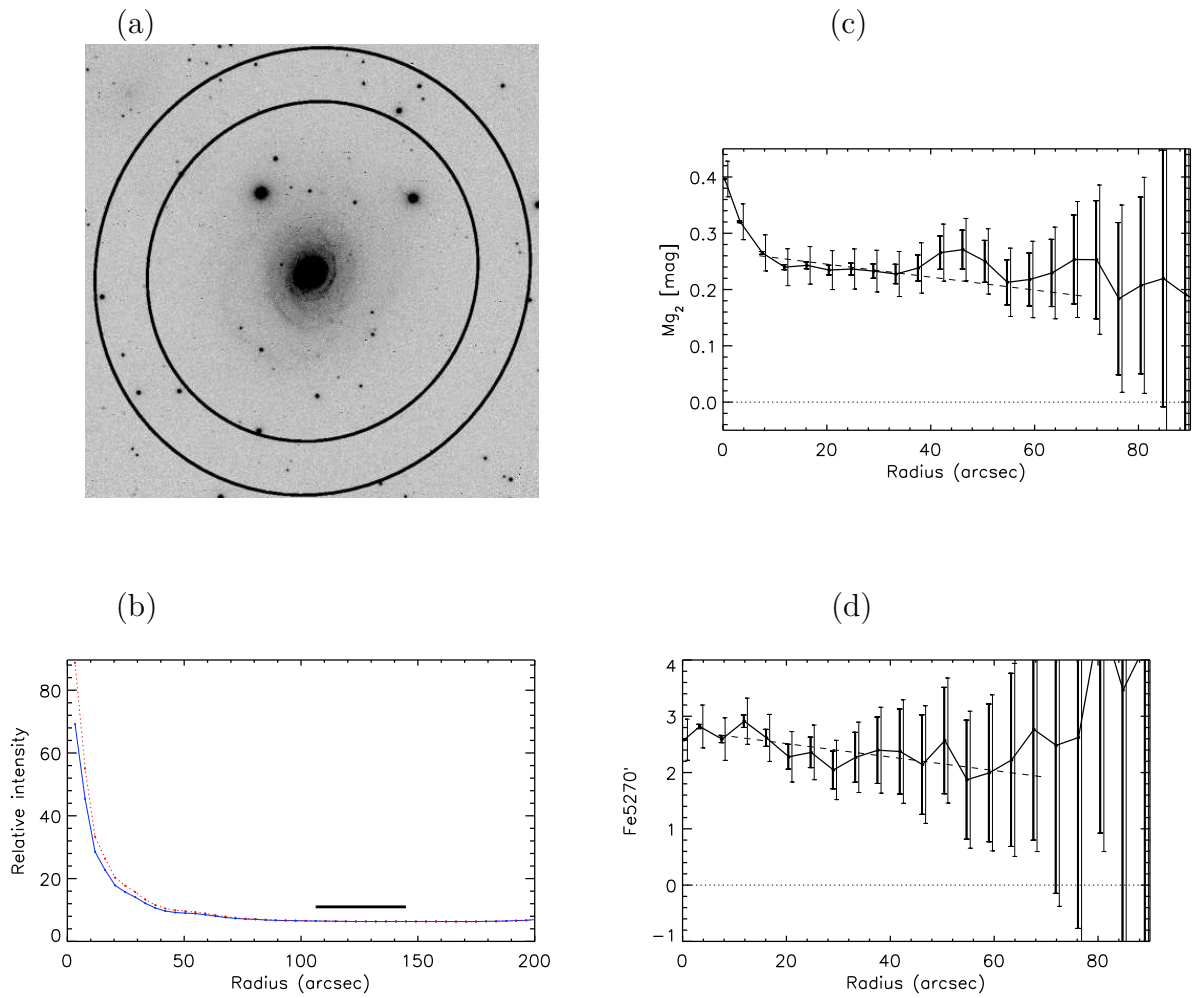


Figure 7.5: Same as Figure 7.3 but for NGC 6753

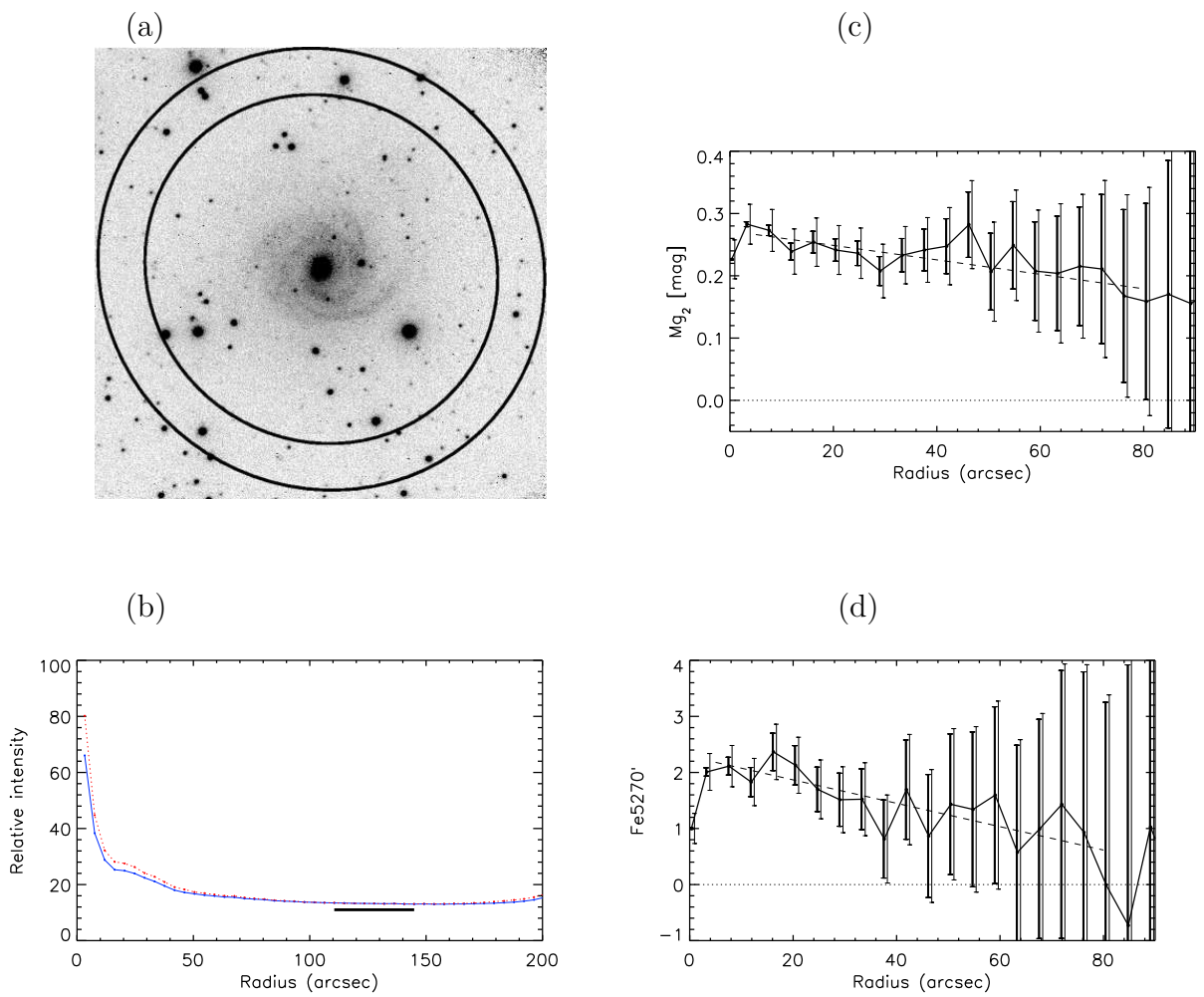


Figure 7.6: Same as Figure 7.3 but for NGC 6814

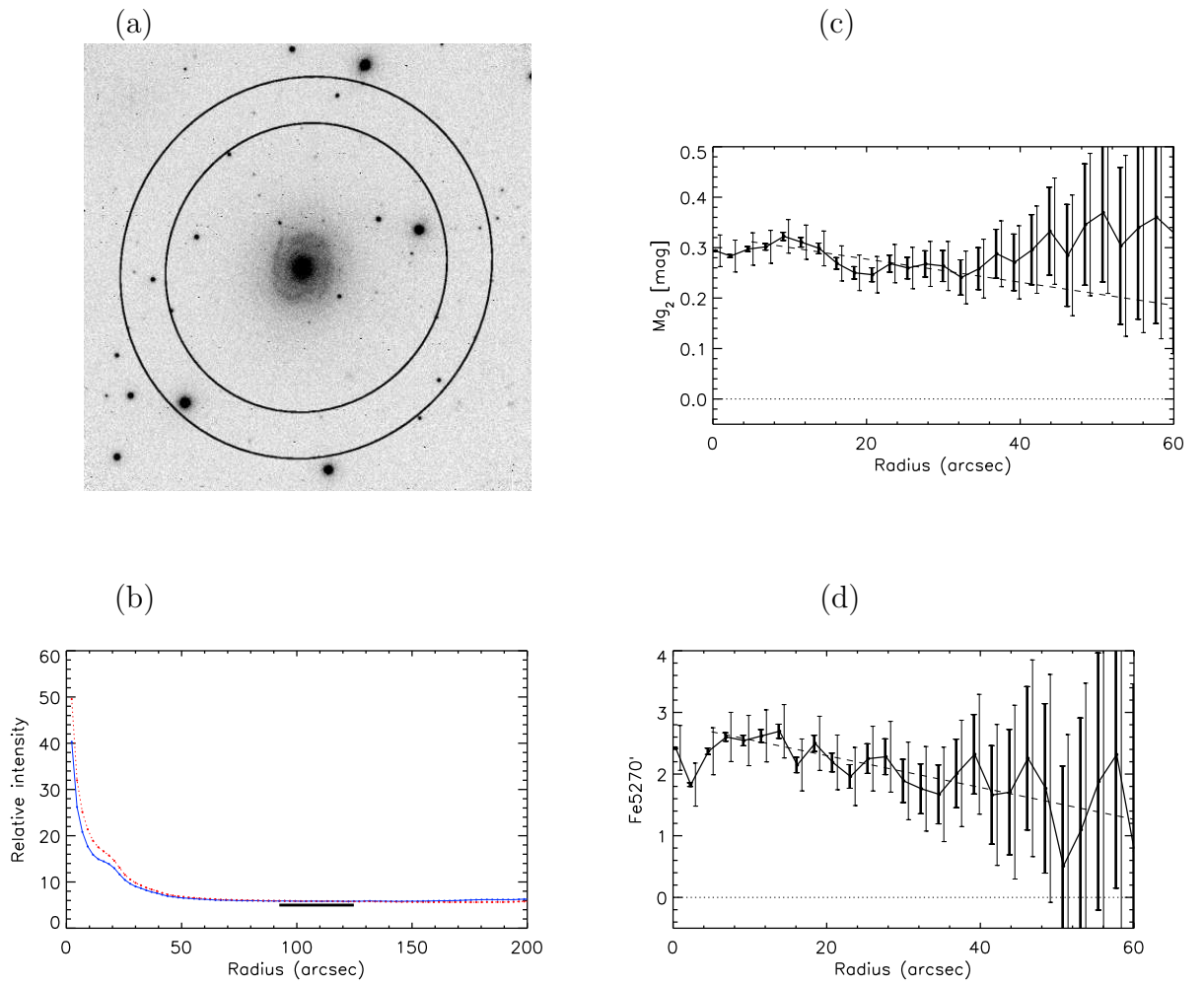


Figure 7.7: Same as Figure 7.3 but for NGC 6935

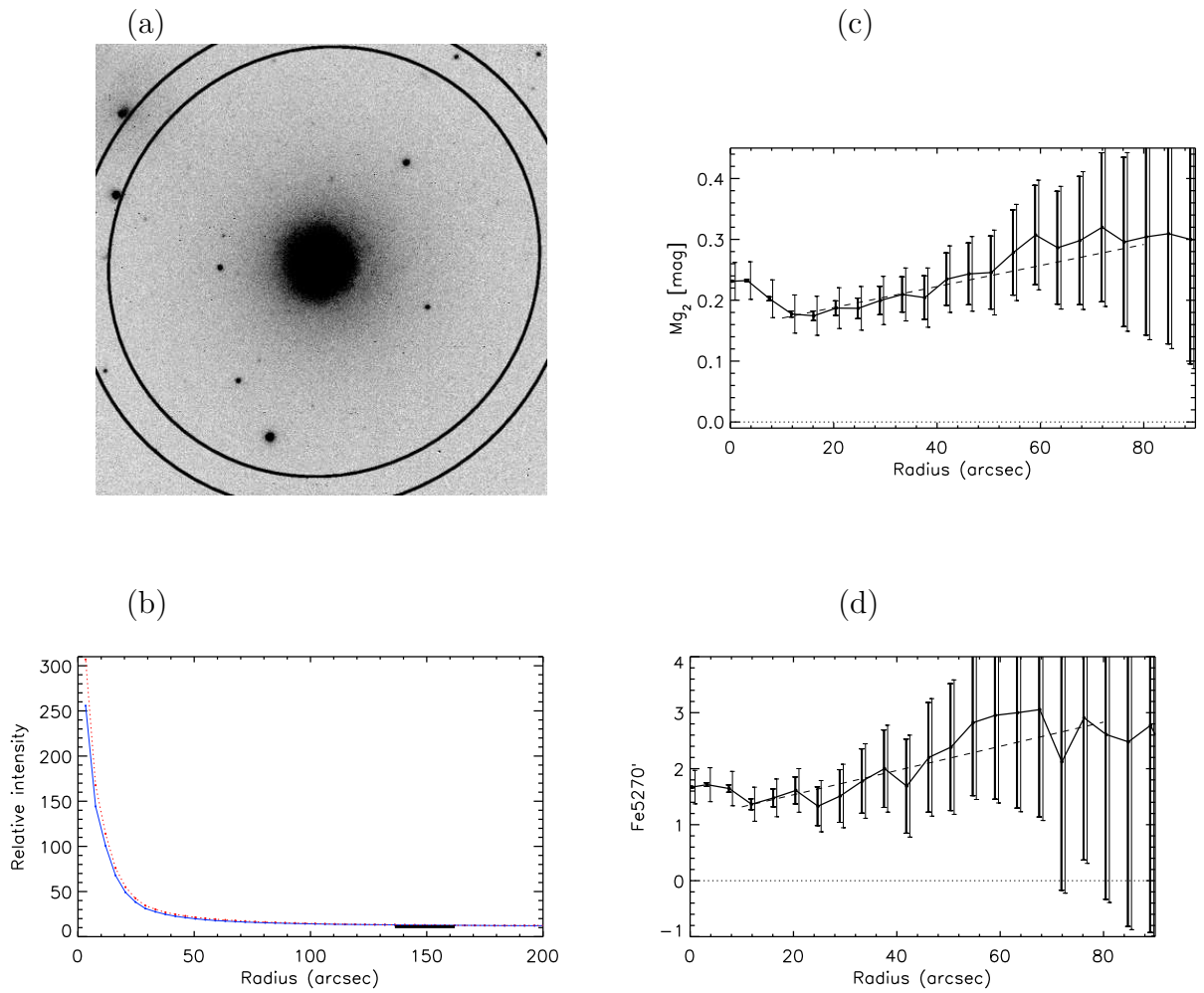


Figure 7.8: Same as Figure 7.3 but for NGC 7213

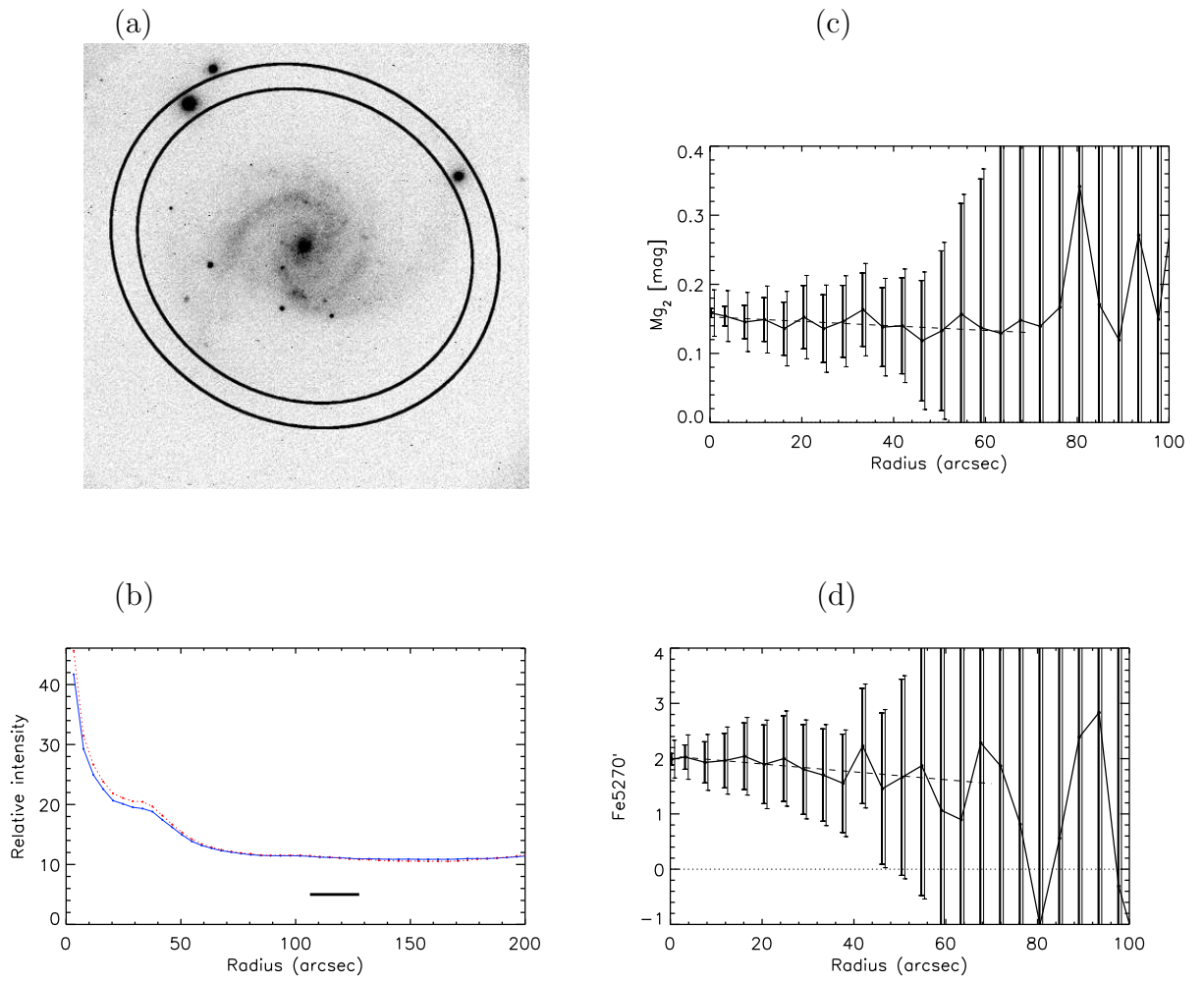


Figure 7.9: Same as Figure 7.3 but for NGC 7412

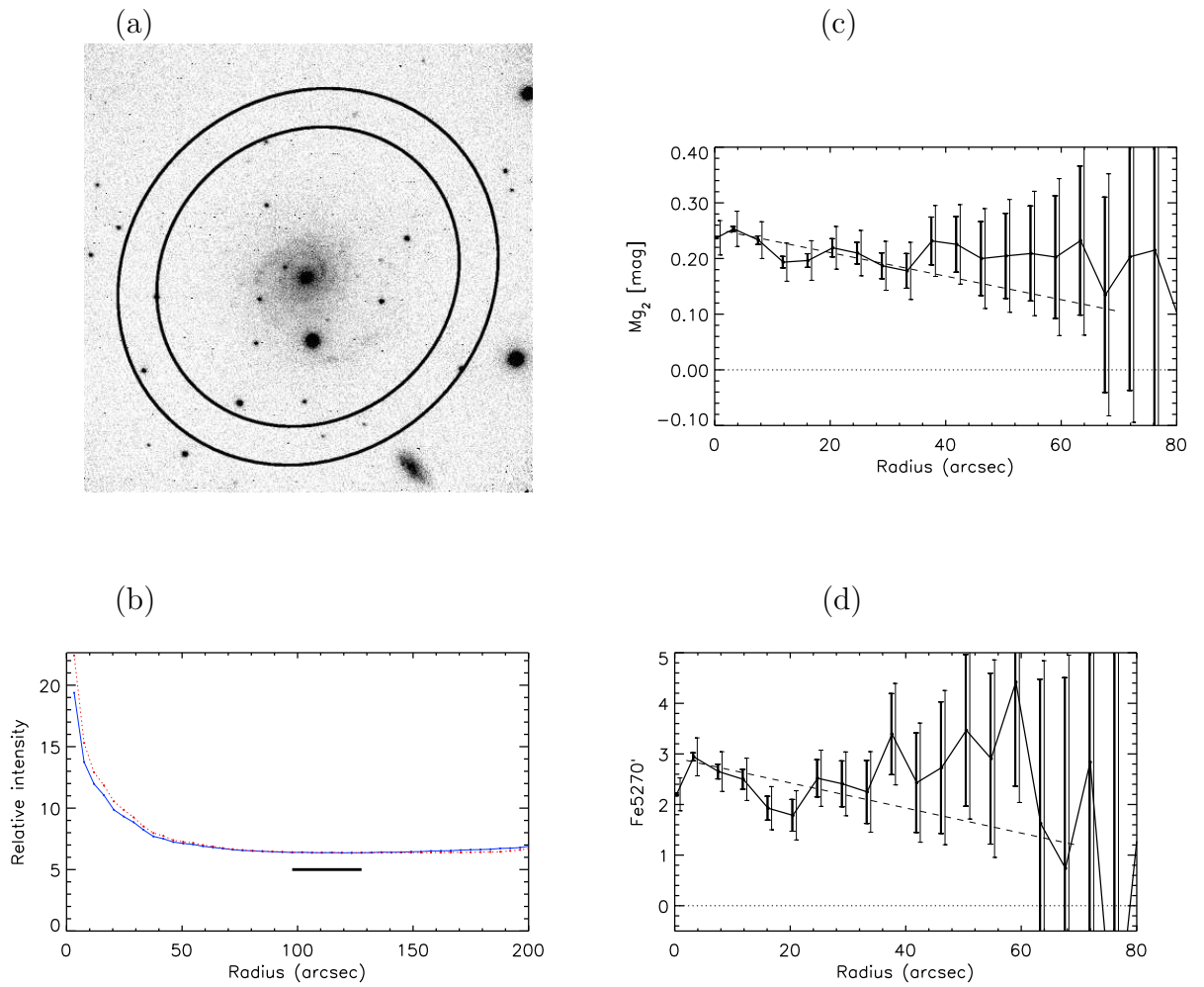


Figure 7.10: Same as Figure 7.3 but for NGC 7637

tures across the face of disk galaxies. The variation of Mg_2 and Fe5270 line-strengths as a function of radius is presented for a sample of eight galaxies. We found that the greatest source of uncertainty in our derived line-strength gradients is associated with background sky subtraction. As well as yielding overall line-strength gradients, the detailed shapes of the profiles may reveal phenomena including merger-induced star formation (NGC 7213), H II rings (NGC 6753 and NGC 7213) and galactic bars (NGC 7412). There is also evidence that NGC 7637 hosts an active galactic nuclei.

Future generations of tunable filters on larger telescopes will be more sensitive to stellar absorption features, enabling this type of study to be extended to lower surface brightness galaxies. Moreover, greater sensitivity will minimise the importance of azimuthal averaging in order to achieve acceptable signal-to-noise. This will facilitate comparisons between arm and interarm regions, thus providing insight into the mechanism of spiral arm triggered star formation.

Conversion of the line-strengths presented in this chapter into absolute abundances involves stellar population synthesis modelling, which will be the subject of future work. Ultimately, the inferred relative abundances of Mg and Fe can be used to piece together star formation and chemical evolution histories of the observed galaxies, providing insight into which aspects of evolution are shared by disk galaxies and which are galaxy-dependent. Moreover, abundance gradients across the face of disk galaxies bears upon the topic of the next two chapters – chemical abundances in QSO absorption systems – because some absorbers are thought to correspond to outer regions of spiral galaxies.

Chapter 8

The abundance pattern of a high-redshift Damped Ly α Absorber: a window on early nucleosynthesis

This chapter is based upon Fenner, Prochaska & Gibson, 2004, ApJ, 606, 116

8.1 Introduction

Chemical abundances in local stars are fossil evidence from which early nucleosynthetic processes may be inferred. An alternative probe into the earliest epochs of the universe is via the direct detection of metals in high redshift neutral gas. This requires a suitable background source such as a quasar, whose spectrum reveals absorption features in the intervening gas clouds. Damped Lyman- α Absorbers (DLAs) are one such class of quasar absorption system, defined as having an HI column density $N(\text{HI}) \gtrsim 2 \times 10^{20} \text{ cm}^{-2}$.

The recent discovery of an intervening galaxy along the sightline to the quasar FJ081240.6+320808 (hereafter DLA-B/FJ0812+32) has led to the most comprehensive abundance pattern measured beyond the local universe (Prochaska, Howk, & Wolfe 2003, hereafter PHW03). The gas-phase abundances of over 20 elements - including B, Cu, Ga, and Ge - have been detected in this galaxy, which has an unusually high column density and metallicity. Many of these elements have never before been measured at high redshift and provide a unique opportunity to probe early conditions of galaxy formation.

Identifying the modern-day counterparts to DLAs is still an open question. Kinematic evidence is consistent with DLAs being large proto-thick disks (Prochaska & Wolfe 1997) or smaller merging protogalactic clumps (Haehnelt et al. 1998), while chemical properties have led others to favour intervening dwarf or irregular galaxies (e.g. Lanfranchi & Friaça 2003 and references therein). Galaxies giving rise to DLAs

are likely to encompass a wide size and morphological range, from dwarf irregulars to giant ellipticals. Indeed, imaging studies of low redshift DLAs expose a variety of galactic types (e.g. Le Brun et al. 1997; Rao et al. 2003). Observed DLAs may tend to probe different types of galaxies at different evolutionary stages as a function of redshift.

The metal-line absorption profiles of the galaxy DLA-B/FJ0812+32 provide a snapshot of the chemical composition in the interstellar gas along only one sightline at one point in time. However a sufficiently detailed abundance pattern opens a window into the past history of star formation because chemical elements are produced on different characteristic timescales depending on their nucleosynthetic origin. The abundance of metals in the gas-phase of galaxies and proto-galaxies reflects the interplay between processes including star formation, the synthesis of elements by stars, the release of metal-rich material via stellar winds and supernovae, and the flow of gas. We have constructed a range of simple chemical evolution models that follow these processes as a means of analysing this DLA. We discuss instances where the inability to correctly predict specific elemental abundances may indicate gaps in our understanding of nucleosynthesis.

In Section 8.2 we describe the observations of the DLA at $z = 2.626$ along the sight-line to FJ081240.6+320808, upon which this study is based. Section 8.3 describes the ingredients of the chemical evolution code used to model this DLA. In Section 8.4 the theoretical predictions are compared with the DLA data and we discuss the sensitivity of the results to age, metallicity, and model ingredients.

8.2 Observations

DLA-B/FJ0812+32 was identified in the discovery spectra of the FIRST Bright Quasar Survey (White et al. 2000). Subsequent $R \approx 8000$ spectroscopy with the ESI spectrometer (Sheinis et al. 2002) revealed its very strong metal-line transitions (Prochaska et al. 2003). PHW03 published HIRES echelle spectra of this ‘metal-rich’ DLA and reported the detection of over 20 elements. The resulting abundance pattern provides an unparalleled laboratory for the study of elemental production in the young universe.

PHW03 derived gas-phase abundances using standard techniques and estimated uncertainties in the measurements by propagating the statistical errors. With only

Table 8.1: Elemental Abundances in DLA-B/FJ0812+32 ^a

El	[X/H] ^b	σ_N^c	$\delta_{DC}(90\% \text{ c.l.})^d$	[X/S] ^e
B	-0.57	0.085	0.1 (0.05)	+0.3
N	> -2.24	0.058	0.0 (0.1)	> -1.47
O	-0.54	0.101	0.1 (0.05)	+0.33
Mg	-0.78	0.053	0.3 (0.1)	+0.29
Al	> -2.00	0.054	> 0.5	> -0.73
Si	-0.91	0.053	0.3 (0.1)	+0.16
P	< -1.06	0.000	< 0.3	< +0.01
S	-0.87	0.050	0.1 (0.05)	0.0
Cl	-1.55	0.000	> 0.0	> -0.78
Ti	-1.87	0.112	> 0.7	> -0.4
Cr	-1.61	0.032	> 0.7	> -0.14
Mn	< -1.85	0.000	0.7 (0.1)	< -0.38
Fe	-1.69	0.017	> 0.7	> -0.22
Co	< -1.48	0.000	> 0.7	> -0.01
Ni	-1.73	0.007	> 0.7	> -0.26
Cu	< -1.11	0.000	> 0.7	< +0.36
Zn	-0.91	0.022	0.2 (0.1)	+0.06
Ga	< -1.45	0.000	0.7 (0.1)	< +0.02
Ge	-0.92	0.035	0.3 (0.1)	+0.15
As	< 0.26	0.000	0.0	< +1.03
Kr	< -0.44	0.000	0.0 (0.1)	< +0.33
Sn	< -0.27	0.000	0.0 (0.1)	< +0.5
Pb	< -0.10	0.000	0.0 (0.1)	< +0.67

^aMeasurements taken by Prochaska, Howk, & Wolfe (2003).

^bGas-phase abundance on a logarithmic scale relative to solar, where $N(\text{HI}) = 10^{21.35} \text{ cm}^{-2}$.

^cStatistical error on gas-phase abundances.

^dDust-corrections and uncertainties estimated from depletions patterns observed in Galactic gas.

^eDust-corrected abundances on a logarithmic scale relative to S.

a few exceptions, the dominant uncertainty in the resulting elemental abundances is the effect of differential depletion. Similar to the ISM of the Milky Way, refractory elements like Ni, Fe, Cr may be depleted from the gas-phase such that their observed abundances are significantly lower than their intrinsic values. This is the principal challenge to studying chemical abundances in the DLA and it has led to competing interpretations of their chemical evolution history (e.g. Lu et al. 1996; Kulkarni, Fall, & Truran 1997; Prochaska & Wolfe 2002; Vladilo 2002). In the following analysis, we adopt the conservative dust corrections imposed by PHW03 based on empirical depletion patterns observed for the Milky Way ISM (e.g. Savage & Sembach 1996). Table 8.1 lists both the gas-phase abundances and dust-corrected abundance ratios

for the elements observed in DLA-B/FJ0812+32 by PHW03, along with statistical errors and dust-correction factors. When relevant, we discuss the implications of dust depletion for our conclusions.

8.3 The Model

We simulated the chemical enrichment history of a DLA using the chemical evolution code described in previous chapters. Under this formalism, primordial gas is allowed to collect and form stars that synthesise new elements. An exponentially decaying gas infall rate was adopted and there were no outflows of gas driven by galactic winds. In this way, the models described below resemble different regions of disk galaxies. The evolution of the gas phase abundance pattern reflects the cumulative history of the dynamic processes of star formation, stellar evolution, and nucleosynthesis. The classic set of equations governing these processes (described in the seminal work of Tinsley 1980), have been numerically solved by defining $\sigma_i(t)$ as the mass surface density of species i at time t , and assuming that the rate of change of $\sigma_i(t)$ is given by:

$$\begin{aligned} \frac{d}{dt}\sigma_i(t) = & \int_{m_{low}}^{m_{up}} \psi(t - \tau_m) Y_i(m, Z(t - \tau_m)) \frac{\phi(m)}{m} dm \\ & + \frac{d}{dt}\sigma_i(t)_{infall} \\ & - X_i(t) \psi(t), \end{aligned} \quad (8.1)$$

where the three terms on the right-hand side of equation (8.1) correspond to the stellar ejecta, gas infall, and star formation, respectively. ψ is the SFR, $Y_i(m, Z(t - \tau_m))$ is the stellar yield of i (in mass units) from a star of mass m and metallicity $Z(t - \tau_m)$, $\phi(m)$ is the initial mass function, and X_i is the mass fraction of element i . By definition, the sum of X_i over all i is unity, and the total surface mass density is identical to the integral over the infall rate. m_{low} and m_{up} are the lower and upper stellar mass limits, respectively, and τ_m is the main-sequence lifetime of a star of mass m . In practice, the first term is split into three equations that deal separately with low-mass stars, Type Ia supernova progenitors, and massive stars.

We now describe each of the model ingredients in turn, distinguishing the inputs that are parameterised using simple analytical prescriptions from the nucleosynthesis

inputs, which are derived numerically from first principles.

8.3.1 Analytical Prescriptions

Initial Mass Function (IMF): The initial mass function determines the relative birth rate of stars as a function of mass. Because different mass stars leave unique chemical signatures on the ISM and operate on different characteristic timescales, the precise form of the IMF is a key factor driving the evolution of abundance ratios. This model assumed the Kroupa, Tout, & Gilmore (1993) three component IMF. The Kroupa et al. function has fewer stars in the low and high mass ends of the distribution than the single power-law Salpeter (1955) function. In Section 8.4.2 we estimate the sensitivity of the results to changes in the upper mass limit of the IMF.

Star Formation Rate (SFR): A simple analytical law for the SFR was adopted. Akin to the Schmidt (1959) law, we varied the SFR in proportion to the square of gas surface density. The efficiency of star formation was adjusted in order to investigate different timescales for metal enrichment.

Infall Rate: The gas infall rate was assumed to decay exponentially on timescales ranging between 3 and 9 Gyr. For the same final metallicity, a shorter infall timescale corresponds to a younger object. The star formation efficiency was also assumed to be higher in the models that became metal-enriched the fastest - this is motivated by the expectation that a deeper potential well corresponds to a faster rate of collapse and a higher efficiency of star formation. We note that it is the combination of both infall rate and star formation efficiency that is of foremost importance and these two effects determine the time taken to reach a specific metallicity. In the present study, the timescale for metal enrichment is more important than either the infall timescale or star formation efficiency considered in isolation. For this reason, we present results as a function of age and base our discussion on “age-sensitivity”.

8.3.2 Stellar Yields and Lifetimes

Intermediate and low mass stars: We incorporate the results of van den Hoek & Groenewegen (1997) whose metallicity-dependent yields are specified over the mass range $0.9\text{--}8 M_{\odot}$. These stars are integral in the synthesis of C and N, however observational constraints for these two elements are lacking for DLA-B/FJ0812+32. Thus this stellar population will be largely ignored in the following discussions. Low-mass stars may be the principle production site for Galactic Pb (Travaglio et al. 2001) as

well as producing modest quantities of As, Kr, and Sn via *s*-process nucleosynthesis. The abundance of these *s*-process elements may prove to be sensitive indicators of age in high redshift protogalaxies because they are generated in 1–4 M_{\odot} stars with typical lifetimes between a few hundred Myr and a few Gyr. However, remaining uncertainties in the theory of the *s*-process, as well as observational complications regarding *s*-element contamination by companions stars, may limit the use of Pb as an age indicator. An investigation into *s*-process enrichment in DLAs will be the focus of a forthcoming paper.

Type Ia supernovae (SNe Ia): A recalculation of the 1986 W7 model (Thielemann, Nomoto, & Yokoi 1986) by Iwamoto et al. (1999) was adopted. About 0.75 M_{\odot} of iron is ejected per event. Our model assumed that 3% of binary systems involving intermediate and low mass stars result in SNe Ia. This fraction provides a good fit for the solar neighbourhood (e.g. Alibés, Labay, & Canal 2001; Fenner & Gibson 2003).

Massive stars: Stars more massive than 8 – 10 M_{\odot} that end their lives in violent supernova explosions are responsible for most of the metals in the cosmos. We investigated chemical evolution using two different sets of SN II yields: 1) the Woosley & Weaver grid (1995, hereafter WW95) covering a mass range 11–40 M_{\odot} ; and 2) a set of 36 Type II SNe models covering the mass range 11–40 M_{\odot} at six metallicities ($Z = 0, 10^{-6}, 10^{-4}, 10^{-3}, 6 \times 10^{-3}, 2 \times 10^{-2}$) recently compiled by Limongi & Chieffi (2003, hereafter FRANECS) using the latest version of the FRANECS code described in Limongi & Chieffi (2002).

For WW95, we took the lower energy “A” models for stars $\leq 25 M_{\odot}$ and the higher energy “B” models for heavier stars. Taking note of the suggestion by Timmes, Woosley, & Weaver (1995) that the WW95 mass cuts may have penetrated too deeply within the iron core, we have uniformly halved the iron yields from these models ¹. The FRANECS models all have arbitrary mass cuts corresponding to 0.09–0.1 M_{\odot} of ^{56}Ni .

The nucleosynthesis models only extend to 40 and 35 M_{\odot} for WW95 and FRANECS, respectively. Since stars as heavy as 100 M_{\odot} are permitted to form in our chemical evolution model (albeit ten times less frequently than 40 M_{\odot} counterparts), the predicted yields were linearly extrapolated for stars outside the mass grid. Section 8.4.2 discusses the sensitivity of the results to the assumed upper mass limit on

¹We note that this violates the self-consistency of the stellar models, since a shift in mass cut that halves the Fe yield is expected to also modify the yield of elements like Co and Ni.

the formation of stars.

Unless otherwise stated, subsequent comparison between theoretical and observed elemental abundances will refer to the models calculated using WW95. In Section 8.4.2 we show that while WW95 and FRANEC make very different predictions regarding the magnitude of the “odd-even” effect, for most of the elements between O and Ni, for which DLA measurements exist, our conclusions drawn from the WW95 models also apply to the FRANEC models.

Stellar lifetimes: We adopt metallicity-dependent main-sequence (MS) lifetimes calculated by Schaller et al. (1992). Stars pollute the interstellar medium with metals over the course of their evolution via stellar winds and planetary nebulae, however this model assumes that all the mass loss takes place at the end of the MS phase. This simplification is not expected to influence our predictions, since the enrichment pattern is mostly controlled by massive stars whose metals are returned to the ISM almost entirely during the supernova explosion.

As a word of caution, this type of model assumes that stellar ejecta is uniformly mixed into the gas phase and therefore predicts *mean* abundance trends. In reality, the products of SNe not only mix inhomogeneously with the ambient gas, but may also be associated with regions in different ionisation states. Despite these caveats, a homogeneous chemical evolution model is a reasonable representation of this DLA for several reasons: firstly, the measured enrichment pattern of this $z = 2.626$ object reflects the average in the gas phase along a line-of-sight; secondly, in order to reach a metallicity of $\sim 1/3$ solar, numerous generations of supernovae must have exploded, which will tend to “smooth out” the spatial distribution of the heavy elements; and, thirdly, similar to the majority of DLA (Prochaska 2003) there are only modest variations in the relative abundances of the DLA across the observed velocity profile. These small variations are likely associated to differences in differential depletion implying a chemically homogeneous system.

8.4 Results

8.4.1 Model versus Data

Figure 8.1 presents the difference between the observed DLA enrichment pattern and the predicted $[X/S]^2$ from our fiducial WW95 model that reaches $[O/H] = -0.44$ after 2.2 Gyr. The dashed line indicates perfect agreement between the model and the data, while the dotted lines represent a factor of two difference. We conservatively consider predictions falling within the dotted lines to be acceptable. The arrows denote the direction in which the difference will move if the observational limits tighten. For elements like Fe, Ni, and Cr, the lower limits are set by dust depletion and are unlikely to change. Error bars reflect statistical errors on gas-phase abundance measurements, where the statistical error on $[X/S]$ equals the quadrature sum of the statistical errors on $[X/H]$ and $[S/H]$ given in Table 8.1. When not reported as limits, uncertainties in the dust corrections range from from 0.05 to 0.1 dex, i.e. comparable to the magnitude of the statistical errors.

There is excellent agreement between the fiducial model and the DLA data for most elements from B to Ge. This agreement is particularly impressive given that the models we are applying to a high redshift object were tuned using local stellar abundance patterns. Part of the explanation is that the DLA pattern is close to solar. Nevertheless, the models match an observed trend in the α -elements of decreasing $[X/S]$ with increasing atomic number (Figure 8.2). Furthermore, the model reproduces the mildly enhanced “odd-even” effect indicated by the limits to the Al, P, and Cl abundances. There is also good agreement for the iron-peak elements Cr, Mn, Fe and Co and the heavier neutron-capture elements Ga and Ge. The Ni and Cu predictions do not violate the observational limits. The most serious disagreement occurs for Mg and Zn, which are underpredicted by the model by about 0.45 and 0.4 dex, respectively. Detailed discussions of these elements are found in Sections 8.4.3 and 8.4.3.

²We do not use Fe as the reference element because its nucleosynthesis is subject to many uncertainties relating to the SN II mass cut and the evolution of the SN Ia rate. Oxygen has a more robust theory of production, but its observational status and solar abundance is less certain. Thus we plot abundances relative to sulfur, for which an ample database of DLA and stellar measurements exists. Moreover, the nucleosynthetic origin of S is thought to be well understood - being mainly generated by hydrostatic burning and explosive O and Si burning in massive stars.

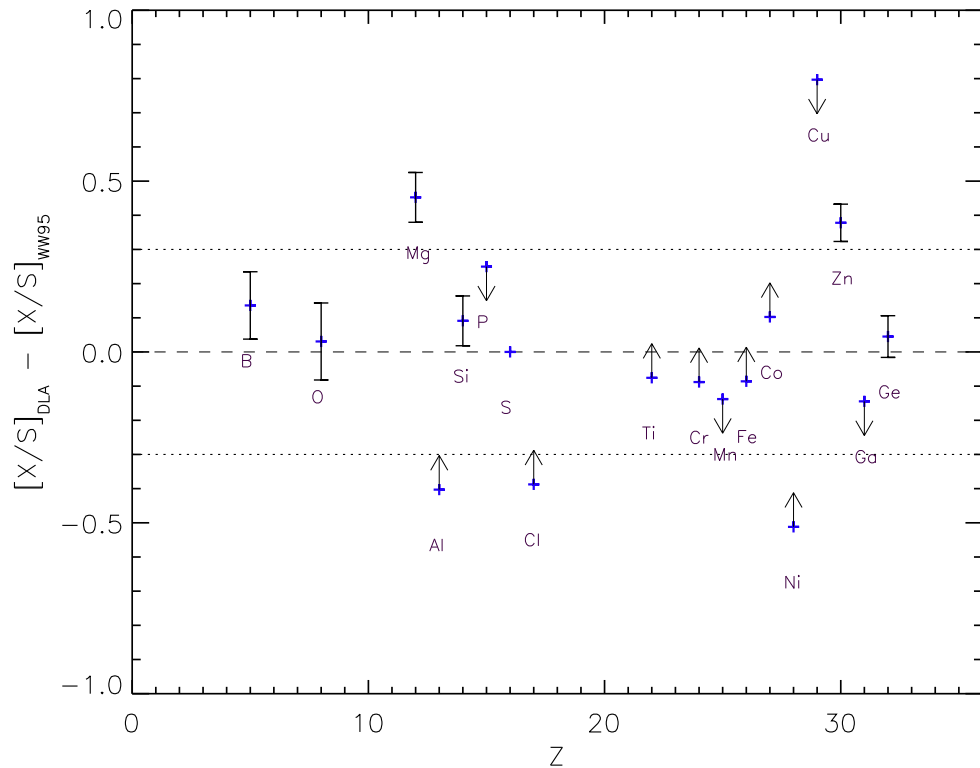


Figure 8.1: Logarithmic ratio of the observed and predicted DLA abundance pattern using Woosley & Weaver 1995 SN II yields for a 2.2 Gyr model with $[O/H] = -0.44$. Arrows indicate the direction in which the difference will move if the upper and lower observational limits tighten. For elements like Fe, Ni, and Cr, the lower limits are set by dust depletion and are unlikely to change. Error bars reflect statistical errors on gas-phase abundance measurements. The level of uncertainty in the dust correction factor is comparable to the statistical errors. The dashed line indicates agreement between observations and predictions, while the dotted lines denote deviations of a factor of two.

8.4.2 Model Sensitivity

Dependence on Age

Figure 8.2 presents the predicted abundance pattern for a model galaxy reaching a final metallicity of $[O/H] = -0.44$ after four different periods: 0.46, 0.9, 1.6, and 2.66 Gyr. The dust-corrected DLA abundance pattern (as presented in column 5 of Table 8.1) is indicated by black circles, with arrows specifying the upper and lower limits, where applicable. Upper limits on As, Kr, Sn, and Pb are shown, although their evolution is not modelled. Abundances are on a solar logarithmic scale relative to sulfur. The dashed line corresponds to the solar pattern and the dotted lines are

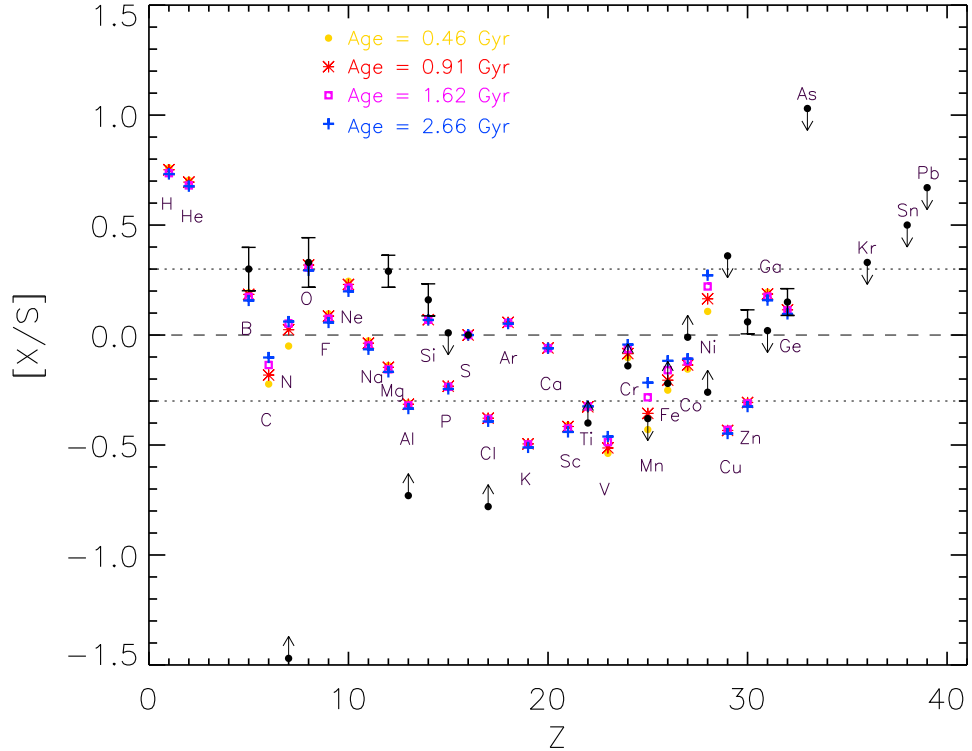


Figure 8.2: Predicted abundance pattern as a function of age. $[O/H] = -0.44$ in each model. Abundances are expressed relative to solar and scaled to sulfur, such that $[X/S] = \log_{10}(m(X)/m(S)) - \log_{10}(m(X)/m(S))_{\odot}$. Four ages ranging from 0.46 - 2.66 Gyr are represented by the symbols indicated. The dust corrected DLA abundance pattern is indicated by black circles. Statistical errors on the gas-phase abundance are indicated by error bars. Arrows reflect the corresponding lower and upper limits. The dotted lines indicate deviations from scaled solar by a factor of two.

deviations by a factor of two. The detection of and limits placed on 23 elements from B to Pb reveal a roughly solar-like enrichment pattern. This may not come as a surprise given the moderate metallicity of the object. However the redshift of this galaxy imposes an upper age limit of ~ 2.5 Gyr, implying a much shorter timescale for metal-enrichment than in the solar neighbourhood.

The abundance of most elements relative to sulfur is virtually constant over the age range shown in Figure 8.2. This is because the enrichment pattern is mostly set by short-lived massive stars. The exceptions are carbon, nitrogen, and the iron-peak elements where modest differences are predicted. Low and intermediate mass stars have long been held to dominate the production of N and possibly that of C, although theoretical (e.g. Carigi 2000) and observational (e.g. Henry, Edmunds, & Köppen

2000) studies also support a strong contribution to C abundance from Type II SNe. Considerable synthesis of C, by the triple-alpha reaction of helium and N, via CNO processing, takes place within low and intermediate mass stars, which are longer lived than SN II progenitors. Hence the enrichment of the interstellar medium with C and N is delayed with respect to products of massive star nucleosynthesis. We stress that the results presented in this chapter are largely insensitive to age.

The main deviation from the solar pattern is the mild enhancement of the alpha-elements O, Mg and Si with respect to Fe or Zn. There is also a trend toward lower relative abundances of α -elements with higher atomic numbers. Massive, short-lived stars culminating in Type II SNe are the primary source of the alpha-elements, while Fe is produced in significant amounts by Type Ia SNe, whose lower mass progenitors have longer main-sequence lifetimes. Similar alpha-enhancement is also seen in halo and thick disk stars where it is understood to signify rapid star formation, whereby most stars formed from gas that had not yet been polluted with iron-rich SN Ia ejecta. Indeed, the ratio of iron-peak elements to sulfur is 30-60% higher in the 2.66 Gyr model compared with the 0.46 Gyr model.

It is apparent from Figure 8.2 that a protogalaxy that has reached 1/3 solar metallicity on a timescale of order 1 Gyr has already been contaminated by the nucleosynthetic products of intermediate mass stars and Type Ia SNe. This is because intermediate mass stars and SN Ia progenitors can have lifetimes as short as a few hundred Myr. Although the relative abundances of C, N, and the iron-peak elements exhibit moderate age sensitivity in Figure 8.2, a better probe of age in an intermediate redshift protogalaxy might be *s*-process elements such as Kr and Pb, since their origin in low mass stars should ensure an enrichment timescale in excess of ~ 1 Gyr (Travaglio et al. 2001). A preliminary examination of Pb evolution indicates that [Pb/S] may increase by roughly an order of magnitude between 0.5 and 2.5 Gyr (Fenner et al. 2005, in preparation). The anticipated detection of *s*-process elements in additional DLAs may prove fruitful in constraining the age.

The Role of Type Ia SNe

Figure 8.2 reveals how the relative contribution from Type Ia SNe increases with the age of the object, for the same metallicity. Type Ia SNe are believed to be the chief source of the iron-peak elements. While the precise identity of SNe Ia progenitors is debated, they must involve intermediate to low mass stars in binary systems.

The explosion occurs when a white dwarf in the binary system accretes enough material from its companion to exceed the Chandrasekhar limit. The timescale for the SN Ia event is thus determined by the evolution of the companion star. The characteristic timescale for SNe Ia is often taken to be 1 Gyr, however this is environment-dependent and moreover, the first Type Ia events may occur within only a few hundred Myr (Matteucci & Recchi 2001).

In theory, the iron-peak abundances might be used to constrain the age of this DLA. This requires assumptions to be made about the incidence of SNe Ia. As mentioned in Section 8.3.2, we have adopted the Milky Way value for the fraction of low and intermediate-mass binary systems that culminate in SNe Ia. In practice, there is a conflict between the predictions for Mn, which imply an age $\lesssim 1$ Gyr and predictions for Fe, which imply that the protogalaxy has been forming stars for more than 1 Gyr. In other iron-peak elements, [Co/S] falls slightly below the lower limit in all models, while Cr and Ni predictions agree with the data.

From Figure 8.2, Mn appears to have a very strong dependence on the age of the simulated galaxy. According to the nucleosynthesis prescriptions adopted in this study, SNe Ia play such a strong role in Mn production that their contribution exceeds that from SNe II after ~ 2.5 Gyr. It has been stated that Timmes et al. (1995) claim Type Ia SNe to be unimportant contributors to Mn synthesis (e.g. Nissen et al. 2000), yet it is clear from Figures 4 and 5 from Timmes et al. (1995) that Type Ia SNe produce $\sim 50\%$ of the solar Mn abundance. What Timmes et al. showed instead was that the same trend of [Mn/Fe] vs [Fe/H] can be obtained either with or without SNe Ia due to the strong metallicity-dependence of the WW95 SN II Mn yields. However, SNe Ia are needed to reach the solar abundance. When the same nucleosynthesis prescriptions used in this study are applied to the solar neighbourhood, we find that $\sim 75\%$ of the solar Mn abundance originates from SNe Ia.

The tendency for Mn to be overpredicted in these DLA models may suggest that the main Mn source is metallicity-dependent. Other DLA systems have been observed for which [Si/Fe] ~ 0 yet [Mn/Fe] is significantly subsolar (e.g. Pettini et al. 2000). Current nucleosynthesis models cannot explain such behaviour, since a solar Si/Fe ratio points to a Type Ia SN contribution, but this is not supported by the low Mn abundance, whose origin is understood to lie mostly in SNe Ia. A similar trend has been identified in stellar abundances of the Sagittarius dSph galaxy (McWilliam, Rich, & Smecker-Hane 2003). Invoking metallicity-dependent SNe Ia Mn yields might help explain these apparently incompatible observations.

In a handful of DLAs with low dust content, Pettini et al. (2000) discern no correlation between $[\text{Mn}/\text{Fe}]$ and $[\text{Fe}/\text{H}]$, even though a clear trend is apparent in local stars at all metallicities (Carretta et al. 2002). They attribute this to the varied histories and morphologies of the objects and suggest that a process in addition to Type II and Ia nucleosynthesis may operate to explain Mn enrichment.

It should be noted that the theoretical yields of Mn from WW95 do not have sufficient metallicity-dependence to account for the low $[\text{Mn}/\text{Fe}]$ ratios observed in very metal-poor stars (e.g. Alibés, Labay, & Canal 2001). Furthermore, Co/Fe ratios up to four times higher than solar are detected in local stars below $[\text{Fe}/\text{H}] \sim -2.5$ (Cayrel et al. 2003), in conflict with the expectations of SNe II models. Thus, it is likely that gaps remain in our understanding of the processes responsible for Mn and Co that limit the power of this model to constrain the DLA age using these elements.

Sensitivity to Metallicity

The production of certain elements (particularly those with odd atomic numbers) by massive stars is a strong function of the initial stellar chemical composition. We examined the dependence of the predicted enrichment pattern on the model galaxy’s metallicity. Figure 8.3 depicts results from three models reaching $[\text{O}/\text{H}] = -0.24, -0.44,$ and -0.64 after 2.2 Gyr of star formation. The ± 0.2 dex variation in $[\text{O}/\text{H}]$ reflects the uncertainty in the measured HI column density.

The model results displayed in Figure 8.3 reveal the so-called “odd-even” effect, whereby the underabundance of odd-numbered elements with respect to their even-numbered neighbours increases with decreasing metallicity. This effect is a signature of massive SNe from subsolar-metallicity stars. Figure 8.4 shows the production factors relative to S from the WW95 SN II models integrated over the Kroupa et al. (1993) IMF over the mass range 11-100 M_{\odot} . The odd-even effect persists from the zero to 1/10th solar metallicity WW95 models, with the trend reversing in the solar model. The strength of the odd-even effect in this DLA can be gauged by comparing abundances between pairs of neighbouring odd-Z and even-Z elements. Evidence for a mild odd-even effect comes from the ratios $[\text{P}/\text{Si}] < -0.15$, $[\text{Mn}/\text{Fe}] < -0.16$, and $[\text{Ga}/\text{Ge}] < -0.13$.

Even-elements behave as primary products in SNe II and their stellar yields are largely independent of the initial metallicity. Conversely, the ratios of odd-elements

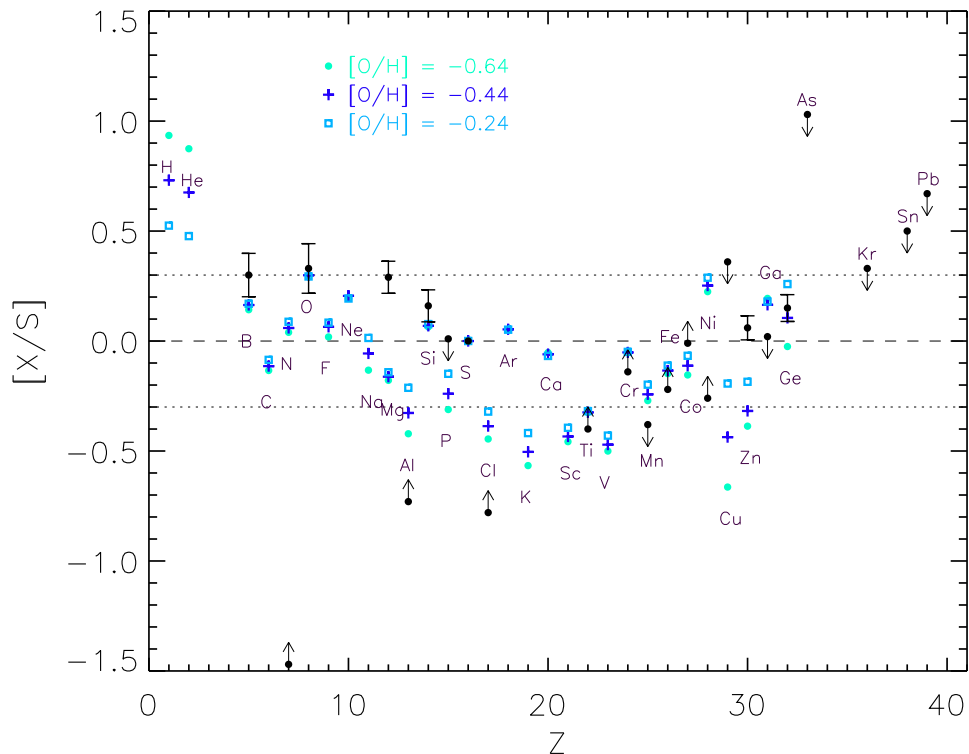


Figure 8.3: Predicted abundance pattern as a function of metallicity. The enrichment pattern for 2.2 Gyr model galaxies at $[O/H] = -0.44 \pm 0.2$ are shown by the symbols indicated. Other symbols have the same meaning as in Figure 8.2.

to S show spreads of typically ~ 0.2 dex over the 0.4 dex range in $[O/H]$. The SNe II yield of odd-elements from fluorine to the iron-peak is understood to be sensitive to the neutron excess and therefore increases with the initial abundance of “seed” nuclei present in the star. Thus the ratio of odd-elements to S is highest in the $[O/H] = -0.24$ model.

Copper exhibits the greatest sensitivity to metallicity, with Cu/S having a stronger than linear dependence on O/H over the metallicity range considered. Thus $[Cu/S]$ has the potential to indirectly constrain the metallicity and the HI column density. The upper limit on the Cu detection arises because of line blending. However the depletion of Cu onto dust grains reduces its abundance in the gas-phase. Accounting for these opposing effects, the intrinsic Cu abundance is likely to fall within 0.4 dex of the current upper limit. Only the highest metallicity models approach the Cu observation. The predicted $[Zn/S]$ value, which is underproduced by ~ 0.4 dex in

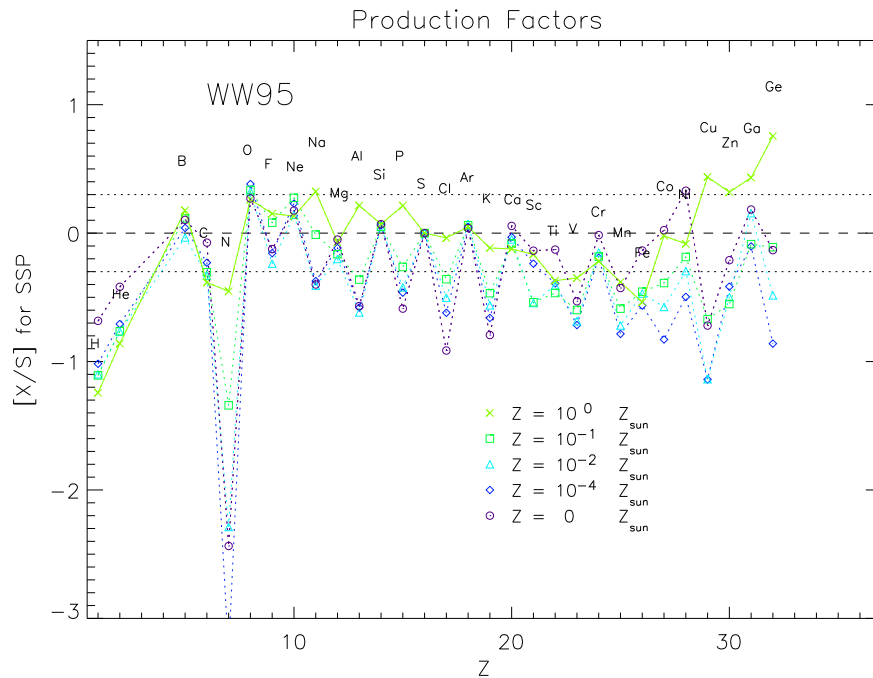


Figure 8.4: Production factors relative to S from a single generation of massive stars from 11–100 M_{\odot} on a solar logarithmic scale using the yields of Woosley & Weaver 1995. Five metallicities are shown from zero to solar. C, N and some of the iron-peak elements are subsolar because they require additional sources such as intermediate- and low-mass stars and Type Ia SNe.

the $[O/H] = -0.44$ model, is also in closer agreement with data for the highest metallicity model.

Abundances of the odd-elements Al, P, and Cl relative to S offer a probe into the nature of the “odd-even” effect. However, only lower (for Al and Cl) and upper limits (for P) exist at present in this DLA. These limits are currently not sufficiently restrictive to eliminate any of the three different metallicity models depicted in Figure 8.3. Owing to the strength of the Al II λ 1670 line, only lower limits can be placed on the Al abundance in many DLAs, yet absorption-line systems present a unique opportunity to acquire empirical evidence for the metallicity-dependent behaviour of P and Cl, whose weak stellar spectral lines mean there is a paucity of data from local stars. A database of measurements of these elements in DLAs will help test the theoretical expectation that Cl, P, and Al follow similar evolutionary paths.

One might expect from the theoretical predictions shown in Figure 8.3 that

improved observations of P and Cl will see both [P/S] and [Cl/S] converging toward ~ -0.4 . However, the abundance of Cl shown in these figures was derived from the Cl I transition, which is not the dominant ion. After correcting for ionisation, the true Cl abundance is likely more than 0.5 dex higher than the current lower limit. Even when these models are evolved to solar metallicity, Al and Cl are still underproduced by 0.1 and 0.3 dex, respectively; suggesting that the odd-even effect may be slightly exaggerated in the stellar models, or that intermediate-mass stars provide an additional source. It should be noted that the solar reference Cl abundance adopted here is ~ 0.15 dex higher than the Anders & Grevesse (1989) value.

Boron is synthesised in a variety of ways including neutrino-induced reactions in the shells of SNe II (the ν -process) and cosmic ray spallation onto seed nuclei in the interstellar medium (Fields & Olive 1999). The relative importance of these processes is expected to vary with metallicity. The ν -process should produce constant B/O regardless of metallicity, whereas a signature of the cosmic ray process would be B/O decreasing with decreasing metallicity. The WW95 models generate B via the ν -process and the satisfactory agreement with the observed B/O ratio lends support to a ν -process origin for B.

Sensitivity to the Stellar Initial Mass Function

It has been estimated that uncertainties in the shape and limits of the IMF correspond to variations in the *absolute* elemental yields by a factor of 2 (Wang & Silk 1993). We have tested the sensitivity of our results to a change in the upper mass limit of the IMF from 100 to 40 M_{\odot} . Figure 8.5 plots the logarithmic ratio of the abundance pattern obtained in these two cases. The abundances of most elements relative to S are unchanged. Prominent exceptions are F, Ne, and Na, whose yields relative to S decrease by factors ranging from 3-5. [O/S] is also lower by ~ 0.25 dex when the IMF is curtailed at 40 M_{\odot} . The magnitude of the offset reflects the dependence of elemental yield on stellar mass. The elements most affected by the shift in upper IMF limit are those whose yields increase most steeply with initial stellar mass. The possible future detection of F in this DLA may help constrain the IMF.

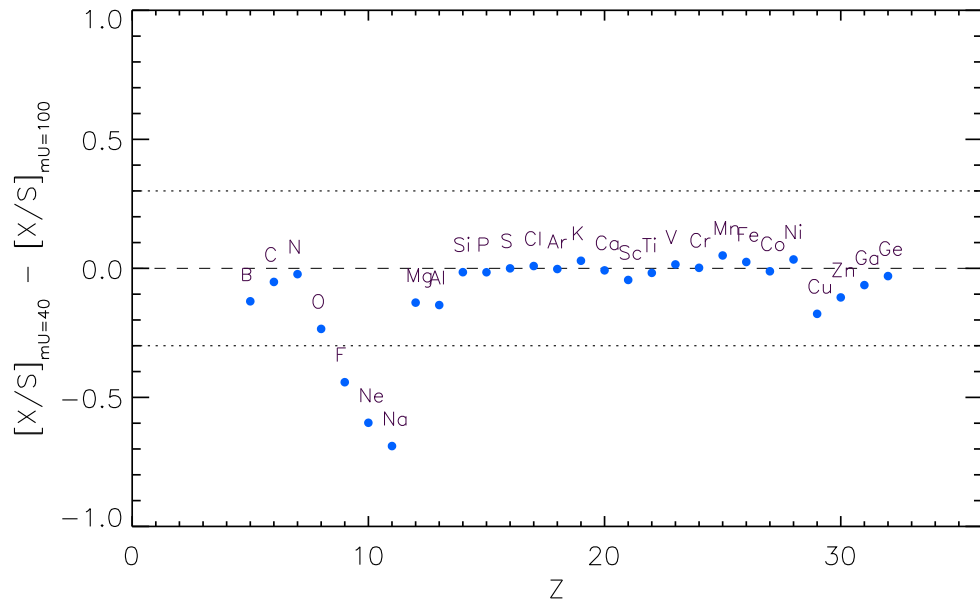


Figure 8.5: Logarithmic ratio of the abundance pattern obtained with an IMF upper limit of $40 M_{\odot}$ and with an upper limit of $100 M_{\odot}$.

Sensitivity to the Type II Supernova Nucleosynthesis Prescriptions

Figure 8.6 compares the standard WW95 model with the same model using FRANEC yields for massive stars. We note several main differences: 1) B and F are produced in negligible amounts in the FRANEC model because neutrino-induced nucleosynthesis processes are omitted from their calculations; 2) the elements from Cu to Kr are present in trace amounts in the FRANEC model; and 3) the odd-even effect is much more pronounced in FRANEC models. In particular, P, Cl, K, and Sc are significantly lower with respect to S in the FRANEC model, whereas the abundance of their even-Z neighbours matches those from the WW95 model. The deficit of Cl from the FRANEC models with respect to the observations suggests that the odd-even effect may be too severe. Despite these differences, there is good consensus between the two models for about half of the elements with DLA measurements and many of the conclusions of this chapter can be reached irrespective of the choice of SN II yields.

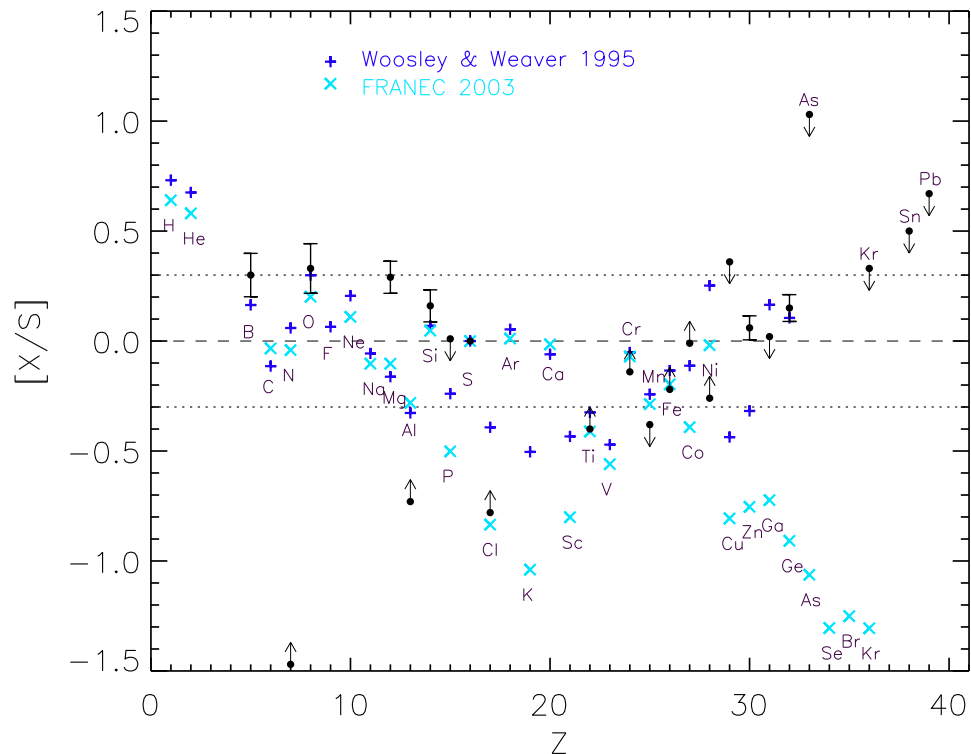


Figure 8.6: Predicted abundance pattern of a 2.2 Gyr object with $[O/H] = -0.44$ obtained using the Woosley & Weaver 1995 yields (plus signs) and FRANEK 2003 yields (crosses). Other symbols have the same meaning as in Figure 8.2.

8.4.3 Discussion of Individual Elements

Oxygen

In the most widely cited set of solar abundances from Anders & Grevesse (1989), the solar oxygen abundance was assumed to be $\log(N_O/N_H)_\odot + 12 = 8.93$. However, recent estimates that account for solar granulation and non-LTE effects and correct for a Ni I blend, lead to significant downward revisions in the Sun's oxygen abundance by almost a factor of two (to $\log(N_O/N_H)_\odot + 12 = 8.69$ - Allende Prieto, Lambert & Asplund 2001). Such a shift partly resolves the long-standing dichotomy between the Sun's oxygen abundance and that of the local ISM (André et al. 2003). This work adopts Holweger's (2001) preferred value of $\log(N_O/N_H)_\odot + 12 = 8.73$, whereas WW95 and FRANEK stellar yields were derived with the Anders & Grevesse (1989) values. Owing to uncertainties in stellar nucleosynthesis

inputs such as the $^{12}\text{C}(\alpha, \gamma)^{16}\text{O}$ reaction rate, convection, and mass-loss (see Langer 1996; Gibson, Loewenstein, & Mushotzky 1997 for useful discussions of these uncertainties), we consider our predictions for the O abundance to be accurate within a factor of ~ 2 .

Magnesium

Figure 8.1 shows that the $[\text{Mg}/\text{S}]$ value predicted by the standard model is 0.45 dex lower than is observed in this DLA. The reason is clear from Figure 8.4, which shows that Mg/S is slightly subsolar in the ejecta from a generation of WW95 metal-poor stars and tends toward the solar value at higher metallicity. The observed value of $[\text{Mg}/\text{S}]_{\text{DLA}} = +0.3$ dex cannot be matched by any single generation of WW95 stars and nor will any superposition of populations fit the data. Alibés et al. (2001) also found that WW95 yields lead to an underproduction of Mg in their models of the local disk; a problem which they suggest could be resolved if intermediate-mass stars or SNe Ia supply additional Mg. Indeed, $4 - 6 M_{\odot}$ stars have been shown to contribute to most of the abundance of the neutron-rich Mg isotopes at low and intermediate metallicities (Fenner et al. 2003; Chapter 4).

Sulfur

Sulfur was used as the reference element in this study in preference to Fe because its nucleosynthetic origin is thought to be better understood. Hydrostatic burning and explosive O and Si burning in massive stars are the main processes responsible for S production. Although Fe has traditionally been a popular metallicity gauge, owing to easily observable stellar spectral lines, the question of its origin is complicated by the fact that both Type Ia and Type II SNe can make important contributions to the interstellar Fe content. Moreover, the Fe yield from massive stars is subject to uncertainties relating to the SN II mass cut. Oxygen is a common alternative reference element, but due to the recent significant revisions in the solar O abundance, we chose to plot abundance ratios relative to S, which has been detected in a reasonable number of DLAs and local stars.

Titanium

Titanium is a curious element given that observationally, it follows the trends of the alpha-elements in nearby stars, but theoretically, is expected to behave as an iron-

peak element. There is currently only a lower limit on Ti in this protogalaxy, however one might expect Ti to be enhanced with respect to iron, given the enhancement of O, Mg, and Si. In contrast, the model predicts $[\text{Ti}/\text{Fe}] \sim -0.2$ dex. The deficit of Ti generated by standard SN II and SN Ia models is a well-known problem (e.g. Timmes et al. 1995, Alibés et al. 2001). Hypernovae - energetic supernovae whose ejecta may be very rich in Ti - offer a possible solution to this problem, provided they were sufficiently frequent in the early Galaxy (Nakamura et al. 2001).

Zinc

Iron is often used as a metallicity gauge in stellar populations because of the ease with which it can be observed. However, the abundance of iron in gas is difficult to estimate because it is readily incorporated into dust grains (Savage & Sembach 1996). Furthermore, all of the elements comprising the Fe-peak are refractory. Thus Zn has become a popular substitute for Fe in DLA studies because it is largely free from the effects of dust-depletion and because the Zn/Fe ratio in local stars is approximately solar over a wide range of metallicities. The constancy of Zn/Fe vs Fe/H has led authors to propose that Zn, like Fe, is generated mostly by Type Ia SNe (e.g. Matteucci et al. 1993, Mishenina et al. 2002). However this need not be the case, since the metallicity dependence of Zn production in massive stars can naturally lead to a time delay that mimics that of SN Ia. As can be inferred from Figure 8.2, Zn yields predicted by the W7 Type Ia SNe model (Iwamoto 1999) are small in comparison to WW95 SNe II yields (whereas the iron-peak elements from V to Ni can be largely attributed to SNe Ia). Figure 8.3 reveals the strength of the metallicity-dependence of Zn production in massive stars. These effects can combine to allow Zn and Fe enrichment to occur in lockstep despite having different nucleosynthetic origins.

Figure 8.7 illustrates potential problems associated with using Zn as a proxy for Fe. The four panels plot $[\text{S}/\text{Fe}]$ (*left panels*) and $[\text{S}/\text{Zn}]$ (*right panels*) versus time (*upper panels*) and metallicity (*lower panels*). The curves correspond to different radii in a Milky Way-like galaxy. The inner radius has the strongest star formation rate and the earliest peak. Star formation proceeds more slowly with increasing radius. Owing to the delayed release of large amounts of Fe from SNe Ia with respect to the release of S from short-lived massive stars, the behaviour of $[\text{S}/\text{Fe}]$ (or $[\text{O}/\text{Fe}]$) vs $[\text{Fe}/\text{H}]$ can be used to diagnose star formation histories. Slower and more

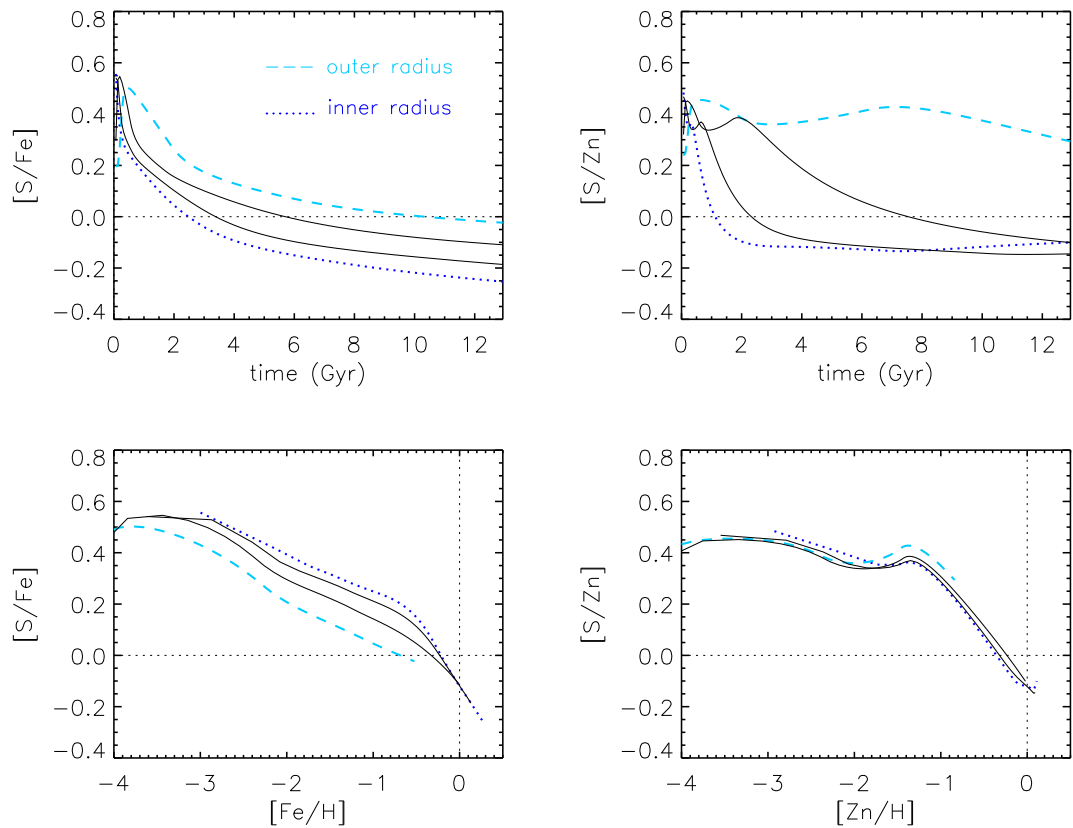


Figure 8.7: The evolution of S relative to Fe (left panels) and relative to Zn (right panels) as a function of time (upper panels) and metallicity (lower panels). The four curves in each figure correspond to different radii in a Milky Way-like disk galaxy. The inner radius (dotted line) reaches subsolar $[S/Fe]$ quickly owing to earlier and stronger star formation. The outer region of the disk (dashed line) is expected to remain enhanced in S and alpha-elements for longer because the drawn-out star formation causes the SNe Ia rate to peak at later times. In $[Fe/H]$ -space the trends are reversed, with the inner disk maintaining supersolar $[S/Fe]$ at higher metallicity because the early intense star formation pushes the gas towards high $[Fe/H]$ before SNe Ia start to dominate Fe production. The upper panels show that only for certain radii does the evolution of Zn resemble that of Fe. Given our adopted SN II and SN Ia nucleosynthesis prescriptions, Zn originates primarily from SNe II with a metallicity-dependent yield. Sulfur also comes mostly from SNe II with a fairly metallicity-independent yield. Thus the curves showing $[S/Zn]$ vs $[Zn/H]$ for various radii overlay one another.

protracted star formation, such as in the outer disk of a galaxy, should lead to subsolar $[S/Fe]$ (and $[O/Fe]$) at lower $[Fe/H]$ (*lower left panel*). But when Fe is replaced by Zn (*lower right panel*), the behaviour at all radii is virtually indistinguishable. This is a consequence of the nucleosynthesis prescriptions adopted in this study that have Zn being produced mostly by massive stars as an increasing function of initial stellar metallicity. Under this formalism, the evolution of Zn mirrors that of Fe only for certain star formation histories, but might deviate markedly in other environments. Note that it is impossible to attain the solar and subsolar values of S/Zn at the low Zn/H that are observed in DLAs (e.g. Centuri3n et al. 2000) using the conventional Type Ia and II SNe models employed in this study, regardless of SF history (*lower right panel*). This may indicate a deficiency in our theories of Zn production from the standard SN II and SN Ia nucleosynthesis models. Other authors (e.g. Calura, Matteucci, & Vladilo 2003) have produced low $[S/Zn]$ at low metallicity using chemical evolution models, but they achieve this by ignoring the theoretically predicted SN II and SN Ia Zn yields and instead assume that Zn comes mostly from SN Ia and scales with the Fe yield.

There are two main weaknesses of the standard models of Type Ia and II SNe that highlight the uncertainties in the nucleosynthetic origins of Zn: firstly, the models are unable to explain the supersolar values of $[Zn/Fe]$ in metal-poor stars; and secondly, the predicted Zn isotopic composition is at odds with solar. Breaking down the theoretical SNe II Zn yield into its main isotopes reveals substantial disagreement with the solar pattern. The dominant isotope in the Sun is ^{64}Zn , yet WW95 Type II models underestimate its abundance by a factor of ~ 3 . Conversely, ^{68}Zn is overproduced by a similar factor. Since the W7 SNe Ia model also underpredicts ^{64}Zn , other processes might need to be invoked to elevate ^{64}Zn to solar proportions. The uncertainty regarding zinc's production sites is unfortunate given its key role in diagnosing DLAs.

Neutrino-driven neutron star winds (Woosley & Hoffman 1992; Hoffman et al. 1996) may be an important supplemental site for Zn synthesis. WW95 claim that neutrino winds accompanying the r -process are probably the chief production site of ^{64}Zn , as opposed to the neutron capture process during helium burning that is included in their SN II models. Alternatively, a blend of fallback and mixing in energetic hypernovae (HNe) have been found to produce ^{64}Zn in prodigious amounts (Umeda & Nomoto 2002), leading to $[Zn/Fe]$ values compatible with stellar observations. Each of these HNe may eject up to $4 \times 10^{-4} M_{\odot}$ of ^{64}Zn ; about ten times

more than a typical SN II.

Figure 8.7 illustrates the tendency for a system with a “burstier” SFH (such as the innermost disk) to maintain elevated $[S/Fe]$ over a wide range of $[Fe/H]$ because the ISM becomes metal-rich before SNe Ia have a chance to dominate Fe production. The age-metallicity relation is gradual in the outer disk, such that for a given $[Fe/H]$, there has been more time for SNe Ia to contribute to the abundance pattern. Thus, the outer radii in Figure 8.7 reaches $[S/Fe] = 0$ at $[Fe/H] = -0.7$, whereas the inner radii has $[S/Fe] = +0.2$ at $[Fe/H] = -0.7$. Note however, that in the time domain, it is the slowly forming systems that maintain elevated $[S/Fe]$ for longer temporal periods. Indeed, it takes about 10 Gyr for the outer disk in this model to reach solar S/Fe. This corresponds to a much lower redshift than is characteristic of most DLAs. The DLA population is characterised by roughly solar α/Fe values, a mean metallicity $\sim 1/10$ th solar, and ages $\lesssim 5$ Gyr. According to our standard disk galaxy model, in which the gas infall timescale increases with Galactocentric radius, only the outer regions of the disk can reach $[\alpha/Fe] \sim 0$ at $[Fe/H] \sim -1$, but on timescales > 5 Gyr. In order to get $[\alpha/Fe] \sim 0$ at $[Fe/H] \sim -1$ on sufficiently short timescales one may invoke a short star formation burst of low efficiency (to keep the metallicity down) or a galactic wind that preferentially removes α -elements (e.g. Calura et al. 2003). Dwarf galaxies are more closely associated with these phenomena than disk galaxies.

Gallium and Germanium

The predictions from our standard model for the abundance of Ga and Ge are in rough agreement with the data, however we refrain from drawing conclusions based on these results owing to the uncertainties surrounding their synthesis. Although Woosley & Weaver (1995) include Ga and Ge in their tables of yields, they state that the synthesis of all isotopes above ^{66}Zn are not considered accurate. Indeed, the WW95 Ga and Ge yields are remarkably sensitive to factors including the explosion energy. We also note that WW95 predict a *stronger* metallicity-dependence for the even-numbered Ge than for the odd-numbered Ga (Figure 8.4). We hope that further observational progress in detecting these and other neutron-capture elements in objects ranging from DLAs to PNe (Sterling, Dinerstein & Bowers 2002; Sterling & Dinerstein 2003) and stars (Vennes et al. 2005; Cowan et al. 2005) will be matched by advances in the nucleosynthetic theories, such that these elements provide more

robust constraints on the chemical evolution models.

8.5 Summary and Future Directions

We have predicted the chemical evolution of a DLA as a function of star formation history, age, and metallicity, and find that the enrichment pattern detected in absorption in a $z = 2.626$ protogalaxy is generally consistent with the nucleosynthetic signature of Type II SNe with a moderate contribution from Type Ia SNe. Despite this gratifying agreement with the data, a few inconsistencies remain that may provide insight into nucleosynthetic processes. The underproduction of Mg and Zn with respect to S in our models lends support to an idea already hinted at by discrepancies between the observed abundances in nearby stars and the yields from standard SN II models, that these elements may require additional production sites such as: intermediate mass stars, in the case of Mg; and neutrino-winds, in the case of Zn. It is also likely that tighter constraints on Cl and Cu in the future will see these elements being underproduced by all but the highest metallicity SN II models. This may indicate that the odd-even effect is weaker than predicted by stellar nucleosynthesis models.

DLA-B/FJ0812+32 is expected to soon be complemented by a growing database of detailed abundance patterns of DLAs covering a range of metallicities and redshifts. These observations will represent a new regime for probing chemical evolution in diverse environments with an assortment of enrichment histories. As well as providing further insight into the nature of the DLA population, such a database will complement local stellar observations to help uniquely constrain nucleosynthesis processes. In particular, we await future detections of Cl and P in this and other DLAs. Detection of these odd-elements should enable the SN II models of WW95 and FRANEC to be assessed in terms of their different predictions for the magnitude of the odd-even effect. We also propose that the detection of s -process elements like Kr and particularly Pb, holds promise as a sensitive measure of the age of intermediate to high redshift DLAs.

Future observations of DLA-B/FJ0812+32 are also expected to yield measurements of C, N, F, Ga, and Sn. Fluorine, like boron, is difficult to measure in stars, but can be detected in absorption in DLAs, providing a test of the ν -process believed to operate during the core-collapse phase of massive stars. It is hoped that

Ga measurements will provide insight into neutron-capture processes in the early universe. Carbon and nitrogen detections will be especially fruitful because they can be compared against the dataset of N in DLAs and C and N in local stars. Furthermore, knowledge of CNO abundances in a single DLA will constrain theories of nucleosynthesis in intermediate mass stars.

Chapter 9

Variations in the fine-structure constant and limits on AGB pollution of quasar absorption systems

This chapter is based upon Fenner, Murphy & Gibson, 2005, MNRAS, 358, 468.

9.1 Introduction

In the past few years, evidence has emerged that the fine-structure constant, $\alpha \equiv e^2/\hbar c$, may have been smaller in high-redshift quasar (QSO) absorption systems than the value measured today on Earth (e.g. Webb et al., 1999; Murphy et al., 2004, hereafter MFW04). A possible explanation for the lower-redshift half of this result is that the abundances of the heavy Mg isotopes (^{25}Mg and ^{26}Mg) in the absorbers are much higher, relative to that of ^{24}Mg , than solar values. Recently, Ashenfelter, Mathews & Olive (2004a) proposed and expanded upon (Ashenfelter, Mathews & Olive, 2004b, hereafter AMO04) a chemical evolution model with an initial mass function (IMF) strongly enhanced at intermediate masses (IMs), whereby highly super-solar abundances of heavy Mg isotopes are produced via asymptotic giant branch (AGB) stars. In this chapter we explore the side-effects of this model with a view to identifying possible observational signatures other than increased heavy Mg isotope abundances.

The chapter is organised as follows. The remainder of this section summarizes the QSO absorption-line evidence for and against variations in α and describes the sensitivity of that evidence to variations in isotopic abundances. Section 9.2 briefly describes the nucleosynthesis of Mg isotopes in stars of different masses. In Section 9.3 we detail our chemical evolution models and compare them with those used by AMO04. Section 9.4 presents our main results for the predicted evolution of the

total and isotopic abundances of various elements typically observed in QSO spectra. In each case we compare these with available data from QSO absorption-line and local stellar and ISM studies and discuss their dominant uncertainties. Section 9.5 assesses the overall validity of the IM-enhanced models in light of our new results and presents other arguments for and against such models. Section 9.6 gives our main conclusions.

9.1.1 Evidence for varying α from QSO absorption systems?

The universality and constancy of the laws of nature rely on the space-time invariance of fundamental constants, such as α . Therefore, since Milne (1935, 1937) and Dirac (1937) first suggested the time-variation of the Newton gravitational constant, a great diversity of theoretical and experimental exploration of possible space-time variations in fundamental constants has been pursued (e.g. see review in Uzan, 2003).

High resolution spectroscopy of absorption systems lying along the lines-of-sight to background QSOs has provided particularly interesting constraints on variations in α over large spatial and temporal baselines. Early work focused on the alkali-doublet (AD) method: since the relative wavelength separation between the two transitions of an AD is proportional to α^2 (e.g. Bethe & Salpeter, 1977), comparison between AD separations seen in absorption systems with those measured in the laboratory provides a simple probe of α variation. Several authors (e.g. Varshalovich & Potekhin 1994; Cowie & Songaila 1995; Varshalovich, Panchuk & Ivanchik 1996; Varshalovich, Potekhin & Ivanchik 2000) applied the AD method to doublets of several different ionic species (e.g. C IV, Si II, Si IV, Mg II and Al III). The strongest current AD constraints come from analysis of many Si IV absorption systems in $R \sim 45\,000$ spectra: $\Delta\alpha/\alpha = (-0.5 \pm 1.3) \times 10^{-5}$ (Murphy et al., 2001c, 21 systems; $2.0 < z_{\text{abs}} < 3.0$) and $\Delta\alpha/\alpha = (0.15 \pm 0.43) \times 10^{-5}$ (Chand et al., 2004b, 15 systems; $1.6 < z_{\text{abs}} < 2.9$)¹

Considerable recent interest has focused on the many-multiplet (MM) method introduced by Dzuba, Flambaum & Webb (1999a,b) and Webb et al. (1999). The MM method is a generalization of the AD method, constraining changes in α by utilizing many observed transitions from different multiplets and different ions associated with each QSO absorption system. It holds many important advantages over

¹ $\Delta\alpha/\alpha$ is defined as $\Delta\alpha/\alpha = (\alpha_z - \alpha_0)/\alpha_0$, for α_z and α_0 the values of α in the absorption system(s) and in the laboratory respectively.

the AD method, including an effective order-of-magnitude precision gain stemming from the large differences in sensitivity of light (e.g. Mg, Si, Al) and heavy (e.g. Fe, Zn, Cr) ions to varying α . At low redshift ($0.5 \lesssim z_{\text{abs}} \lesssim 1.8$), Mg lines, whose red transition wavelengths ($\lambda > 2700 \text{ \AA}$) are relatively insensitive to changes in α , act as anchors against which the larger expected shifts in the bluer ($2300 < \lambda < 2700 \text{ \AA}$) Fe transition wavelengths can be measured. At higher z_{abs} , transitions from Si and Al provide anchor lines distributed in wavelength space amongst a variety of Cr, Fe, Ni and Zn transitions which shift by large amounts in both positive and negative directions as α varies. This diversity at high- z_{abs} ensures greater reliability in the face of simple systematic effects compared with the low- z_{abs} Mg/Fe systems.

The MM method, applied to Keck/HIRES QSO absorption spectra, has yielded very surprising results, with the first tentative evidence for a varying α by Webb et al. (1999) becoming stronger with successively larger samples (Murphy et al. 2001a; Webb et al. 2001; Murphy, Webb & Flambaum 2003). The most recent Keck/HIRES constraint comes from 143 absorption systems over the range $0.2 < z_{\text{abs}} < 4.2$ (MFW04): $\Delta\alpha/\alpha = (-0.57 \pm 0.11) \times 10^{-5}$. This result is quite internally robust: it comprises three different observational samples and approximately equal low- and high- z_{abs} subsamples, all of which give consistent results. Stubbornly, it has also proven resistant to a range of potential instrumental and astrophysical systematic effects (Murphy et al., 2001b, 2003).

Intriguingly, Chand et al. (2004a) (see also Srianand et al., 2004) have analysed 23 Mg/Fe absorption systems in higher signal-to-noise ratio (S/N) spectra from a different telescope and spectrograph, the VLT/UVES, claiming a precise, null result over the range $0.4 < z_{\text{abs}} < 2.3$: $\Delta\alpha/\alpha = (-0.06 \pm 0.06) \times 10^{-5}$. Quast, Reimers & Levshakov (2004) and Levshakov et al. (2004) also find null results in individual UVES absorbers. The discrepancy between the VLT/UVES and Keck/HIRES results is yet to be resolved. However, it is important to note that low-order distortions of the Keck/HIRES wavelength scale, as might be expected from simple instrumental systematic errors, produce opposite effects on the low- and high- z_{abs} samples and so cannot fully explain the HIRES–UVES difference (Murphy et al., 2003, 2004). If the HIRES result is incorrect, the nature of the contributory systematic errors must be subtle and somewhat conspiratorial.

9.1.2 Isotopic abundance evolution?

Murphy et al. (2001b) first identified the potential systematic error introduced into the MM method if the relative isotopic abundances of crucial anchor elements like Mg and Si underwent strong cosmological evolution. This is because the absorption lines of the different isotopes are spaced widely enough ($\sim 0.5 \text{ km s}^{-1}$) in these light ions to affect the measured line centroids (Figure 9.1, left panel). MFW04 calculated $\Delta\alpha/\alpha$ from their HIRES absorption line data as a function of the assumed relative isotopic abundances of Mg and Si. The results are presented in the right panel of Figure 9.1. Note the relative insensitivity of $\Delta\alpha/\alpha$ in the high- z_{abs} systems to the Si heavy isotope ratio, $(^{29}\text{Si}+^{30}\text{Si})/^{28}\text{Si}$. As noted above, this is expected because of the greater diversity of transitions and line-shifts available in the high- z_{abs} regime. It is therefore important to note that evolution in the Si isotopic abundance cannot explain the high- z_{abs} HIRES results. Until recently, no information about the isotopic shifts in transitions from heavier ions used at high- z_{abs} (e.g. Cr II, Fe II, Ni II, Zn II) were available. However, due to their higher masses, the shifts are expected to be smaller with respect to the sensitivity of the lines to varying α . Indeed, the recent isotopic shift calculations of Kozlov et al. (2004) confirm this.

However, Figure 9.1 emphasises the strong dependence of $\Delta\alpha/\alpha$ in the low- z_{abs} systems on the Mg heavy isotope ratio, $(^{25}\text{Mg}+^{26}\text{Mg})/^{24}\text{Mg}$. The importance of this potential systematic effect therefore depends entirely on the evolution of Mg isotopic ratios in QSO absorption systems. Unfortunately, no direct measurement of $(^{25}\text{Mg}+^{26}\text{Mg})/^{24}\text{Mg}$ in QSO absorbers is currently feasible due to the small separation of the isotopic absorption lines. Fortunately however, Mg is one of the few elements for which stellar isotopic abundances can be measured through molecular absorption lines, in this case transitions of MgH. Gay & Lambert (2000) and Yong, Lambert & Ivans (2003b) have shown that observed stellar values of $(^{25}\text{Mg}+^{26}\text{Mg})/^{24}\text{Mg}$ generally decrease with decreasing $[\text{Fe}/\text{H}]$, as predicted in the Galactic chemical evolution models of Timmes, Woosley & Weaver (1995). The (normal IMF) model we present in Section 9.3 also predicts such a decrease (Figure 9.2). This has been used to argue that in the low-metallicity environments of Mg/Fe absorbers (typically, $[\text{Zn}/\text{H}] \sim -1.0$), one should expect sub-solar values of $(^{25}\text{Mg}+^{26}\text{Mg})/^{24}\text{Mg}$ and so, if anything, one expects the low- z_{abs} values of $\Delta\alpha/\alpha$ to be *too positive* (Murphy et al., 2001b, 2003, 2004; Chand et al., 2004a).

Contrary to this trend, Yong et al. (2003a) have found very high values of

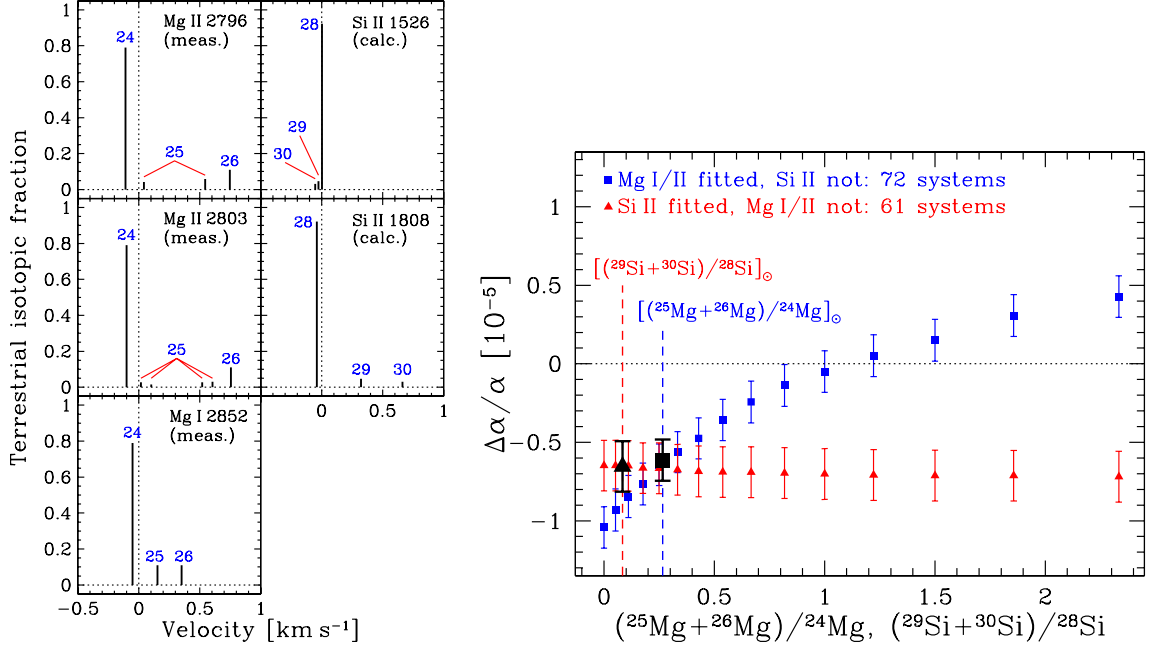


Figure 9.1: Left panel: Isotopic structures for the relevant Mg/Si transitions from measurements (Hallstadius, 1979; Drullinger et al., 1980; Pickering et al., 1998) or calculations (Berengut et al., 2003). Zero velocity corresponds to the isotopic structure’s centre of gravity. Right panel: Sensitivity of $\Delta\alpha/\alpha$ measured by MFW04 to variations in Mg and Si isotopic abundance variations. Absorption systems containing no measured Si lines (i.e. most low- z_{abs} systems) contribute to the square points while only systems containing Si lines and no measured Mg lines (i.e. most high- z_{abs} systems) contribute to the triangular points. The large square and triangle mark the values of $\Delta\alpha/\alpha$ obtained with terrestrial relative isotopic abundances (Rosman & Taylor, 1998): $(^{24}\text{Mg}:^{25}\text{Mg}:^{26}\text{Mg})_{\odot} = (79:10:11)$ and $(^{28}\text{Si}:^{29}\text{Si}:^{30}\text{Si})_{\odot} = (92.2:4.7:3.1)$. The abundance ratio of the heavy isotopes [i.e. $(^{25}\text{Mg}:^{26}\text{Mg})$ and $(^{29}\text{Si}:^{30}\text{Si})$] was held at the terrestrial value along the abscissa.

$(^{25}\text{Mg}+^{26}\text{Mg})/^{24}\text{Mg}$ for some giant stars in the globular cluster NGC 6752, which has metallicity $[\text{Fe}/\text{H}] \sim -1.6$. One extreme star had $(^{25}\text{Mg}+^{26}\text{Mg})/^{24}\text{Mg} = 0.91$ (cf. $[(^{25}\text{Mg}+^{26}\text{Mg})/^{24}\text{Mg}]_{\odot} = 0.27$). Since IM AGB stars are thought to produce significant quantities of ^{25}Mg and ^{26}Mg (see Section 9.2), Yong et al. (2003a) proposed that low-metallicity, IM AGB stars may have polluted this globular cluster. This prompted Ashenfelter et al. (2004a,b) to propose a chemical evolution model with a strongly enhanced population of IM stars as a possible explanation for the low- z_{abs} HIRES varying- α results. In the following sections we describe in detail the nucleosynthesis of Mg isotopes and construct a chemical evolution model, similar to that of AMO04, to investigate the various effects of an IM-enhanced IMF.

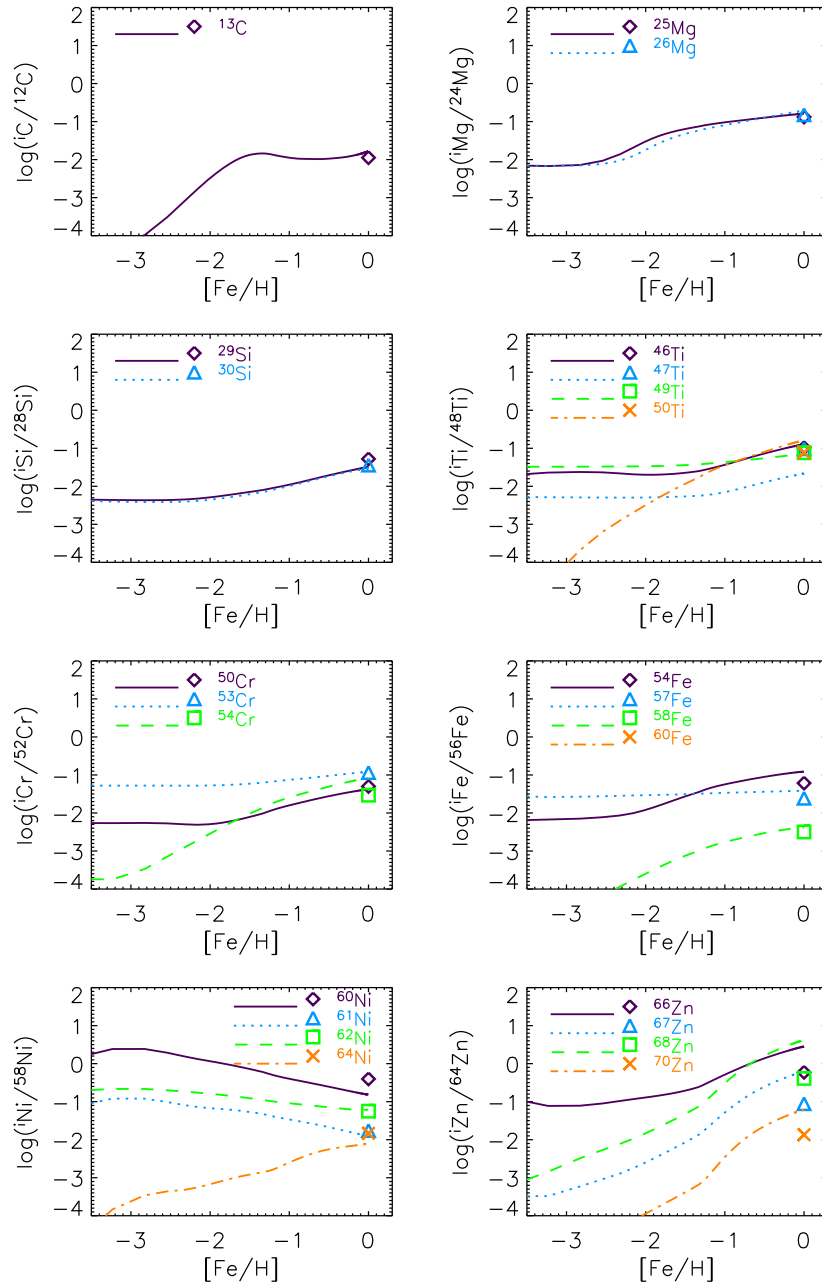


Figure 9.2: The evolution of isotopic ratios with metallicity $[\text{Fe}/\text{H}]$ for the elements C, Mg, Si, Ti, Cr, Fe, Ni, Zn, which are used in varying $\Delta\alpha/\alpha$ analyses. Isotopic abundances are shown on a logarithmic scale relative to the dominant isotope for that element. Different curves illustrate the predicted behaviour of the various isotopes from a standard solar neighbourhood chemical evolution model. Symbols show the corresponding solar values. In general, the minor isotopes accrue more slowly in the ISM with respect to the dominant isotope for each element. A notable exception is Ni, for which $^{60,61,62}\text{Ni}/^{58}\text{Ni}$ declines over time. The departure of Ni from the general rule of thumb may reflect uncertainties in its nucleosynthesis, including an overproduction from SNe Ia, that have been pointed out in the literature (e.g. Timmes et al. 1995; Iwamoto et al. 1999).

9.2 Nucleosynthesis of magnesium isotopes

Massive stars culminating in Type II SNe are responsible for most of the Mg isotopes in the present-day Galaxy. However, there is evidence that intermediate-mass stars may dominate the production of the neutron-rich Mg isotopes in the metal-poor regime. According to standard models of stellar nucleosynthesis, the yield of the heavy Mg isotopes, $^{25,26}\text{Mg}$, scales with the initial stellar metallicity. Conversely, the generation of ^{24}Mg from SNe II operates fairly independently of initial metallicity. Since massive stars alone are insufficient to account for the higher than expected values of $^{25,26}\text{Mg}/^{24}\text{Mg}$ detected in metal-poor stars (Gay & Lambert 2000; Yong et al. 2003b), it has been suggested that there is a supplemental source of the neutron-rich Mg isotopes.

Karakas & Lattanzio (2003) have shown that ^{25}Mg and ^{26}Mg production is substantial in metal-poor intermediate-mass stars (IMs). At low metallicities, asymptotic giant branch stars are believed to generate ^{25}Mg and ^{26}Mg from α -capture onto ^{22}Ne triggered by He-shell thermal pulsing. Temperatures at the base of the convective envelope in $4 < m/M_{\odot} < 6$ stars can be high enough to burn ^{24}Mg via hot bottom burning (HBB) as well as synthesise large amounts of ^{25}Mg and ^{26}Mg . Based on the recent nucleosynthetic calculations from Karakas & Lattanzio (2003), AGB stars have been shown to produce sufficient quantities of $^{25,26}\text{Mg}$ to resolve the discrepancy between local stellar observations and previous model predictions (Fenner et al. 2003; Chapter 4). For the present study, we have incorporated the same grids of low- and intermediate-mass stellar yields that successfully reproduced the solar neighbourhood Mg isotopic evolution.

9.3 Chemical evolution models

The distribution of elements and isotopes as a function of time and radius was simulated for a Milky Way-like disk galaxy using `GETool`. We present predictions for (i) the solar annulus ($r = 8.5$ kpc) because it is the solar neighbourhood for which we have the most comprehensive set of empirical constraints, and (ii) the outer disk ($r = 16.5$ kpc) because it is possible that many quasar absorption systems correspond to the outer regions of spiral disks (e.g. Dessauges-Zavadsky et al. 2004). To summarise the details of the model: we define $\sigma_i(r, t)$ as the mass surface density of species i at time t and radius r , and assume that its rate of change of is given by:

$$\begin{aligned} \frac{d}{dt}\sigma_i(r, t) &= \int_{m_{\text{low}}}^{m_{\text{up}}} \psi(r, t - \tau_m) Y_i(m, Z(r, t - \tau_m)) \frac{\phi(m)}{m} dm \\ &+ \frac{d}{dt}\sigma_i(r, t)_{\text{infall}} - X_i(r, t) \psi(r, t), \end{aligned} \quad (9.1)$$

where the three terms on the right-hand side correspond to the stellar ejecta, gas infall, and star formation, respectively. The star formation rate, ψ , varies with the square of the gas surface density in our models, consistent with the empirical Schmidt (1959) law. $Y_i(m, Z(r, t - \tau_m))$ denotes the stellar yield of i (in mass units) from a star of mass m and metallicity $Z(r, t - \tau_m)$, $\phi(m)$ is the initial mass function, and X_i is the mass fraction of element i . By definition, the sum of X_i over all i is unity. The total surface mass density is identical to the integral over the infall rate. The lower and upper stellar mass limits, m_{low} and m_{up} , are $0.08 M_{\odot}$ and $60 M_{\odot}$, respectively, while τ_m is the main-sequence lifetime of a star of mass m . We split the first term into three equations that deal separately with low- and intermediate-mass stars, Type Ia supernova progenitors, and massive stars.

9.3.1 Infall scheme

We assumed that the Milky Way-like disk galaxy formed during two main gas accretion episodes. The first occurs on a rapid timescale (< 0.5 Gyr) and is associated with the formation of the halo and thick disk, while the second episode occurs on a longer timescale and fuels the formation of stars in the disk. For simplicity, we have assumed no prior metal-enrichment of the gas infalling onto the disk, although there is some evidence from observations of high-velocity clouds that gas falling into the Galaxy may contain traces of heavy elements (e.g. Wakker et al. 1999; Gibson et al. 2001; Sembach et al. 2002). Exponentially decaying infall rates have been adopted, such that the evolution of total surface mass $\sigma_{\text{tot}}(r, t)$ density is given by

$$\frac{d\sigma_{\text{tot}}(r, t)}{dt} = A(r)e^{-t/\tau_{\text{H}}(r)} + B(r)e^{-(t-t_{\text{delay}})/\tau_{\text{D}}(r)} \quad (9.2)$$

where the infall rate coefficients $A(r)$ and $B(r)$ are chosen in order to reproduce the present-day surface mass density of the halo/thick disk and thin disk components, which we take to be 10 and $45 M_{\odot} \text{pc}^{-2}$, respectively. The adopted timescales for the infall phases are $\tau_{\text{H}} = 0.1$ Gyr and $\tau_{\text{D}} = 9.0$ Gyr at the solar Galactocentric radius

$r_{\odot} = 8.5$ kpc. Disk formation starts after an initial delay $t_{\text{delay}} = 0.5$ Gyr. The ‘inside-out’ functional form for $\tau_{\text{D}}(r)$ (Romano et al. 2000) is adopted, whereby the timescale for disk gas accretion increases linearly with radius. The Milky Way age is taken to be 13 Gyr.

9.3.2 Initial mass function (IMF)

The shape of the stellar initial mass function (IMF) influences the quantity of Galactic material locked up in stars of different masses, which in turn determines the rate at which different elements are released into the ISM. The models presented in Section 9.4 compare the Kroupa, Tout & Gilmore (1993) three-component IMF with one enhanced in AGB stars at low metallicities. The shape of the IM-enhanced IMF at time $t = 0$ is illustrated in Figure 9.3. The height and width of the AGB bump was chosen to approximate that in AMO04. It is centred on $5 M_{\odot}$ with a narrow mass range, although not as narrow as the AMO04 Model 1, for which the extra AGB population consists almost entirely of $5 \pm 1 M_{\odot}$ stars (compare our Figure 9.3 with their figure 3). Their preferred models (i.e. Models 2 and 3) adopt a wider IM-bump and we also favour a broader peak, on the grounds that it is more physically realistic².

In our IM-enhanced models, the amplitude of the IM-bump decays exponentially with increasing gas metallicity. This differs from AMO04, who adopted time-dependent decay. Imposing a metallicity- rather than time-dependent IM-enhancement was designed to reflect the different physical properties of metal-poor gas clouds. The decreased cooling rate and magnetic field strength in metal-poor material is expected to influence the mass distribution of newly formed stars. For consistency with AMO04 Model 1, our scale-factor for the exponentially decaying IM-bump was chosen to correspond to the predicted metallicity at the solar radius at time = 0.2 Gyr. This corresponds to $[Z/H] \sim -1.3$, or roughly 1/20th solar metallicity. The transformation from a time- to a metallicity-dependent IMS burst makes it reasonable to apply the same IMF formalism across all Galactic radii. Because the outer disk has a more protracted star formation rate and builds up metals more slowly than in the solar radius, the effects of an IMS burst would be suppressed by adopting a fixed timescale. Instead, conversion to metallicity-dependence prolongs

²As a check, we ran a model using a narrower and taller IM-bump, conserving the mass contained in the AGB-enhancement. The final results were similar in both cases.

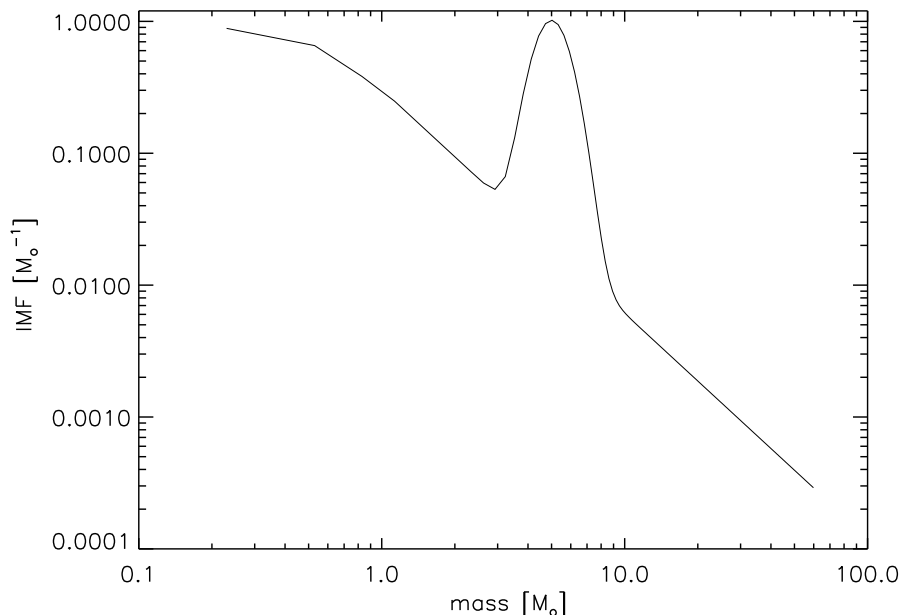


Figure 9.3: The shape of the IM-enhanced IMF used in this study at time $t = 0$. The IMF is composed of an AGB-biased bump superimposed on a standard Kroupa, Tout & Gilmore (1993) 3-component power-law. The height and width of the AGB bump was chosen to emulate that in AMO04. The amplitude of the bump decays exponentially with increasing gas metallicity.

the temporal duration of the IMS burst at outer radii and amplifies the chemical signature of an IM-enhanced IMF.

9.3.3 Stellar Yields and Lifetimes

Low and intermediate mass stars (LIMS): For stars less massive than $8 M_{\odot}$, we incorporated the yields from the stellar evolution and nucleosynthesis code described in Karakas & Lattanzio (2003), supplemented with yields for additional isotopes from hydrogen to sulfur and for the iron-peak, as well as unpublished yields for the metallicity $Z=0.0001$. The wide range of heavy elements and isotopes incorporated in these AGB nucleosynthesis models allows us to self-consistently predict the contribution from low- and intermediate-mass stars (LIMS) to the elemental and isotopic abundance of many species of interest in DLA and varying α studies. These include C, N, Mg, Al, Si, Ni and Fe. We also ran identical chemical evolution models using two alternative sets of LIMS yields: those of (i) van den Hoek & Groenewegen (1997) and (ii) Marigo (2001) (using mixing length parameter $\alpha = 2$ for consistency with

AMO04). These two alternative inputs do not predict yields for elements beyond O, but they provide an indication of the uncertainty in the CNO yields, as will be discussed in Section 9.4.6.

Type Ia supernovae (SNe Ia): We adopted a recalculation of the Thielemann, Nomoto, & Yokoi (1986) W7 model by Iwamoto et al. (1999) to estimate the yields from SNe Ia. It was assumed that 4% of binary systems involving intermediate and low mass stars result in SNe Ia, since this fraction provides a good fit to the solar neighbourhood (e.g. Alibés, Labay, & Canal 2001; Fenner & Gibson 2003).

Massive stars: For stars more massive than 8–10 M_{\odot} that end their lives in violent supernova explosions, we implemented the yields from Woosley & Weaver (1995). Their yields span metallicities from zero to solar and cover the mass range 11–40 M_{\odot} . Since the upper mass limit of our stellar IMF extends beyond this mass range, we extrapolated the 35 and 40 M_{\odot} yields for $m > 40 M_{\odot}$. We took the lower energy ‘A’ models for stars $\leq 25 M_{\odot}$ and the higher energy ‘B’ models for heavier stars. Taking note of the suggestion by Timmes, Woosley, & Weaver (1995) that the WW95 mass-cuts may have penetrated too deeply within the iron core, we have uniformly halved the iron yields from these models. In the uncertain mass range 8–12 M_{\odot} , we make the conservative assumption that these stars do not synthesise new heavy elements, but expel material with the same heavy element abundance pattern as the gas from which they were born.

Stellar lifetimes: We adopt metallicity-dependent main-sequence lifetimes calculated by Schaller et al. (1992). Although stars lose material over the course of their evolution via stellar winds and planetary nebulae, this model assumes that all the mass loss takes place at the end of the main-sequence phase. Our predictions are not significantly affected by this simplification.

9.3.4 Comparison with Ashenfelter et al. (2004)

We now list some key differences between our model and that of Ashenfelter et al. (2004b) and describe the impact on the results:

- **AGB yields:** We have adopted the low- and intermediate-mass stellar yields from Karakas & Lattanzio (2003), with additional yields for isotopes up to S as well as the Fe-peak, along with unpublished yields for the metallicity $Z=0.0001$. Thus, the AGB yields of species such as N and the Mg isotopes are internally self-consistent. AMO04 added the Mg isotopic yields from Karakas

& Lattanzio (2003) onto the Marigo (2001) C, N and O yields. Although this means that their N yields were not drawn from the same AGB models as the Mg yields, the predicted evolution of N is very similar in either case, as discussed in Section 9.4.6.

- **Type Ia SNe yields:** AMO04 employed a metallicity-dependent Type Ia supernovae rate from Kobayashi, Tsujimoto & Nomoto (2000) that prohibits the formation of SNe Ia below a minimum $[\text{Fe}/\text{H}]$ threshold of -1.1 . This metallicity-dependence was postulated mostly on theoretical grounds. Observationally however, α/Fe ratios in dwarf galaxies (e.g. Shetrone et al. 2001) and S/Zn ratios in DLAs (Pettini, Ellison, Steidel & Bowen 1999) provide evidence for SN Ia activity below $[\text{Fe}/\text{H}] \sim -1$. Furthermore, the trend of $[\text{O}/\text{Fe}]$ with $[\text{Fe}/\text{H}]$ seen in local stars can be satisfactorily explained without imposing a SN Ia metallicity threshold (e.g. Alibés et al. 2001). Thus, the present study does not impose a metallicity threshold and the SN Ia rate is calculated following the method of Greggio & Renzini (1983) and Matteucci & Greggio (1986). While a $[\text{Fe}/\text{H}] \sim -1$ SN Ia threshold would have only a minor effect on the solar radius results, the outer disk remains metal-poor for at least several Gyr and would be more sensitive to the precise SN Ia prescription, as will be discussed in Section 9.4.
- **Standard IMF:** In recalculating the model of Timmes et al. (1995), AMO04 adopted the Salpeter (1955) single power-law IMF. We adopt a three-component Kroupa et al. (1993) law, which is flatter at lower masses and steeper at the high end of the IMF. This empirically derived function leads to a lower overall effective yield that is more consistent with local data (Pagel 2001). Although the choice of IMF does influence the evolution of the chemical species of interest in this investigation, the impact is not large enough to affect our final conclusions. Model 1 from AMO04 also differs from our IM-enhanced model through the inclusion of an exponential 0.5 Gyr time scale before the onset of the “normal” stellar IMF component. Thus, at the very earliest times, most of the star-forming gas ends up inside stars with $m \sim 5 M_{\odot}$. In contrast, we retain our normal IMF component at all times (akin to AMO04’s Model 2).
- **IM-enhanced IMF:** While the AMO04 IM-bump decays exponentially on a fixed timescale (ranging from 0.2 to 0.4 Gyr depending on the model), we

transformed this from a time to a metallicity dependence. As discussed in Section 9.3.2, the assumption that the shape of the IMF is governed primarily by the chemical composition of the star forming gas cloud is presumably more physically justified than imposing a uniform time-dependence. Converting from the time to the metallicity domain allows us to apply the same IMF prescription to systems with various star formation histories, such as the slowly evolving outer Galactic disk, which we investigate in this chapter.

- **Dual-phase infall:** AMO04 assumed that the Galactic disk forms during a *single* phase of gas infall, in order to directly compare with the results of Timmes et al. (1995). We model the Milky Way formation using a *dual*-phase infall scheme, since this has been shown to provide a better match than single-infall models to the number distribution of G- and K-dwarfs in the solar neighbourhood (e.g. Chiappini et al. 1997). We stress that our final conclusions are largely insensitive to our choice of infall scheme.

9.4 Results

We now present the predicted chemical evolution for the solar radius and the outer Galactic disk in the case of an enhanced population of intermediate-mass stars at low metallicity. These results are compared with those obtained using a normal IMF and plotted against observations of local stars and DLAs, where applicable. In all the following figures, solid and dashed lines denote the evolution at the solar (8.5 kpc) and outer radii (16.5 kpc), respectively. Models adopting a normal IMF are shown with thin lines, while thick lines correspond to models with the IM-enhanced IMF, as illustrated in Figure 9.3.

9.4.1 Type Ia supernova rate and the age-metallicity relationship

The evolution of the Type Ia supernova rate predicted by the model described in Section 9.3 is shown in the upper panel of Figure 9.4. The incidence of Type Ia SNe in the solar region (solid lines) is predicted to have risen to a peak about 7 Gyr ago and steadily declined thereafter. In contrast, the predicted SN Ia rate in the outer disk (dashed lines) has continued to increase up to the present-day. This difference

reflects the more rapid and efficient conversion of gas into stars in regions of higher surface density.

A consequence of an IMF that increases the number of intermediate-mass stars is the birth of more Type Ia SNe progenitors. Type Ia SNe are understood to be associated with binary systems of low- and intermediate-mass stars, in which the mass lost by the more evolved star is accreted by its white dwarf (WD) companion until the WD can no longer be sustained by electron degenerate pressure and a violent explosion ensues. Comparing the thick and thin solid lines in the upper panel of Figure 9.4, it can be seen that the IM-enhanced IMF has no significant affect on the local solar neighbourhood SN Ia rate. In the outer disk, however, the AGB-enhancement elevates the SN Ia rate by up to a factor of six between 0.5–1 Gyr and about a factor two at 3 Gyr before converging with the normal IMF model after ~ 6 Gyr (compare the thick and thin dashed lines). The different impact of the IM-enhanced IMF on the solar and outer radii is due to a faster build-up of metals in the solar radius relative to the outer disk. This causes the IM-bump to decay more quickly and leads to only a minor increase in the SN Ia rate. In contrast, the slower rate of enrichment in the outer radius leads to a longer-lasting IM-bump, which has a significant impact on the SN Ia rate at early times. IM-enhanced IMFs at low metallicity could leave an observable trace on the cosmic SN Ia rate, which could be used to discriminate between these models (Fields et al. 2001).

Type Ia SNe are major producers of iron and are responsible for 1/3–2/3 of the solar Fe content (e.g. Timmes et al. 1995). Thus, any increased incidence of SN Ia leads inevitably to the production of more Fe, as seen in the lower panel of Figure 9.4 where the evolution of $[\text{Fe}/\text{H}]$ is plotted. The inclusion of an enhanced IM AGB population increases the abundance of iron in the ISM of the outer disk by a factor of 2–3 between 1–3 Gyr. Once again, the solar radius is less sensitive to the IM-enhanced IMF because the amplitude of the IM-bump decays on a shorter timescale.

As well as being SN Ia progenitors, AGBs leave behind white dwarf remnants that can be indirectly detected through microlensing experiments. We found that the IM-enhanced IMF increases the present-day number of WD remnants by only about 5% and 10% for the solar and outer radii, respectively. Thus, the number of WDs is not expected to be a sensitive discriminant of the different IMF scenarios. This echos the Galactic halo results of Gibson & Mould (1997) and Fields, Freese, & Graff (2000), who found that stellar C and N abundances provide far stronger

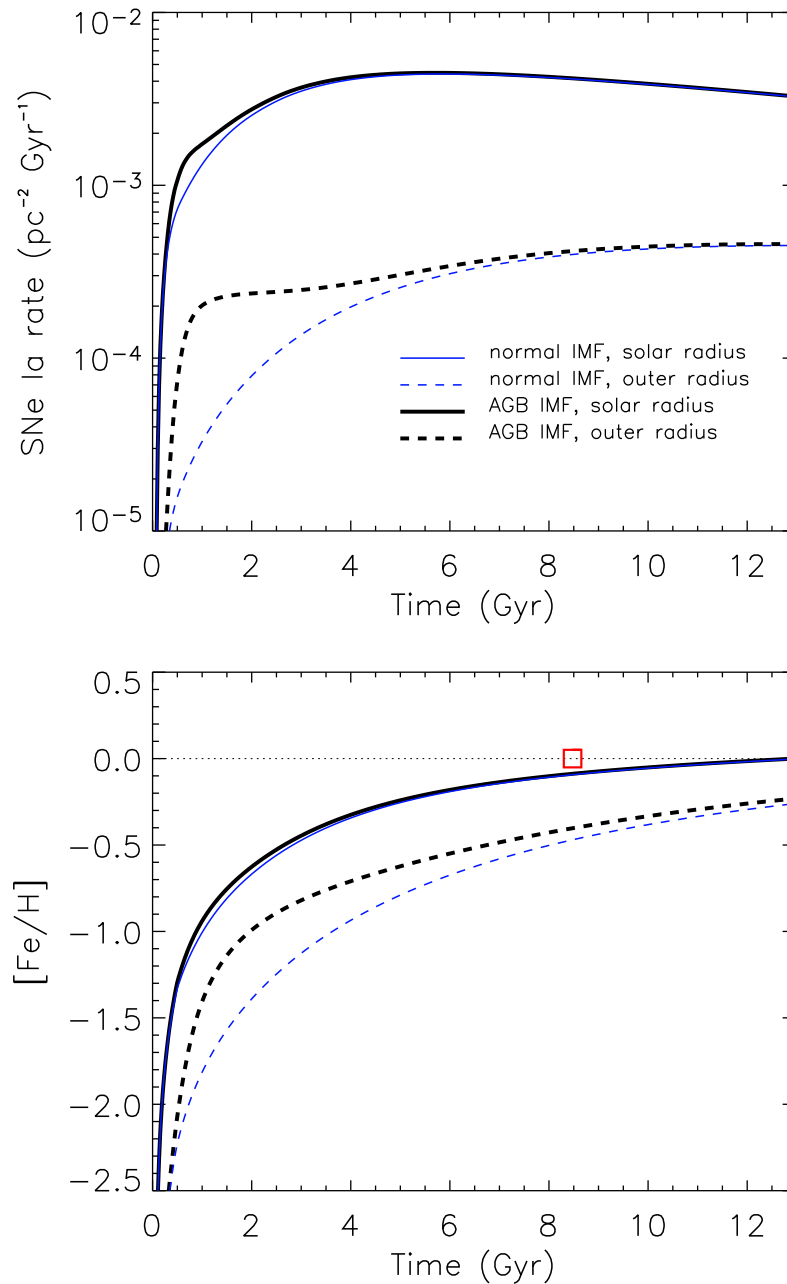


Figure 9.4: **Upper panel:** Type Ia supernovae rate as a function of time for the solar neighbourhood (solid lines) and the outer disk (dashed lines) in the case of a normal IMF (thin lines) versus the IM-enhanced IMF (thick lines). **Lower panel:** Trend of $[\text{Fe}/\text{H}]$ vs time. The square shows the position of the sun, while lines have the same meaning as in the panel above. Due to a faster build-up of metals in the solar radius relative to the outer disk, the IM-bump decays more quickly and leads to only a minor increase in the SN Ia rate and, consequently, the $[\text{Fe}/\text{H}]$ evolution. In contrast, the slower rate of enrichment in the outer radius leads to a longer-lasting IM-bump, which has a significant impact on the SN Ia rate and Fe content at early times.

constraints than WD counts on any enhancement in the number of LIMS at early times.

It should be noted that although AMO04 only predict the evolution at the solar radius, if their IM-enhanced model were applied to the outer disk we expect that they would *not* predict an increase in either the SN Ia rate or [Fe/H] because their SN Ia prescription prohibits the formation of Type Ia SNe in metal-poor environments.

9.4.2 Magnesium isotopic ratio

Figure 9.5 shows the sensitivity of $(^{25}\text{Mg}+^{26}\text{Mg})/^{24}\text{Mg}$ versus [Fe/H] to the choice of IMF for both the solar (8.5 kpc) and outer (16.5 kpc) radius models. Predictions are plotted against abundances observed in nearby dwarf stars by Gay & Lambert (2000; circles) and Yong et al. (2003b; diamonds). It has been suggested that the production of heavy Mg isotopes by IMSs is needed to explain the observations in metal-poor stars (e.g. Timmes et al. 1995; Goswami & Prantzos 2000; Alibés et al. 2001). Indeed, Fenner et al. (2003) found that IMSs were responsible for most of the heavy Mg isotopes in the solar neighbourhood for [Fe/H] < -1. The inclusion of AGB nucleosynthesis within the framework of the standard IMF model provides a good match to both datasets at low [Fe/H], as illustrated by the thin solid line in Figure 9.5. At higher [Fe/H], the normal IMF solar model matches the Gay & Lambert (2000) data but not those of Yong et al. (2003b). We caution that our predictions are best compared against the Gay & Lambert (2000) sample because Yong et al. (2003b) used kinematics to preferentially select halo and thick disk stars. Consequently, their sample contains relatively few thin disk members and perhaps some stars belonging to an accreted component (although inspection of figure 13 from Yong et al. 2003 indicates that the fraction of accreted stars is small if one employs the Gratton et al. 2003 criteria to specify the accreted component). An uncertainty in the ^{25}Mg and ^{26}Mg yields of ± 0.2 dex is illustrated for the IM-enhanced solar radius model by the shaded region in Figure 9.5, and will be discussed further in Section 9.4.6.

Although the mean $(^{25}\text{Mg}+^{26}\text{Mg})/^{24}\text{Mg}$ for all stars with [Fe/H] < -1 is about 0.15, Figure 9.1 demonstrates that a value 5–9 times larger than this is required to explain the $\Delta\alpha/\alpha$ measured by MFW04, under the assumption of a solar $^{25}\text{Mg}:^{26}\text{Mg}$ ratio). AMO04 estimated that a ratio of $(^{25}\text{Mg}+^{26}\text{Mg})/^{24}\text{Mg} = 0.62$ would remove the need for any time-variation in α . This is lower than our calculated value of

1.1 ± 0.3 (see Figure 9.1) because theirs is only a rough approximation and ours is based on the QSO absorption-line spectra. However, to aid comparison, we followed AMO04 in imposing an IM-enhanced IMF capable of elevating $(^{25}\text{Mg}+^{26}\text{Mg})/^{24}\text{Mg}$ to ~ 0.62 for the solar radius model (thick solid line).

The behaviour of the Mg isotopic ratios in our IM-enhanced solar radius model is very similar to AMO04 Model 1, reaching a maximum of $(^{25}\text{Mg}+^{26}\text{Mg})/^{24}\text{Mg} = 0.63$ at $[\text{Fe}/\text{H}] = -1.65$. The prolonged impact of the IM-enhanced IMF in the more metal-poor outer disk leads to a maximum $(^{25}\text{Mg}+^{26}\text{Mg})/^{24}\text{Mg}$ ratio of 0.92 at $[\text{Fe}/\text{H}] = -1.7$. This is seven times higher than the corresponding ratio in the case of the normal IMF. If we assume that (i) the level of AGB stellar enhancement is a function of gas metallicity and declines with the build-up of metals, and (ii) that many QSO absorption systems consist of slowly evolving objects such as dwarfs or outer disks of spirals, then these findings are qualitatively consistent with a scenario in which much higher neutron-rich Mg isotopic abundances are found in QSO absorption systems than in local stars of the same metallicity.

9.4.3 Nitrogen

The types of AGB stars responsible for expelling enough heavy Mg isotopes at early times to explain an apparent variation in α are also thought to be the main factories of primary nitrogen. Thus, an enhanced AGB population should leave a strong imprint on the N abundances in local stars and in DLAs. The predicted variation of $[\text{N}/\alpha]$ with $[\alpha/\text{H}]$ is plotted against DLA measurements in Figure 9.6. The model results are plotted using Si as the reference element, while for the Centuri3n et al. (2003) data, the α -element is O, Si or S. It is reassuring that the normal IMF solar model (thin solid line) passes through the DLA data before rising to roughly solar value. However, no single homogeneous chemical evolution model will account for the broad spread in the DLA data and, worryingly, the outer disk normal IMF model (thin dashed line) overproduces N with respect to the data. Since the normal IMF models (thin lines) already tend to produce more N than is observed in DLAs, it is not surprising that the IM-enhanced IMF models (thick lines) overproduce N by more than an order of magnitude. An indication of the sensitivity of these results to the stellar nucleosynthesis models is given by comparing the thick solid line with the thin dotted line, which corresponds to the IM-enhanced solar radius model in the case of van den Hoek & Groenewegen (1997) IMS yields. Section 9.4.6 describes

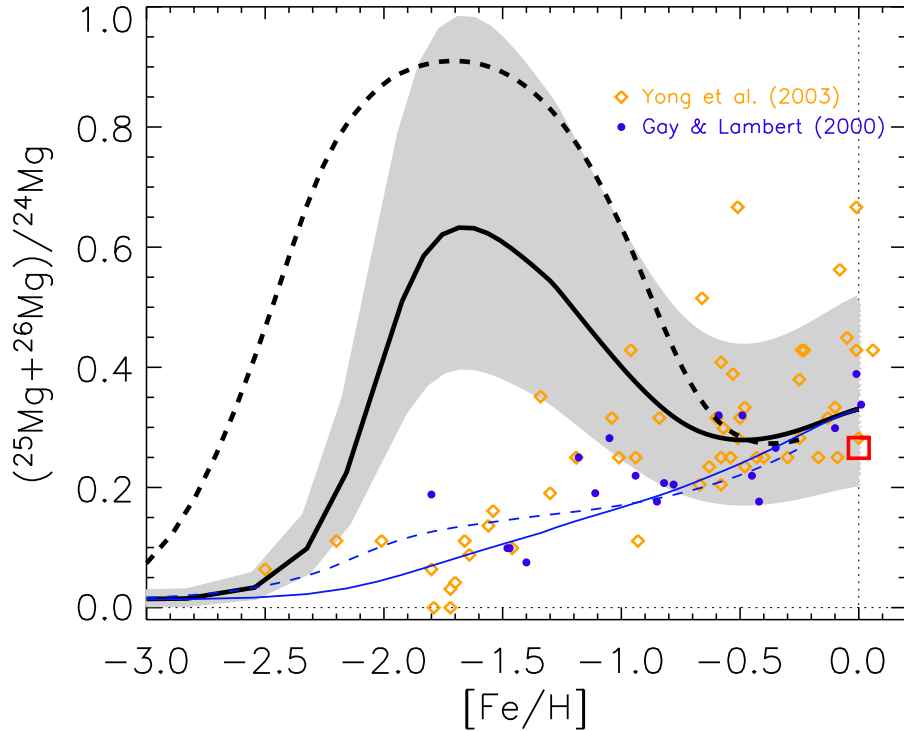


Figure 9.5: Evolution of $(^{25}\text{Mg}+^{26}\text{Mg})/^{24}\text{Mg}$ as a function of $[\text{Fe}/\text{H}]$. As for Figure 9.4, the solid and dashed lines show predictions for the solar radius and outer disk, respectively. Thin lines denote a normal IMF model and thick lines represent the model with an IM-enhanced IMF. Circles and diamonds show stellar data from Gay & Lambert (2000) and Yong et al. (2003b), respectively. The square shows the solar value. The shaded area indicates a ± 0.2 dex uncertainty range for the thick solid line.

the uncertainties in these predictions in greater detail.

Inspection of Figures 9.5 & 9.6 reveals that the empirical constraints imposed by DLA nitrogen abundances are strongly violated by the models capable of producing sufficient $^{25,26}\text{Mg}$ relative to ^{24}Mg to mimic the variation in the α obtained by MFW04. AMO04 encountered the same problem with their Model 1, which they sought to rectify in Model 2 by increasing star formation efficiency (SFE) by a factor of ~ 2.5 . Figure 9.7 shows how our $[\text{N}/\alpha]$ versus $[\alpha/\text{H}]$ varies with a factor of 2.5 increase in SFE. The agreement with the data is improved, but $[\text{N}/\alpha]$ is still too high, except at the lowest metallicities.

The curve corresponding to our increased SFE model in Figure 9.7 is extremely similar to the dot dash line in figure 15 from AMO04. We note that their Models 1 and 2 differ not just in SFE, but in the location, width, amplitude, and decay timescale of the IMF IM-bump. Nevertheless, we wish to point out a troublesome

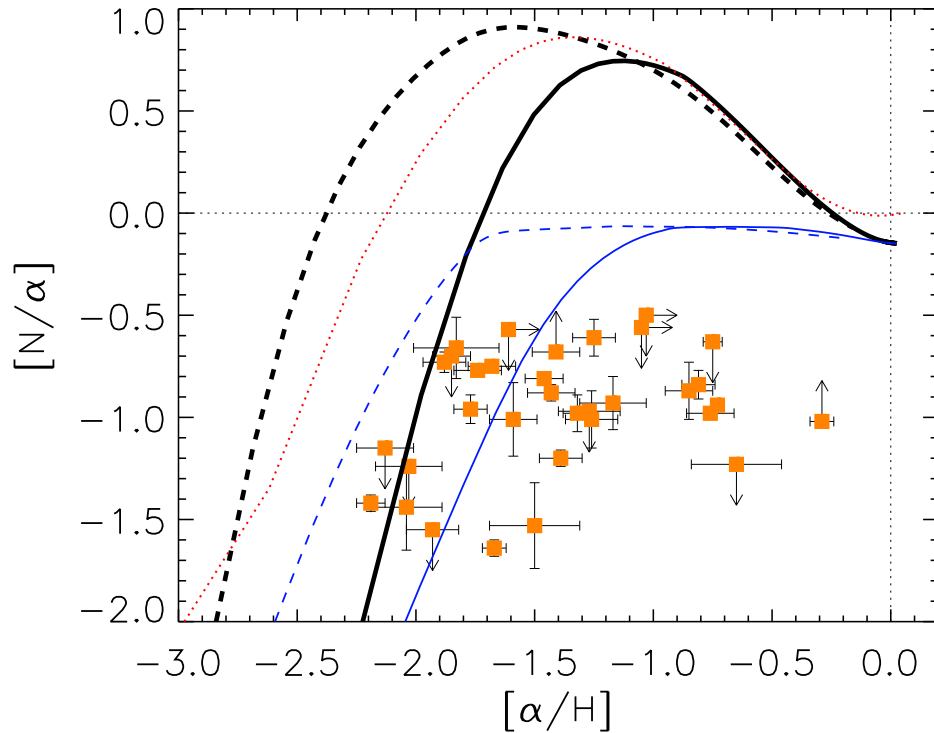


Figure 9.6: Evolution of $[N/\alpha]$ as a function of $[\alpha/H]$. Dashed and solid lines have the same meaning as in Figure 9.4. Model results employ Si as the reference α -element. Data points with limits and error bars show DLA measurements by Centuri3n et al. (2003), where the α -element is either O, Si, or S. The thin dotted line shows the IM-enhanced solar Galactocentric radius model in the case of van den Hoek & Groenewegen (1997) IMS yields rather than Karakas & Lattanzio (2003), to give an indication of the uncertainties associated with N production in the stellar models.

consequence of such an increase in SFE that is robust to those differences. Figure 9.8 shows the present-day gas surface density profile expected in the case of normal or enhanced SFE. The standard model agrees with the data from Dame (1993) to within a factor of two. However, a factor of 2.5 increase in the SFE leads to severe gas depletion, in conflict with the observations. While the chemical evolution model that applies to quasar absorption systems need not satisfy the empirical constraints from the Milky Way, we caution that increasing star formation efficiency in order to alleviate overproduction of N might not be appropriate given the gas-rich nature of many absorption systems.

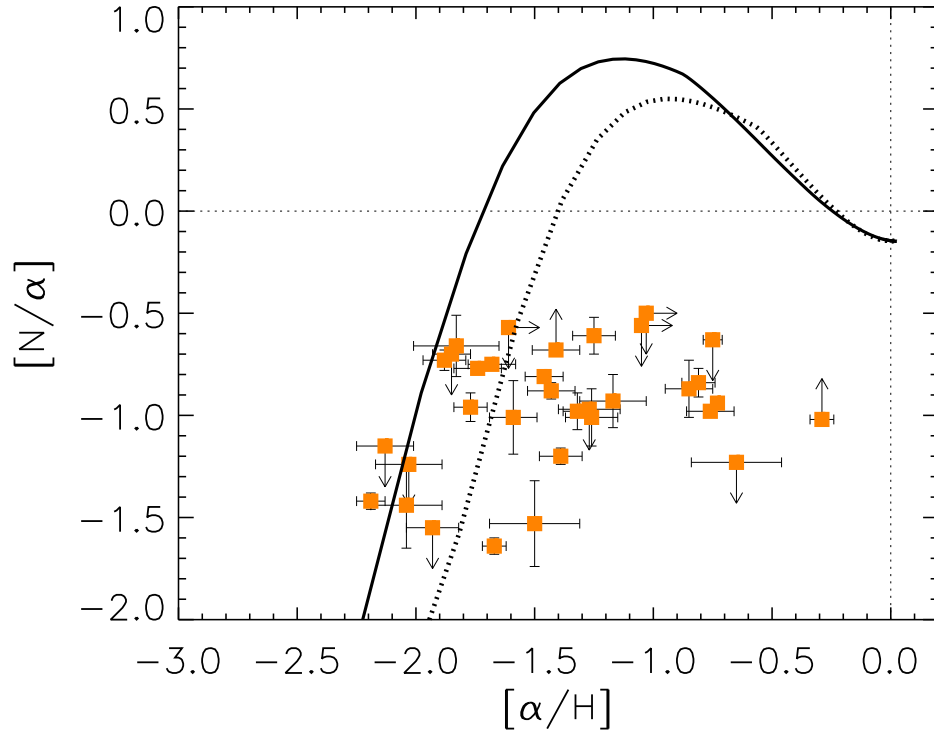


Figure 9.7: Sensitivity of $[N/\alpha]$ vs $[\alpha/H]$ to the star formation efficiency. The solid line represents the IM-enhanced solar radius model, as seen in Figure 9.6. The dotted line shows the effect of increasing star formation (SF) efficiency by a factor of 2.5. Increased SF efficiency improves the agreement with the DLA data (symbols), but still overproduces N at $[\alpha/H] \sim -1$.

9.4.4 $^{13}\text{C}/^{12}\text{C}$ abundance ratio

Along with any significant contribution to the abundance of N and the heavy Mg isotopes in metal-poor environments, low- and intermediate-mass stars should leave an additional observable chemical signature in the form of high ^{13}C abundance relative to ^{12}C . Metal-poor AGB stars with mass $\sim 4 M_{\odot}$ are a major source of ^{13}C , produced during hot bottom burning when the CN cycle converts ^{12}C into ^{13}C . Since the important factories of ^{12}C are less massive $2\text{--}3 M_{\odot}$ stars, the $^{13}\text{C}/^{12}\text{C}$ ratio in the ejecta of IMSs is strongly mass-dependent, peaking sharply between 4 to $5 M_{\odot}$. Figure 9.9 shows the predicted evolution of $^{13}\text{C}/^{12}\text{C}$ as a function of $[\text{Fe}/\text{H}]$. For both the solar and outer radii models, the introduction of an IM-enhanced IMF increases the $^{13}\text{C}/^{12}\text{C}$ ratio 4–6-fold in the metallicity range corresponding to the greatest enhancement of the heavy Mg isotopes. To estimate the uncertainty in these results due to the stellar yields, we also ran identical models using the LIMS

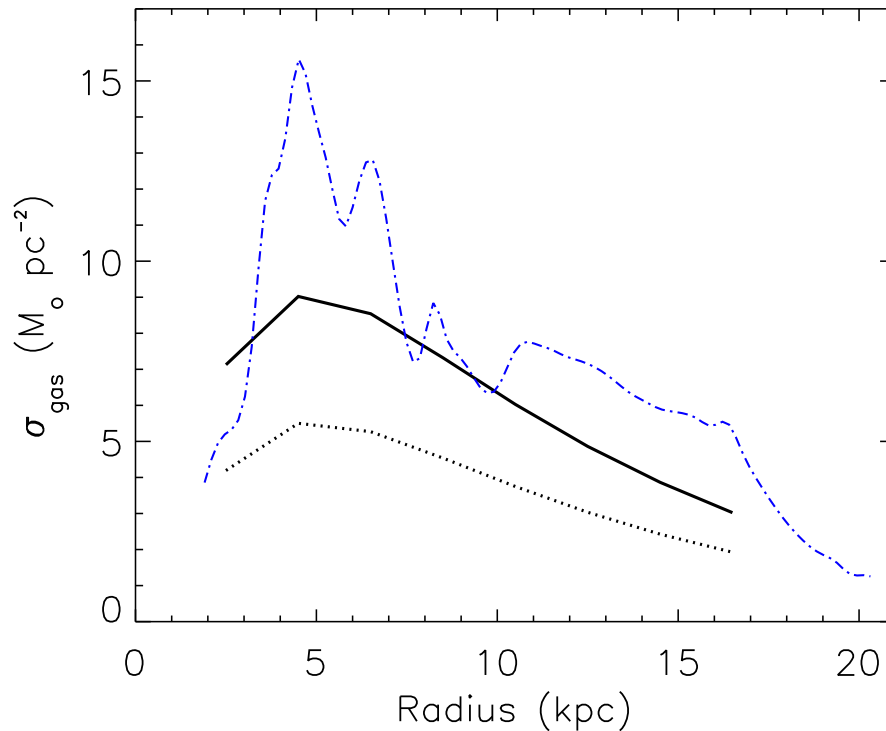


Figure 9.8: Present-day gas surface density profile. The dotted line presents the result for the model with star formation efficiency increased by a factor of 2.5 with respect to the standard model (solid line). The dot-dashed line corresponds to data from Dame (1993) based on observations of atomic and molecular hydrogen. The standard model replicates the observations to within a factor of two, whereas increased star formation efficiency leads to excess depletion of interstellar gas.

yields from van den Hoek & Groenewegen (1997) and Marigo (2001), depicted with thin dotted and dot-dashed lines, respectively. High values of $^{13}\text{C}/^{12}\text{C}$ may conflict with the symmetry of C IV line profiles observed in some QSO absorbers and could impose a further constraint on the shape of the IMF at early times. This will be discussed in more detail in Section 9.6.

9.4.5 Silicon, aluminium and phosphorus

Since transitions from Si are important anchor lines in the many-multiplet method, we show the predicted behaviour of $(^{29}\text{Si}+^{30}\text{Si})/^{28}\text{Si}$ as a function $[\text{Fe}/\text{H}]$ in Figure 9.10. The relative abundance of Si isotopes is not affected by an enhanced early population of AGB stars to the extent of N and the heavy Mg and C isotopes. Indeed, $(^{29}\text{Si}+^{30}\text{Si})/^{28}\text{Si}$ remains well below the solar value (open square) for both the

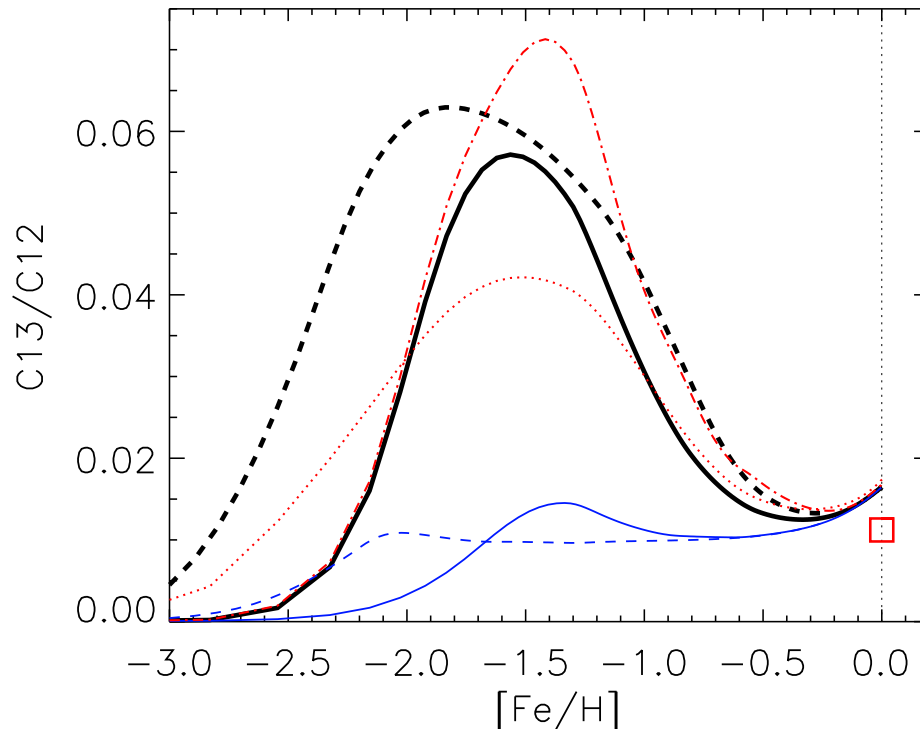


Figure 9.9: Evolution of $^{13}\text{C}/^{12}\text{C}$ as a function of $[\text{Fe}/\text{H}]$. Symbols and lines have the same meaning as in Figure 9.4. The thin dotted and dot-dashed lines show the IM-enhanced solar radius model in the case of van den Hoek & Groenewegen (1997) and Marigo (2001) IMS yields, respectively.

local and outer disk models (thick lines). Nevertheless, the $\Delta\alpha/\alpha$ measured in high- z_{abs} QSO absorption systems is largely independent of the Si isotopic composition, as highlighted in Section 9.1.2. Thus, even a dramatic elevation in $(^{29}\text{Si}+^{30}\text{Si})/^{28}\text{Si}$ due to AGB stars would not account for the high-redshift results from MFW04.

Aluminium is another element whose production by AGB stars is expected to be important (e.g. Karakas & Lattanzio 2003). The synthesis of Al via the Mg-Al chain is particularly efficient in metal-poor 4–6 M_{\odot} stars. The evolution of $[\text{Al}/\text{Fe}]$ with $[\text{Fe}/\text{H}]$ in the ISM is depicted in Figure 9.11. Observations of Al in both DLAs (solid squares) and nearby stars (circles and open squares) covering a wide range of metallicities make this element a potentially useful discriminant of the different IMF models. Unfortunately, most of the DLA measurements are lower limits, owing to line saturation (Prochaska & Wolfe 2002). The normal IMF models (thin lines) pass through the lowermost DLA *detections*, but only the IM-enhanced IMF models (thick lines) can satisfy the highest DLA upper limits. The power of Al to constrain

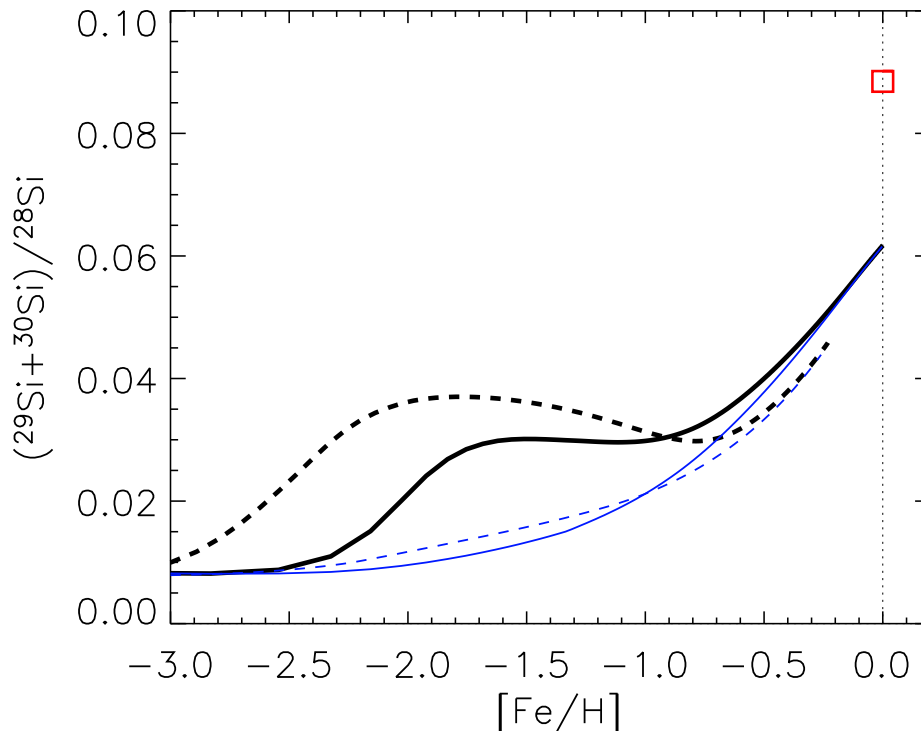


Figure 9.10: Evolution of $(^{29}\text{Si}+^{30}\text{Si})/^{28}\text{Si}$ as a function of $[\text{Fe}/\text{H}]$. Symbols and lines have the same meaning as in Figure 9.4.

the shape of the early IMF is diminished by the inability of either solar radius model to match the stellar observations at high and low metallicity. The overproduction of Al with respect to metal-poor halo stars and the underproduction relative to thin-disk stars is a problem of standard Galactic chemical evolution models that has been noted by other authors (e.g. Timmes et al. 1995; Alibés et al. 2001). However, we note that local thermodynamic equilibrium (LTE) calculations underestimate the Al abundance in metal-poor stars. The open squares in Figure 9.11 would be about 0.6 dex higher if non-LTE effects were included (e.g. Gehren et al. 2004).

The production of phosphorus from IMs leads to a ~ 0.5 dex increase in $[\text{P}/\text{Fe}]$ when the IM-bump is added to the standard IMF, as shown in Figure 9.12. Stars in the $4\text{--}6 M_{\odot}$ mass range are the chief culprits for the additional ^{31}P , which is understood to be generated through neutron-capture onto Si followed by β -decay to ^{31}P (J. Lattanzio, private communication). As is the case for Al, the difference between the two IMF models is significant, but the DLA measurements do not allow the elimination of either scenario. In the case of P, the DLA data are very scant

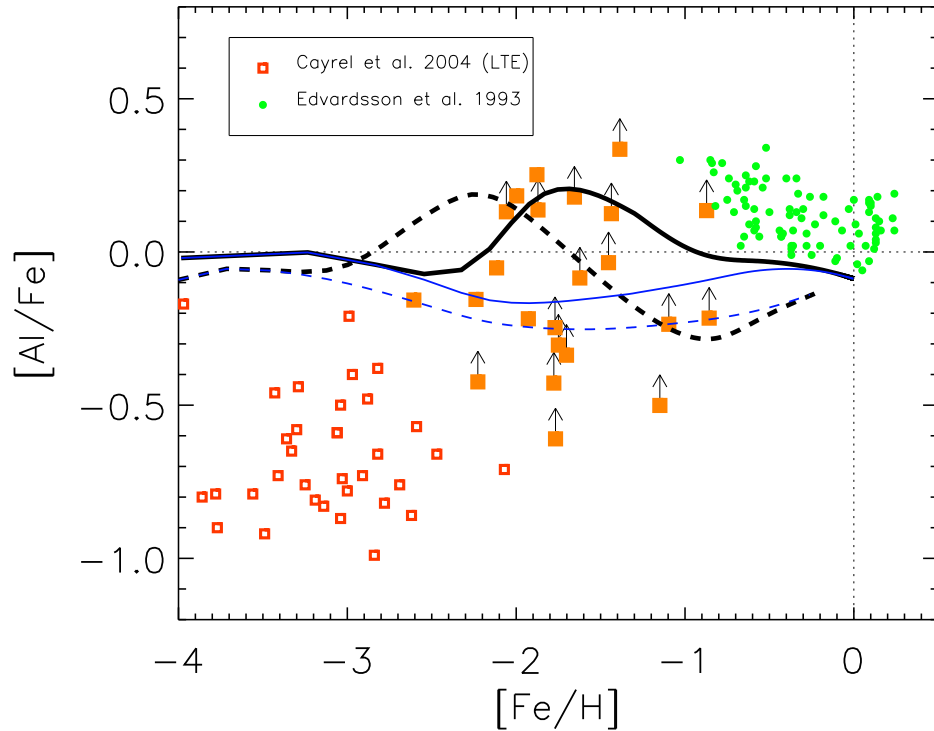


Figure 9.11: Variation of $[Al/Fe]$ as a function of $[Fe/H]$. Dashed and solid lines have the same meaning as in Figure 9.4. DLA measurements from Prochaska et al. are plotted with solid square symbols, while circles and open squares show stellar observations from Edvardsson et al. (1993) and Cayrel et al. (2004), respectively.

and consists mostly of upper limits since the P II line is often blended in the Ly α forest (Dessauges-Zavadsky et al. 2004). Nevertheless, we present our predictions for Al and P in the event that the growing collection of DLA measurements may eventually provide a more stringent test of the models presented in this chapter.

9.4.6 Uncertainties

Magnesium

Denissenkov & Herwig (2003) and Denissenkov & Weiss (2004) showed that the production of ^{25}Mg and ^{26}Mg in a typical $5 M_{\odot}$ AGB star is fairly robust to the number of thermal-pulses, the HBB temperature, and the third dredge-up efficiency. The final envelope abundance of ^{25}Mg and ^{26}Mg in their series of models agreed within ~ 0.1 dex and ~ 0.2 dex, respectively. Fenner et al. (2004) estimated the sensitivity of the AGB yields of ^{25}Mg and ^{26}Mg to the mass-loss prescription, finding

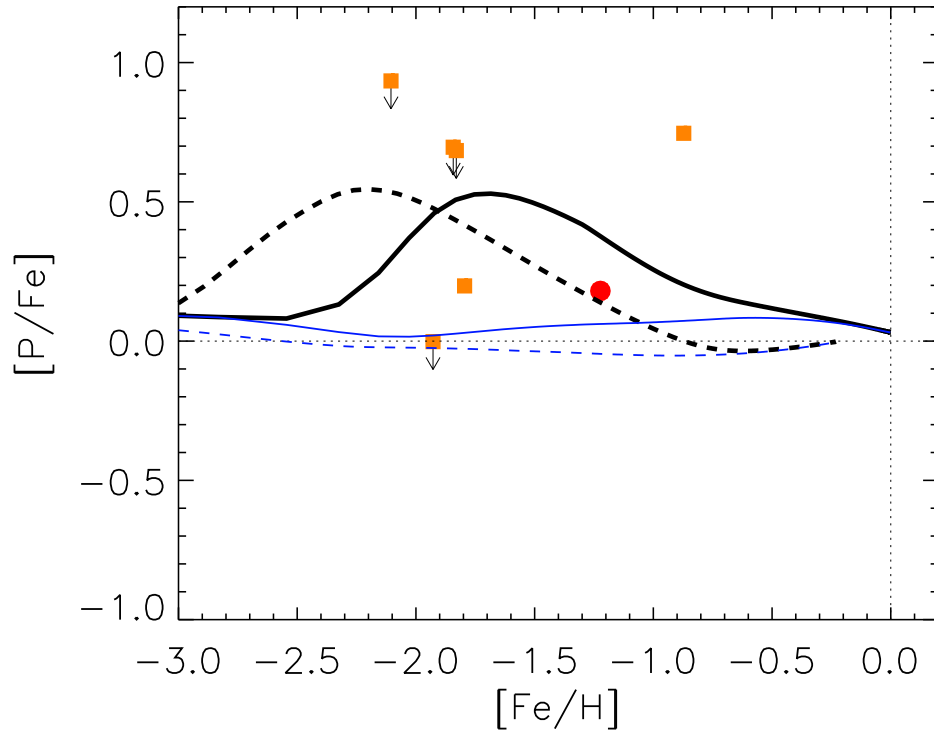


Figure 9.12: Variation of $[P/Fe]$ as a function of $[Fe/H]$. Dashed and solid lines have the same meaning as in Figure 9.4. DLA measurements from Prochaska et al. are plotted with square symbols, while the circle is from Outram, Chaffee, & Carswell (1999).

them reduced by ~ 0.2 dex when the Vassiliadis & Wood (1993) mass-loss law was replaced with a steadier rate from Reimers (1975) (with $\eta = 3.5$ on the AGB). The treatment of convection in AGB models has recently been investigated by Ventura (2004), who found that the yields were very sensitive to the adoption of standard mixing length theory (MLT) versus the full spectrum of turbulence (FST) model. The latter case results in greater mass-loss rates, shorter AGB lifetimes, less third dredge-up, and reduced yields of heavy elements including CNO and the Mg isotopes. The FST model faces serious hurdles of its own, since it predicts a deficit of Na in AGB ejecta and a *positive* O-Na correlation: at odds with observations of globular cluster stars believed to be polluted by AGBs (Ventura, D'Antona, & Mazzitelli 2004).

A further uncertainty relates to the presence of a ^{13}C pocket, which is neglected in the AGB models implemented in this study. One might expect that the inclusion of this additional source of neutrons would increase the production of ^{25}Mg and ^{26}Mg . However the impact of a ^{13}C pocket on nucleosynthesis in metal-poor IMS should be

marginal in comparison to the effects of HBB (M. Lugaro, *private communication*). Despite these unknowns, the ability of our standard Galactic chemical evolution model to reproduce the Mg isotopic ratios in metal-poor stars by adding in the Karakas & Lattanzio (2003) yields, suggests that their Mg predictions are reasonably accurate.

The total production of $^{25,26}\text{Mg}$ with respect to ^{24}Mg from Type II SNe is uncertain to a similar degree due to internal uncertainties in the stellar models as well as sensitivity to the shape and upper mass limit of the IMF. Fenner et al. (2003) found that a Salpeter (1955) IMF leads to 50 per cent higher present-day $^{26}\text{Mg}/^{24}\text{Mg}$ ratio than in the case of a Kroupa et al. (1993) function, because the Salpeter law gives rise to a greater fraction of massive stars (see their figures 5 and 6). The shaded region in Figure 9.5 indicates the ± 0.2 dex uncertainty in the results due to errors in both the AGB and SN II contribution.

Nitrogen and $^{13}\text{C}/^{12}\text{C}$

To estimate the uncertainty in the predicted evolution of N and the $^{13}\text{C}/^{12}\text{C}$ ratio, we ran identical models using two alternative sets of IMS yields: those of van den Hoek & Groenewegen (1997) and Marigo (2001). The Marigo yields for N were in close agreement with those of Karakas & Lattanzio (2003) while the implementation of the van den Hoek & Groenewegen (1997) yields produced even more N. The dotted line in Figure 9.6 displays the results from an IM-enhanced solar radius model using the van den Hoek & Groenewegen (1997) yields in place of Karakas et al. (i.e. compare dotted with thick solid curve). It is clear that the problem of excess nitrogen is further exacerbated in this case.

The dotted and dot-dashed lines in Figure 9.9 show the behaviour of $^{13}\text{C}/^{12}\text{C}$ assuming van den Hoek & Groenewegen (1997) and Marigo (2001) IMS yields, respectively. The Marigo yields generate the highest $^{13}\text{C}/^{12}\text{C}$ peak [with $(^{13}\text{C}/^{12}\text{C})_{max} = 0.073$] and those of van den Hoek & Groenewegen (1997) the lowest [with $(^{13}\text{C}/^{12}\text{C})_{max} = 0.042$]. The region encompassed by these two extreme models is indicative of the level of uncertainty afflicting the models.

9.5 Discussion

9.5.1 Summary of Results

Murphy et al. (2001b) pointed out that $\Delta\alpha/\alpha$ measurements are sensitive to the isotopic composition of Mg in the gas-phase of the low- z absorbers used in varying- α studies. Standard models of chemical evolution predict that the abundance of the neutron-rich isotopes of Mg relative to ^{24}Mg decreases with lookback time, making the MFW04 $\Delta\alpha/\alpha$ result even more significant. However, AMO04 demonstrated that a sufficiently enhanced early population of intermediate-mass stars can raise $(^{25}\text{Mg}+^{26}\text{Mg})/^{24}\text{Mg}$ to the supersolar levels needed to render the MFW04 $\Delta\alpha/\alpha$ result null.

A major problem with this scenario is the almost inevitable overproduction of N when compared against the DLA data (Figure 9.6). This is because the AGB stars responsible for significant $^{25,26}\text{Mg}$ production are also important sources of N. There are various ways to reconcile an IM-enhanced IMF with the low N abundances in DLAs, but none are entirely satisfactory. For instance, since nucleosynthesis within very metal-poor IMSs is not well understood, the theoretical N yields may be overestimated. However, in this case, it would be difficult to explain the high N abundance found in some of the most iron-depleted stars in our galaxy (e.g. Norris, Beers & Ryan 2000; Christlieb et al. 2004). Another way to mitigate the problem of excess $[\text{N}/\alpha]$ is through increased star formation efficiency, however this leads to severe gas depletion that may be inconsistent with the gas-rich nature of DLAs (Figure 9.8). Finally, the history of many DLAs may be marked by periods of supernova-driven outflows, but it is not clear how such galactic winds could preferentially remove N but not the heavy Mg isotopes. Thus, the observed N abundance in QSO absorbers still stands as a robust test of a putative IM-enhanced early IMF.

The enhanced $^{13}\text{C}/^{12}\text{C}$ ratio predicted by these types of chemical evolution models (Figure 9.9) holds promise as a future probe of the AGB contribution to QSO absorption line abundances. Carlsson et al. (1995) has calculated the isotopic shifts in the ubiquitous C IV $\lambda 1548/1550$ alkali doublet, finding the ^{14}C line to lie $\Delta v = 10.3 \text{ km s}^{-1}$ to the blue of the ^{12}C line. Recent calculations by Berengut et al. (in preparation) confirm these large shifts to within 1 per cent precision and show the ^{13}C - ^{12}C separation to be $\Delta v = 5.5 \text{ km s}^{-1}$. Enhancements as large as

$^{13}\text{C}/^{12}\text{C} \approx 0.1$ may already be ruled out by the symmetric C IV line profiles observed in $R \gtrsim 45\,000$ (FWHM $\lesssim 6.7\text{ km s}^{-1}$) spectra of highly ionized QSO absorbers with simple velocity structure (e.g. Petitjean & Aracil, 2004). However, placing limits at lower ^{13}C abundances may be unconvincing unless the laboratory wavelengths of the C IV doublet transitions can be measured with better precision than 0.4 km s^{-1} (Griesmann & Kling, 2000). If the calculated isotopic separations for transitions of other C species (e.g. C I and C II) prove to be as large as those for C IV, they may provide a more reliable probe of the $^{13}\text{C}/^{12}\text{C}$ ratio in gas more closely related to DLAs and, therefore, the chemical evolution models presented here.

Given that many QSO absorbers are thought to probe slowly evolving systems such as dwarf galaxies and the outer regions of galactic disks, we simulated chemical evolution at large galactocentric radii, where metal-enrichment is more gradual. We found that the chemical signature from an enhanced IMS population at low metallicities was more pronounced in the outer disk, with respect to the solar neighbourhood. This follows directly from the assumed metallicity-dependence of the IMS enhancement. Thus, our IM-enhanced models predict that systems with the slowest build-up of metals will bear the strongest signature of AGB-pollution.

The chemical abundance constraints imposed by QSO absorption systems do not support excess numbers of AGB stars being formed in the types of systems from which MFW04 derived a varying α . Moreover, a significantly enhanced AGB population in the local Galaxy is ruled out by the sub-solar ratios of the neutron-rich Mg isotopes to ^{24}Mg in nearby metal-poor stars. We now summarise other arguments for and against the IMF having a non-standard shape in the early universe.

9.5.2 Other arguments for and against an early, IM-enhanced IMF

Observations of deuterium, carbon and nitrogen

Motivated by the large observed scatter and possible trends with metallicity of local and high- z_{abs} D abundance determinations, Fields et al. (2001) and Prantzos & Ishimaru (2001) speculated that D could be destroyed within stars without an accompanying increase in metals, provided that: (i) the earliest populations of stars were strongly enhanced in IMSs, and (ii) zero-metallicity IMSs do not release their synthesized C and N. Prantzos & Ishimaru (2001) emphasize that if the second

provision is not met, C and N abundances should be highly enhanced in high- z_{abs} systems if their D has been depleted through astration alone. They note that this is inconsistent with the DLA data. Indeed, based on the N/α trend in DLAs, Prochaska et al. (2002) presented a case for a top-heavy IMF, with the birth of IMSs actually *suppressed* in many QSO absorption systems.

The abundance of C and N in Galactic stars and DLAs provides one of the strongest constraints on any enhancement in the population of LIMS in the early Galaxy (Gibson & Mould 1997; Fields, Freese, & Graff 2000). However, this is contingent upon how much C and N is released by extremely metal-poor IMSs. Fujimoto et al. (2000) provide evidence favouring the suppression of C and N yields from zero-metallicity IMSs, whereas Chieffi et al. (2001) reach the opposite conclusion. Abia et al. (2001) propose that an early IMF peaked between $3 - 8 M_{\odot}$ helps explain the presence of metal-poor Galactic stars with enhanced C and N abundances, presuming that LIMS release C and N in large quantities. Thus, the stellar models do not offer a cohesive picture of the level of C and N enrichment from metal-poor LIMS, nor do observations of DLAs and metal-poor stars clarify the situation. However, if AGBs are responsible for $^{25,26}\text{Mg}$ enhancements large enough to mimic a varying α in the redshift range $0.5 \lesssim z_{\text{abs}} \lesssim 1.8$, they will tend to have had a much higher initial metallicity than primordial. Thus, their yields are not subject to the very large uncertainties afflicting zero-metallicity models.

White dwarfs

Evidence from microlensing surveys initially led to speculation that white dwarf remnants contribute up to half of the mass of the Milky Way halo (e.g. Bennett et al. 1996; Alcock et al. 1995). Populating the halo with such a large fraction of white dwarfs requires the early IMF to be heavily biased toward stars with initial mass in the range $1-8 M_{\odot}$. Adams & Laughlin (1996) constructed IMFs capable of producing a white-dwarf dominated halo, and AMO04 adopted IMF parameters that were consistent with their deduced constraints. However, the white dwarf contribution to the dynamical mass of the Galactic halo has since been drastically revised downwards to less than a few percent (Gibson & Mould 1997; Flynn, Holopainen & Holmberg 2003; Garcia-Berro et al. 2004; Lee et al. 2004), obviating the need to invoke non-standard IMFs.

Theoretical star formation

Theoretical models of star formation suggest that the IMF of primordial gas would be biased toward higher mass stars (e.g. Abel, Bryan & Norman 2000; Kroupa 2001; Hernandez & Ferrara 2001; Mackey, Bromm & Hernquist 2003; Clarke & Bromm 2003). This is due to diminished cooling efficiency in metal-poor gas. However, recent hydrodynamical simulations of the collapse and fragmentation of primordial gas have predicted bimodal primordial IMFs with peaks at about 100 and 1 M_{\odot} (Nakamura & Umemura 2001) and 30 and 0.3 M_{\odot} (Omukai & Yoshii 2003).

Extragalactic observations

Empirical support exists for an early IMF skewed toward high stellar masses in extragalactic environments. For instance, to explain the high metal content of the intra-cluster medium various top-heavy IMFs have been proposed (e.g. Gibson & Matteucci 1997; Elbaz, Arnaud & Vangioni-Flam 1995). The photometric properties of ellipticals have also been well-explained assuming a top-heavy IMF (Arimoto & Yoshii 1987). AMO04 note that their model is not inconsistent with the notion of a very early population of very massive stars that enrich the ISM to $Z \sim 10^{-3}$.

In light of the uncertainties besetting theoretical simulations of star formation and the interpretation of extragalactic photometric data, careful analysis of the nucleosynthetic enrichment patterns of QSO absorption systems may be a vital step in deciphering the shape of the IMF in different astrophysical environments.

9.6 Conclusions

An early IMF heavily biased towards intermediate-mass stars is a potential explanation of the α -variation apparent in Keck/HIRES QSO spectra. During their AGB phase these stars produce large quantities of $^{25,26}\text{Mg}$ which later pollute QSO absorption systems at $z_{\text{abs}} \lesssim 1.8$, causing an apparent shift in the Mg absorption lines and a spurious $\Delta\alpha/\alpha < 0$. However, such a strong contribution from AGBs should be evident in the detailed abundance patterns obtained in a growing number of DLAs. Using chemical evolution models of a Milky Way-like spiral galaxy at different radii, we have tested the idea that AGB stars were more prevalent in the metal-poor Universe. The predicted chemical ramifications of an enhanced AGB population are not supported by the available data, with the strongest argument

against severe AGB pollution coming from the low $[N/\alpha]$ values observed in DLAs. Contrary to the conclusions of AMO04, we do not find consistent model parameters which simultaneously explain the Keck/HIRES varying- α and abundance data. We also contend that a variety of other arguments for invoking an IM-enhanced IMF are, at best, unclear. Future measurements of (or limits on) the $^{13}\text{C}/^{12}\text{C}$ ratio from line-profile asymmetries and further DLA observations of other elements synthesised by AGB stars, such as Al and P, may provide additional constraints on the IMF's shape at early epochs.

The sensitivity of low- z Mg/Fe $\Delta\alpha/\alpha$ measurements to isotopic abundance variations in Mg (Figure 9.1) and the clear link to the nucleosynthetic history of QSO absorbers demonstrates the importance of careful $\Delta\alpha/\alpha$ measurements, even in the absence of real variations in α . If $\Delta\alpha/\alpha$ is measured to be zero in $z_{\text{abs}} \lesssim 1.8$ absorbers via independent means (e.g. by combining H I 21-cm and molecular absorption lines; Darling, 2003) then future samples of Mg/Fe absorbers might reveal Mg isotopic abundance variations in two ways: (i) through the bulk relative line shifts between Mg and Fe transitions studied previously and, (ii) if we assume that AGB pollution of the absorbers is not uniform, through an increased scatter in the line shifts. Note that no increased scatter is observed in the current HIRES or UVES samples (MFW04; Chand et al. 2004a).

Chapter 10

Conclusions

10.1 Summary

Since each chapter ends with a detailed conclusion, I summarise here the general outcomes of this thesis.

- *Milky Way Model successes:* We have demonstrated the efficacy of Galactic chemical evolution models in accounting for the general behaviour of elements and isotopes in Milky Way stars. In Chapter 3 it was shown that a well-calibrated chemical evolution model can provide insight into the formation history of a galaxy and help constrain the nature of the accretion episodes fueling Galactic star formation.
- *Importance of intermediate-mass stars:* The contribution from intermediate-mass stars (IMS) on the asymptotic giant branch (AGB) to the chemical enrichment of the interstellar medium has long been appreciated, but owing to a lack of self-consistent grids of non-parametric stellar models for low- and intermediate-mass stars (LIMS), there have been few quantitative studies of their impact on elemental and isotopic abundances beyond C, N and O. Motivated by the inability of Galactic chemical evolution models to recover all the observed elemental and isotopic distributions, we have revisited the relevant stellar and Galactic models in an effort to resolve these long-standing discrepancies. To this end, we are fortunate to have access to a new physically self-consistent suite of stellar models covering an extensive mass and metallicity range generated by A. Karakas, S. Campbell & J. Lattanzio using the Mount Stromlo Stellar Structure code. In Chapter 4 we demonstrated that dis-

crepancies between model predictions and observed stellar Mg isotopic abundances can be resolved by including the new intermediate-mass stellar yields. In Chapter 6 we explored whether IMS pollution can explain the mysterious abundances observed in Galactic globular clusters. Although the current theories of IMS nucleosynthesis are unable to account for all the data, hope is not yet lost for the IMS-pollution model. Indeed, the globular cluster abundance anomalies may help refine the nucleosynthetic models. In Chapter 9, we examined the expected chemical signature from an enhanced early population of IMS on QSO absorbers. The abundance of chemical species such as the heavy C and Mg isotopes, N, Al, and P in absorption systems were shown to place constraints on the preponderance of IMS in metal-poor environments.

- *Nucleosynthesis in distant QSO absorbers:* Chapters 8 and 9 highlighted how DLAs and other QSO absorption systems represent new avenues for exploring early nucleosynthesis and galaxy evolution. In particular, we firstly investigated chemical evolution in the young universe by analysing the detailed enrichment pattern of a high- z metal-rich galaxy in Chapter 8. Given a strict upper age of ~ 2.5 Gyr and a gas-phase metallicity about one third solar, we showed the DLA abundance pattern to be consistent with a scenario in which the interstellar enrichment is dominated by massive stars with a moderate contribution from Type Ia supernovae. Discrepancies between the empirical data and the models were used to highlight outstanding issues in nucleosynthesis theory, including a tendency for Type II supernovae models to overestimate the magnitude of the “odd-even” effect at subsolar metallicities. Then in Chapter 9, we constructed models capable of partially explaining recent Keck/HIRES evidence for a varying α in $z_{\text{abs}} < 2$ absorption clouds, using enhanced populations of intermediate-mass stars at low metallicities. We demonstrated that such models over-produce N, violating observed abundance trends in high- z_{abs} damped Lyman- α systems (DLAs), and also elevate the abundance of Si, Al and P. We found that the $^{13}\text{C}/^{12}\text{C}$ ratio, as measured in absorption systems, could constitute a future diagnostic of non-standard models of the high-redshift IMF.

10.2 Future directions

The current work can naturally be extended in many directions. Below I outline just some of the proposed future investigations that follow-on from the work presented in this thesis.

- *Intermediate-mass stars and neutron-capture elements:* Because certain rare isotopes and heavy *s*-process elements originate in IMS of characteristic mass, metallicity and lifetime, the distribution of these chemical species contains supplementary information to help constrain formation histories. Indeed, IMS may be missing pieces of the puzzle that allow us to make sense of the detailed abundance patterns now being obtained in local and extragalactic stars and in distant gas clouds. This thesis presented preliminary results from an ambitious program incorporating a detailed suite of low- and intermediate-mass stellar models within chemical evolution simulations. We highlighted specific examples for which the new LIMS yields have led to interesting new insights into the distribution of elemental and isotopic abundances. We will continue pursuing this line of research, focusing on the interpretation of the growing database of neutron-capture elements. Nucleosynthetic predictions calculated by M. Lugaro and R. Gallino for the heavy neutron-capture elements from IMS have recently been incorporated into `GEtool`, enabling the study of an even wider range of astrophysical problems. For instance, evidence is emerging for high abundances of Pb in some DLAs. Since Pb is believed to originate primarily in low-mass metal-poor stars with relatively long lifetimes, the presence of Pb can place limits on the age of DLAs.
- *Inhomogeneous chemical evolution:* The models presented in this thesis were based on the assumption that stellar nuclear debris is instantaneously and uniformly mixed into the surrounding gas. It is perhaps surprising that homogeneous models can reproduce the mean abundance trends in the Milky Way. They owe their success to the “smoothing” of the distribution of the elements that naturally occurs over time, as the ISM abundance pattern is set by the integrated effects of multiple generations of stars. Nevertheless, when one probes further back in time, the homogeneous approximation begins to break down, as revealed by increasing scatter in abundance ratios with decreasing metallicity. The most metal-deficient stars are believed to be composed of

material that was polluted by just one or two stars. By their nature, homogeneous models are not equipped to interpret the very low-metallicity data – to do so, one must carefully consider the way SN products are dispersed and the mechanisms triggering star formation. Curiously, metal-poor stars exhibit considerable star-to-star scatter in heavy neutron-capture elements (e.g. Sneden & Cowan 2003), yet appear remarkably uniform in $[\text{Mg}/\text{Fe}]$ (Arnone et al. 2004). A major challenge for any inhomogeneous chemical evolution model will be to simultaneously account for these observations.

- *Dwarf galaxy chemical evolution with feedback:* Theoretical studies of the chemical evolution of *spiral* galaxies have a rich history, having benefited enormously from the wealth of data of our own Milky Way. The chemical evolution of *dwarf* galaxies is less certain. Unlike spiral galaxies, their low mass makes them more vulnerable to feedback from starbursts and SNe. Hydrodynamical simulations find that the amount of gas and metals escaping from dwarf galaxies is strongly dependent on the depth of the dark matter dominated potential well, star formation history, merger history, and ram-pressure stripping (e.g. Marcolini et al. 2004; Fujita et al. 2004). `GETool` will be modified to enable the simulation of dwarf galaxies, including a sophisticated treatment of galactic winds that permits preferential loss of metals from different types of SNe. The theoretical models will be compared against observational yardsticks such as: star formation histories of neighbouring dwarf galaxies inferred from colour-magnitude-diagrams (Tolstoy 2003); emission-lines in local starbursts revealing stellar and SN feedback effects (Calzetti et al. 2004); and the detailed chemical abundance patterns of individual stars in nearby dwarf galaxies (Shetrone et al. 2003).
- *Cosmic Chemical Evolution and the Galaxy/IGM connection:* Structure formation, the birth of stars, and feedback from SNe are intimately connected with the chemical evolution of galaxies and the intergalactic medium (IGM). The IGM contains the material that seeds galaxy formation, while star formation within these galaxies affects the IGM through chemical, radiative and mechanical feedback. The precise details of these interactions are poorly known, however, as most of this activity occurred at high redshifts. Understanding the early evolution of galaxies and the connection with the IGM remains one of the primary challenges in astrophysics.

I plan on constructing calibrated chemical evolution models of a wide range of galaxies and coupling these with semi-analytic models of hierarchical structure formation. This will replace the smoothly varying mass accretion histories employed in `GEtool` thus far with more realistic assembly histories. The resultant *cosmic* chemical evolution simulation will enable important and testable predictions to be made, such as: the colours and redshifts of dwarf and starbursting galaxies; the chemical evolution of DLAs; and the composition of the IGM. Recently, sophisticated attempts to simulate cosmic chemical evolution have been made (e.g. Cora et al. 2003; Nagashima & Okamoto 2004; Okoshi et al. 2004). However, these have monitored a very limited number of elements coming from Type II and Ia SNe only and don't take advantage of the detection of elements produced by intermediate-mass stars that are useful diagnostics of age and formation history. Moreover, galactic winds have either been ignored or treated simplistically. I plan to incorporate galactic winds and starbursts within cosmic chemical evolution models, with the goal of bridging the gap between galaxies and the IGM at low- and high-redshift. By following the abundance of the most extensive network of chemical isotopes up to Pb in any chemical evolution model to date, these models will have a unique capacity to interpret the growing database of detailed abundance patterns in quasar absorption systems and local dwarf galaxies.

Bibliography

- Abel, T., Bryan, G. L. & Norman, M. L. 2000, *ApJ*, 540, 39
- Abia, C., Domínguez, I., Straniero, O., Limongi, M., Chieffi, A. & Isern, J. 2001, *ApJ*, 557, 126
- Adams, F. C. & Laughlin, G. 1996, *ApJ*, 468, 586
- Alibés, A., Labay, J. & Canal, R. 2001, *A&A*, 370, 1103
- Allende Prieto, C., Lambert, D. L. & Asplund, M. 2001, *ApJL*, 556, L63
- Anders, E. & Grevesse, N. 1989, *GeCoA*, 53, 197
- André, M. K. et al. 2003, *ApJ*, 591, 1000
- Angulo C., Arnould M., Rayet M., et al. (NACRE collaboration), 1999, *Nuclear Physics A* 656, 3
- Argast, D., Samland, M., Thielemann, F. -K. & Gerhard, O. E. 2002, *A&A*, 388, 842
- Arimoto, N. & Yoshii, Y. 1987, *A&A*, 173, 23
- Arnone, E., Ryan, S. G., Argast, D., Norris, J. E., & Beers, T. C. 2005, *A&A*, 430, 507
- Arnould, M., Goriely, S. & Jorissen, A. 1999, *A&A*, 347, 572
- Ashenfelter T. P., Mathews G. J., Olive K. A., 2004a, *Phys. Rev. Lett.*, 92, 041102
- Ashenfelter T. P., Mathews G. J., Olive K. A., 2004b, *ApJ*, 615, 82
- Bazan, G. & Mathews, G.J. 1990, *ApJ*, 354, 644

- Beauchamp D., Hardy E., 1997, *AJ*, 113, 1666
- Berengut J. C., Dzuba V. A., Flambaum V. V., 2003, *Phys. Rev. A*, 68, 022502
- Bethe H. A., Salpeter E. E., 1977, *Quantum mechanics of one- and two-electron atoms*. Plenum, New York, NY, USA
- Bland-Hawthorn J., Jones D.H., 1998, *PASA*, 15, 44
- Bland-Hawthorn J., Kedziora-Chudczer L., 2003, *PASA*, 20, 242
- Boissier, S. & Prantzos, N. 2000, *MNRAS*, 312, 398
- Buser, R., Rong, J. & Karaali, S. 1998, *A&A*, 331, 934
- Calura, F., Matteucci, F. & Vladilo, G. 2003, *MNRAS*, 340, 59
- Calzetti, D., Harris, J., Gallagher, J. S., Smith, D. A., Conselice, C. J., Homeier, N., & Kewley, L. 2004, *AJ*, 127, 1405
- Campbell, S. W., 2005, in prep
- Cannon, R. D., Croke, B. F. W., Bell, R. A., Hesser, J. E. & Stathakis, R. A. 1998, *MNRAS*, 298, 601
- Carigi, L. 2000, *Revista Mexicana de Astronomia y Astrofisica*, 36, 171
- Carlsson J., Jonsson P., Godefroid M. R., Fischer C. F., 1995, *J. Phys. B*, 28, 3729
- Carretta, E., Gratton, R. G. & Sneden, C. 2000, *A&A*, 356, 238
- Carretta, E., Gratton, R., Cohen, J. G., Beers, T. C. & Christlieb, N. 2002, *AJ*, 124, 481
- Carter, B., 1983, in *Proc. R. Soc. Discussion Meeting on the Constants of Physics* ed McRea W. H. and Rees M. J., R. Soc. London and in *Philos. Trans. R. Soc. London* A310, 347
- Cayrel, R., et al. 2004, *A&A*, 416, 1117
- Centurión, M., Bonifacio, P., Molaro, P. & Vladilo, G. 2000, *ApJ*, 536, 540

- Centurión, M., Molaro, P., Vladilo, G., Péroux, C., Levshakov, S. A., & D'Odorico, V. 2003, *A&A*, 403, 55
- Chaboyer B., Sarajedini, A. & Armandroff, T.E. 2000, *AJ*, 120, 3102
- Chand H., Srianand R., Petitjean P., Aracil B., 2004a, *A&A*, 417, 853
- Chand H., Petitjean P., Srianand R., Aracil B., 2004b, *A&A*, accepted, preprint (astro-ph/0408200)
- Chen, B., Stoughton, C., Smith, J.A., et al. 2001, *ApJ*, 553, 184
- Chiappini, C., Matteucci, F. & Gratton, R. 1997, *ApJ*, 477, 765
- Chiappini, C., Matteucci, F. & Padoan, P. 2000, *ApJ*, 528, 711
- Chiappini, C., Matteucci, F. & Romano, D. 2001, *ApJ*, 554, 1044
- Chieffi, A. & Limongi, M., 2002, *ApJ* 577, 281
- Chieffi, A., Domínguez, I., Limongi, M. & Straniero, O. 2001, *ApJ*, 554, 1159
- Cid Fernandes, R. J., Storchi-Bergmann, T. & Schmitt, H. R. 1998, *MNRAS*, 297, 579
- Clark, D. H., McCrea, W. H. & Stephenson, F. R. 1977, *Nature*, 265, 318
- Clarke, J. N. 1981, *Icarus*, 46, 94
- Clarke, C. J. & Bromm, V. 2003, *MNRAS*, 343, 1224
- Cohen, J. G., Blakeslee, J. P., & Côté, P. 2003, *ApJ*, 592, 866
- Corsini, E. M., Pizzella, A., Coccato, L. & Bertola, F. 2003, *A&A*, 408, 873
- Corwin H.G., de Vaucouleurs A., de Vaucouleurs G., 1985, *Southern Galaxy Catalogue*. Univ. Texas, Austin
- Cottrell, P. L. & Da Costa, G. S., 1981, *ApJ*, 245L, 79
- Cowan, J. J., et al. 2005, *ApJ*, 627, 238
- Cowie L. L., Songaila A., 1995, *ApJ*, 453, 596

- Crocker D.A., Baugus P.D., Buta R., 1996, *ApJS*, 105, 353
- Dame, T. M. 1993, *AIP Conf. Proc.* 278: Back to the Galaxy, 278, 267
- D'Antona, F., Gratton, R. & Chieffi, A., 1983, *Mem. Soc. Astron. It.*, 54, 173
- D'Antona, F., Caloi, V., Montalbán, J., Ventura, P. & Gratton, R. 2002, *A&A*, 395, 69
- Darling J., 2003, *Phys. Rev. Lett.*, 91, 011301
- Dekel, A. & Silk, J. 1986, *ApJ*, 303, 39
- Denissenkov, P. A. & Herwig, F. 2003, *ApJL*, 590, L99
- Denissenkov, P. A. & Weiss, A. 2004, *ApJ*, 603, 119
- Dessauges-Zavadsky, M., Calura, F., Prochaska, J. X., D'Odorico, S., & Matteucci, F. 2004, *A&A*, 416, 79
- de Vaucouleurs G., de Vaucouleurs A., Corwin H.G., Buta R.J., Paturel G., Fouqué P., 1991, *Third Reference Catalogue of Bright Galaxies*. Springer-Verlag, New York
- Dinescu, D. L., Girard, T. M. & van Altena, W. F., 1999, *AJ* 117, 1792
- Dirac P. A. M., 1937, *Nat*, 139, 323
- Dopita, M.A. & Ryder, S.D. 1994, *ApJ*, 430, 163
- Drullinger R. E., Wineland D. J., Bergquist J. C., 1980, *Appl. Phys.*, 22, 365
- Durrell, P.R., Harris, W.E. & Pritchett, C.J. 2001, *AJ*, 121, 2557
ESA, 1997, *The Hipparcos and Tycho Catalogues*, ESA, SP-1200
- Dzuba V. A., Flambaum V. V., Webb J. K., 1999a, *Phys. Rev. A*, 59, 230
- Dzuba V. A., Flambaum V. V., Webb J. K., 1999b, *Phys. Rev. Lett.*, 82, 888
- Edvardsson, B., Andersen, J., Gustafsson, B., Lambert, D. L., Nissen, P. E. & Tomkin, J. 1993, *A&A*, 275, 101
- Eggen, O.J., Lynden-Bell, D. & Sandage, A.R. 1962, *ApJ*, 136, 748

- Elbaz, D., Arnaud, M. & Vangioni-Flam, E. 1995, *A&A*, 303, 345
- Eskridge, P. B., et al. 2003, *ApJ*, 586, 923
- Evans, I. N., Koratkar, A. P., Storchi-Bergmann, T., Kirkpatrick, H., Heckman, T. M. & Wilson, A. S. 1996, *ApJS*, 105, 93
- Faber S.M., Friel E.D., Burstein D., Gaskell C.M., 1985, *ApJS*, 57, 711
- Feltzing, S., Holmberg, J., & Hurley, J. R. 2001, *A&A*, 377, 911
- Fenner, Y. & Gibson, B. K. 2003, *Publications of the Astronomical Society of Australia*, 20, 189
- Fenner, Y., Gibson, B.K. & Limongi, M. 2002, *Ap&SS*, 281, 537
- Fenner, Y., Gibson, B. K., Lee, H.-c., Karakas, A. I., Lattanzio, J. C., Chieffi, A., Limongi, M. & Yong, D. 2003, *Publications of the Astronomical Society of Australia*, 20, 340
- Fenner, Y., Prochaska, J. X. & Gibson, B. K. 2004, *ApJ*, 606, 116
- Fenner, Y., Campbell, S., Karakas, A. I., Lattanzio, J. C. & Gibson, B. K. 2004, *MNRAS*, 280
- Fields, B. D. & Olive, K. A. 1999, *ApJ*, 516, 797
- Fields, B. D., Mathews, G. J. & Schramm, D. N. 1997, *ApJ*, 483, 625
- Fields, B. D., Freese, K. & Graff, D. S. 2000, *ApJ*, 534, 265
- Fields, B. D., Olive, K. A., Silk, J., Cassé, M. & Vangioni-Flam, E. 2001, *ApJ*, 563, 653
- Fisher, D., Franx, M. & Illingworth, G., 1996, *ApJ*, 459, 110
- Flynn, C., Holopainen, J. & Holmberg, J. 2003, *MNRAS*, 339, 817
- Friel E.D., Janes K.A., 1993, *A&A*, 267, 75
- Frost, C. A. & Lattanzio, J. C. 1996, *ApJ*, 473, 383
- Fujimoto, M. Y., Ikeda, Y. & Iben, I. J. 2000, *ApJL*, 529, L25

- Fujita, A., Mac Low, M., Ferrara, A., & Meiksin, A. 2004, *ApJ*, 613, 159
- García-Berro, E., Torres, S., Isern, J. & Burkert, A. 2004, *A&A*, 418, 53
- Gay P. L., Lambert D. L., 2000, *ApJ*, 533, 260
- Gibson, B.K. 1997, *MNRAS*, 290, 471
- Gibson, B. K. & Matteucci, F. 1997, *MNRAS*, 291, L8
- Gibson, B. K. & Mould, J. R. 1997, *ApJ*, 482, 98
- Gibson, B. K., Loewenstein, M., & Mushotzky, R. F. 1997, *MNRAS*, 290, 623
- Gibson, B.K., Giroux, M.L., Penton, S.V., Stocke, J.T., Shull, J.M. & Tumlinson, J. 2001, *AJ*, 547, 3280
- Gilmore, G., Reid, N. 1983, *MNRAS*, 202, 1025
- Gilmore, G., Wyse, R.F.G. & Kuijken, K. 1989, *ARA&A*, 27, 555
- Gilmore, G., Wyse, R.F.G., Jones, B.J., 1995, *AJ*, 109, 1095
- Gonzalez, G., Brownlee, D. & Ward, P. D. 2001a, *Scientific American*, 285, 52
- Gonzalez, G., Brownlee, D. & Ward, P. D. 2001b, *Icarus*, 152, 185
- Gonzalez Delgado, R. M., Perez, E., Tadhunter, C., Vilchez, J. M. & Rodriguez-Espinosa, J. M. 1997, *ApJS*, 108, 155
- Goswami, A. & Prantzos, N., 2000, *A&A*, 359, 191
- Gratton, R. G. et al., 2001, *A&A* 369, 87
- Greggio, L. & Renzini, A. 1983, *A&A*, 118, 217
- Griesmann U., Kling R., 2000, *ApJ*, 536, L113
- Grundahl, F., Briley, M, Nissen, P. E. & Feltzing, S. 2002, *A&A* 385, L14
- Gusten, R. & Mezger, P. G., 1982, *Vistas Astron.* 26, 159
- Haehnelt, M. G., Steinmetz, M. & Rauch, M. 1998, *ApJ*, 495, 647
- Hallstadius L., 1979, *Z. Phys. A*, 291, 203

- Hameed, S., Blank, D. L., Young, L. M. & Devereux, N. 2001, *ApJL*, 546, L97
- Hamuy, M., Walker, A. R., Suntzeff, N. B., Gigoux, P., Heathcote, S. R. & Phillips, M. M. 1992, *PASP*, 104, 533
- Hansen, B.M.S., Brewer, J., Fahlman, G.G., Gibson, B.K., Ibata, R., Limongi, M., Rich, R.M., Richer, H.B., Shara, M.M. & Stetson, P.B. 2002, *ApJ*, 574, L155
- Harris, G.L.H. & Harris, W.E. 2000, *AJ*, 120, 2423
- Harris, W.E. & Harris, G.L.H. 2002, *AJ*, 123, 3108
- Haywood, M. 2001, *MNRAS*, 325, 1365
- Henry, R. B. C., Worthey G., 1999, *PASP*, 111, 919
- Henry, R. B. C., Edmunds, M. G. & Köppen, J. 2000, *ApJ*, 541, 660
- Hernandez, X. & Ferrara, A. 2001, *MNRAS*, 324, 484
- Hoffman, R. D., Woosley, S. E., Fuller, G. M. & Meyer, B. S. 1996, *ApJ*, 460, 478
- Holweger, H. 2001, *AIP Conf. Proc.* 598: Joint SOHO/ACE workshop "Solar and Galactic Composition", 23
- Hou, J.L., Chang, R. & Fu, C. 1998, in *Pacific Rim Conference on Stellar Astrophysics*, ed. K.L. Chan, K.S. Cheng & H.P. Singh (San Francisco: ASP), p. 143
- Hoyle, F. 1946, *MNRAS*, 106, 343
- Huchra J.P., Brodie J.P., Caldwell N., Christian C., Schommer R., 1996, *ApJS*, 102, 29
- Ibata, R., Limongi, M., Rich, R.M., Richer, H.B., Shara, M.M. & Stetson, P.B. 2002, *ApJ*, 574, L155
- Ibukiyama, A. & Arimoto, N. 2002, *A&A*, 394, 927
- Idiart T.P., de Freitas Pacheco J.A., Costa R.D.D., 1996, *AJ*, 112, 2541
- Iliadis, C., et al. 1990, *Nucl. Phys. A*, 512, 509

- Iliadis, C., Buchmann, L., Endt, P. M., Herndl, H. & Wiescher, M. 1996, *Phys. Rev. C*, 53, 475
- Imbriani, G., Limongi, M., Gialanella, L., Terrasi, F., Straniero, O. & Chieffi, A., 2001, *ApJ*, 558, 903
- Ivans, I. I., Sneden, C., Kraft, R. P., Suntzeff, N. B., Smith, V. V., Langer, G. E. & Fulbright, J. P. 1999, *AJ*, 118, 1273
- Iwamoto, K., Brachwitz, F., Nomoto, K., Kishimoto, N., Umeda, H., Hix, W. R. & Thielemann, F. 1999, *ApJS*, 125, 439
- Jablonka, P., Gorgas, J., & Goudfrooij, P. 2002, *Ap&SS*, 281, 367
- Jehin, E., Magain, P., Neuforge, C., Noels, A. & Thoul, A. A., 1998, *A&A*, 330, L33
- Jones D.H., Shopbell P.L., Bland-Hawthorn J., 2002, *MNRAS*, 329, 759
- Kaeppler, F., et al. 1994, *ApJ*, 437, 396
- Karakas, A. I. & Lattanzio, J. C., 2003a, *Carnegie Observatories Astrophysics Series*, Vol. 4: *Origin and Evolution of the Elements*, ed. A. McWilliam and M. Rauch
- Karakas, A. I. & Lattanzio, J. C. 2003b, *Publications of the Astronomical Society of Australia*, 20, 279
- Kasting, J. F., Whitmire, D. P. & Reynolds, R. T. 1993, *Icarus*, 101, 108
- Kobayashi, C., Tsujimoto, T. & Nomoto, K. 2000, *ApJ*, 539, 26
- Koribalski B., Dickey J.M., 2004, *MNRAS*, 348, 1255
- Kotoneva, E., Flynn, C., Chiappini, C. & Matteucci, F. 2002, *MNRAS*, 336, 879
- Kozlov M. G., Korol V. A., Berengut J. C., Dzuba V. A., Flambaum V. V., 2004, *Phys. Rev. A*, submitted, preprint (astro-ph/0407579)
- Kraft, R. P. 1994, *PASP*, 106, 553
- Kroupa, P., 2001, *MNRAS*, 322, 231
- Kroupa, P., Tout, C. A. & Gilmore, G. 1993, *MNRAS*, 262, 545

- Kulkarni, V. P., Fall, S. M. & Truran, J. W. 1997, *ApJL*, 484, L7
- Kunz, R., Fey, M., Jaeger, M., Mayer, A., Hammer, J. W., Staudt, G., Harissopoulos, S. & Paradellis, T., 2002, *ApJ*, 567, 643
- Lacey, C. G., & Fall, S. M. 1983, *MNRAS*, 204, 791
- Lanfranchi, G. A. & Friaça, A. C. S. 2003, *MNRAS*, 343, 481
- Langer, N. 1996, *ASP Conf. Ser.* 112: The History of the Milky Way and Its Satellite System, 169
- Larson, R.B. 1974, *MNRAS*, 169, 229
- Larson, R.B. 1976, *MNRAS*, 176, 31
- Larson, R. B., 1998, *MNRAS*, 301, 569
- Laws, C., Gonzalez, G., Walker, K. M., Tyagi, S., Dodsworth, J., Snider, K. & Suntzeff, N. B. 2003, *AJ*, 125, 2664
- Le Brun, V., Bergeron, J., Boisse, P. & Deharveng, J. M. 1997, *A&A*, 321, 733
- Lee, H., Gibson, B. K., Fenner, Y., Brook, C. B., Kawata, D., Renda, A., Holopainen, J. & Flynn, C. 2004, *Publications of the Astronomical Society of Australia*, 21, 153
- Levshakov S. A., Centurion M., Molaro P., D'Odorico S., 2004, *A&A*, submitted, preprint (astro-ph/0408188)
- Limongi, M. & Chieffi, A. 2002, *Publications of the Astronomical Society of Australia*, 19, 246
- Limongi, M., & Chieffi, A. 2003, *ApJ*, 592, 404
- Limongi, M., Straniero, O. & Chieffi, A. 2000, *ApJS*, 129, 625
- Lineweaver, C. H. 2001, *Icarus*, 151, 307
- Livio, M. 1999, *ApJ*, 511, 429
- Lu, L., Sargent, W. L. W., Barlow, T. A., Churchill, C. W. & Vogt, S. S. 1996, *ApJS*, 107, 475

- Mackey, J., Bromm, V. & Hernquist, L. 2003, *ApJ*, 586, 1
- Maeder, A. 1992, *A&A*, 264, 105
- Maloney, P. R. & Bland-Hawthorn, J. 2001, *ApJL*, 553, L129
- Marcolini, A., Brighenti, F., & D'Ercole, A. 2004, *MNRAS*, 352, 363
- Marigo, P. 2001, *A&A*, 370, 194
- Márquez, I., et al. 1999, *A&AS*, 140, 1
- Martin P., 1998, in Friedli D., Edmunds M.G., Robert C., Drissen L., eds, ASP Conf. Ser. Vol. 147, Abundance Profiles: Diagnostic Tools for Galaxy History. Astron. Soc. Pac., San Francisco, p.68
- Matteucci, F. 2001, *The Chemical Evolution of the Galaxy*, Dordrecht:Kluwer
- Matteucci, F. & Greggio, L. 1986, *A&A*, 154, 279
- Matteucci, F. & Recchi, S. 2001, *ApJ*, 558, 351
- Matteucci, F. & Tornambé, A. 1987, *A&A*, 185, 51
- Matteucci, F., Raiteri, C. M., Busson, M., Gallino, R. & Gratton, R. 1993, *A&A*, 272, 421
- McKay, C. P., 1996, in *Circumstellar Habitable Zones*, ed Doyle L. R., Travis House Pub., Menlo Park CA, 405
- McWilliam, A. 1997, *ARA&A*, 35, 503
- McWilliam, A., Rich, R. M. & Smecker-Hane, T. A. 2003, *ApJL*, 592, L21
- Melendez, J., Barbuy, B. & Spite, F. 2001, *ApJ*, 556, 858
- Milne E. A., 1935, *Relativity, Gravitation and World Structure*. Clarendon Press, Oxford, UK
- Milne E. A., 1937, *Proc. R. Soc. A*, 158, 324
- Mishenina, T. V., Kovtyukh, V. V., Soubiran, C., Travaglio, C. & Busso, M. 2002, *A&A*, 396, 189

- Mollá M., Hardy E. & Beauchamp D., 1999, *ApJ*, 513, 695
- Mulchaey, J. S., Regan, M. W., & Kundu, A. 1997, *ApJS*, 110, 299
- Murphy M. T., Webb J. K., Flambaum V. V., Dzuba V. A., Churchill C. W., Prochaska J. X., Barrow J. D., Wolfe A. M., 2001a, *MNRAS*, 327, 1208
- Murphy M. T., Webb J. K., Flambaum V. V., Churchill C. W., Prochaska J. X., 2001b, *MNRAS*, 327, 1223
- Murphy M. T., Webb J. K., Flambaum V. V., Prochaska J. X., Wolfe A. M., 2001c, *MNRAS*, 327, 1237
- Murphy M. T., Webb J. K., Flambaum V. V., 2003, *MNRAS*, 345, 609
- Murphy M. T., Flambaum V. V., Webb J. K., Dzuba V. V., Prochaska J. X., Wolfe A. M., 2004, *Lecture Notes Phys.*, 648, 131
- Nakamura, F. & Umemura, M. 2001, *ApJ*, 548, 19
- Nakamura, T., Umeda, H., Nomoto, K., Thielemann, F. & Burrows, A. 1999, *ApJ*, 517, 193
- Nakamura, T., Umeda, H., Iwamoto, K., Nomoto, K., Hashimoto, M., Hix, W. R., & Thielemann, F. 2001, *ApJ*, 555, 880
- Nissen, P. E., Chen, Y. Q., Schuster, W. J. & Zhao, G. 2000, *A&A*, 353, 722
- Norris, J.E. & Ryan, S.G., 1991, *ApJ*, 380, 403
- Norris, J., Cottrell, P. L., Freeman, K. C. & Da Costa, G. S. 1981, *ApJ*, 244, 205
- Norris, J. E., Beers, T. C., & Ryan, S. G. 2000, *ApJ*, 540, 456
- Omukai, K. & Yoshii, Y. 2003, *ApJ*, 599, 746
- Outram, P. J., Chaffee, F. H. & Carswell, R. F. 1999, *MNRAS*, 310, 289
- Pagel, B. E. J. 2001, *PASP*, 113, 137
- Pagel, B.E.J. & Patchett, B.E. 1975, *MNRAS*, 172, 13

- Parmentier, G., Jehin, E., Magain, P., Neuforge, C., Noels, A. & Thoul, A. A., 1999, A&A, 352, 138
- Pastoriza, M. G., Donzelli, C. J. & Bonatto, C. 1999, A&A, 347, 55
- Payne, C. H. 1925, Ph.D. Thesis
- Petitjean P., Aracil B., 2004b, A&A, 422, 523
- Pettini, M., Ellison, S. L., Steidel, C. C. & Bowen, D. V. 1999, ApJ, 510, 576
- Pettini, M., Ellison, S. L., Steidel, C. C., Shapley, A. E. & Bowen, D. V. 2000, ApJ, 532, 65
- Pickering J. C., Thorne A. P., Webb J. K., 1998, MNRAS, 300, 131
- Portinari, L. & Chiosi, C. 1999, A&A, 350, 827
- Portinari, L. & Chiosi, C. 2000, A&A, 355, 929
- Powell, D. C., Iliadis, C., Champagne, A. E., Grossmann, C. A., Hale, S. E., Hansper, V. Y. & McLean, L. K., 1999, Nucl. Phys. A, 660, 349
- Prantzos, N. & Ishimaru, Y. 2001, A&A, 376, 751
- Prantzos, N. & Silk, J., 1998, ApJ, 507, 229
- Prochaska, J. X. 2003, ApJ, 582, 49
- Prochaska, J. X. & Wolfe, A. M. 1997, ApJ, 487, 73
- Prochaska, J. X. & Wolfe, A. M. 2002, ApJ, 566, 68
- Prochaska, J. X., Henry, R. B. C., O'Meara, J. M., Tytler, D., Wolfe, A. M., Kirkman, D., Lubin, D. & Suzuki, N. 2002, PASP, 114, 933
- Prochaska, J. X., Gawiser, E., Wolfe, A. M., Cooke, J. & Gelino, D. 2003, ApJS, 147, 227
- Prochaska, J. X., Howk, J. C. & Wolfe, A. M. 2003, Nature, 423, 57
- Proctor, R. N. & Sansom, A. E. 2002, MNRAS, 333, 517
- Quast R., Reimers D., Levshakov S. A., 2004b, A&A, 415, L7

- Raimann, D., Storchi-Bergmann, T., Bica, E., & Alloin, D. 2001, MNRAS, 324, 1087
- Rao, S. M., Nestor, D. B., Turnshek, D. A., Lane, W. M., Monier, E. M. & Bergeron, J. 2003, ApJ, 595, 94
- Recchi, S., Matteucci, F. & D'Ercole, A. 2001, MNRAS, 322, 800
- Reimers, D. 1975, Memoires of the Societe Royale des Sciences de Liege, 8, 369
- Renzini, A. & Voli, M. 1981, A&A, 94, 175
- Robin, A.C., Reylé, C., Derrière, S. & Picaud, S. 2003, A&A, 409, 523
- Rocha-Pinto, H.-J. & Maciel, W.J. 1996, MNRAS, 279, 447
- Rocha-Pinto, H.-J. & Maciel, W.J. 1997, A&A, 325, 523
- Rocha-Pinto, H. J., Scalo, J., Maciel, W. J., & Flynn, C. 2000, ApJL, 531, L115
- Romano, D., Matteucci, F., Salucci, P. & Chiappini, C. 2000, ApJ, 539, 235
- Rosman K. J. R., Taylor P. D. P., 1998, J. Phys. Chem. Ref. Data, 27, 1275
- Russell, H. N. 1929, ApJ, 70, 11
- Ryan, S. G. Norris, J. E. & Beers, T. C. 1996, ApJ, 471, 254
- Ryan, S. G. 2000, Liege International Astrophysical Colloquia, 35, 101
- Ryder S.D., 1995, ApJ, 444, 610
- Salpeter, E. E. 1955, ApJ, 121, 161
- Sandage A., Bedke J., 1994, The Carnegie Atlas of Galaxies (Washington: Carnegie Inst.)
- Santos, N. C., Israelian, G., Mayor, M., Rebolo, R. & Udry, S. 2003, A&A, 398, 363
- Saraiva Schroeder, M. F., Pastoriza, M. G., Kepler, S. O. & Puerari, I. 1994, A&AS, 108, 41
- Savage, B. D. & Sembach, K. R. 1996, ApJ, 470, 893
- Scalo, J. M., 1986, Fund. Cosm. Phys., 11, 1

- Scalo, J. & Wheeler, J. C. 2002, *ApJ*, 566, 723
- Schaller, G., Schaerer, D., Meynet, G. & Maeder, A. 1992, *A&AS*, 96, 269
- Schmidt, M. 1959, *ApJ*, 129, 243
- Searle, L. & Zinn, R. 1978, *ApJ*, 225, 357
- Sembach, K.R., Gibson, B.K., Fenner, Y. & Putman, M.E. 2002, *ApJ*, 572, 178
- Shaver P.A., McGee R.X., Newton L.M., Danks A.C., Pottasch S.R., 1983, *MNRAS*, 204, 5
- Sheinis, A. I., Bolte, M., Epps, H. W., Kibrick, R. I., Miller, J. S., Radovan, M. V., Bigelow, B. C. & Sutin, B. M. 2002, *PASP*, 114, 851
- Shetrone, M. D., Côté, P. & Sargent, W. L. W. 2001, *ApJ*, 548, 592
- Shetrone, M., Venn, K. A., Tolstoy, E., Primas, F., Hill, V., & Kaufer, A. 2003, *AJ*, 125, 684
- Shigeyama, T., Tsujimoto, T. & Yoshii, Y. 2003, *ApJ*, 586, L57
- Smartt, S.J. & Rolleston, W.R.J. 1997, 481, L47
- Smecker-Hane, T.A. & Wyse, R.F.G. 1992, *AJ*, 103, 1621
- Smith, G., 1999, *PASP* 762, 980
- Smith, G. H. & Norris, J. E. 1993, *AJ*, 105, 173
- Snedden, C., & Cowan, J. J. 2003, *Science*, 299, 70
- Snedden, C., Kraft, R. P., Guhathakurta, P., Peterson, R. C., & Fulbright, J. P. 2004, *AJ*, 127, 2162
- Sommer-Larsen, J., Götz, M., & Portinari, L. 2003, *ApJ*, 596, 47
- Srianand R., Chand H., Petitjean P., Aracil B., 2004, *Phys. Rev. Lett.*, 92, 121302
- Sterling, N. C., & Dinerstein, H. L. 2003, *Revista Mexicana de Astronomia y Astrofisica Conference Series*, 18, 133
- Sterling, N. C., Dinerstein, H. L., & Bowers, C. W. 2002, *ApJL*, 578, L55

- Suntzeff, N. B. & Smith, V. V. 1991, *ApJ*, 381, 160
- Thielemann, F.-K., Nomoto, K. & Yokoi, K. 1986, *A&A*, 158, 17
- Thielemann, F., Arnould, M. & Truran, J. W. 1991, in *Advances of Nuclear Astrophysics*, ed. E. Vangioni-Flam et al. (France: Editions Frontières), 525
- Thielemann, F.-K., Nomoto, K., Hashimoto, M., 1993, in Prantzos, N., Vangioni-Flam, E., Casse, M., eds, *Origin and Evolution of the Elements*, Cambridge Univ. Press, Cambridge, p. 297
- Thoul, et al. 2002, *A&A* 383, 491
- Timmes F. X., Woosley S. E., Weaver T. A., 1995, *ApJS*, 98, 617
- Tinsley, B. M. 1980, *Fundamentals of Cosmic Physics*, 5, 287
- Tolstoy, E. 2003, *A Decade of Hubble Space Telescope Science*, 128
- Trager S.C., Worthey G., Faber S.M., Burstein D., González J.J., 1998, *ApJS*, 116, 1
- Travaglio, C., Gallino, R., Busso, M. & Gratton, R. 2001, *ApJ*, 549, 346
- Travaglio, C., Kifonidis, K. & Müller, E. 2003, *Carnegie Observatories Astrophysics Series*, Vol. 4: *Origin and Evolution of the Elements*, eds. A. McWilliam and M. Rauch
- Trimble, V., 1997, *Origin of Life and Evolution of the Biosphere*, 27, 3
- Tripicco M.J., Bell R.A., 1995, *AJ*, 110, 3035
- Tucker, W. H., 1981, in *Life in the Universe*, ed J. Billingham, MIT Press, Cambridge MA.
- Twarog B.A., 1980, *ApJ*, 242, 242
- Umeda, H. & Nomoto, K. 2002, *ApJ*, 565, 385
- Uzan J., 2003, *Rev. Mod. Phys.*, 75, 403
- van den Hoek, L. B. & Groenewegen, M. A. T. 1997, *A&AS*, 123, 305

- van der Kruit, P.C. & Searle, L. 1982, *A&A*, 110, 79
- Varshalovich D. A. & Potekhin A. Y., 1994, *Astron. Lett.*, 20, 771
- Varshalovich D. A., Panchuk V. E., Ivanchik A. V., 1996, *Astron. Lett.*, 22, 6
- Varshalovich D. A., Potekhin A. Y., Ivanchik A. V., 2000, in Dunford R. W., Gemmel D. S., Kanter E. P., Kraessig B., Southworth S. H., Young L., eds, *AIP Conf. Proc. Vol. 506, X-Ray and Inner-Shell Processes*. Argonne National Laboratory, Argonne, IL, USA, p. 503
- Vassiliadis, E. & Wood, P. R. 1993, *ApJ*, 413, 641
- Vennes, S., Chayer, P., & Dupuis, J. 2005, *ApJL*, 622, L121
- Vila-Costas M.B., Edmunds M.G., 1992, *MNRAS*, 259, 121
- Vladilo, G. 2002, *A&A*, 391, 407
- Wakker, B.P., Howk, J.C., Savage, B.D., van Woerden, H., Tufte, S.L., Schwarz, U.J., Benjamin, R., Reynolds, R. J., Peletier, R. F. & Kalberla, P. M. W. 1999, *Nature*, 402, 388
- Wang, B. & Silk, J. 1993, *ApJ*, 406, 580
- Webb J. K., Flambaum V. V., Churchill C. W., Drinkwater M. J., Barrow J. D., 1999, *Phys. Rev. Lett.*, 82, 884
- Webb J. K., Murphy M. T., Flambaum V. V., Dzuba V. A., Barrow J. D., Churchill C. W., Prochaska J. X., Wolfe A. M., 2001, *Phys. Rev. Lett.*, 87, 091301
- White, R. L. et al. 2000, *ApJS*, 126, 133
- Woosley, S. E. & Hoffman, R. D. 1992, *ApJ*, 395, 202
- Woosley, S. E. & Weaver, T. A. 1995, *ApJS*, 101, 181
- Worthey, G. & Espana, A.L. 2003, *Carnegie Observatories Astrophysics Series, Vol. 4: Origin and Evolution of the Elements*, eds. A. McWilliam and M. Rauch
- Worthey, G., Faber, S. M., Gonzalez, J. J. & Burstein, D. 1994, *ApJS*, 94, 687

- Wyse, R.F.G. 2001, in ASP Conf. Ser. 230, Galaxy Disks and Disk Galaxies, eds. J. G. Funes & E. M. Corsini (San Francisco: ASP), 71
- Wyse, R.F.G. & Gilmore, G. 1993, ASP Conf. Ser. 48: The Globular Cluster-Galaxy Connection, 727
- Wyse, R.F.G. & Gilmore, G. 1995, AJ, 110, 2771
- Wyse, R.F.G. & Gilmore, G. 1988, AJ, 95, 1404
- Yong, D. & Lambert, D. L., 2003, PASP, 115, 22
- Yong D., Grundahl F., Lambert D. L., Nissen P. E., Shetrone M. D., 2003a, A&A, 402, 985
- Yong D., Lambert D. L., Ivans I. I., 2003b, ApJ, 599, 1357
- Yoshii, Y. & Rodgers, A.W. 1989, AJ, 98 853
- Zaritsky D., Kennicutt R.C., Huchra J.P., 1994, ApJ, 420, 87
- Zinnecker, H. 2004, IAU Symposium, 213, 45

Appendix A

Nomenclature

The following glossary defines the various mathematical symbols and acronyms used throughout the thesis.

AGB	Asymptotic giant branch
AMR	Age-metallicity relation
GC	Globular cluster
DLA	Damped Lyman- α absorber
GCE	Galactic Chemical Evolution
HBB	hot-bottom burning
IMS	Intermediate-mass star
ISM	Interstellar medium
IMF	Initial mass function
IMS	Intermediate-mass star
LIMS	Low- and intermediate-mass star
LTE	Local thermodynamic equilibrium
MDF	Metallicity distribution function
QSO	Quasar
SFE	Star-formation efficiency
SFR	Star-formation rate
SN II	Type II supernova
SN Ia	Type Ia supernova
Z	Mass fraction of metals (metallicity)
z	Redshift
M_{\odot}	Unit: Solar mass (mass; $\sim 1.99 \times 10^{30}$ kg)
α	Fine-structure constant
σ_{gas}	Gas mass surface density
ψ	Star formation rate
ϕ	Initial mass function
Y_i	Stellar yield of element i (in mass units)